

AARETTI KALEVA

# Zinc Surface Functionalization: Artificial Patination with CO<sub>2</sub>



AARETTI KALEVA

Zinc Surface Functionalization:  
Artificial Patination with CO<sub>2</sub>

ACADEMIC DISSERTATION

To be presented, with the permission of  
the Faculty of Engineering and Natural Sciences  
of Tampere University,  
for public discussion in the Pieni Sali 1  
of the Festia building, Korkeakoulunkatu 6, Tampere,  
on 12<sup>th</sup> of March 2021, at 12 o'clock.

ACADEMIC DISSERTATION

Tampere University, Faculty of Engineering and Natural Sciences  
Finland

*Responsible  
supervisor  
and Custos*

Professor Erkki Levänen  
Tampere University  
Finland

*Supervisors*

Antti Markkula  
SSAB Europe Oy  
Finland

Juha-Pekka Nikkanen  
Tampere University  
Finland

*Pre-examiners*

Dr. Michael Rohwerder  
Max Planck Institut für  
Eisenforschung GmbH  
Germany

Professor Polina Volovitch  
Nationale Supérieure de Chimie de  
Paris  
France

*Opponents*

Dr. Michael Rohwerder  
Max Planck Institut für  
Eisenforschung GmbH  
Germany

Dr. Ralph Bäßler  
Federal Institute for Materials  
Research and Testing  
Germany

The originality of this thesis has been checked using the Turnitin OriginalityCheck service.

Copyright ©2021 author

Cover design: Roihu Inc.

ISBN 978-952-03-1875-8 (print)

ISBN 978-952-03-1876-5 (pdf)

ISSN 2489-9860 (print)

ISSN 2490-0028 (pdf)

<http://urn.fi/URN:ISBN:978-952-03-1876-5>

PunaMusta Oy – Yliopistopaino  
Joensuu 2021

Dedicated to my wife Thanida for enduring me throughout this journey, being there for me, and for the sacrifices you made to make this possible.



# PREFACE

“There are no mistakes, just happy little accidents.”

–Bob Ross (Artist)

As with many of life’s wondrous things, this doctoral dissertation also started with the preceding thought while experimenting in the laboratory. The initial discovery was then developed so that it would solve real-life problems in two separate industries while contributing to sustainable development in those domains. The dissertation was completed at Tampere University from 2017 to 2020. This journey was a great experience for me personally by getting to work with exceptional people, learning from them and seeing myself develop throughout the process. I would like to express my gratitude to these exceptional people here.

I would like first to thank Mr. Antti Markkula, Dr. Pasi Väisänen and the whole SSAB organization for the research funding and providing significant independence in conducting this project. Thank you also to the Doctoral School of Industrial Innovations (DSII) and Tampere University for introducing a great concept for companies and doctoral students to solve real and meaningful problems together.

Thank you to Dr. Juha-Pekka Nikkanen and Prof. Erkki Levänen for supervising the thesis and your substantial effort in guiding me in all aspects of the research. I want to express great thanks to Dr. Ville Saarimaa for his exceptional support, help and advice throughout the entire process without which this thesis would not have been completed in the time nor as well as it has been. Thank you, Dr. Thierry Tassaing, and Dr. Gwenaëlle Le Bourdon from Bordeaux University, who kindly welcomed me to their facilities and supported me in answering some of the most fundamental problems within the research as well as ensuring a pleasant time in Bordeaux during my experiments. Thank you to also all co-authors Mr. Leo Hyvärinen, for performing the XRD measurements, Dr. Mari Honkanen for the TEM imaging and Dr. Tommi Vuorinen from VTT for conducting the band-gap determination. Thank you also to all co-authors from Top Analytica Dr. Ville Saarimaa, Dr. Jyrki Juhanoja, Dr. Jere Manni, Dr. Tero Laihininen, Dr. Carl Lange and Dr. Teemu Paunikallio.

I want to thank all people from the Materials Science unit. Thank you very much to friends and colleagues who helped me during these years: Arnold Ismailov, Saara Söyrinki, Matti Järveläinen, Setareh Zakeri, Risto Kari, Nelli Palmu, Niina Merilaita, Teemu Vastamäki, and especially Amandeep Singh, whom with we shared the most insightful coffee break discussions as well as a near-simultaneous doctoral journey.

I am very grateful to my parents Hannu Kaleva and Tiina Tuulasvaara-Kaleva who always supported and encouraged me as well as raising me to be the person that I now am. I am also grateful to my sister Veera Kaleva and my cousin Seppo Anttola for their support with everything. Finally, I am tremendously grateful to my wife Thanida who decided to move across the world without hesitation, encouraged me and showed understanding during the best and the worst times for me to be able to finish this PhD.

In Tampere, September 6<sup>th</sup> 2020

**Aaretti Kaleva**



# ABSTRACT

Material processing technologies are required to be increasingly cleaner and safer for the globe to prevent excessive exposure to toxins and pollutants. This work presents a solution for two processes that currently use such harmful chemicals. The method uses pressurized carbon dioxide ( $\text{CO}_2$ ) to produce an artificial patina on metallic zinc. The artificial patina shows promise in enhancing corrosion protection and promoting adhesion of organic coatings applied on hot-dip galvanized steels that are currently treated with other chemicals for the same effect. Additionally, the artificial patina can be converted into distinct zinc oxide ( $\text{ZnO}$ ) nanostructures that could have applications in, e.g. antibacterial surfaces, gas sensors or solar cells.

The thesis details a holistic description of the treatment method by exploring the fundamental interactions and formation mechanisms of the artificial patina. The artificial patina could be formed uniformly throughout a substrate surface using a supercritical carbon dioxide ( $\text{scCO}_2$ ) treatment together with only water or with the addition of catalysts. The supercritical treatment was able to form a homogeneous layer of the artificial patina on the substrate surfaces. The formed artificial patina was composed of zinc carbonate ( $\text{ZnCO}_3$ ) as well as a new kind of zinc hydroxy carbonate compound with a nanowire morphology.

The chemistry and structure of the carbonates were advantageous for applying organic coatings onto the hot-dip galvanized surfaces, and they created a dense barrier layer that could help prevent corrosion. The artificial patina could be converted to  $\text{ZnO}$  with a simple heat-treatment which produced semiconducting  $\text{ZnO}$  nanostructures. Therefore, this method could help by reducing the usage of harmful chemicals significantly, achieving a comparable outcome only  $\text{CO}_2$  and water in a facile and environmentally-friendly process.

# CONTENTS

Preface .....	iii
Abstract.....	v
Abbreviations and symbols .....	viii
Original publications .....	x
Author's contribution.....	xi
1 Introduction .....	13
2 Zinc and zinc oxide coatings .....	15
2.1 Zinc coatings.....	15
2.1.1 Galvanizing process .....	16
2.1.2 Surface pretreatments of zinc coatings.....	18
2.1.3 Organic coatings on zinc.....	19
2.2 Zinc oxide nanostructures .....	20
2.2.1 Synthesis of nanosized ZnO coatings.....	21
2.2.2 Properties and applications.....	24
2.3 Corrosion of zinc and electrochemical reactions.....	26
2.3.1 Corrosion reactions.....	27
2.3.2 Atmospheric corrosion.....	29
3 Processing with carbon dioxide and carbonation .....	31
3.1 Utilization of carbon dioxide .....	31
3.2 Supercritical carbon dioxide (scCO <sub>2</sub> ).....	33
3.3 Carbon dioxide in aqueous environment.....	35
4 The purpose of the study .....	38
5 Materials and methods.....	40
5.1 Materials.....	40
5.2 Supercritical carbon dioxide (scCO <sub>2</sub> ) treatment .....	41
5.2.1 ScCO <sub>2</sub> -treatment procedure (Publications I – IV) .....	41
5.2.2 In-situ scCO <sub>2</sub> and droplet test procedure (Publication V) .....	43

5.2.3	Isotope water droplet tests (Publication VI) .....	44
5.3	Characterization techniques .....	44
6	Artificial patina formation .....	47
6.1	The carbon dioxide treatment .....	47
6.1.1	Reactions and phenomena during the isostatic holding phase of the scCO <sub>2</sub> treatment .....	49
6.1.2	Reactions and phenomena during the dynamic depressurization phase of the scCO <sub>2</sub> treatment .....	54
6.2	Characterization of the carbonate structures .....	60
6.2.1	Zinc carbonate (ZnCO <sub>3</sub> ) structure .....	60
6.2.2	Needle carbonate structure .....	62
7	Applications of artificial patina .....	66
7.1	Pretreatment for hot-dip galvanized substrates .....	66
7.2	Conversion to ZnO structures .....	69
8	Concluding remarks .....	73
8.1	Future research suggestions .....	75
	Bibliography .....	76
	Publications .....	76

# ABBREVIATIONS AND SYMBOLS

## Symbols

$\rho$	Density
$E_g$	Band-gap energy
$e^-$	Electron
$h^+$	Electron hole
E	Energy
$\nu$	Resonance mode of a molecule detected in FTIR
T	Temperature
P	Pressure

## Abbreviations

APBR	Automatic back-pressure regulator
CO <sub>2</sub>	Carbon dioxide gas
CO <sub>3</sub> <sup>2-</sup>	Carbonate ion
Cu(hfac) <sub>2</sub>	Copper (II) hexafluoro acetyl acetonate hydrate
CVD	Chemical vapor deposition
EDS	Energy dispersive x-ray spectroscopy
EPMA	Electron probe microanalyzer
eV	Electron volt
FE-SEM	Field emission scanning electron microscopy
FTIR	Fourier transform infrared spectroscopy
GIXRD	Grazing-incidence x-ray diffraction spectroscopy
H <sub>2</sub>	Hydrogen molecule
H <sup>+</sup>	Hydrogen ion
H <sub>2</sub> CO <sub>3</sub>	Carbonic acid
HCO <sub>3</sub> <sup>-</sup>	Bicarbonate ion
HDG	Hot-dip galvanized

H <sub>2</sub> O	Water
ITO	Indium-tin-oxide
NaCl	Sodium chloride
NHE	Normal hydrogen electrode
O <sub>2</sub>	Oxygen molecule
OH <sup>-</sup>	Hydroxyl ion
PVD	Physical vapor deposition
scCO <sub>2</sub>	Supercritical carbon dioxide
SEM	Scanning electron microscopy
SO <sub>2</sub>	Sulfur dioxide
TEM	Transmission electron microscopy
ToF-SIMS	Time-of-flight secondary ion mass spectrometry
VLS	Vapor-liquid-solid
XRD	X-ray diffraction spectroscopy
XPS	X-ray photon spectroscopy
Zn	Metallic zinc
Zn <sup>2+</sup>	Zinc ion
ZnO	Zinc oxide
Zn(OH) <sub>2</sub>	Zinc hydroxide
Zn(OH) <sub>4</sub> <sup>2-</sup>	Zincate ion
Zn <sub>5</sub> (CO <sub>3</sub> ) <sub>2</sub> (OH) <sub>6</sub>	Hydrozincite
Zn <sub>a</sub> (CO <sub>3</sub> ) <sub>b</sub> (OH) <sub>c</sub> ·dH <sub>2</sub> O	Zinc hydroxy carbonate with water of crystallization

# ORIGINAL PUBLICATIONS

- Publication I **A. Kaleva**, V. Saarimaa, S. Heinonen, J.-P. Nikkanen, A. Markkula, P. Väisänen, E. Levänen, Dissolution-induced nanowire synthesis on hot-dip galvanized surface in supercritical carbon dioxide, *Nanomaterials*. 7 (2017) 181.
- Publication II **A. Kaleva**, J.-P. Nikkanen, S. Heinonen, V. Saarimaa, T. Vuorinen, M. Honkanen, L. Hyvärinen, E. Levänen, Synthesis of ZnO nanowires with supercritical carbon dioxide and post heat treatment, *Nanotechnology*. 29 (2018) 445601.
- Publication III V. Saarimaa, **A. Kaleva**, J.-P. Nikkanen, S. Heinonen, E. Levänen, P. Väisänen, A. Markkula, J. Juhanoja, Supercritical carbon dioxide treatment of hot dip galvanized steel as a surface treatment before coating, *Surf. Coatings Technol.* 331 (2017) 137–142.
- Publication IV V. Saarimaa, **A. Kaleva**, J.-P. Nikkanen, J. Manni, C. Lange, T. Paunikallio, T. Laihin, S. Heinonen, E. Levänen, P. Väisänen, A. Markkula, Tailoring of Versatile Surface Morphologies on Hot Dip Galvanized Steel in Wet CO<sub>2</sub>: Aspects on Formation, Barrier Properties, and Utilization as a Substrate for Coatings, *ACS Appl. Mater. Interfaces*. 10 (2018) 21730–21739.
- Publication V **A. Kaleva**, T. Tassaing, V. Saarimaa, G. Le Bourdon, P. Väisänen, A. Markkula, E. Levänen. Formation of corrosion products on zinc in supercritical and subcritical CO<sub>2</sub>: In-situ spectroscopic study. *Corros. Sci.* 174 (2020) 108850.
- Publication VI V. Saarimaa, **A. Kaleva**, J.-P. Nikkanen, E. Levänen, P. Väisänen, A. Markkula. Time-of-flight secondary ion mass spectrometry study of zinc carbonation in the presence of stable oxygen-18 and deuterium isotopes. *Mat. Chem. Phys.* 256 (2020) 123673.

# AUTHOR'S CONTRIBUTION

- Publication I The author planned, designed and executed all sample preparations and FTIR characterizations. The author was also the corresponding author for the publication and performed analysis and discussions presented in the manuscript with support from the co-authors. SEM investigations were performed by Dr. Saara Söyrinki (née Heinonen), XPS characterization and analysis was performed by Dr. Ville Saarimaa from Top Analytica. Prof. Erkki Levänen, Dr. Juha-Pekka Nikkanen, Mr. Antti Markkula and Dr. Pasi Väisänen supervised the study and commented on the manuscript.
- Publication II The author planned, designed and executed all sample preparations and the FTIR characterizations. The author was also the corresponding author for the publication and performed analysis and discussions presented in the manuscript with support from the co-authors. SEM investigations were performed by Dr. Saara Söyrinki and band-gap determinations were conducted by Dr. Tommi Vuorinen from VTT Technical Research Centre of Finland. XRD characterizations were performed by Mr. Leo Hyvärinen. Prof. Erkki Levänen and Dr. Juha-Pekka Nikkanen supervised the study and commented on the manuscript.
- Publication III The author planned, designed and executed all sample preparations regarding the CO<sub>2</sub> treatments and assisted in the analysis, discussion as well as manuscript planning and commenting. Dr. Ville Saarimaa was the corresponding author and performed the application of the coil coating as well as the XPS, contact angle measurements characterizations, analysis and manuscript writing. Prof. Erkki Levänen, Mr. Antti Markkula and Dr. Pasi Väisänen supervised the study and commented on the manuscript.

Publication IV The author planned, designed and executed all sample preparations regarding the CO<sub>2</sub> treatments and assisted in the analysis, discussion as well as manuscript planning and commenting. Dr. Ville Saarimaa was the corresponding author and performed the application of the coil coating as well as the XPS, ToF-SIMS, SEM and FTIR characterizations, analysis and manuscript writing. Dr. Teemu Paunikallio assisted in Raman characterizations. Dr. Carl Lange and Dr. Tero Laihinen performed the contact angle measurements. Dr. Jere Manni was responsible of cross-section preparation for SEM analysis. Dr. Saara Heinonen commented the manuscript. Dr. J.-P. Nikkanen, Prof. Erkki Levänen, Mr. Antti Markkula, Dr. Pasi Väisänen and PhL Jyrki Juhanoja supervised the study and commented on the manuscript.

Publication V The author planned, designed and executed all sample preparations and characterizations. The author was also the corresponding author for the publication and performed analysis and discussions presented in the manuscript with support from the co-authors. The apparatus used in the infrared and Raman measurements tests were provided by Dr. Thierry Tassaing and Dr. Gwenaëlle le Bourdon from Bordeaux University. They also helped with the spectroscopic analysis and setting up the experiments. XRD characterizations were performed by Mr. Leo Hyvärinen. Prof. Erkki Levänen, Mr. Antti Markkula and Dr. Pasi Väisänen supervised the study and commented on the manuscript.

Publication VI The author planned, designed and executed the sample preparations regarding the CO<sub>2</sub> treatments and assisted in the analysis, discussion as well as manuscript planning and commenting. Dr. Ville Saarimaa was the corresponding author and performed the ToF-SIMS characterizations, SEM imaging, analysis and manuscript writing. Prof. Erkki Levänen, Mr. Antti Markkula and Dr. Pasi Väisänen supervised the study and commented on the manuscript.



# 1 INTRODUCTION

Sustainable and clean technologies have never been more sought-after than in the current state of the world. Often, in materials processing, harmful chemicals or energy-intensive methods are used to obtain the wanted material properties which result in pollution of the earth's soil, water and atmosphere. Therefore, it is necessary to develop safer material processing methods. The purpose of this thesis is to introduce such a method which has direct applications in two industries where it can help to reduce the use of harmful chemicals and create more sustainable processes. The method uses pressurized carbon dioxide ( $\text{CO}_2$ ) and water to produce a functionalized zinc surface that we call an artificial patina.

Zinc and zinc oxide ( $\text{ZnO}$ ) materials are used everywhere from common applications like house roofs to more specialized applications such as gas sensors. The versatility of the materials' end-applications has been made possible by the development of many processing techniques.

The most common use of zinc is in galvanized steel, in which a thin zinc coating provides steel with enhanced corrosion prevention due to its sacrificial role. Hot-dip galvanizing is the prevailing galvanizing technique, in which steel is immersed in molten zinc. Hot-dip galvanized steel is used to construct e.g. light poles, façades, roofs and car panels. Due to its noticeable outdoor end-uses, aesthetics and corrosion resistance play vital roles in the functionality of the material. Therefore, it is often favourable to paint hot-dip galvanized steel, but the poor adherence of paint to the zinc surface necessitates an additional process step [1, 2] that is often performed using harmful chemicals [3]. Alternatively, hot-dip galvanized steel can be installed at the end location and its surface left to be weathered in the surrounding atmospheric conditions. After reacting with water, oxygen and  $\text{CO}_2$  from the air, the zinc surface will be covered with a natural patina layer consisting of zinc corrosion products. The patina layer promotes adhesion with the paints that can then be applied on the hot-dip galvanized surface. However, the natural patina can take years to develop and its composition and stability are difficult to control. Consequently, natural patina is less used for adhesion promotion due to its drawbacks [4, 5]. The artificial patination method, in contrast, does not need harmful chemicals nor long

formation times. Furthermore, the method exhibits high reproducibility and control over the composition of the artificial patina structures.

The oxidized form of zinc is ZnO which is most commonly used in cosmetic products. However, its semiconductor properties have found use also in high-end technology applications such as solar cells, gas sensors, antibacterial surfaces and piezoelectric devices. Most of these applications require nanostructured ZnO with highly tailored morphologies, such as nanowires. Synthesizing such nanomaterials of ZnO is usually done by using expensive and often harmful chemicals as well as energy-intensive and time-consuming techniques [6, 7]. The artificial patination method, in contrast, can be used to produce ZnO films and nanowires using only CO<sub>2</sub> and water.

Carbon dioxide (CO<sub>2</sub>) is a side product of many harmful and energy-intensive processes, and it is posed as the leading cause of current global environmental problems. Almost paradoxically, however, CO<sub>2</sub> can be used directly in many processes as an extremely safe and clean processing gas. CO<sub>2</sub> is non-toxic and non-flammable, which makes it easy for workers to handle and for the environment. It is also inexpensive, and easily and abundantly available, which makes it economically viable for many applications [8–10]. The economic case for using CO<sub>2</sub> are increasingly alluring due to changes in the political climate and governmental incentives [8, 11].

The aim of this thesis is first to introduce the method for producing the artificial patina. A holistic description of the principles, interactions and reactions relevant for the technique are presented to outline the possibilities of the method. Furthermore, the two industrial applications are presented as case studies to evaluate the artificial patination method's feasibility in the applications while comparing it to the industries' established and currently used techniques. Although this thesis will provide a comprehensive description of the technique, it is not intended to present a finished product for immediate use: further process engineering would be necessary.

## 2 ZINC AND ZINC OXIDE COATINGS

This chapter provides a general background survey about zinc and zinc oxide (ZnO) coatings. Their most common applications as well as production and processing methods are described. Moreover, the reactivity and electrochemistry of zinc are presented from the aspects that are relevant to this thesis.

### 2.1 Zinc coatings

Zinc's main application is galvanizing, which involves coating steel structures with metallic zinc to protect the steel surface from corrosion. Zinc protects the steel due to their difference in electrochemical properties. Fig. 1 shows the electrochemical series that describes the ability of some elements to accept (reduce) or donate (oxidize) electrons by their standard potential; this measure is also called reduction/oxidation potential. In addition to the standard potential, also other factors (i.e. electrolyte composition) affect the overall electrochemical potential that determines the corrosion behaviour of the system. The higher the electrochemical potential is, the less likely the element reacts with surrounding materials. Iron (Fe) has a higher reduction potential than zinc, so zinc is more likely to react in a corrosive environment [1].

Substance	Standard Potentials at 25°C (NHE)
Au $\rightarrow$ Au <sup>3+</sup> + 3e <sup>-</sup>	+1.498
Pt $\rightarrow$ Pt <sup>2+</sup> + 2e <sup>-</sup>	+1.2
Ag $\rightarrow$ Ag <sup>+</sup> + e <sup>-</sup>	+0.799
Cu $\rightarrow$ Cu <sup>2+</sup> + 2e <sup>-</sup>	+0.337
2H <sup>+</sup> + 2e <sup>-</sup> $\rightarrow$ H <sub>2</sub>	0.00 (Reference)
Fe $\rightarrow$ Fe <sup>2+</sup> + 2e <sup>-</sup>	-0.440
Zn $\rightarrow$ Zn <sup>2+</sup> + 2e <sup>-</sup>	-0.763

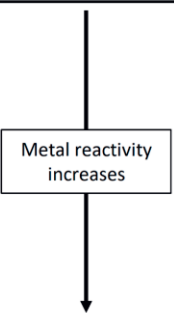


**Figure 1.** Standard potentials of some metals measured at 25°C relative to normal hydrogen electrode (NHE). Data from [12].

When zinc and steel are in electrical contact with each other, they form a galvanic pair. In a galvanic pair, the metal with higher electrochemical potential becomes a cathode (iron) and the metal with lower electrochemical potential becomes an anode (zinc). When a galvanic pair is in contact with a corroding species, i.e. water, the metals undergo galvanic corrosion in which the anode metal dissolves into the water (electrolyte), leaving the cathode unchanged (Fig. 2). Corrosion is an electrochemical process in which an electrical current flow causes the dissolution of metals [12, 13]. In galvanized steel, the metallic zinc (anode) dissolves in the electrolyte as ions, producing free electrons in the process. These electrons are consumed at the cathode, e.g. with dissolved oxygen, forming cathodic products (Fig. 2). The dissolved metals and cathodic products can further react with other substances present into more stable substances such as oxides and carbonates. The nature of the corrosion products also determines the overall corrosion resistance of the metal. Flaky and brittle corrosion product layers can lead to more corrosion, whereas tightly packed layers inhibit corrosion. Consequently, zinc has better corrosion resistance than some steels due to the formation of a compact carbonate layer called patina [1].

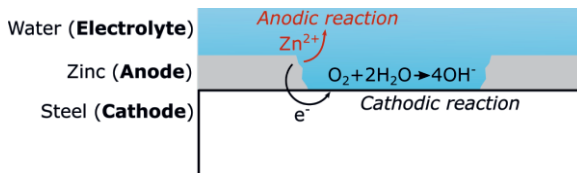


**Figure 2.** Galvanic corrosion of galvanized steel in the presence of water.

The production of galvanized steel starts with manufacturing the steel part. The steel can be then galvanized by various methods depending on the properties required for the end application. After galvanizing, the surface usually undergoes a surface treatment. This treatment provides corrosion resistance for the zinc surface. The treatment may also provide an adhesion layer for organic coatings applied for even better corrosion protection or for an aesthetic surface finish [1].

### 2.1.1 Galvanizing process

The galvanizing process includes several steps throughout the production line. First, the steel surface must be prepared. The unrolled steel sheet is first degreased with an alkaline solution and subsequent rinsing. The next step, called pickling, removes mill scale and rust off of the steel. Just before the application of the zinc coating, the

surface oxides are removed by a process called fluxing that uses reducing gases. Fluxing is done especially to prepare hot-dip galvanized parts [1].

The galvanizing itself can be done in various ways. The most common techniques include electroplating, sherardizing, thermal spraying and hot-dipping.

Electroplating is used for applications requiring a uniform coating thickness as well as excellent surface quality suitable for painting, e.g. in the automotive industry. The process involves two electrodes, of which one is the material to be coated. While electroplating provides an excellent surface quality, and a thin and uniform coating, it is expensive [1].

Sherardizing bonds powdered zinc onto the steel substrate in a heated diffusion process. Its advantage is that the part maintains its geometry and provides good corrosion resistance. Sherardizing is widely used for nuts, bolts, nails and other small articles [1, 14].

Hot-dip galvanizing involves submerging steel parts into a zinc bath. Hot-dip galvanizing provides very good bonding with the steel surface, is rapid, and is inexpensive. Batch hot-dip galvanizing involves dipping individual parts (batch hot-dip), useful for parts with complex shapes.

Continuous hot-dipping is used for coating sheets, wires and other simple-shaped articles, such as in the Sendzimir process, shown in Fig. 3 [15]. The Sendzimir process is a so-called 'roll-to-roll' process, in which a roll of steel is unwound at the start, passes through the production line, and is re-wound at the end. The production line includes multiple surface preparation steps, and immersion in a molten zinc bath containing 0.1–0.2% aluminium that prevents the formation of brittle Fe–Zn intermetallic phases and reduces zinc bath oxidation. Air knives control the thickness of the zinc coating as it exits the bath. Continuous hot-dip galvanizing is used to produce e.g. metal roofing, façades and ductwork. [1, 16].

Hot-dip is the most prevalent galvanizing method due to its economics and properties. Therefore, the rest of this thesis focusses primarily on the context of continuous hot-dip galvanized steel as a case study towards application to other methods of galvanizing as well.

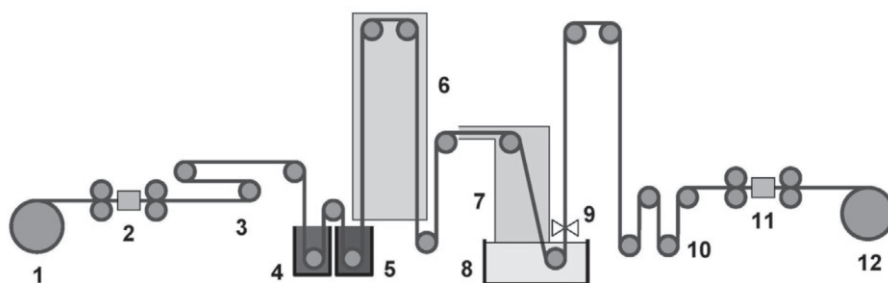


**Figure 3.** Continuous hot-dip galvanizing line. 1. Strip unwinding, 2. Welding, 3. Levelling loop, 4. Degreasing, 5. Pickling, 6. Full annealing, 7. Surface activation in a reducing atmosphere, 8. Zinc bath, 9. Air wiping knives, 10. Levelling, 11. Shearing, 12. Winding the galvanized strip in a coil [15].

## 2.1.2 Surface pretreatments of zinc coatings

After hot-dip galvanizing, the galvanized surface is treated to increase corrosion resistance and adhesiveness for the later-applied organic coatings. Organic coatings are generally not applied without surface preparation due to poor adhesion. Most commonly, chemical pretreatments are used to produce a conversion coating on the zinc surface. Conversion coatings can also be useful merely for their corrosion resistance even without a subsequent organic coatings. The most commonly applied chemical pretreatments are chromate, phosphate, zirconium-based and titanium-based coatings. The conversion coating process is easy and rapid [1, 17–19].

Chromate conversion coating treatments were among the most used. The chromate conversion layer is produced using chromic and hydrofluoric acids which are applied on the zinc surfaces. The acids react with the zinc surface, to form a thin chromium hydroxide layer on the order of 15 nm thick [17]. The layer adheres well to organic coatings. It provides good protection from corrosion even by itself, so can also be used without a subsequent organic coating. Chromium conversion coatings can be performed using either hexavalent or trivalent chromium solutions. Using hexavalent chromium produces a conversion coating with excellent properties, but hexavalent chromium is considered highly toxic, and therefore its use is heavily regulated [20]. Trivalent chromium conversion coatings were developed to replace hexavalent chromium due to its being less harmful while producing similar results [2].

Another conversion method uses phosphates. Phosphate conversion uses phosphoric acid together with zinc and nickel phosphates. Phosphate conversion is mainly used to enhance organic coating adhesion and corrosion resistance [17, 21].

Other conversion methods such as zirconium-based or titanium-based conversion coatings are also used. Zirconium-based conversion coatings use hexafluoro zirconic acid. The zirconium conversion coatings offer properties similar to those of the other conversion coatings, though the coating layer is thicker, approximately 50 nm [17]. Titanium conversion coatings are performed with titanium hexafluoride, manganese salts and phosphoric acid [22].

The zinc surface can alternatively be prepared for organic coatings by waiting for a sufficient natural patina layer to develop: the hot-dip galvanized article is installed in its destination and left to react with the environment. In approximately two years' time, the surface has patinated through atmospheric corrosion (detailed description in chapter 2.3) [4, 23]. Although the overall formation time and composition of patina is highly dependent on the prevailing exposure conditions, the patina layer mostly comprises of hydrozincite, a type of zinc hydroxy carbonate. Hydrozincite increases the adhesion of organic coatings and provides a barrier layer that inhibits further corrosion. The process is very inexpensive but requires a long waiting time, and the patination is highly dependent on weather conditions which makes the process uncontrollable [5, 23].

The modern galvanizing industry still primarily uses the conversion coatings for its adhesion promotion and anti-corrosive properties. The main disadvantages are the use of extremely harmful chemicals like strong acids, although much progress has been made lately by developing more environmentally-friendly conversion coatings. Continuing to use harmful chemicals creates operating risks for the environment and workers [3]. Natural patination, on the other hand, takes a very long time to develop, which is undesirable for both the manufacturer and the end-user. Therefore, more environmentally friendly, sustainable and rapid techniques could be of use to replace these treatments in part.

### 2.1.3 Organic coatings on zinc

Zinc surfaces are often coated with organic paints to provide extra corrosion protection as well as for aesthetic purposes. The corrosion resistance of organically coated hot-dip galvanized steel (Fig. 4) improves significantly as a result of both the zinc coating and the organic coating. Organic coatings are non-polar polymers that

seal the substrate surface and greatly inhibit the transport of corroding species such as water or atmospheric gases [5, 24].

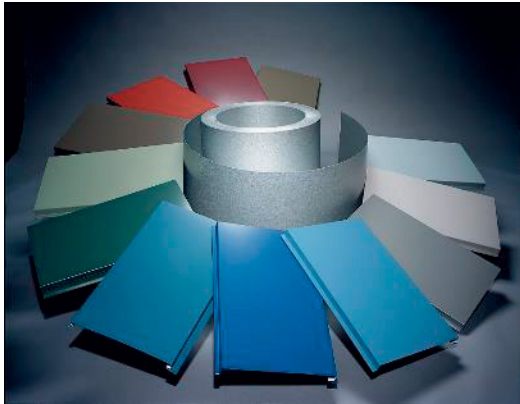


**Figure 4.** Painted hot-dip galvanized steel. From [25].

Organic coatings can be applied on the hot-dip galvanized surface in a coil coating line (Fig.5) that follows the continuous galvanizing line. The hot-dip galvanized sheet is first washed and rinsed after which it is passivated or pretreated with the to form conversion coatings as described before. Subsequently, two different paints a primer coating and a top coat are applied on the surface.

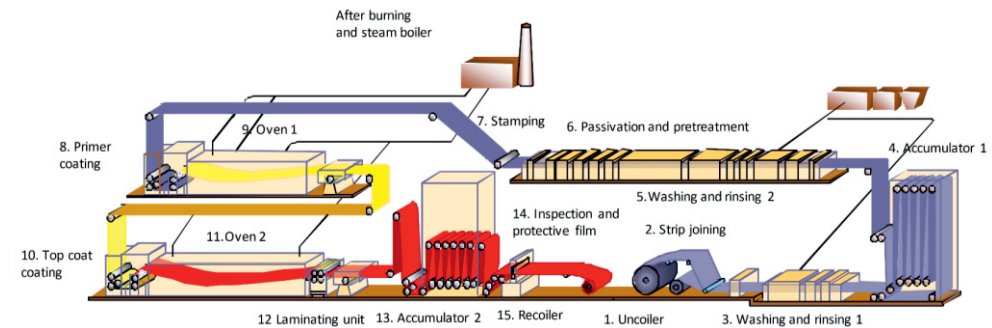


**Figure 5.** Coil coating of hot-dip galvanized steel sheet. From [26].

## 2.2 Zinc oxide nanostructures

When zinc is exposed to humid air, ZnO can easily form as so-called ‘white rust’ which comprises ZnO and zinc hydroxide ( $Zn(OH)_2$ ) [27,28]. ZnO formed in this



manner is usually non-adherent, irregularly shaped and partly amorphous [29, 30]. However, with proper synthesis techniques producing a controlled structural morphology, stoichiometry and crystallinity, ZnO has versatile properties and wide application areas. Traditionally, ZnO has been used as a filler in the rubber, food, pharmaceutical and cosmetics industries. Furthermore, the recent development of nanotechnology and nanomaterials has led to high-technology applications for ZnO because of its semiconductor nature. These include a range of optical applications, dye-sensitized solar cells (DSSC), mechanical energy harvesting, sensor technologies and photocatalysis [6, 31].

Nanoscale ZnO has aroused great interest because of the large number of feasible synthesis techniques available for tailoring a range of morphologies [6]. ZnO has been synthesized into a variety of nanoscale structures, e.g. thin films, nanospheres, nanorods and nanowires (Fig. 6) [6, 32]. The nanowires can be formed in many different sizes, aspect ratios and crystallinities. The different material characteristics of various ZnO nanostructures provide properties useful for various specific applications [6, 33, 34].

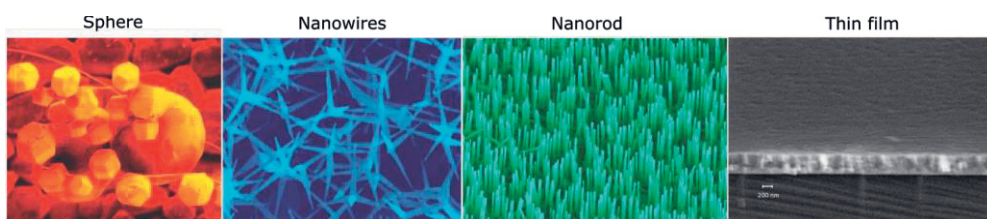


**Figure 6.** ZnO nanostructures. Edited from references [35] and [36].

## 2.2.1 Synthesis of nanosized ZnO coatings

ZnO thin films and nanowires are the most commonly produced ZnO nanostructures. These nanostructures have been of interest due to their easy synthesis and a wide range of uses. ZnO thin films are uniform coatings on substrates, whereas ZnO nanowires are needle-like 1D structures. The focus on ZnO nanowires originates from the higher surface area that they provide by protruding above surface [34, 37, 38].

ZnO thin films can be produced with chemical vapour deposition (CVD), physical vapour deposition techniques (PVD), sol-gel methods, among other methods [39]. Similarly, ZnO nanowires can be synthesized by a variety of techniques, e.g. the hydrothermal method, vapour-liquid-solid (VLS) and

aluminium oxide templating [6, 33, 40]. Due to the wide variety of existing techniques, only the most commonly used techniques are described in this chapter.

Sputtering is a PVD technique that is used to form thin films of many materials. A ZnO target is bombarded by ions, generated by exposing a gas (e.g. argon) to an electromagnetic field inside the sputter chamber. The high-energy ions detach atoms from the target surface, which then travel towards and land on a substrate, usually located opposite the target. The substrate is consequently covered with the target material in the wanted thickness. The main benefits of sputtering are great uniformity and control over the film thickness as well the possibility of using a variety of coating materials. However, the sputtering process requires the use of high vacuum, large potential generation, and it is typically a batch process [41].

The sol-gel method is another ZnO thin film technique where the coating is applied by using liquid precursors. The method typically uses metal alkoxides and water as the main precursors, together with a solvent. The metal alkoxide and water react together by hydrolysis and condensation reactions, eventually forming a metal-oxygen bond network that results in the solid ZnO structure. The solvent provides a sufficient surrounding volume for the reaction. As soon as the precursors are mixed, the solution needs to be deposited on the substrate surface. The depositing can be done in various ways, e.g. by dip coating or, more commonly, by spin coating (Fig. 7). In spin coating, the mixed precursor solution is placed on a substrate which is then rotated so that the solution spreads into a uniform layer. Heat treatment takes the coating into its final form. The sol-gel method, together with spin coating, produces thin ZnO films with fairly good uniformity and easy processing. The downside is that metal alkoxides are expensive [33].

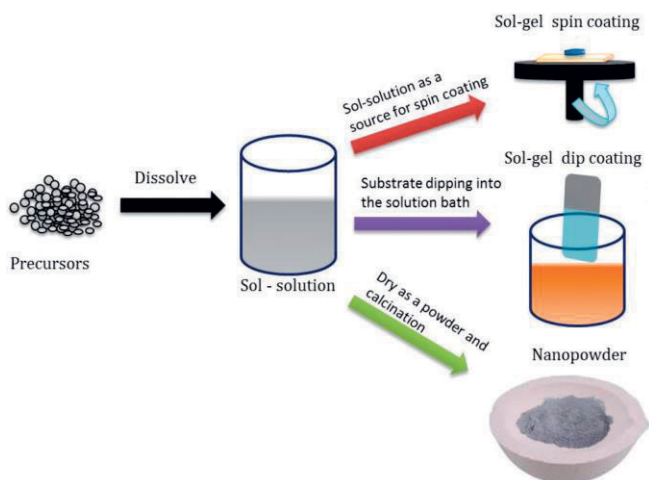


**Figure 7.** The principles of producing coatings or nanopowder with sol–gel method [42].

ZnO nanowires are most commonly synthesized through hydrothermal growth. Variable surface topographies can be obtained through careful control of the treatment parameters [6, 43]. Typically, the method is used for producing a nanowire structure on a substrate surface [6]. Fig. 8 shows, schematically, a typical hydrothermal process. The hydrothermal method starts by producing a ZnO thin film called a seed layer. The seed layer is usually formed using sol–gel or sputtering techniques. The substrate and seed layer are then immersed in a heated solution containing specific solvents and zinc compounds. The reaction time can be from hours to days. The advantages are the use of low temperatures, low cost, ease of synthesis and high crystallinity [6, 44]. The main disadvantages are the long, multi-stepped process, as well as the use of potentially harmful chemicals [45,46].

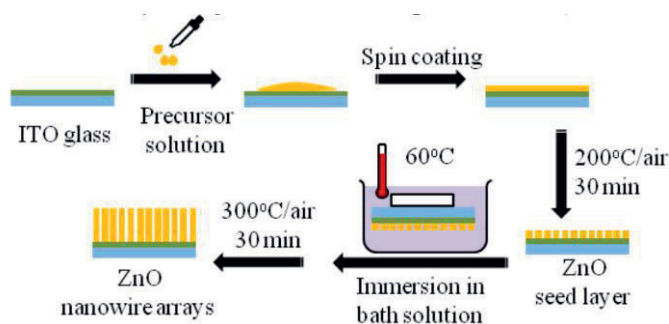


**Figure 8.** Hydrothermal procedure with spin coated seed layer on a ITO glass substrate [47].

VLS is a nanowire growth technique used for many semiconductor materials including ZnO [40, 48, 49]. The method involves a metal catalyst (e.g. Cu, Au) as the initiation point for the nanowire growth. The precursor material, e.g. ZnO powder, is vaporized and transported in the gaseous phase into the metal catalyst droplet with which it merges, forming an alloy droplet consisting of the metal and ZnO. The droplet is supersaturated with the ZnO, and a nanowire starts to grow between the metal droplet and substrate [40]. The growth stops when the temperature falls below the eutectic temperature of the alloy, or when the supply of the precursor vapour stops [34]. Materials used for the VLS technique are fairly simple and the result is crystalline nanowires, but the process requires high temperatures of approximately 800–900°C and the nanowire growth can be difficult to control [48, 49].

## 2.2.2 Properties and applications

Nanostructured ZnO has variety of applications. The most common of these are gas sensors, solar cells and piezoelectric applications.

ZnO nanowires have been researched as a gas sensor material for several gases (i.e. NO<sub>2</sub>, CO, NH<sub>3</sub>), humidity, pressure, biomolecules and glucose molecules. The sensing mechanism can be based on either mechanical or chemical interaction [37, 50–52]. ZnO nanowires are optimal for sensor applications due to their high surface area, chemical stability, low-cost synthesis and optical properties [50]. The sensing is based on the adsorption of molecules on the ZnO surface changing the resistivity of the material, resulting in measurable response.

Piezo- and pyroelectricity are material properties where electric current is produced by mechanical movement or heating, respectively. Applications include energy harvesting and sensor applications [53, 54]. ZnO has been studied a lot as both a piezo- and pyroelectric material [34, 37, 55, 56]. ZnO has been found to have a very high piezoelectric coefficient and high elasticity; both of which properties are valued for piezoelectric use. Compared to other piezoelectric materials, i.e. barium titanate, ZnO is more durable and easier to synthesise, which makes it better for piezoelectric applications [57].

ZnO nanowires can be used also in two different types of solar cells: Dye-Sensitized Solar Cells (DSSC) and Quantum Dot Sensitized Solar Cells (QDSSC) [58, 59]. Both types operate on the same working principle with the main difference being the different photosensitive dye used. ZnO functions as the charge transport material within the solar cells due to its wide band-gap and electron transport

capabilities [58]. The solar cell consists of two electrodes, one of them transparent. The ZnO nanowires are deposited on top of the transparent electrode. The nanowires are then coated with a photosensitive dye compound on their surface, and an electrolyte is applied on this nanowire array. Finally, the counter-electrode is applied on top of the nanowire array to finalize the circuit and ensure charge transport [58].

ZnO is also a photocatalytic material, i.e. incident photons can excite its electrons from the valence band to the conduction band (Fig. 9). The excited electron and hole produced on the material surface can then react with water or gases in the immediate environment to produce radicals. These radicals can then react further with the environment, converting nearby molecules into others [60]. Photocatalytic material surfaces are antibacterial as the radicals are able to puncture bacteria membranes, killing them [45, 61]. Furthermore, the radicals can react with environmental pollutants and toxic substances by converting them into less harmful substances [60].

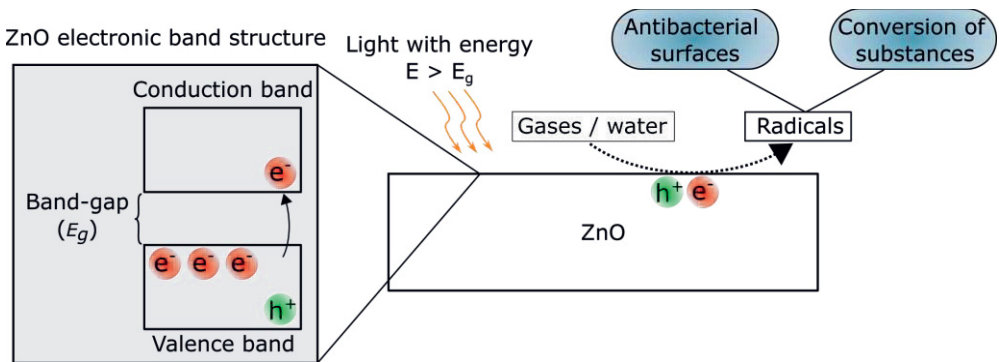


**Figure 9.** Schematic of basic principle of ZnO photocatalysis.

The advantages of ZnO nanowires for photocatalytic applications lies in the easy nanostructure synthesis and high photocatalytic activity [45, 62]. There are some studies showing that the photocatalytic activity of ZnO is higher than that of titanium dioxide (TiO<sub>2</sub>), the most common photocatalytic material [63, 64]. However, there are contradictory results regarding ZnO's photocatalytic activities. A major disadvantage of ZnO nanowires in photocatalysis is the high band-gap energy which inhibits their activity in sunlight. Additionally, ZnO exhibits photocorrosion which leads to deterioration of the material [65].

## 2.3 Corrosion of zinc and electrochemical reactions

Metal corrosion entails the electrochemical dissolution of the metal surface into an electrolyte. The dissolving metals tend to either wash away or react with environmental species to form other compounds such as oxides, carbonates or other corrosion products. The formation of corrosion products can protect the metal from further corrosion by different means, such as reducing the aggressiveness of corrosive species, inhibiting electron transfer and especially by creating a barrier layer between the metal and environment. A barrier layer inhibits transport of water or other reactants to the underlying metal surface [1, 12]. However, if the corrosion products are non-adherent and detach easily, they do not create such a barrier layer enabling corrosion to occur when they are continuously removed from the surface like in the case of iron [66].

As was previously mentioned, zinc is low on the electrochemical series. This means that it is fairly reactive, constantly interacting with the environmental species. However, the zinc's reactivity protects the material through the formation of a compact corrosion product layer that prevents further corrosion and material loss. Consequently, the corrosion rate of zinc is 10 to 100 times slower than certain steels due to its corrosion product layer [1].

The corrosion product layer, i.e. the patina, typically consists of multiple compounds. The final composition depends highly on environmental conditions such as temperature, humidity, surrounding gases and impurities. The main contributors to atmospheric corrosion of zinc are carbon dioxide ( $\text{CO}_2$ ) and water from humidity or rain. The initial corrosion products on zinc are most typically  $\text{ZnO}$  and  $\text{Zn}(\text{OH})_2$ , which convert in subsequent reactions towards different zinc hydroxy carbonates [1, 27, 66].

Even though the patina significantly inhibits corrosion, it can also wear over time through runoff. Runoff occurs typically when the zinc surface is exposed to weather; the patina itself dissolves into rainwater, contributing to material loss and exposing fresh surface to further corrosion (Fig. 10).

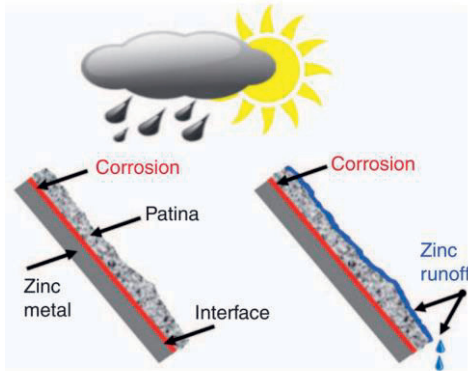
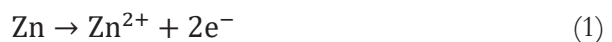


**Figure 10.** Zinc patina runoff. From [27].

### 2.3.1 Corrosion reactions

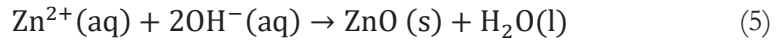
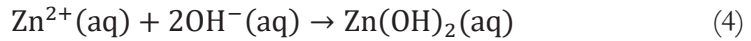
Corrosion is driven by the electrochemistry that occurs when an anode, cathode, and an electrolyte that are in electrical contact as was shown in Fig. 2. Electrons from the anode travel through the metal to the cathode where they participate in further reactions such as oxidation. Consequently, there is always reaction occurring on the anode and cathode. Water, the most common electrolyte, acts as a medium of transport for the species, i.e. dissolved ions [1]. In galvanic corrosion, the anode and cathode are defined by the difference in their standard potential. When the system comprises only one metal, minute differences on the metal surface create localised anodic and cathodic areas [12]. The anodic reaction for zinc is



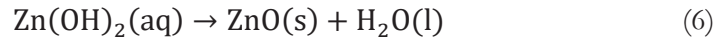
Conversely, the cathodic reactions are hydrogen gas evolution or oxygen reduction shown in Eq. 2 and 3. Oxygen reduction is a more prevalent cathodic reaction for zinc rather than hydrogen evolution, due to the high overpotential of hydrogen compared to zinc. Hydrogen gas evolution can, however, occur in certain environments, especially under highly acidic conditions [1].



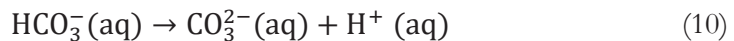
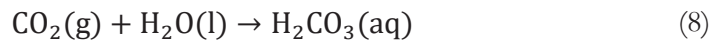
After the anodic dissolution of zinc, the liberated  $Zn^{2+}$  ions react with hydroxyl ions ( $OH^-$ ) forming  $ZnO$  and  $Zn(OH)_2$  as the initial corrosion products (Eq. 4 and 5). The formation of these species depends on the environmental conditions, especially pH and temperature [29, 67, 68].  $ZnO$  and  $Zn(OH)_2$  typically form simultaneously [27, 69, 70] although some studies have shown the formation of  $Zn(OH)_2$  before  $ZnO$  under aqueous NaCl solution [67].  $Zn(OH)_2$  formation is more prevalent at lower temperatures and  $ZnO$  formation at higher temperatures [69]. Both species form under alkaline conditions [29] although  $Zn(OH)_2$  is even more predominant under higher pH [72].



$Zn(OH)_2$  can also be converted to  $ZnO$  through the reaction in Eq. 6 [72].  $Zn(OH)_2$  can also redissolve, depending on pH, forming zincate ions ( $Zn(OH)_4^{2-}$ , Eq. 7), or other zinc hydroxide-based ions, e.g.  $ZnOH^+$  [73]. More complex reaction sequences, leading to  $Zn(OH)_2$ ,  $ZnO$  and the subsequent corrosion products, are also possible [73, 74].

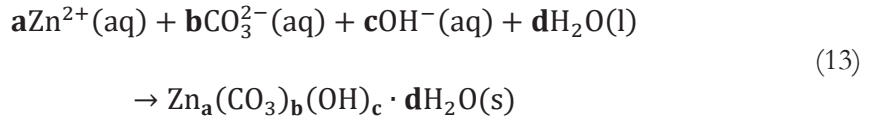
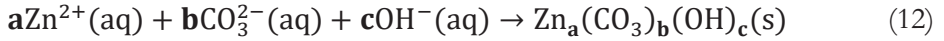
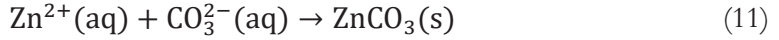


Carbon dioxide is a critical constituent in zinc patination. It contributes by first dissolving into water to form carbonic acid shown in Eq. 8. The carbonic acid then dissociates into bicarbonate and carbonate ions (Eq. 9 and 10).





These carbonate ions react further with the dissolved Zn-species to form smithsonite ( $\text{ZnCO}_3$ , Eq. 12) and zinc hydroxy carbonates (Eq. 13, 14). Since the actual carbonate ion concentration is typically low [76], the more abundant bicarbonate ions likely participate in the reactions as well. The bicarbonate ions could react to form zinc carbonates as shown in Eq. 15, for example [77].



Zinc hydroxy carbonates occur as various compounds with the most common being hydrozincite ( $\text{Zn}_5(\text{CO}_3)_2(\text{OH})_6$ ), and others with varied stoichiometry [77, 78]. The zinc hydroxy carbonates contain varying amounts of each of the ions ( $\text{Zn}^{2+}$ ,  $\text{OH}^{-}$ ,  $\text{CO}_3^{2-}$ ) and can also exist with water of crystallization. These species have been found in nature and as products of several synthesis methods [71, 74, 78].

The carbonates can further react in complex reaction sequences with impurities from the air and other environmental substances, e.g. sulfur dioxide ( $\text{SO}_2$ ) and sodium chloride ( $\text{NaCl}$ ). The final reaction products vary greatly, resulting in a variety of different zinc compounds. The compounds include different hydrated zinc sodium sulfates and chlorides [80].

### 2.3.2 Atmospheric corrosion

Zinc corrosion in the atmosphere is affected by prevailing weather conditions as well as the surrounding environmental factors such as nearby marine or industrial areas [27]. As discussed earlier, the initial steps of zinc corrosion involve the formation of  $\text{ZnO}$  and  $\text{Zn}(\text{OH})_2$ , which occurs in a relatively short time — from seconds to hours [80]. This is followed by subsequent reactions with  $\text{CO}_2$  dissolved in water. In case the atmosphere does not contain pollutants, the reaction with  $\text{CO}_2$  results in the formation of the most abundant zinc corrosion product hydrozincite in only a few

days. The atmosphere typically contains both NaCl and SO<sub>2</sub>. These species will eventually convert into a more developed patina layer in numerous reaction sequences by forming a variety of zinc hydroxy chlorides and sulfates [27,80]. Examples of some possible atmospheric corrosion reaction sequences are shown in Fig. 11.

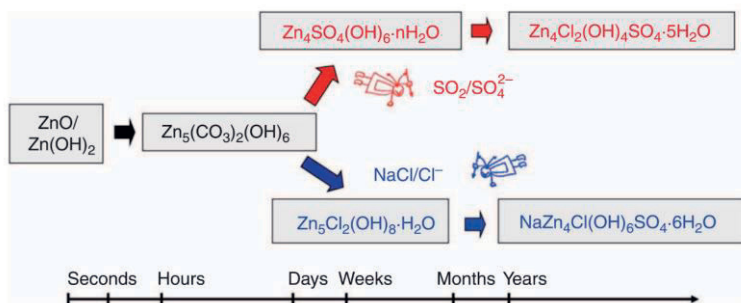


**Figure 11.** Zinc patina compounds and their formation times [27].

The zinc patination process is affected by prevailing environmental conditions as well as the pattern of alternating wet and dry cycles. The type and duration of wetting affects the final patina formation significantly. The process starts when the zinc surface is contacted with water, whether by rain or humidity, dissolving zinc from the surface. Drying of the water layer results in initial precipitation of ZnO, Zn(OH)<sub>2</sub>, and finally hydrozincite as well as other zinc-based compounds depending on the air pollutants and gases [1, 27, 80].

The patina layer changes constantly throughout its lifetime. The patina is affected by continuous dissolution resulting in further corrosion, product precipitation, and runoff [27]. However, the layer is sufficiently developed after one or two years that organic coatings can be applied [4].

## 3 PROCESSING WITH CARBON DIOXIDE AND CARBONATION

This chapter discusses aspects of carbon dioxide use, and the interactions between carbon dioxide and water.

### 3.1 Utilization of carbon dioxide

The air in the atmosphere comprises 0.04% CO<sub>2</sub>, makes it the fourth most abundant atmospheric gas after nitrogen (N<sub>2</sub>), oxygen (O<sub>2</sub>) and argon (Ar) [82]. CO<sub>2</sub> is a greenhouse gas which means it absorbs heat radiation that would otherwise escape the atmosphere, resulting in a temperature rise of the earth. The exponential increase in CO<sub>2</sub> levels during modern times has created great concern about global warming and its effects on the earth. Therefore, developing technologies to gather CO<sub>2</sub> from the atmosphere and transform it into other forms has become a matter of global urgency. There are two main options currently discussed within the research community: carbon capture and storage (CCS) and carbon capture and utilization (CCU), as shown in Fig. 12. The main difference between them is that CCU aims to convert CO<sub>2</sub> into products, whereas CCS tries to find storage options for the CO<sub>2</sub>. Both CCS and CCU will likely be needed for urgent disposal of CO<sub>2</sub> in the current state of the world. The primary example of CCS technologies is sequestering CO<sub>2</sub> into the ground to form mineral carbonates buried deep in the earth's crust. CCU technologies include a variety of possible applications, ranging from the carbonation of mineral by-products of the concrete industry, to synthesizing polymers or fuels [83].

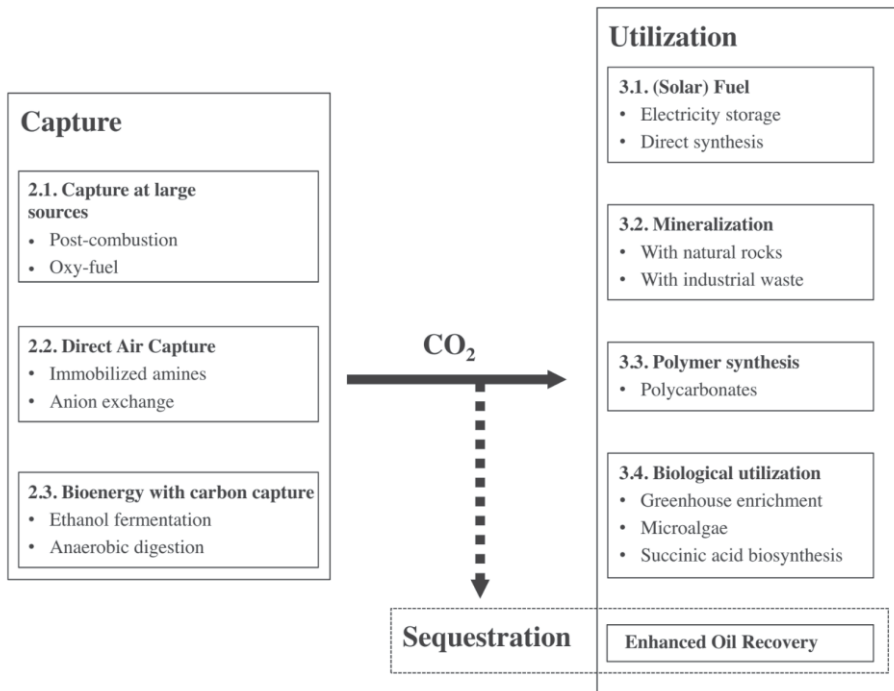


**Figure 12.** Carbon capture technologies and subsequent utilization or sequestration applications [84].

Currently, the motivation for CO<sub>2</sub> utilization is to reduce its levels in the atmosphere. However, CO<sub>2</sub> provides many advantages in processing. Processing with CO<sub>2</sub> is non-toxic and it's non-flammable, which facilitates its use [9]. Furthermore, CO<sub>2</sub> is inexpensive and easily available [83]. Incentivization policies implemented by governments also implicate good financial prospects for CO<sub>2</sub> utilization processes [11].

In atmospheric conditions, CO<sub>2</sub> exists in gaseous form (Fig. 13). CCU technologies usually aim to use CO<sub>2</sub> in gas or liquid state so that only little pressurizing and no excessive cooling or heating is required, in order to keep processing economical. When pressurized and heated, CO<sub>2</sub> turns into a supercritical fluid.

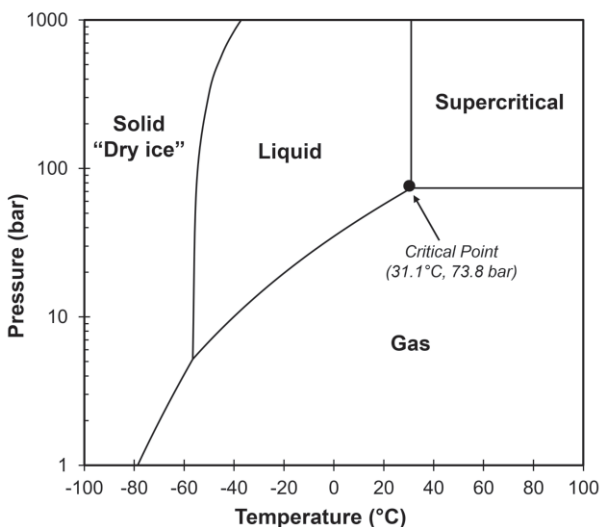


**Figure 13.** Phase diagram of CO<sub>2</sub>. Drawn with CO<sub>2</sub> tab v.1.0 (© 1999 ChemicalLogic Corporation) and edited.

### 3.2 Supercritical carbon dioxide (scCO<sub>2</sub>)

Supercritical fluid is a state of matter with properties between those of liquids and solids. The main characteristics of supercritical fluids are high density and solvability, low surface tension, low viscosity, as well as gas-like flow and diffusivity. These properties make the supercritical state particularly optimal for solvent applications where high solvability and fluid flow control are essential process parameters. Moreover, the solvation power and selectivity properties of supercritical fluids can be controlled by changing the process pressure and temperature. Supercritical CO<sub>2</sub> (scCO<sub>2</sub>) has a low supercritical point (73.8 bar, 31°C), which makes its use more energy-efficient, safer and more economical than other supercritical fluids [85]. Consequently, scCO<sub>2</sub> is the most used supercritical fluid, and it is used in many applications such as power generation, and in the food and chemical industries [9, 10, 85].

ScCO<sub>2</sub> is especially useful as a solvent due to its environmentally friendly processing and high solvability. The excellent solvent properties of supercritical fluids are due to their high density resulting in so-called 'solute-solvent clustering' in which a higher number of solvent molecules surround the solute molecule compared with the lower number in lower-density gases. The density of supercritical CO<sub>2</sub>

correlates well with an increase in solvent solvability [10]. As seen from Fig. 14, the density significantly increases when gas is compressed over the critical point, which results in higher solvation capability as well. Even though CO<sub>2</sub> is non-polar, it has a significant quadrupole moment that allows minor solvability of polar substances as well, e.g. water, in certain conditions [10, 86].

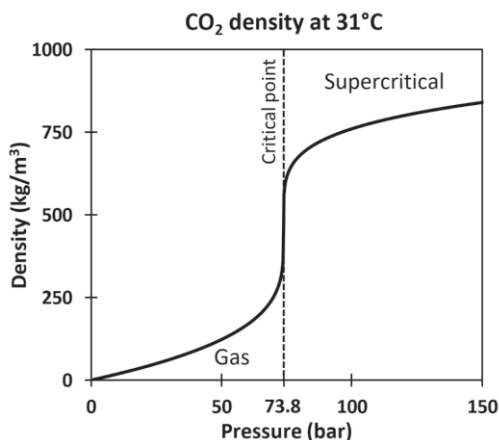


**Figure 14.** The density of CO<sub>2</sub> at 31°C. Data acquired from [85].

The liquid-like dissolving capability of scCO<sub>2</sub> is of great advantage in many applications. Supercritical extraction is currently the main application for scCO<sub>2</sub>, separating specific compounds from the original raw material, useful in the food and pharmaceutical industries [10, 85]. The best-known example is caffeine extraction from coffee beans or tea leaves to produce decaffeinated coffee or tea, along with a highly concentrated caffeine extract [86]. Another example is the production of highly porous aerogels, in which scCO<sub>2</sub> removes solvent from the pores of a highly porous material; these gels have uses in the space and construction industries [88]. Furthermore, the solvent properties of scCO<sub>2</sub> can be adjusted by changing the pressure and temperature. This control of solvability enables the dissolving of multiple substances at high pressures and subsequently releasing them in different pressure ranges, resulting in a fractional separation of the individual substances without need for further post-processing [86].

Like gas, scCO<sub>2</sub> occupies the whole reaction volume and easily infiltrates into small pores and structures due to its high diffusivity. Furthermore, zero surface tension ensures that the structure is left undamaged by removing the scCO<sub>2</sub>. These properties are used both for depositing new substances into structures, and also for

removing unwanted substances from within the structures such as in the aforementioned case of aerogels [9].

The unique properties of supercritical fluids, and especially of  $\text{scCO}_2$ , have found use in many application possibilities within various industries. The problems with  $\text{scCO}_2$  processing are mainly to do with the requirement of high-pressure: equipment is needed to handle the high pressure, and high-pressure operations incur high operational costs. Furthermore, supercritical fluid processes are often limited to batch or semi-batch processing. These factors have limited the utilization of  $\text{scCO}_2$  processing [86].

### 3.3 Carbon dioxide in aqueous environment

The pH of water falls as the  $\text{CO}_2$  dissolves into it (Eq. 9–11). The acidity and the dissolved ionic species within the water can cause the formation of corrosion products. Corrosion due to pressurized carbon dioxide has been widely studied in steel pipelines used in the oil and gas industry [88, 89]. The role of  $\text{CO}_2$  is essential also in the corrosion behaviour of zinc surfaces in atmospheric corrosion [91].

Generally, the corrosivity of  $\text{CO}_2$  can be attributed to the increasing concentration of hydrogen ions ( $\text{H}^+$ ) in water as  $\text{CO}_2$  concentration increases, leading to the dissolution of the metal ions. Consequently, the hydrogen ions will reduce, forming hydrogen gas ( $\text{H}_2$ ) [92]. Thus,  $\text{CO}_2$  concentration influences the corrosion of metals in aqueous solutions. In water, dissolved  $\text{CO}_2$  exists in different components:

1. Dissolved carbon dioxide ( $\text{CO}_2$ )
2. Carbonic acid ( $\text{H}_2\text{CO}_3$ )
3. Bicarbonate ion ( $\text{HCO}_3^-$ )
4. Carbonate ion ( $\text{CO}_3^{2-}$ )

These species of  $\text{CO}_2$  are in equilibrium with each other, and their concentrations are determined by pH, as shown in Fig. 15.

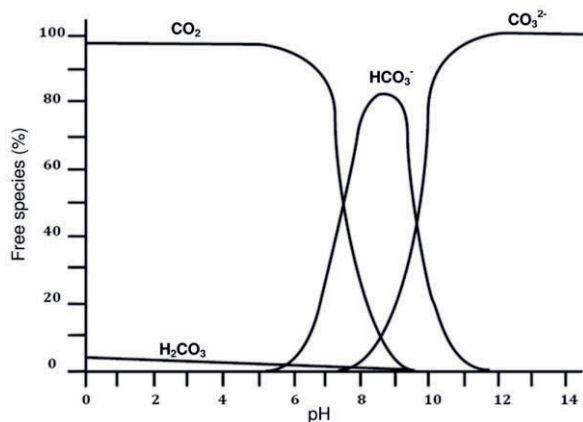


**Figure 15.** The equilibrium fractions of dissolved CO<sub>2</sub> in water at 1 atm and 25°C [93].

The acidic environment induces metal dissolution from the surface, increasing corrosion according to the total CO<sub>2</sub> in the solution. However, once the bicarbonate and carbonate species have formed, they combine with the dissolved metal ions forming carbonates. The deposition of the carbonate species on the metal surface can affect the corrosion behaviour depending on the barrier properties of the carbonate [94–96].

The total amount of carbon dioxide species within solutions depends on the partial pressure of carbon dioxide in the atmosphere as well as temperature (Fig. 16). The amount of CO<sub>2</sub> in water increases rapidly with pressure until the vicinity of the critical point, and is higher at lower temperatures.

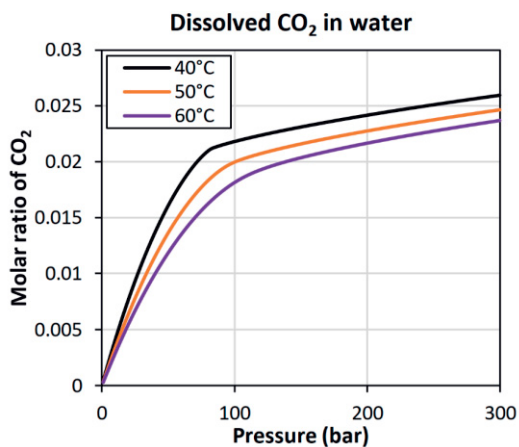


**Figure 16.** CO<sub>2</sub> solubility in water at 40, 50 60°C as a function of pressure. Data from [87].



The concentration values in Fig. 16 are reached when the  $\text{CO}_2$  has had sufficient time to dissolve in the water and attain equilibrium. However, the diffusion rate of  $\text{CO}_2$  in water is slow and also affects the rates of corrosion and corrosion product formation [97]. Water layer thickness has also been found important for the overall corrosion rate, for example, for steel [98].

At low pressures, the gas diffusion and the concentration of  $\text{CO}_2$  in water are the main factors influencing  $\text{CO}_2$ 's reactivity. When the pressure rises close to the supercritical region and above, water dissolves in  $\text{CO}_2$  as well. This wet supercritical carbon dioxide has been shown to cause corrosion on steels [75, 98, 99]. Furthermore, it has been shown to cause carbonation reactions on mineral surfaces [101–103]. In contrast, pure  $\text{CO}_2$  — i.e. without water — on metal or mineral surfaces does not result in any surface reactivity [99, 101]. Fig. 17 shows how the dissolution of water in  $\text{CO}_2$  in different temperatures where it can be seen that the dissolved water amount increases significantly when pressure increases above the critical point.

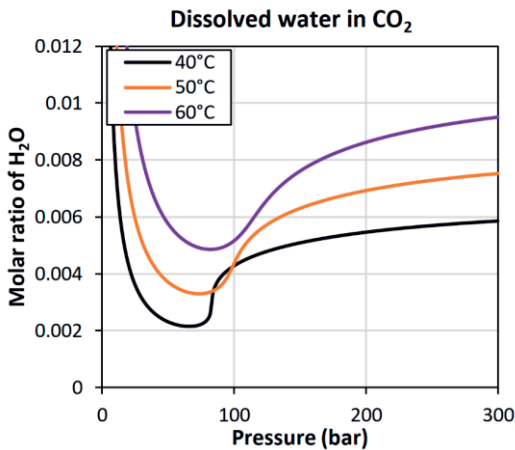


**Figure 17.** Water solubility in  $\text{CO}_2$ . Data from [87].

The mechanism of corrosion in wet  $\text{scCO}_2$  phase is not well known. However, the corrosivity of wet  $\text{scCO}_2$  is likely a result of the formation of a very thin, liquid-like water film on the reaction surfaces. It has been suggested that the water film is caused by small pressure variations near the reaction surfaces, which results in precipitation of water at specific areas or, alternatively, from water adsorption on the surfaces [75, 101]. Furthermore, precipitation of water during depressurization of the wet  $\text{scCO}_2$  phase induces corrosion, e.g. on steel surfaces [95, 103].

## 4 THE PURPOSE OF THE STUDY

The aim of this thesis was to develop a carbon dioxide-based treatment method for functionalizing zinc surfaces. The potential of the method in different application areas was evaluated. The research aimed to answer the following questions:

- I. Can a pressurized carbon dioxide-based treatment be used to functionalize zinc surfaces with artificial patina?**
  - a. What aspects of the treatment influence the final surface properties of the artificial patina?
  - b. Can the treatment be optimized for efficient processing?
- II. How do the functionalized surfaces benefit particular applications?**
  - a. What is the treatment's viability as an environmentally-friendly pretreatment method for preparing hot-dip galvanized surfaces for organic coatings?
  - b. Can the treatment be used as a method for synthesizing ZnO nanostructures for semiconductor applications?

The study investigated several aspects of the treatment to develop a comprehensive overview of how zinc reacts with pressurized carbon dioxide and water to form the artificial patina. The experiments showed the formation of different zinc carbonate structures which have not been detected in atmospheric conditions. The treatment method required no chemical catalysts, and was investigated for its prospects for efficient processing.

The main scientific contributions of the thesis are as follows:

- The study provides a comprehensive understanding of zinc surface behaviour under wet pressurized CO<sub>2</sub> conditions and the formation of unprecedented carbonate structures in pressurized CO<sub>2</sub>
- A method for investigating corrosion behaviour in wet carbon dioxide environments
- The development of a novel surface modification treatment method for zinc surfaces as a potential, environmentally-friendly pretreatment for the galvanizing industry
- Easy synthesis of ZnO nanostructures.

The scientific contribution of publication I is to show the synthesis of zinc hydroxycarbonate structures on hot-dip galvanized steel with a novel technique based on supercritical CO<sub>2</sub>. In publication II, it is shown that these needle-like carbonate structures could be converted into ZnO and could therefore be utilized in semiconductor applications as well as presents a Cu-based catalyst for the method. Publication III evaluates the synthesis technique of the zinc hydroxy carbonate and ZnCO<sub>3</sub> structures (Artificial patina) as a pretreatment method for subsequently organically coated hot-dip galvanized substrates. Furthermore, the preliminary suitability of the artificial patina compared to natural patina and fresh is evaluated. Publication IV expands on the results of publication III about the suitability as a pretreatment and provides a more in-depth characterization of the individual zinc hydroxy carbonate and ZnCO<sub>3</sub> structures, as well as their combination structure, on hot-dip galvanized steel. Publication V focuses on the in-situ investigation of the artificial patination method. The publication shows and discusses the interactions between pure zinc surface and wet-scCO<sub>2</sub>, zinc surface and lower pressure CO<sub>2</sub> and the effect of O<sub>2</sub> on the reaction. The results provide essential information about the method's different treatment phases and fundamental knowledge about the corrosion processes of zinc under pressurized CO<sub>2</sub>. Finally, publication VI shows how different species contribute to the growth of the zinc hydroxy carbonate and ZnCO<sub>3</sub> structure by investigations with isotope waters.

## 5 MATERIALS AND METHODS

This chapter describes the materials and sample preparation procedures used in the studies. Furthermore, detailed information about the treatment equipment and characterization techniques are presented.

### 5.1 Materials

The main substrate materials used for experiments were either pure zinc or hot-dip galvanized steel. The pure zinc sheet substrates had a thickness of 0.62 mm and 99,9 m-% purity and supplied by Alfa Aesar (USA). The zinc substrates were ground and polished using silicon carbide sandpaper with ethanol (99 v-%) to a mirror finish. Hot-dip galvanized (HDG) steel sheets had a thickness of 0.5 mm and were supplied by SSAB Europe (Finland). The HDG sheets had zinc coating weight of 275 g/m<sup>2</sup> with approximately 0.2 wt-% of aluminium as an alloying element. The hot-dip galvanized substrates were cleaned in an alkaline bath with Gardoclean 338 (Chemetall, Germany) to remove residual aluminium and aluminium oxide from the surface. All substrates were cleaned by using deionized water and ethanol before the tests.

Carbon dioxide was supplied by Linde ( $\geq 99\%$ , Finland) or Air Liquide ( $\geq 99.95\%$ , France). Oxygen was supplied by Air Liquide ( $\geq 99.99\%$ ). Deionized water was used in all tests and had a conductivity of 2 – 10  $\mu\text{S}$ . The catalyst copper (II) hexafluoro acetyl acetonate hydrate ( $\text{Cu}(\text{hfac})_2$ ) was supplied by Merck.

Organic coatings that were used in publication IV were polyester melamine primer supplied by Becker Industrial Coatings (Sweden) and topcoat supplied by Valspar Finland Corporation (Finland) were used. The coatings were applied by Top Analytica by bar coating in the laboratory and cured in an oven (H12-850AA, Aalborg Company, USA). The peak metal temperature for the primer was 228°C and for topcoat 230°C. The dry film thicknesses were 6  $\mu\text{m}$  and 20  $\mu\text{m}$  for the primer and topcoat, respectively.

The isotopes waters used in Publication VI were deuterium oxide (D<sub>2</sub>O, 99.9 at-%, Sigma Aldrich, Canada) and <sup>18</sup>O water (≥99 at-%, Taiyo Nippon Sanso Corporation, Japan).

## 5.2 Supercritical carbon dioxide (scCO<sub>2</sub>) treatment

The equipment and procedure for the scCO<sub>2</sub>-treatments are described here. The treatment procedure for publications I – IV is described first in chapter 5.2.1. The in-situ procedure for publication V and VI are described separately in chapters 5.2.2 and 5.2.3, respectively.

### 5.2.1 ScCO<sub>2</sub>-treatment procedure (Publications I – IV)

The scCO<sub>2</sub>-tests were performed in Tampere University by the author mostly with a PC-controlled Thar Technologies INC. (Pittsburgh, PA, USA) RESS 250 system, which is shown in Fig. 18 together with the schematic description of the apparatus. The system includes a high-pressure pump that pumps the liquid CO<sub>2</sub>. A preheater heats the pumped CO<sub>2</sub> into the desired temperature before entering the reaction chamber. A co-solvent pump, which allows for the introduction of catalyst solution, is adjoined into the flow of CO<sub>2</sub>. The heating elements inside the reaction chamber walls further heat the pressurized CO<sub>2</sub> into the supercritical state. The reaction chamber is 256 cm<sup>3</sup> and made from 316L stainless steel. An automatic back pressure regulator (APBR) is connected in the outlet after the chamber, which is used to control the depressurization rate. Needle valves (V1 and V2) are used to obtain a closed system during the treatment.

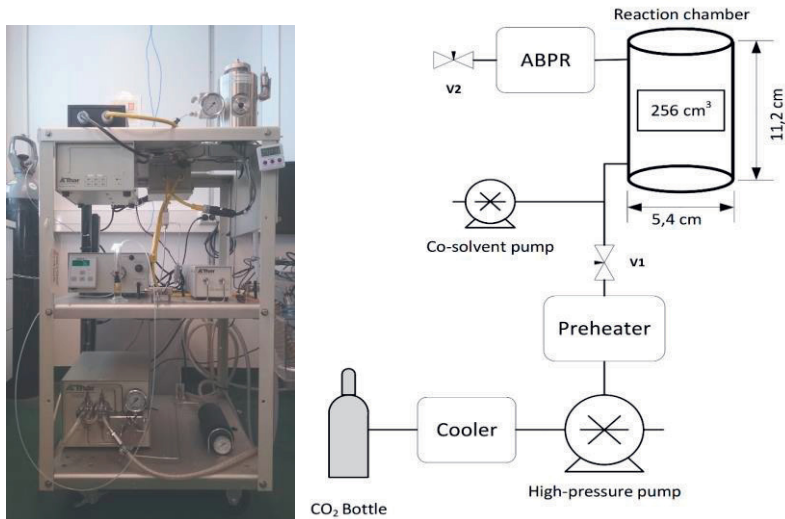


**Figure 18.** Image of the Thar RESS 250 system in the left picture and schematic view of components in the right picture (Publication I).

The treatment procedure used to prepare samples in publications I – IV is performed as follows. The hot-dip galvanized (HDG) substrate with typical dimensions of 25 mm width, 50 mm height and 0.5 mm thickness, is first placed diagonally into the reaction chamber. The chamber is then pressurized and heated into the reaction conditions. After stabilization, the co-solvent pump was used to introduce a co-solvent. The treatment time used was 60 minutes after which the depressurization was performed using the APBR with an integrated heater to minimize ice formation. The depressurization time was approximately 10 minutes and was performed in an identical way in all tests.

The reaction conditions used in publications I – III were the pressure of 300 bar and 50°C temperature. In publication II, also a one-hour post-heat treatment with a temperature of 400°C was performed for the scCO<sub>2</sub>-treated sample. Three different reaction conditions were used in publication IV: 80 bar 40°C, 80bar 60°C and 65 bar 22°C (liquid CO<sub>2</sub> conditions). The co-solvent in publications I and II was 5 mL of deionized water. In publications III and IV, also a catalyst solution was used consisting of 0.5 m-% Cu(hfac)<sub>2</sub> dissolved in 5 mL of H<sub>2</sub>O/EtOH (40/60 vol-%) solution.

## 5.2.2 In-situ scCO<sub>2</sub> and droplet test procedure (Publication V)

The in-situ FTIR and Raman tests were performed with the same reaction chamber setup in University of Bordeaux by the author. The in-situ Raman setup is shown in Fig. 19. The FTIR setup was identical to the Raman with the only difference being the characterizing spectrometer. The FTIR and Raman spectrometers are described in detail in the characterization techniques.

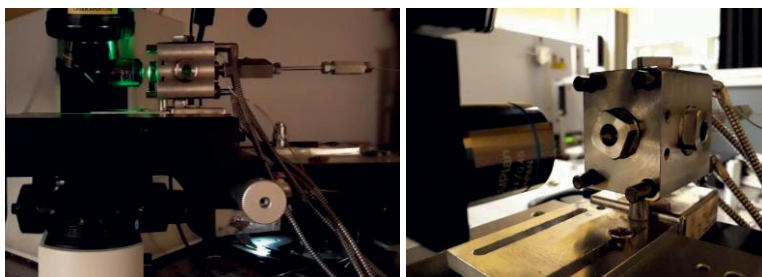


**Figure 19.** The in-situ Raman setup.

The reaction chamber had a volume of 5.4 mL with retractable heating elements embedded into the chamber walls. The CO<sub>2</sub> was introduced to the chamber using a manual pump. The chamber had a window used for the in-situ investigations. A sapphire window was used for the Raman experiments and Calcium Fluoride (CaF<sub>2</sub>) for the FTIR measurements. A mechanical moving table was used to focus the microscopes and spectroscopes on the sample surface. The zinc samples were first cut into 12 mm diameter circular samples with two holes of 1 mm diameter drilled to enable transport of the reaction gases on the measurement surface.

In the Raman and FTIR scCO<sub>2</sub> experiments, a stirrer and 0.2 mL of water were placed inside the chamber before the scCO<sub>2</sub> tests. A magnetic stirrer plate was placed under the chamber as seen from Fig. 19. The samples were placed near the measurement window, as shown in Fig. 20. Depressurization was performed manually using a sensitive needle valve and a heating system. The optical images as well as Raman and FTIR measurements were taken from the middle of the sample. The reaction pressure for all tests were 100 bar with temperatures of 40°C and 60°C.

The sessile droplet tests were performed by placing a 3 μL water droplet ( $D = 2.19 \pm 0.06$  mm) on the zinc surface. The sample was placed on an appropriate distance from the window to ensure no contact of the droplet with the window. The optical images and Raman measurements were taken from the middle of the droplet. The reaction conditions were pressure of 5 bar at 22°C and 40°C temperatures.

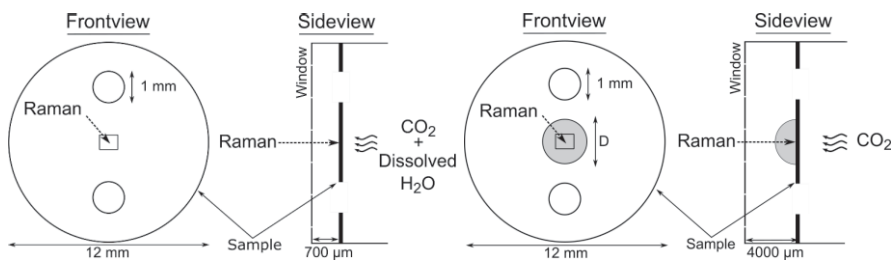


**Figure 20.** The schematic description of in-situ scCO<sub>2</sub> (left) and droplet test (right) sample setups (Publication V).

### 5.2.3 Isotope water droplet tests (Publication VI)

The tests were conducted in the same apparatus as described in chapter 5.2.1 in Tampere University. The experiments were conducted identically by first placing a droplet of the isotope water on a pure zinc substrate and exposing it to 300 bar of CO<sub>2</sub> in 50°C to form the ZnCO<sub>3</sub> structure. In a separate exposure, a new droplet of the isotope water was placed on the same substrate and exposed to liquid CO<sub>2</sub> in 65 bar and 22°C. The aforementioned procedure was performed separately with D<sub>2</sub>O water and <sup>18</sup>O water.

## 5.3 Characterization techniques

Various scanning electron microscopes (SEM) from Top Analytica and Tampere University were used in the publications. In publications I – II: Zeiss ultra plus (FEG-SEM, Zeiss, Germany) with INCA Energy 350 energy dispersive spectrometer (EDS, Oxford Instruments, UK), In publications III – IV: JSM-6335F (SEM, JEOL, Japan) and JSM-IT100 (SEM, JEOL, Japan). In publication V: JSM-IT500 (SEM, JEOL, Japan) with silicon drift detector (JEOL, Japan). In publication VI: Zeiss Gemini (SEM, Zeiss, Germany) with a QUANTAX FlatQUAD (EDS, Bruker, Germany). Sample preparation for the SEM characterizations did not require any coatings.

In publication III, also an electron probe microanalyzer (EPMA) with a wavelength-dispersive X-ray spectrometer (WDS, JEOL, Japan) was used for elemental mapping. Furthermore, an Ilion + Advantage Precision Cross-Section System (Gatan Inc., USA) was used to prepare cross-section samples.



Transmission electron microscope (TEM) JEM 2010 (JEOL, Japan) with EDS (Thermo Scientific Noran Vantage) was used to characterize the needle-structure in publication II. The sample was prepared by using a surgical blade to carefully scrape the surface structure on a nickel TEM grid with a holey carbon film.

The crystal structures were examined with x-ray diffraction (XRD, Panalytical Empyrean) with monochromatized  $\text{CuK}_\alpha$  radiation. In some cases, a grazing incidence x-ray diffraction x-ray measurements (GIXRD) for thin film characterization was used.

Fourier transform infrared spectroscopy (FTIR, Bruker tensor 27, Germany) with attenuated total reflectance (ATR) sample holder with a DLaTGS detector was used in publications I – II. In publication IV, a FTIR (Bruker Vertex 70) with the same sample holder and detector as in publication I – II was used.

The in-situ measurements performed in publication V were done in a transfection mode using a Nicolet infrared microscope (Thermo Scientific, France) with a Thermo Optek interferometer using a globar source and a KBr/Ge beamsplitter. The detector was Mercury Cadmium Telluride (MCT) capable of investigating a spectral range of 400 to 7500  $\text{cm}^{-1}$  and a 2  $\text{cm}^{-1}$  resolution.

The Raman measurements in publication IV were performed with Renishaw inVia Qontor confocal microscope with a 100x objective. The measurements were done with  $\lambda = 532$  excitation and a grating of 1800 1/mm. The resolution of the spectra was 4  $\text{cm}^{-1}$  with multiple spectral accumulations to reduce signal-to-noise ratio.

The experiments in publication V were performed with a Jobin-Yvon Horiba XploRA confocal Raman microscope with a 50x objective. Excitation of  $\lambda = 532$  excitation and rating of 1800 1/mm were used for the measurements. The measured spectral range was 200 – 1900  $\text{cm}^{-1}$  with 4  $\text{cm}^{-1}$  resolution.

The optical band-gap of the ZnO structure in publication II was performed with a spectrophotometer (Shimadzu UV 3600) equipped with an integrating sphere coated with barium sulphate. The absorption spectra were recorded from 800 to 220 nm with 2 nm intervals in a reflectance mode. Barium sulphate was used as a reflectance reference. The band-gap was determined using the Tauc plot [105].

In publications I and III, X-ray Photoelectron Spectroscopy (XPS, PHI Quantum 2000) was used for elemental analysis. The XPS used monochromatic Al  $\text{K}\alpha$  beam (50W, 14 kV) with a 100  $\mu\text{m}$  spot size. The carbon peak at 284.9 eV was used for charge-shift correction.

CAM 200 Optical Contact Angle Meter (KSV Instruments) was used for the water contact angle measurements of HDG substrates. Surface free energy (SFE)

was calculated using the Wu method based on measurements were performed with three liquids: water, ethylene glycol and diiodomethane.

Phi Thrift II Time-of-flight secondary ion mass spectrometer (ToF-SIMS, Physical Electronics, USA) was used for mapping of ions. The measurements were performed with 25 kV with a 50  $\mu\text{m}$  raster size with a total time for mapping of 1 h.  $\text{Ga}^+$  ion mild sputtering was carried out prior to the measurements.

-

## 6 ARTIFICIAL PATINA FORMATION

This chapter describes the CO<sub>2</sub> treatment that is used to functionalize the zinc surface by forming the artificial patina layer. The stages of the treatment and how they affect the final patina layer are described. Finally, the carbonate structures in the artificial patina layer are characterized.

### 6.1 The carbon dioxide treatment

The carbon dioxide treatment produces a carbonate structure layer on zinc, also-called the artificial patina layer. The artificial patina forms on the zinc surface in pressurized CO<sub>2</sub> conditions and in the presence of water. The treatment can be controlled by changing the pressure, temperature, depressurization conditions and addition of catalysts. The catalysts provide means for accelerated growth of reaction products but do not directly participate in the carbonate reactions that form the artificial patina structures. The treatment has been shown to be applicable for most zinc coatings, whether pure or alloyed.

The artificial patina is composed of two components: **zinc carbonate (ZnCO<sub>3</sub>)** and **needle carbonate**. The zinc carbonate structure is an anhydrous carbonate species with chemical formula of ZnCO<sub>3</sub>. The needle carbonate is a mixed zinc hydroxy carbonate species which is termed simply as needle carbonate for the remainder of the thesis. The needle carbonate has a complex but consistent structure which is described more in-depth later in the characterization section (6.2.2).

The artificial patina treatment can produce surfaces with only one of the carbonates (ZnCO<sub>3</sub> and needle carbonate) present on the surface, or both, by adjusting the treatment parameters. However, in general, some applications benefit from a dual carbonate structure, i.e. containing both of the structures, covering the substrate's entire surface. Fig. 21 shows the plain hot-dip galvanized surface before treatment (left) and after two different treatments producing an only-ZnCO<sub>3</sub> structure (middle) and a dual-carbonate structure (right). The SEM images show the morphologies of the spherical ZnCO<sub>3</sub> and the nanowire needle carbonate structures.

The close-up SEM image of the dual carbonate structure is shown in Fig. 22, which shows that the spherical  $ZnCO_3$  is composed of very fine cubic structures.

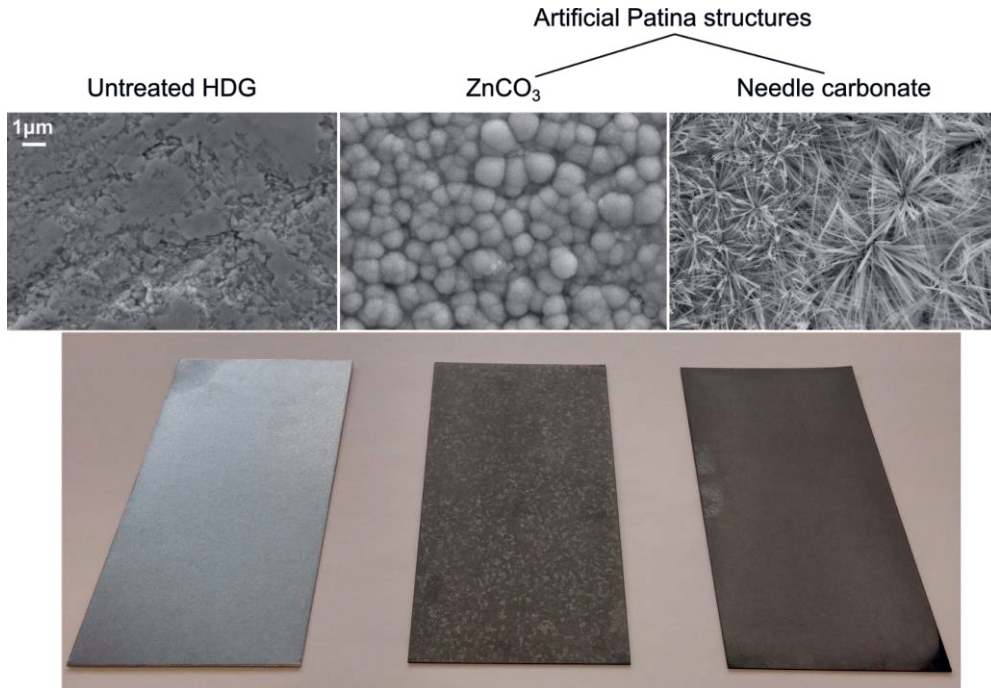


**Figure 21.** Effect of the carbon dioxide treatment on hot-dip galvanized substrates. Treatments performed with  $Cu(hfac)_2$ -catalyst.

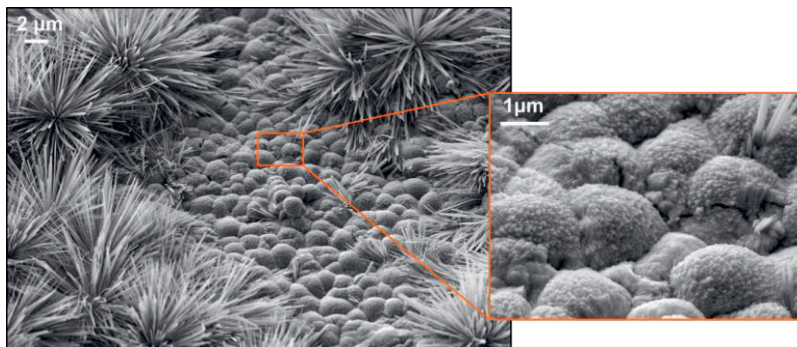


**Figure 22.** SEM images of the dual carbonate structure with close-up of the  $ZnCO_3$  carbonate surface.

The carbon dioxide treatment is typically performed in  $scCO_2$ , but these structures can also form under significantly lower pressures, down to 5 bar. However, the

scCO<sub>2</sub> treatment enables better treatment control as well as an exceptional surface coverage. The treatment procedures differ between critical and subcritical conditions, but the same reactions and principles of the carbonate formation apply in both cases.

The wet scCO<sub>2</sub> treatment is diagrammed in Fig. 23. The treatment starts by enclosing the substrate in a chamber, which is then filled with CO<sub>2</sub>, and heated and pressurized into the treatment conditions. Subsequently, distilled water or catalyst solution is added into the chamber. After the liquid reactants are added, the **holding phase** begins in which the conditions are held static, and the zinc surface starts to react with CO<sub>2</sub> and with water dissolved in the CO<sub>2</sub>. The holding phase is followed by a dynamic **depressurization phase** in which the scCO<sub>2</sub> is evacuated from the reaction chamber, causing the dissolved water to precipitate as fine droplets inside the reaction volume. Both the holding phase and the depressurization phase affect the formation of the carbonate structures. The final artificial patina layer results when the depressurization phase is complete. Publication V studied in-situ the behaviour of the zinc surface during the holding and depressurization phases.

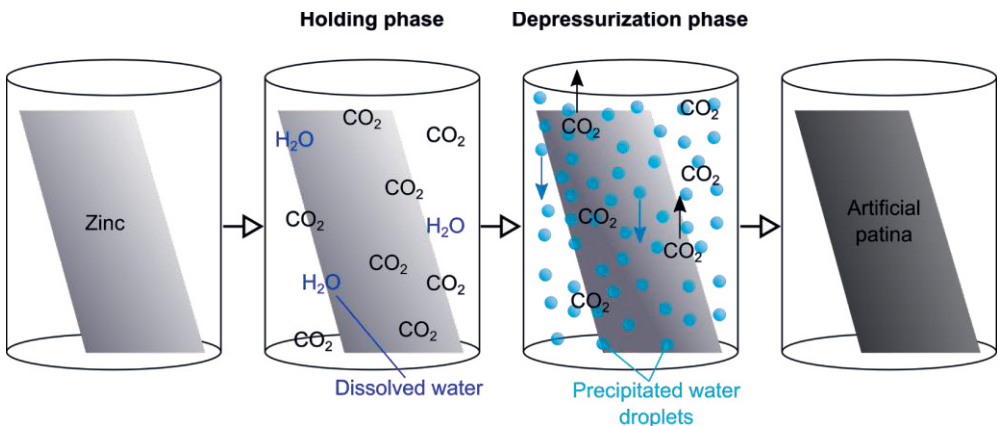


**Figure 23.** Schematic of the wet-scCO<sub>2</sub> treatment stages.

### 6.1.1 Reactions and phenomena during the isostatic holding phase of the scCO<sub>2</sub> treatment

During the isostatic holding phase, water or the catalyst solution first dissolves into the scCO<sub>2</sub> and starts to react with the zinc surface. The reaction products are visible as dark deposits on the surface (Fig. 24, shown at 100 bar and at 40°C and 60°C).

The products are ZnO and ZnCO<sub>3</sub>, as shown by in-situ Raman measurements (Fig. 25) with peaks at 570 cm<sup>-1</sup> for ZnO, and at 1093 cm<sup>-1</sup>, 300 cm<sup>-1</sup>, and 730 cm<sup>-1</sup> corresponding to the  $\nu_1$  symmetric stretching mode, lattice mode, and  $\nu_4$  antisymmetric bending mode of ZnCO<sub>3</sub>.

ZnO is the initial reaction product due to the corrosion due to the water, CO<sub>2</sub> and trace amounts of O<sub>2</sub> remaining in the reaction chamber from air. Although no water was detected on the zinc surface, it is expected that a thin film of water is adsorbing on the surface allowing the ZnO and ZnCO<sub>3</sub> reactions to occur. The formation of the thin water film has been reported in other studies performed on mineral surfaces in similar conditions [100, 101]. The ex-situ Raman spectra also show the presence of unreacted residual ZnO on the surface after treatment. The in-situ and ex-situ results in Fig. 25 are representative of the scCO<sub>2</sub> treatment with negligible effect from the following depressurization phase as a result of the minute volume between the window and sample in the tests (see Fig. 20 for description of the experiment setup).

Needle carbonate formation has not been observed in the experiments. It is possible that small amounts of needle carbonate form during tests but the Raman and FTIR are too insensitive for their characterization (see Publication V), or that needle carbonate does not form during the holding period. As the needle structure protrudes significantly from the surface, it requires a large enough reaction medium to grow which is lacking in the supercritical medium due to small water amount and could, therefore, explain absence of needle structure during holding phase.

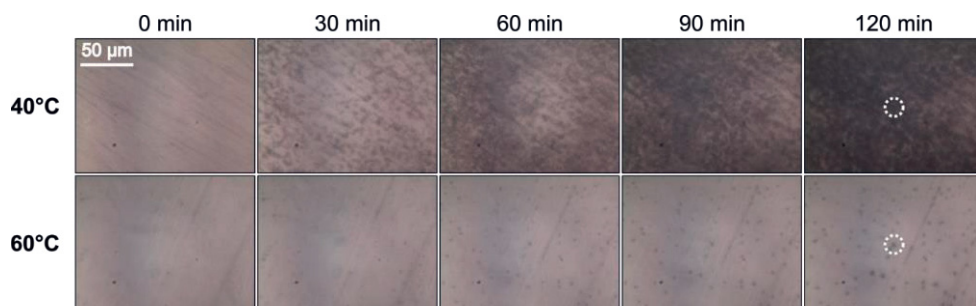


**Figure 24.** The zinc surface during the holding phase at 100 bar, at both 40°C and 60°C. The white circle shows the location of the in-situ Raman spectra shown in Fig. 25 (Publication V).

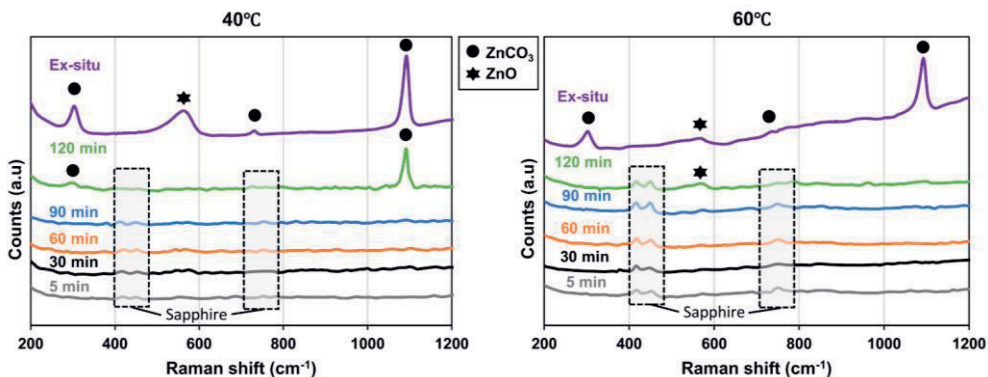


**Figure 25.** In-situ and ex-situ Raman spectra of ZnO and ZnCO<sub>3</sub> formation in scCO<sub>2</sub> treatment at 100 bar 40°C (left) and 60°C (right). Peaks in the area denoted as “Sapphire” are due to the sapphire window and not representative of the zinc surface (Publication V).

Pressure and temperature affect the carbonate formation in different ways during the holding period, notably because pressure and temperature greatly influence the amount of dissolved water, as mentioned in chapter 3. The absolute amount of dissolved water<sup>1</sup> in the chamber is shown in Fig. 26. The in-situ images (Fig. 24) show that, during a holding period of 120 minutes, the occurrence of the dark deposits is much more prevalent at 40°C, with more dissolved water than at 60°C. The effect of dissolved water was confirmed using in-situ FTIR measurements in Publication V. Therefore, the higher amount of ZnCO<sub>3</sub> formation at 40°C compared to 60°C is most likely due to the higher dissolved water amount resulting in greater reactivity at the zinc surface. In addition to affecting water solvability, temperature affects also the thermodynamical aspects of carbonate formation; this relationship will be discussed further in the depressurization chapter below.

As seen in Fig. 24, the amount of ZnCO<sub>3</sub> increases as the reaction time proceeds. If the supercritical treatment is performed in a large-volume vessel, the amount of dense ZnCO<sub>3</sub> formed could influence the formation processes during the following depressurization phase. Greater ZnCO<sub>3</sub> coverage over the surface could then inhibit the availability of the dissolving Zn<sup>2+</sup> ions because less metallic zinc is exposed to the environment.

In-situ Raman measurements showed that the ZnCO<sub>3</sub> formation correlates with the dissolved water amounts (Fig. 26). The treatment pressure has not been shown

<sup>1</sup>Two different sized chambers, 255 mL and 5.4 mL, were used throughout the thesis. The amounts in the y-axis shown in Fig. 27 are for the 5.4 mL chamber. Although the amounts are different for each chamber, the relative trend is still identical.

to affect outcomes by any means other than through the amount of dissolved water during the holding phase. All of the in-situ measurements (performed with FTIR and Raman spectroscopy) have identified only  $\text{ZnCO}_3$  without the presence of the needle carbonate species. However, since the characterization techniques have certain sensitivity limits as shown in Publication V, the possibility of minor needle carbonate formation cannot be excluded.

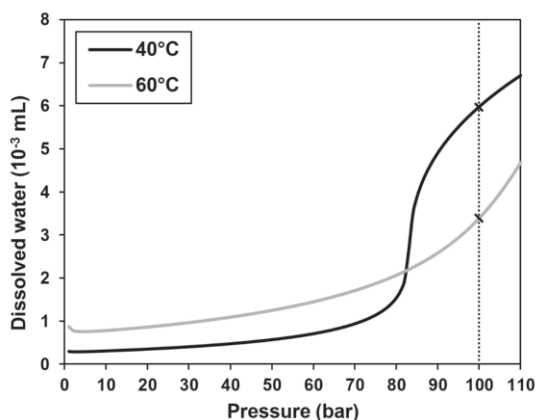


**Figure 26.** Dissolution of water in  $\text{scCO}_2$  (Publication V).

The amount of water added to the reaction chamber does not affect the treatment, assuming saturated conditions in  $\text{scCO}_2$ , as is the case in the  $\text{CO}_2$  treatment. It was found in experiments that the  $\text{scCO}_2$  has no effect when no water is present. This agrees well with other studies done by other authors [101, 105].

Although water is a sufficient reactant to form the carbonate structures, the addition of a  $\text{Cu}(\text{hfac})_2$ -ethanol catalyst solution has a significant effect on the zinc surface. The catalyst solution has two main effects on the treatment. First, it increases the amount of dissolved water due to the co-solvent effect of ethanol [107]. Secondly, the copper forms visible deposits on the zinc surface, as evidenced by the colour changes shown in Fig. 27. This is further confirmed by electron-probe microanalysis of a sample treated in similar conditions; metallic copper precipitated on the original zinc surface, and was subsequently surrounded by  $\text{ZnCO}_3$  (Fig. 28).



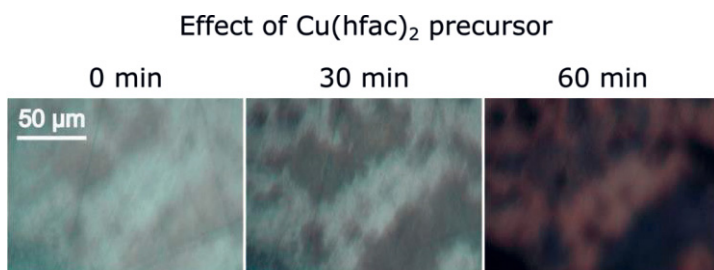


**Figure 27.** Optical in-situ image of the colour change on zinc surface from reducing copper derived from  $\text{Cu}(\text{hfac})_2$  catalyst during the holding phase of the wet  $\text{scCO}_2$  treatment. Treatment conditions were 85 bar 40°C with the catalyst dissolved in 50-50 v-% water ethanol solution (unpublished data).

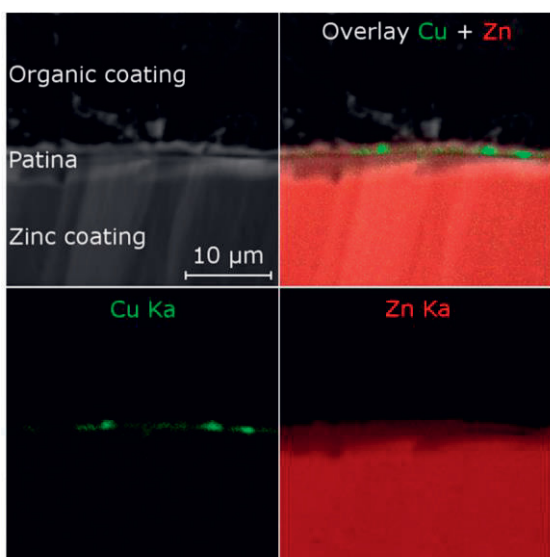


**Figure 28.** EPMA element maps of Zn and Cu measured from a cross-section of a coated artificial patina sample 80 bar 60°C (Publication IV).

The formation of corrosion products can be limited by the anodic reaction rate (dissolution of  $\text{Zn}^{2+}$  ions), by the cathodic reaction rate (equations 2, 3) and by the availability of other reaction constituents (carbonate species) [12]. Insufficient carbonate is unlikely in pressurized  $\text{CO}_2$  conditions so the rate of carbonate formation is limited mostly by the dissolution of  $\text{Zn}^{2+}$  ions. Slow dissolution of  $\text{Zn}^{2+}$  ions could result from insufficient anodic or cathodic action. Nonetheless, the catalyzing effect of the copper can be explained by copper deposition on the surface

which can accelerate the reactions by many means. First, it can increase the anodic dissolution of  $Zn^{2+}$  ions as follows:



The result, in addition to the deposition of metallic copper, is a greater supply of the  $Zn^{2+}$  ions needed for the carbonate reactions (equations 12–14). Furthermore, the galvanic coupling at the Zn-Cu surface accelerates the cathodic reactions (oxygen dissolving and hydrogen evolution) resulting in overall catalysing effect on the dissolution and carbonate forming reactions [1].

In conclusion, the main interactions in the holding phase are twofold. First, the water and catalyst solution dissolve into the reaction phase. Second, the water adsorbs on the substrate surface and initiates reactions between zinc,  $CO_2$  and  $O_2$  to form ZnO and  $ZnCO_3$  on the zinc surface.

### 6.1.2 Reactions and phenomena during the dynamic depressurization phase of the sc $CO_2$ treatment

The holding phase is followed by the depressurization phase in which the  $CO_2$  is vented out of the reaction chamber, with the flow rate under careful control. The temperature decreases along with the pressure, and the chamber heating is turned off to allow further cooling during depressurization. Consequently, as the pressure and temperature decrease, solvability decreases, and the dissolved species precipitate in the sc $CO_2$  phase. Fig. 29 shows water precipitation from the in-situ FTIR spectra as the chamber is vented after a 120-minute holding time. It can be seen that, once the  $CO_2$  is flowing out (intensity of  $CO_2$  peaks decrease), there is emergence of a wide hydroxyl ( $OH^-$ ) peak at  $3200\text{ cm}^{-1}$  indicating liquid water. Furthermore, the peak at  $1607\text{ cm}^{-1}$ , indicating dissolved water (D), shifts towards  $1650\text{ cm}^{-1}$  which indicates precipitated water (C).

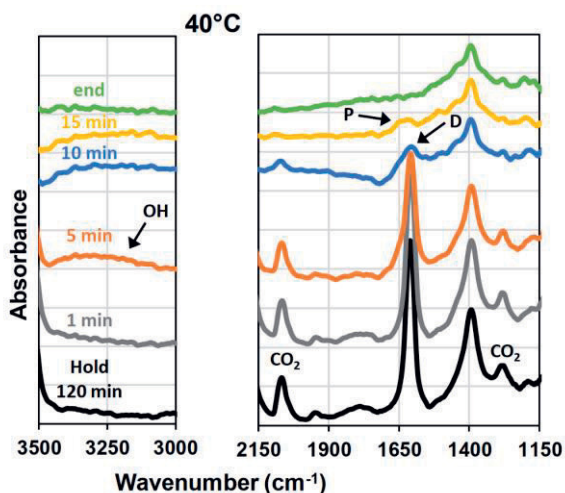


**Figure 29.** FTIR spectra of depressurization phase of 100 bar, 40°C sample. “P” refers to precipitated water and “D” to dissolved water (Publication V).

The precipitation of water inside a scCO<sub>2</sub> chamber during depressurization is shown in Fig. 30. The image shows, through a sapphire window, a horizontally oriented HDG sheet that has been exposed to wet-scCO<sub>2</sub> for 60 minutes at 300 bar and 50°C, and subsequently depressurized. The scCO<sub>2</sub> medium is clear when saturated with dissolved water. As the solvability of scCO<sub>2</sub> decreases with decreasing pressure and temperature, a fine mist can be seen precipitating inside the chamber. After the mist has descended, the substrate surface is covered with a water film as the depressurization completes. As the water droplets start to contact the substrate surface, they initiate new reaction dynamics as will be described below.

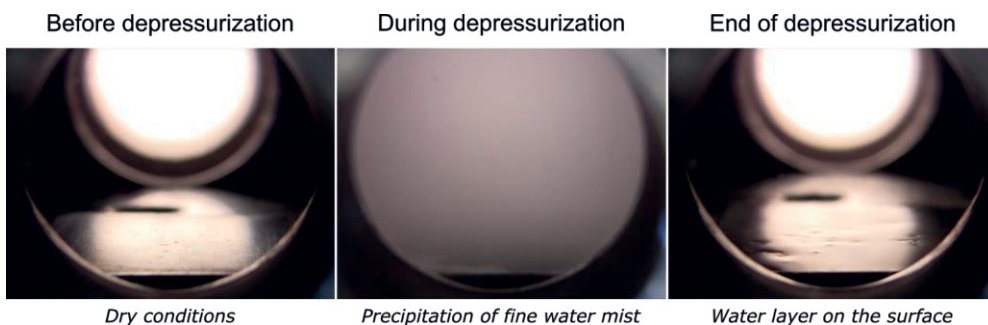


**Figure 30.** Precipitation of water during the depressurization phase in treatment at 300 bar and 50°C shown through snapshots of a video recording (unpublished data).

The depressurization phase, being highly dynamic in terms of changing conditions, poses many issues for direct investigations of the carbonate formation. Therefore, a series of tests were performed on water droplets on zinc under static CO<sub>2</sub> conditions, specifically at 5 bar and 22°C. Furthermore, the effect of O<sub>2</sub> addition was studied for a more in-depth understanding of its role in the cathodic reactivity. The test setup can be seen in Fig. 20.

The tests revealed formation of the needle carbonate and ZnCO<sub>3</sub> as shown in the post-treatment SEM pictures in Fig. 31. Adding O<sub>2</sub> increased the coverage and amount of needle carbonate structure over the entire droplet area. Conversely, the sample without added O<sub>2</sub> showed increased needle carbonate on the droplet edge and less coverage in the middle of the droplet.

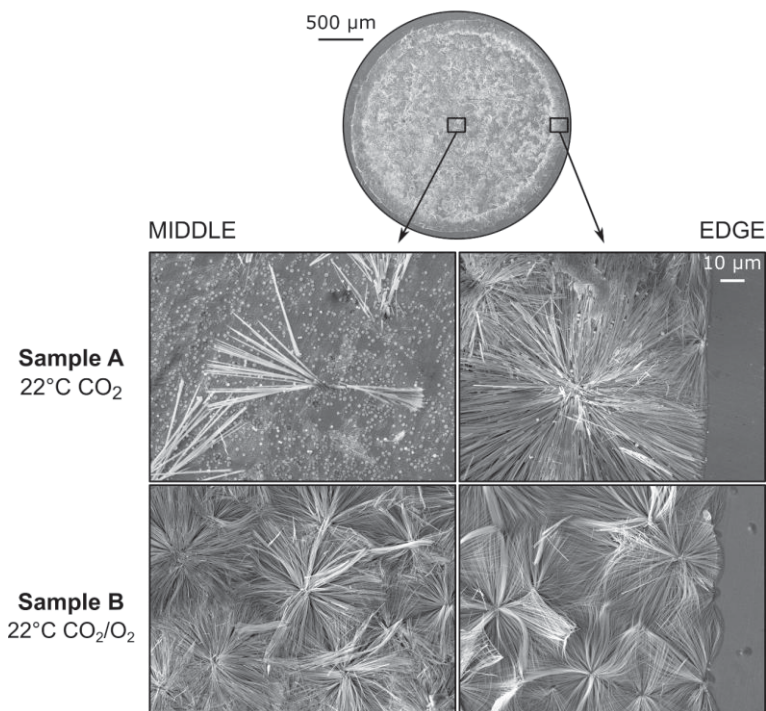


**Figure 31.** SEM images of droplets treated for 60 minutes in 5 bar CO<sub>2</sub> (sample A) and added 2 bar of O<sub>2</sub> to reach total pressure of 7 bar (Sample B) at 22°C (Publication V).

Fig. 32 shows in-situ observations during the treatment. Both samples exhibit dark deposits after 60 minutes, but they appear much earlier on the sample with added O<sub>2</sub>. Fig. 33 reveals that the initial dark deposits in sample B are ZnO which later converts into the needle carbonate structure. Furthermore, formation of

ZnCO<sub>3</sub> was also observed during the in-situ measurements. The carbonate structure formed only after 30 minutes into the experiment, most likely due to the slow diffusion of CO<sub>2</sub> to supply enough bicarbonate and carbonate ions inside the droplet. However, gas diffusion in the depressurization phase of the scCO<sub>2</sub> experiments is not a limiting factor as in the droplet tests. In the depressurization phase, the water precipitates as small droplets and the droplets grow larger subsequently. It can be assumed that the precipitated water is always saturated with CO<sub>2</sub>. Therefore, the needle carbonate is able to form even during the 10–15 minutes of depressurization as documented in Publications I–IV. As seen from Fig. 24, the amount of the ZnCO<sub>3</sub> formation increases as the reaction time increases, resulting in greater coverage of the surface with the structure.

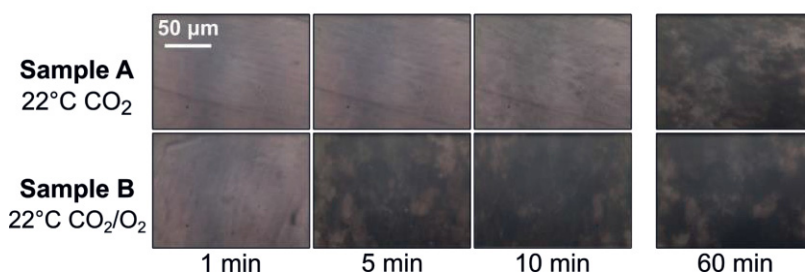


Figure 32. In-situ images of droplet tests (Publication V).

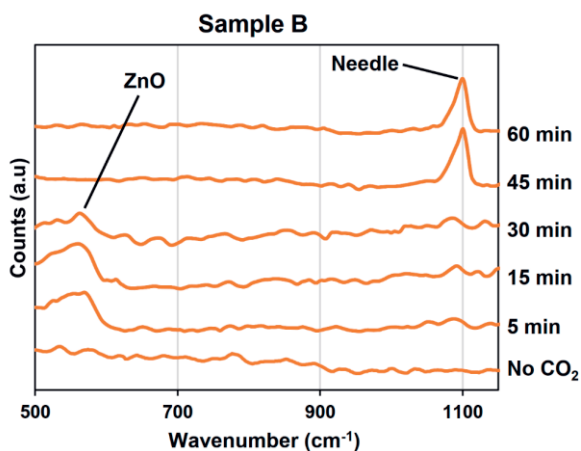
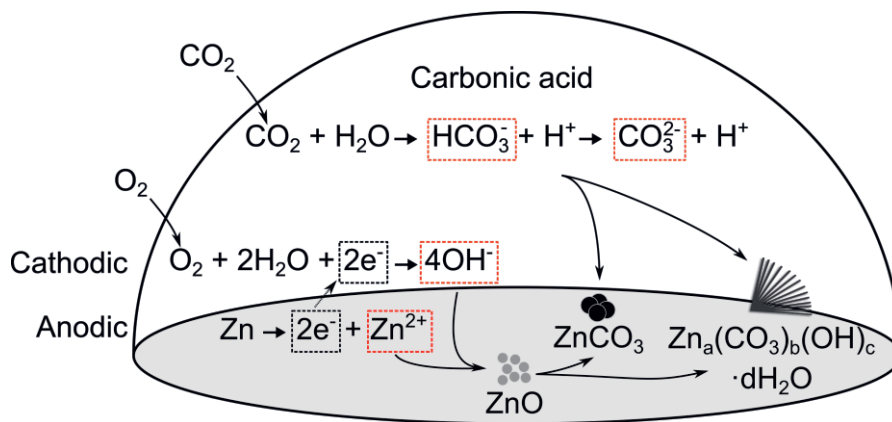


Figure 33. In-situ Raman spectrum from the middle of the sample B with 5 bar CO<sub>2</sub> and 2 bar O<sub>2</sub> (Publication V).

The reactions occurring inside the precipitating droplet are illustrated schematically in Fig. 34. The main limiting reactions are the diffusion of  $\text{CO}_2$  and diffusion and reduction of  $\text{O}_2$  as well as  $\text{Zn}^{2+}$  dissolution. The dissolving oxygen will supply sufficient cathodic action for the anodic zinc dissolution to occur. The main cathodic reaction for zinc has been shown to be oxygen reduction, which is expected to be the predominant cathodic reaction taking place as well [1, 107–109]. However, hydrogen may also form due to the acidic conditions. Oxygen dissolving in water will produce hydroxyl ions ( $\text{OH}^-$ ) that can react with zinc forming  $\text{ZnO}$ , and subsequently forming the needle carbonate structure. As was established earlier, the first corrosion product that forms is  $\text{ZnO}$  which is followed by formation of the carbonate structures, though, carbonates could also form without  $\text{ZnO}$  by reacting directly with the free  $\text{Zn}^{2+}$  ions. Other studies have also shown that zinc hydroxide ( $\text{Zn}(\text{OH})_2$ ) forms together with  $\text{ZnO}$  as an initial corrosion product [67]. However,  $\text{Zn}(\text{OH})_2$  was not observed in our in-situ studies, which may be explained by the low pH under the higher  $\text{CO}_2$  partial pressures used here.

The  $\text{CO}_2$  dissociates into bicarbonate and carbonate ions that can then react with already-formed  $\text{ZnO}$  or free  $\text{Zn}^{2+}$  and  $\text{OH}^-$  ions inside the droplet to form the needle and zinc carbonates. The needle carbonate formed readily at room temperature but its presence decreased as the temperature increased, in line with the greater stability of zinc hydroxy carbonates at lower temperatures [110, 111].  $\text{ZnCO}_3$  formed in all temperatures but was much more pervasive than needle carbonate at temperatures above  $60^\circ\text{C}$ .



**Figure 34.** Schematic of reaction sequences of carbonate formation inside a water droplet in pressurized  $\text{CO}_2$  conditions (Publication V).

In order to confirm the proposed reaction sequences (Fig. 34) as well as to investigate the origins of the reaction constituents forming the structures, a series of isotopic water droplet experiments combined with ToF-SIMS investigations were conducted. Fig. 35 shows formation of both carbonate structures when zinc surface was reacted with a droplet of  $^{18}\text{O}$  water that was then exposed to pressurized  $\text{CO}_2$ . The  $^{18}\text{O}^{2-}$  ions were found in both the  $\text{ZnCO}_3$  and needle carbonate structures, demonstrating that the oxygen from the water was transported into both structures. This confirms the carbonic acid formation (Eq. 8) and its subsequent dissociation to bicarbonate- (Eq. 9) or carbonate ions (Eq. 10) that then react with the  $\text{Zn}^{2+}$  ions.

An identical test, but utilizing deuterium water ( $\text{D}_2\text{O}$ ) instead of  $^{18}\text{O}$ -water, is shown in Fig. 36. The deuterium was found specifically in the needle carbonate and was absent from the  $\text{ZnCO}_3$  structures. The  $\text{OH}^-$  ions must therefore have formed through the oxygen dissolution process or other  $\text{OH}^-$  forming processes originating from water. These  $\text{OH}^-$  ions participated in the needle carbonate formation reaction by attaching as water of crystallization or  $\text{OH}$ -groups to the carbonate structure. The  $\text{ZnCO}_3$  structures did not contain the deuterium and therefore did not, as expected, contain  $\text{OH}$ -groups. The  $\text{O}^-$  and  $\text{OH}^-$  ions shown in the figures are from adventitious species so could not be used for evaluations.

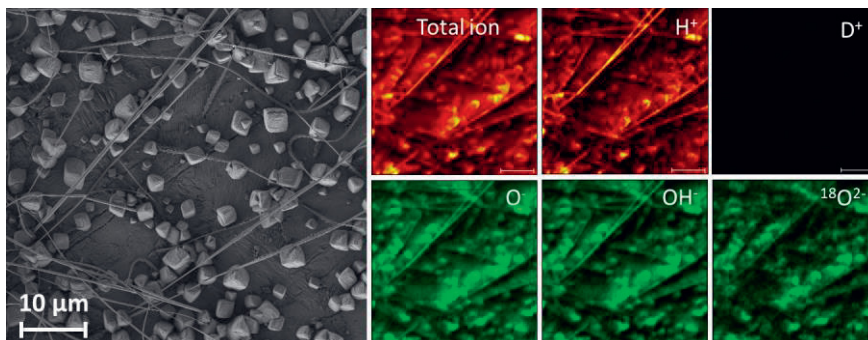


**Figure 35.** Zinc surface reacted with a  $^{18}\text{O}$ -water droplet that was exposed to pressurized  $\text{CO}_2$  to form both carbonate structures of which ion distributions were characterized with ToF-SIMS (Publication VI).

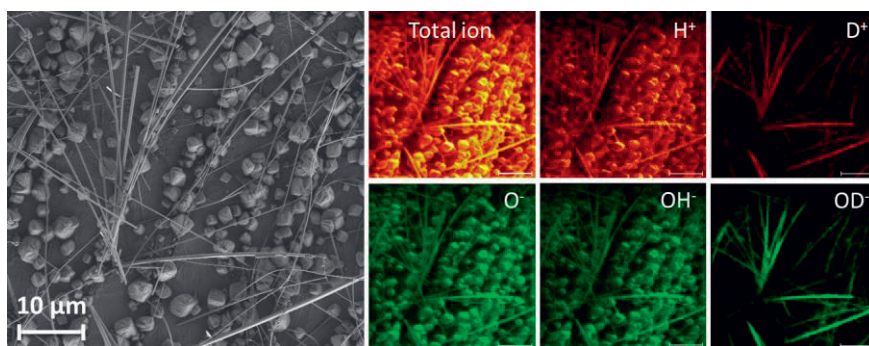


**Figure 36.** Zinc surface reacted with a  $D_2O$ -water droplet that was exposed to pressurized  $CO_2$  to form both carbonate structures of which ion distributions were characterized with ToF-SIMS (Publication VI).

## 6.2 Characterization of the carbonate structures

The carbon dioxide treatment results in two functional carbonate structures: zinc carbonate and needle carbonate. The structures can be produced individually or as a mixed layer consisting of both carbonates. This chapter discusses the characteristics and chemical structures of the carbonates.

### 6.2.1 Zinc carbonate ( $ZnCO_3$ ) structure

The zinc carbonate structure is shown in Fig. 37. The structure is composed of fine cubic structures that are arranged in spherical clusters on the zinc surface. The immediate substrate surface is fully covered with the zinc carbonate, which isolates the zinc surface by inhibiting transport of external species that could cause corrosion.



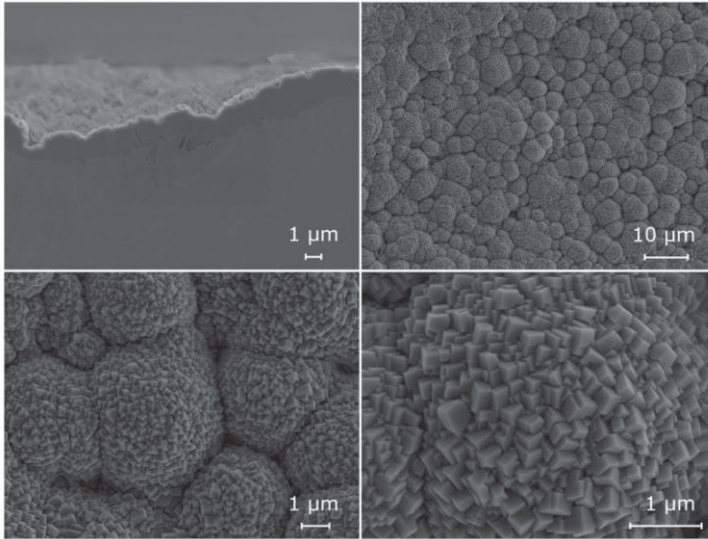


**Figure 37.** SEM of zinc carbonate structure (Publication IV).

The larger spherical clusters of the initial cubic structures (Fig. 37) could be formed in the depressurization phase of the treatment when water droplets precipitate on the surface. Sun et al. showed almost identical behaviour in steel corrosion product formation as a result of water droplet precipitation [113]. The SEM images of the samples exposed only to  $\text{scCO}_2$  (Fig. 38) show a morphology distinctly different from a surface that has undergone the depressurization phase as well.

The zinc carbonate has been characterized with XRD (Fig. 39). The XRD, Raman and FTIR characterizations documented in the publications confirm that the structure is identical to smithsonite, a naturally occurring mineral form of  $\text{ZnCO}_3$ .

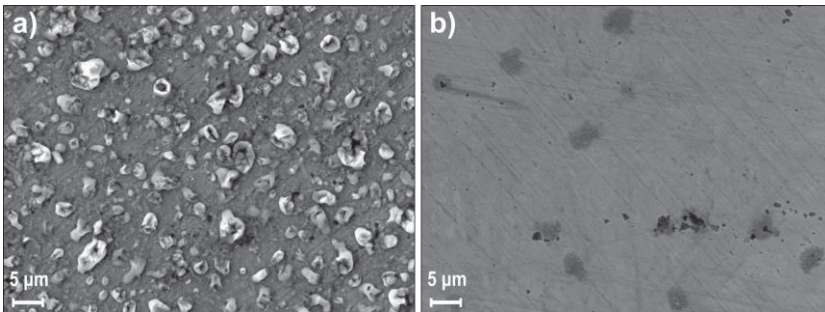


**Figure 38.** SEM images of sample surfaces with  $\text{ZnCO}_3$  exposed to water-saturated  $\text{scCO}_2$  in 40°C (a) and 60°C (b) (Publication V).

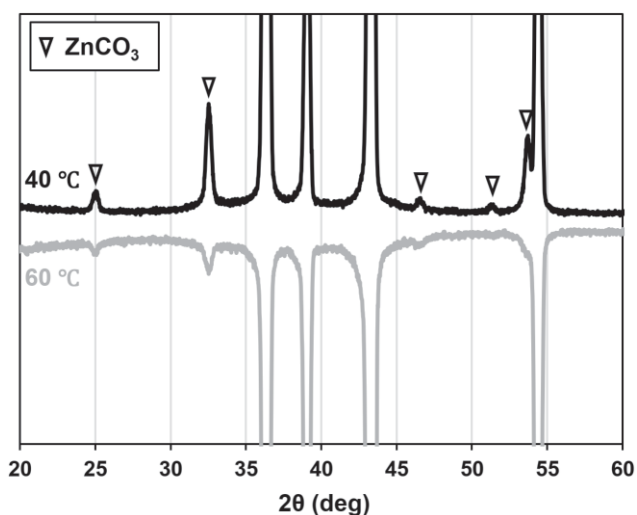


**Figure 39.** GIXRD of zinc carbonate structure (Publication V).

The zinc carbonate tends to form at higher temperatures than the needle carbonate, most likely due to its anhydrous nature. Hydrozincite is the most common product in atmospheric corrosion. However,  $\text{ZnCO}_3$  is rarely seen during natural patination [80]. This could be a consequence of low  $\text{CO}_2$  pressures in the atmosphere that result in low concentration of carbonic acid. This explanation is supported by the occurrence of  $\text{ZnCO}_3$  in environments with a higher  $\text{CO}_2$  concentration as opposed to hydrozincite, based on the calculations of Preis et al. [114]. Studies using  $\text{CO}_2$  as a reactant for  $\text{ZnCO}_3$  synthesis report similar results [115].

## 6.2.2 Needle carbonate structure

The needle structure is shown in Fig. 40 as an individual structure and in Fig. 41 as a dual carbonate structure together with the  $\text{ZnCO}_3$ . The needle structure protrudes from the zinc surface in many directions. The structures can cover the surface uniformly as shown in Fig. 40 or can grow from distinct spots on the surface, forming a flower-like clusters. The structure has a high surface area, providing multiple benefits for applications discussed in the next chapter. This needle-like morphology is not typically formed in atmospheric corrosion.

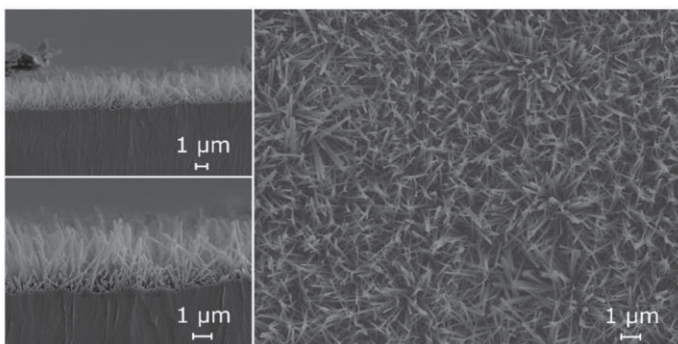


**Figure 40.** SEM image of only needle carbonate structure (Publication IV).

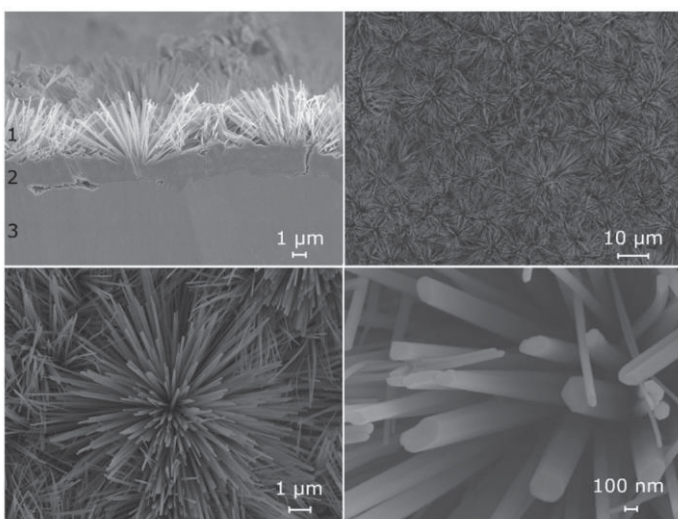


**Figure 41.** SEM of dual structure containing both needle carbonate and zinc carbonate (Publication IV).

The chemical structure of the needle carbonate was characterized with Raman and FTIR spectroscopy (Fig. 42). The FTIR spectrum shows  $\text{CO}_3^{2-}$  groups from the peaks at  $1383\text{ cm}^{-1}$  and  $1520\text{ cm}^{-1}$  which indicate the antisymmetric  $\nu_4$  stretching modes of carbonate [113, 114]. The double peak is typical for zinc hydroxy carbonate containing hydroxyl groups, i.e. hydrozincite [79]. However, the spectrum has also another peak at  $1435\text{ cm}^{-1}$  which does not occur for hydrozincite. Furthermore, the Raman spectrum includes a peak at  $1098\text{ cm}^{-1}$  that corresponds to the  $\nu_1$  symmetric stretching mode of  $\text{CO}_3^{2-}$ , with a shoulder at lower wavenumbers, related to overlapping  $\nu_1$  symmetric C–O stretching bands [101]. The peak at  $1076\text{ cm}^{-1}$  is not

active in IR-measurements for hydrozincite [78, 113]. However, this peak could appear due to symmetry reduction caused by the structure's distortion [115]. The needle carbonate has a broad absorption peak around  $3200\text{ cm}^{-1}$  which is attributed to OH stretching vibrations. Finally, the  $1610\text{ cm}^{-1}$  peak is typical for structures with  $\text{H}_2\text{O}$  bending which derives from structural water within the structure [117]. TEM studies in publication II confirm that no other species, e.g. Fe or Al, are present in the structure. Consequently, the needle carbonate is a zinc hydroxy carbonate species although with clear differences from many of the various similar structures shown in the literature [77, 78, 116]. The needle carbonate is of the form  $\text{Zn}_a(\text{CO}_3)_b(\text{OH})_c \cdot d\text{H}_2\text{O}$  although its exact stoichiometry remains unclear.

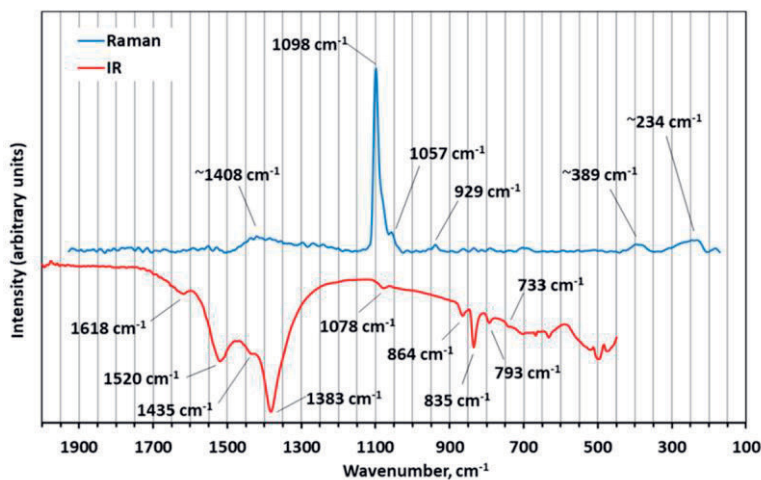


**Figure 42.** FTIR and Raman of needle carbonate structure (Publication IV).

The XPS measurements (Fig. 43) show the presence of Zn, C and O. The results also present the evidence of C=O bonding ( $289.9\text{ eV}$ ) within the needle structure, indicating carbonate species. The EDS measurements discussed in Publication IV show the difference between the atomic ratios of the needle carbonate and reference hydrozincite. The atomic ratio of Zn:C:O is 1:0.4:2.5 in the needle carbonate whereas for hydrozincite, it is 1:0.4:2.4, i.e. the needle carbonate contains more oxygen than hydrozincite. This could be because of the crystalline water present in the structure, or the presence of more  $\text{OH}^-$  groups. The oxygen content calculated from the XPS measurements (Fig. 43) was 55.3 at%, in line with the previous notion.

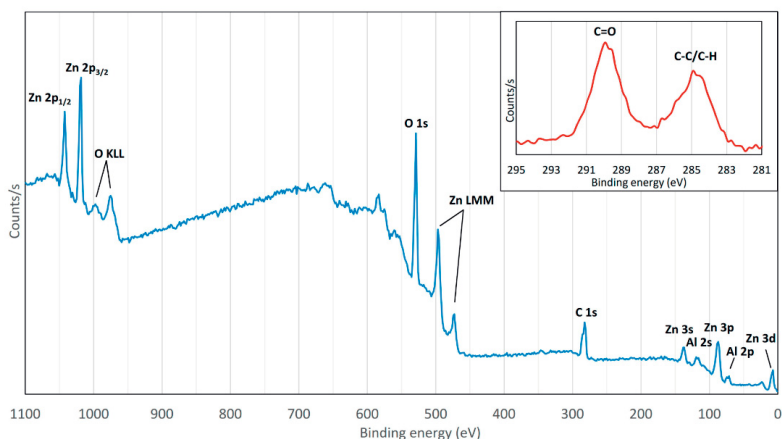


**Figure 43.** XPS of needle carbonate structure (Publication I).

The XRD results shown in Fig. 44 confirm that the needle carbonate is not hydrozincite. There are variety of XRD spectra of different zinc hydroxy carbonates in the literature which shows the ability of these species to arrange their structure differently depending on the synthesis conditions [74, 77, 78, 116]. The XRD of needle carbonate does not match exactly to the spectra shown in the aforementioned studies but presents strong resemblance to some of them.

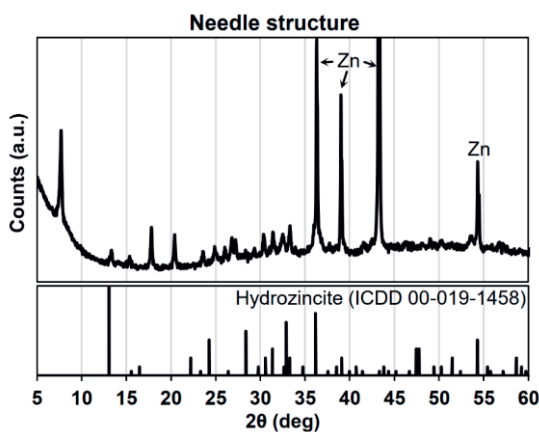


**Figure 44.** GIXRD of needle carbonate structure with reference spectra of hydrozincite (Publication V).

## 7 APPLICATIONS OF ARTIFICIAL PATINA

This chapter presents applications for the carbon dioxide treatment. The main applications are pretreatment of hot-dip galvanized substrate before applying organic coatings. Furthermore, the method can be used for easy ZnO nanowire synthesis.

### 7.1 Pretreatment for hot-dip galvanized substrates

It was mentioned in chapter 2 that newly hot-dipped galvanized surfaces have poor adhesion to organic coatings. Coated hot-dip galvanized steel is essential for applications where aesthetics and long-term corrosion prevention are important. Currently, the hot-dip galvanized surfaces are pretreated with various different conversion coatings which typically use strong acids or other environmentally harmful and toxic chemicals. The CO<sub>2</sub> treatment, using mainly CO<sub>2</sub> and water, is an environmentally friendly technique that can be applied to provide better adhesion to later organic coatings. Furthermore, the compact artificial patina would provide an extra barrier layer between the underlying zinc surface and the surrounding air. This would further limit the transport of corrosive species on the substrate and therefore enhance corrosion inhibition.

Organic coatings include organic solvents which are nonpolar substances that are attracted to the nonpolar surface with low surface energy. The applicability of organic coatings on a surface can be evaluated by considering the chemical nature of the surface and the area of contact between the surface and coating [5, 117].

Chemical compatibility can be tested by measuring contact angles to evaluate the surface energy and interaction between polar and nonpolar substances. Fig. 45 shows a comparison of water contact angle measurements for a fresh hot-dip galvanized substrate (HDG), a substrate with a dual-carbonate structure (Sample 1) and a sample with only ZnCO<sub>3</sub> (Sample 2). The contact angles for the dual-carbonate structure and plain ZnCO<sub>3</sub> are significantly higher than for the untreated HDG substrate. This indicates better chemical compatibility of the surfaces with organic coatings compared to the original HDG surface. A more detailed investigation of the total surface free energy of surfaces is shown in Fig. 46, comparing the artificial

patina, HDG and a natural patina (Outdoor exposure 6 years). Natural patination has been used as a low-cost pretreatment before organic coatings [4, 5]. The results show a considerable reduction in the surface energy due to the CO<sub>2</sub> treatment between the fresh HDG and artificial patina. Furthermore, the artificial patina has an even lower surface energy than the natural patina. The chemical features of the artificial patina surfaces are advantageous for applying organic coatings.

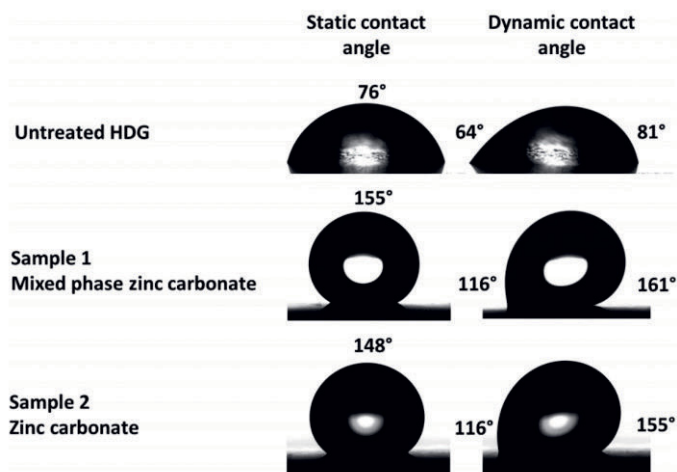


**Figure 45.** Static and dynamic water contact angles on untreated HDG and patina surfaces (Publication IV).

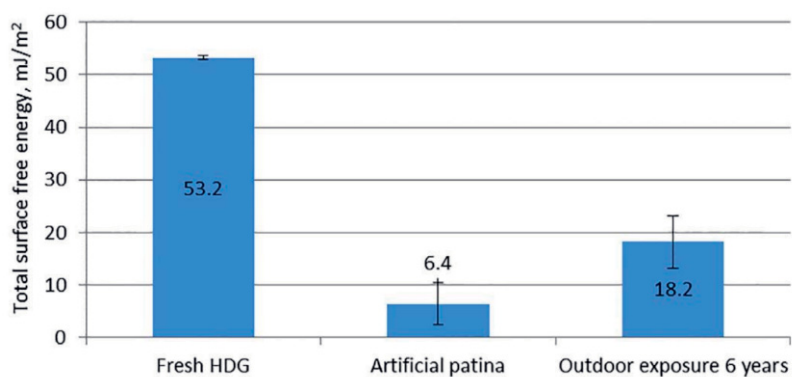


**Figure 46.** Total surface free energy (according to Wu) measurement for HDG, artificial patina and outdoor exposed HDG surfaces (Publication III).

The needle carbonate structure protrudes from the surface creating a porous layer which increases the overall surface area of the surface. This enables the organic coatings to obtain more mechanical interlocking area with the surface. Fig. 47 and 48 present the cross-section images of melamine-polyester-coated dual-carbonate structures. The images show excellent surface wetting without any pore formation in the coating or the patina. Furthermore, chemical changes within the patina structure that could occur in the heated curing phase were not observed according to the Raman measurement shown in Fig. 48. All in all, the artificial patina structures had excellent paintability and have potential mechanical and chemical features for application of organic coatings.

The chemical and physical properties of the artificial patina structures predict advantageous organic coating adhesion promotion capabilities as well as corrosion inhibiting barrier properties. The artificial patina resembles natural patina structures which are known to promote adhesion for organic coatings [5, 23]. Furthermore, the good paintability of the surfaces also predicts adhesion promotion properties. The compactness and high surface coverage of the  $ZnCO_3$  structure is good indication of enhanced barrier properties. However, comprehensive testing is still required to be performed outside of this thesis to provide conclusive evidence about the adhesion and corrosion inhibition properties of the artificial patina.

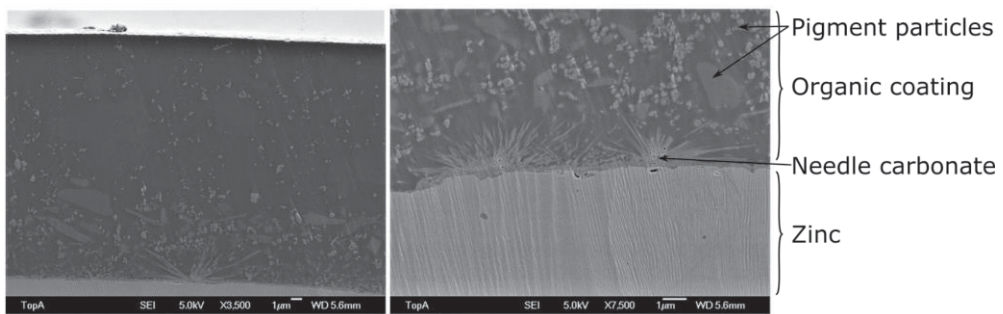


**Figure 47.** Cross-section SEM image of organic coating on needle carbonate structure. Edited from Publication III.



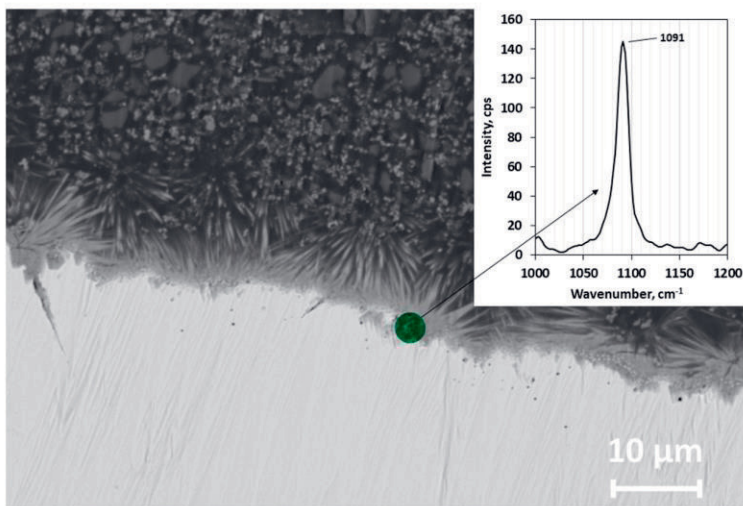


**Figure 48.** SEM image of an low-angle cross section from the coated dual-patina structure. Raman spectrum of the patina is shown in the inset (Publication IV).

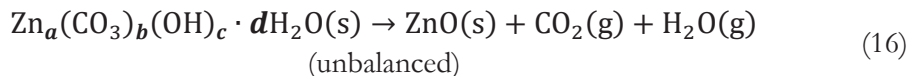
In conclusion, the artificial patina shows promise for the application of organic coatings in increasing adhesion promotion and inhibiting corrosion as a result of the CO<sub>2</sub>-based treatment. Achieving supercritical conditions, however, can pose practical problems when implementing the treatment in a continuous production line. As shown in the previous chapter, the CO<sub>2</sub> treatment can also be performed in relatively low pressures of 5 bar which could facilitate the treatment's use in a production line. The lower pressure would also lower energy usage by reducing the need for pumping, heating and cooling. This would, naturally, lead to lower operating costs as well.

## 7.2 Conversion to ZnO structures

The needle carbonate grows outwards from the substrate surface into long structures which provide a large surface area for the overall structure. Such structures can also be termed as nanowires which is typical within the field of nanotechnology. Nanowires are a desirable morphology in many nanotechnologies for this reason because, the more surface area the structure has, the more area there is to react with the outside environment. When zinc carbonate structures are heated, they can be converted into ZnO [120–122]. ZnO is a semiconductor material whereas carbonates function as insulators. ZnO nanowires are researched for use in e.g. gas

sensors, mechanical energy harvesting, solar cells and photocatalytic applications [6, 54, 61, 74, 121].

The conversion of zinc hydroxy carbonate structures to ZnO under heating follows the following Eq. 16 (the equation is left unbalanced for clarity):



The conversion of the needle carbonate (nanowire) structure can be seen from the FTIR spectra in Fig. 49. Before heat treatment, the spectrum shows distinct carbonate and OH peaks formed by CO<sub>2</sub> treatment of the zinc surface as presented in earlier chapters. After heat treatment at 400°C for 1 hour, most of those peaks have disappeared, leaving behind only one steep peak around 400 cm<sup>-1</sup> that corresponds to ZnO. This conversion was confirmed in our other study as well, where the ZnCO<sub>3</sub> structure also converted into ZnO with the same heat treatment [124].

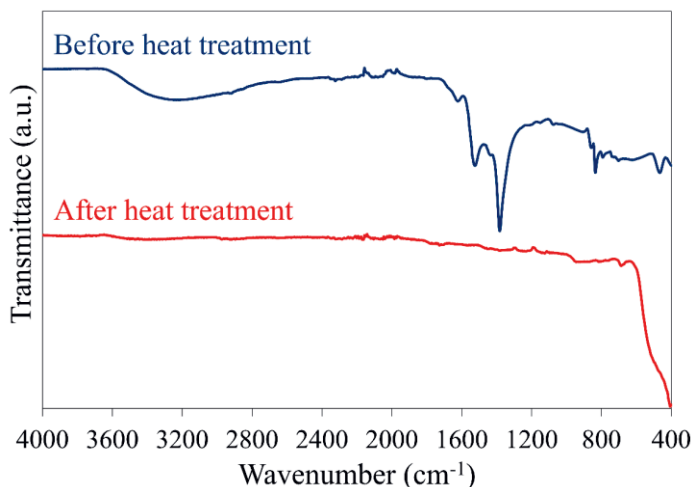


**Figure 49.** FTIR before and after heat treatment of needle carbonate (Publication II).

SEM images in Fig. 50 show the needle structure before and after heat treatment from the same area on the surface. The needle structure has maintained its overall morphology with only minor distortion. The green-highlighted area shows that the needles have experienced slight bending due to the escaping gases during the heat treatment. Furthermore, other studies have shown changes in similar zinc hydroxy carbonate structures during conversion to ZnO [75]. TEM measurements found the

ZnO needles to be polycrystalline, and approximately 50 nm thick, as detailed in Publication II.

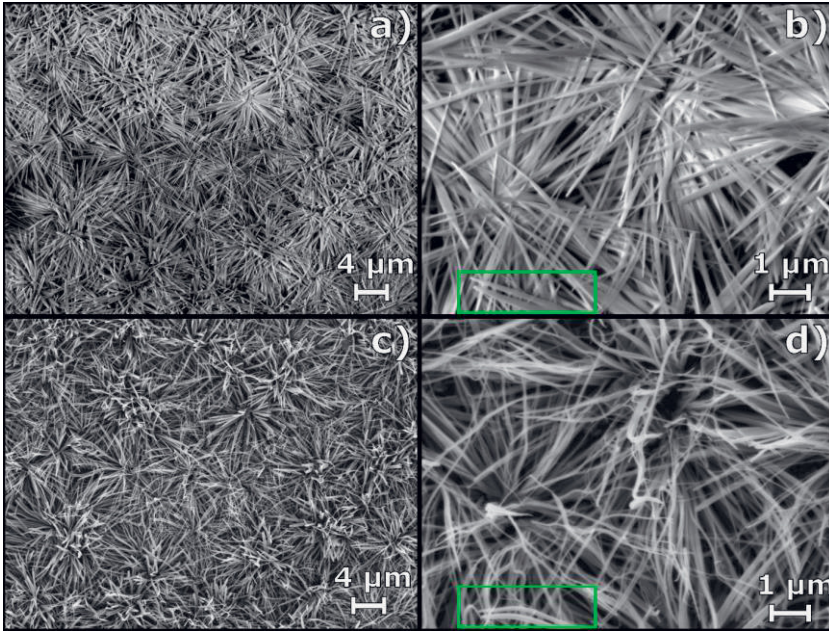


**Figure 50.** Conversion of needle carbonate to ZnO. The green area highlights a distinct transformation of the structure (Publication II).

The band gaps of the needle carbonate and the transformed ZnO needle structure were measured using a UV-vis spectrophotometer and determined using a Tauc plot as shown in Fig. 51. The needle carbonate surface (before heat treatment) did not show any band gap, whereas the ZnO structure (after heat treatment) shows a steep cut-off around 380 nm. This cut-off indicates a distinct band-gap value which was determined to be 3.23 eV from the  $(\alpha h\nu)^2$  vs. energy plot. This value is slightly lower than the typical band gap value for ZnO (3.37 eV) [6]. The dependence of band gap on the size of nanostructures, and especially on the diameter of the nanowires, has been shown in the literature, and may explain the lower band gap measured. Additionally, the ratio of Zn to O might vary within the structures and could result in variation in band gap values [125–127]. The reduction in the band gap is helpful for many semiconductor uses, e.g. in photocatalytic applications, because excitation can be achieved at lower energies [128–130].

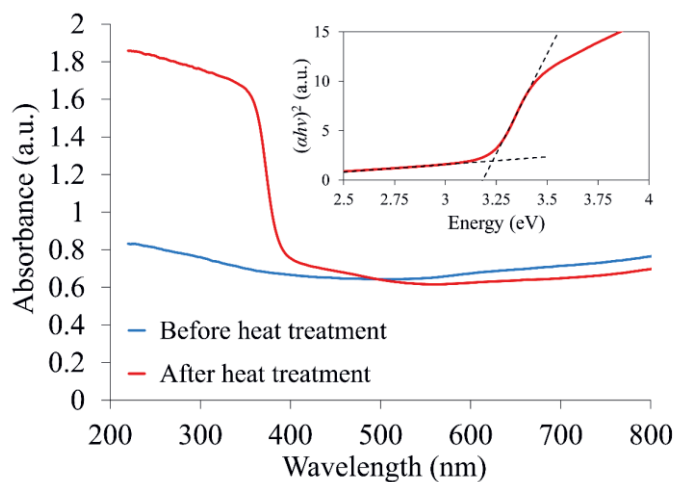


**Figure 51.** Band-gap measurements of ZnO needle structure (Publication II).

The transformed needle carbonate was determined to be suitable for semiconductor applications because of its distinct band gap and its advantageous nanowire morphology. Moreover, according to our preliminary studies, both carbonate structures ( $\text{ZnCO}_3$  and needle carbonate) were, when converted into ZnO, photocatalytically active. The transformed needle carbonate was much more active, likely due to the higher specific surface area of the nanowire morphology [131]. However, more studies of their suitability for photocatalytic applications are needed.

## 8 CONCLUDING REMARKS

This work presented a novel technique for functionalizing zinc surfaces with carbon dioxide, which we call “the artificial patina method”. The method is environmentally friendly and can help reduce the use of harmful chemicals in certain industrial applications. In particular, the artificial patina could provide benefits to painted galvanized steel and ZnO semiconductors. The core findings of this thesis can be summarized as follows:

- Presented novel data on early-stage corrosion of zinc in wet supercritical and non-supercritical CO<sub>2</sub> conditions and developed the artificial patination treatment method based on these findings
  - The artificial patina formation in scCO<sub>2</sub> conditions was influenced by reaction temperature, pressure, catalysts and reaction time in the holding and depressurization phases (**Answer to research question I.a.**)
  - It was also shown that the artificial patina structures could be formed also in lower CO<sub>2</sub> pressure indicating possibility for more efficient processing routes (**Answer to research question I.b.**)
- Demonstrated an environmentally-friendly formation process of artificial zinc patina that
  - Improved certain chemical and physical properties that indicate advantageous adhesion for organic coatings and barrier properties on hot-dip galvanized steel surfaces (**Answer to research question II.a.**)
  - Converted into semiconducting ZnO nanostructures when heat-treated (**Answer to research question II.b.**).

The artificial patina could be formed on pure zinc or on zinc-containing surfaces, i.e. hot-dip galvanized steel, by reacting the substrate under pressurized or supercritical CO<sub>2</sub> atmospheres containing water. Treatments in the supercritical atmosphere fully covered the substrate with the artificial patina structures. In contrast, the formation of the artificial patina under much lower CO<sub>2</sub> pressures (a few bars) showed the

possibility for more efficient processing avenues, an important consideration for sustainable industrial implementation. However, the lower-pressure treatments resulted in a lesser surface covering of the substrate by the artificial patina than was achieved by the supercritical treatments leaving room for process improvements.

The artificial patination process was affected by reaction pressure, temperature, reaction time in the holding and depressurization phases as well as by the introduction of catalysts. Water and CO<sub>2</sub> were fundamental precursors for the artificial patina. Temperature and pressure were critical parameters in the supercritical treatments as they determined the dissolved water amount in the supercritical phase. Lower temperatures and higher pressures increased the amount of dissolved water, resulting in a greater amount of ZnCO<sub>3</sub> in the holding phase as well as greater wetting of substrate during the depressurization phase, enabling better needle carbonate growth. When zinc was exposed to a liquid water layer under a pressurized CO<sub>2</sub> atmosphere, lower temperatures resulted in a prevalence of the needle carbonate structure. As the temperature increased, the prevalence shifted towards the ZnCO<sub>3</sub> formation. The reaction time of the holding phase increased the amount of ZnCO<sub>3</sub> but decreased needle carbonate formation in the depressurization due to the reduced exposure of the zinc surface. Greater reaction time in the depressurization phase, or when exposed to water film, increased the amount of both structures. Catalysts like Cu(hfac)<sub>2</sub> solution or O<sub>2</sub> increased the reaction kinetics but had no apparent direct influence on the carbonate structure formation mechanisms.

As already mentioned, the artificial patina comprised two zinc carbonates: ZnCO<sub>3</sub> and needle carbonate. The ZnCO<sub>3</sub> has a cubic or spherical morphology that adheres densely on the substrate surface. It was concluded that the ZnCO<sub>3</sub> structure could improve the corrosion resistance of the artificial patina due to the compact barrier layer it formed. The needle carbonate was found to be a previously unknown type of mixed zinc hydroxy carbonate with a nanowire morphology protruding from the substrate surfaces. The needle carbonate increased the surface area of the artificial patina as well as the overall substrate surface and therefore indicates increased mechanical interlocking with applied organic coatings. Additionally, the higher surface area of the needle carbonate could provide enhanced reactivity for possible semiconducting applications. Both carbonates also showed favourable chemical characteristics for application of non-polar organic coatings.

The research questions presented in Chapter 4 have been answered. It was concluded that pressurized CO<sub>2</sub> could be used to functionalize zinc surfaces, and the mechanisms of the technique and possibilities for more efficient processing have been thoroughly explained. It was also shown that the functionalized zinc surfaces

are suitable for the intended applications. The artificial patina improved the corrosion resistance and organic coating adherence on HDG substrates. Moreover, the artificial patina carbonate structures could be converted into semiconducting ZnO nanostructures.

## 8.1 Future research suggestions

This thesis focused on explaining the prevailing phenomena and mechanisms of the formation of the artificial patina. Furthermore, the thesis concluded that this method could successfully be used in two applications providing beneficial aspects in these implementations. Nonetheless, there were some features left unanswered that, when investigated further, could reveal for example more efficient processing and new application areas.

The author suggests that, to improve the efficiency of the artificial patina formation process in industrial setting, the low CO<sub>2</sub> pressure route should be researched further. This would eliminate the use of high pressures which would present more economic route for the artificial patination. Furthermore, the use of environmentally-friendly catalysts such as O<sub>2</sub> or other oxidising species should be researched as well. More environmentally-friendly catalysts would result in even lower environmental effect of the method and easier processing.

As the thesis presented largely fundamental data on the artificial patina treatment and the patina, more studies about the applicability of this method as a pretreatment for HDG surfaces needs to be conducted. Although preliminary testing was performed during the writing of this thesis which supported the other results, more comprehensive studies are needed to evaluate the adhesion promotion and corrosion prevention capabilities of the patina structures in organic coating application for conclusive results on the viability of the method.

In terms of new applications, the semiconducting capabilities of the converted ZnO nanostructures should be evaluated in more detail. For example, the photocatalytic activities of the structures were preliminary evaluated (not included in this thesis) but need further investigations for in-detail determination of the photocatalytic activities of the structures. In addition to the photocatalytic applications, the nanostructures could be suitable for other ZnO applications, e.g. gas sensors. A more thorough investigation of the applicability of the artificial patina derived ZnO structures would help confirm how well the properties could be utilized in semiconducting application.

# BIBLIOGRAPHY

- [1] X.G. Zhang, *Corrosion and Electrochemistry of Zinc*, Springer US, Boston, MA, 1996. doi:10.1007/978-1-4757-9877-7.
- [2] M. Oliveira, J. Mário, F. Jr, W.I.A. Santos, C.R. Tomachuk, J.L. Rossi, I. Costa, *Passivation Treatments for Galvanized Steel as Potential Replacements to Chromate Conversion Coatings*, (2012) 2–4.
- [3] A.E. Hughes, *Conversion coatings*, Elsevier, 2018. doi:10.1016/B978-0-12-409547-2.13441-9.
- [4] J.F. Malone, *Painting hot-dip galvanized sheet*, *Mater. Perform.* 31 (1992) 39–42.
- [5] I. Cabanelas, A. Collazo, M. Izquierdo, X.R. Nóvoa, C. Pérez, *Influence of galvanised surface state on the duplex systems behaviour*, *Corros. Sci.* 49 (2007) 1816–1832. doi:10.1016/j.corsci.2006.10.018.
- [6] A. Kolodziejczak-Radzimska, T. Jesionowski, *Zinc oxide—from synthesis to application: A review*, *Materials (Basel)*. 7 (2014) 2833–2881. doi:10.3390/ma7042833.
- [7] Saara Söyrinki, *Structured ZnO and Al<sub>2</sub>O<sub>3</sub> / Ag Surfaces*, Tampere University of Technology, 2018.
- [8] E.I. Koytsoumpa, C. Bergins, E. Kakaras, *The CO<sub>2</sub> economy: Review of CO<sub>2</sub> capture and reuse technologies*, *J. Supercrit. Fluids.* 132 (2018) 3–16. doi:10.1016/j.supflu.2017.07.029.
- [9] X. Zhang, S. Heinonen, E. Levänen, *Applications of supercritical carbon dioxide in materials processing and synthesis*, *RSC Adv.* 4 (2014) 61137–61152. doi:10.1039/C4RA10662H.
- [10] Y.-P. Sun, *Supercritical fluid technology in materials science and engineering*, Marcel Dekker, South Caroline, United States, 2002.
- [11] N. Berghout, S. McCulloch, *Putting CO<sub>2</sub> to Use*, Report (2012).
- [12] F. Khoshnaw, R. Gubner, *Part I: General Aspects of Corrosion, Corrosion Control, and Corrosion Prevention*, in: *Corros. Atlas Case Stud.*, Elsevier, 2020: p. 284. doi:10.1016/B978-0-12-818760-9.02002-X.
- [13] M.J. Pryor, D.J. Astley, *Bimetallic Corrosion*, in: *Corros. Third Ed.*, 2013: pp. 1:213-1:243. doi:10.1016/B978-0-08-052351-4.50015-7.
- [14] V. Kuklík, J. Kudláček, *List of selected zinc coating technologies*, *Hot-Dip Galvaniz. Steel Struct.* (2016) 1–5. doi:10.1016/b978-0-08-100753-2.00001-x.
- [15] P.G. Rahrig, *Hot dip galvanizing*, *Mod. Steel Constr.* 35 (1995) 36–41. doi:10.1016/b978-0-08-100753-2.00002-1.
- [16] A.R. Marder, *Metallurgy of zinc-coated steel*, *Prog. Mater. Sci.* 45 (2000). doi:10.1016/S0079-6425(98)00006-1.
- [17] P. Puomi, H.M. Fagerholm, J.B. Rosenholm, K. Jyrkäs, *Comparison of different commercial pretreatment methods for hot-dip galvanized and Galfan coated steel*, *Surf. Coatings Technol.* 115 (1999) 70–78. doi:10.1016/S0257-8972(99)00170-X.
- [18] L.F.G. Williams, *The mechanism of formation of chromate conversion films on zinc*, *Surf. Technol.* 4 (1976) 355–366. doi:10.1016/0376-4583(76)90006-6.
- [19] N.R. Short, H.G. Cole, *Chromate Treatments*, in: *Corros. Third Ed.*, 2013: pp. 15:38-15:48. doi:10.1016/B978-0-08-052351-4.50120-5.



- [20] L. Hua, Y.C. Chan, Y.P. Wu, B.Y. Wu, The determination of hexavalent chromium (Cr6+) in electronic and electrical components and products to comply with RoHS regulations, *J. Hazard. Mater.* 163 (2009) 1360–1368. doi:10.1016/j.jhazmat.2008.07.150.
- [21] M.O.W. Richardson, R.E. Shaw, Phosphate Coatings, in: *Corros. Third Ed.*, 2013: pp. 15:22-15:37. doi:10.1016/B978-0-08-052351-4.50119-9.
- [22] V. Saarimaa, A. Markkula, J. Juhanoja, B.-J. Skrifvars, Determination of Surface Topography and Composition of Cr-Free Pretreatment Layers on Hot Dip Galvanized Steel, *J. Coat. Sci. Technol.* 1 (2014) 88–95.
- [23] A. Collazo, C. Pérez, M. Izquierdo, P. Merino, Evaluation of environmentally friendly paints over weathering galvanised steel, *Prog. Org. Coatings.* 46 (2003) 197–210. doi:10.1016/S0300-9440(02)00101-7.
- [24] V. Saarimaa, A. Markkula, K. Arstila, J. Manni, J. Juhanoja, Effect of Hot Dip Galvanized Steel Surface Chemistry and Morphology on Titanium Hexafluoride Pretreatment, *Adv. Mater. Phys. Chem.* 07 (2017) 28–41. doi:10.4236/ampc.2017.72004.
- [25] M. Gaber, Metal Roof Coatings: What to Look for When Choosing a Durable Topcoat, *Met. Roof Coatings What to Look When Choos. a Durable Topcoat.* (n.d.). <https://www.englertinc.com/blog/metal-roof-coatings-what-to-look-for-when-choosing-a-durable-topcoat/>.
- [26] A. Markkula, Organic coatings for steel applications, Presentation (2017).
- [27] I. Odnevall Wallinder, C. Leygraf, A critical review on corrosion and runoff from zinc and zinc-based alloys in atmospheric environments, *Corrosion.* 73 (2017) 1016–1077. doi:10.5006/2458.
- [28] R.D. Klassen, P.R. Roberge, C. V. Hyatt, Study of the initial stage of white rust formation on zinc single crystal by EIS, STM/AFM and SEM/EDS techniques, *Electrochim. Acta.* 46 (2001) 3743–3754. doi:10.1016/S0013-4686(01)00656-9.
- [29] N.S. Azmat, K.D. Ralston, B.C. Muddle, I.S. Cole, Corrosion of Zn under acidified marine droplets, *Corros. Sci.* 53 (2011) 1604–1615. doi:10.1016/j.corsci.2011.01.044.
- [30] C.C. Ivan, Recent progress and required developments in atmospheric corrosion of galvanised steel and zinc, *Materials (Basel).* 10 (2017). doi:10.3390/ma10111288.
- [31] Y.W. Heo, F. Ren, D.P. Norton, Gas, Chemical and Biological Sensing with ZnO, *Zinc Oxide Bulk, Thin Film. Nanostructures.* (2006) 491–523. doi:10.1016/B978-008044722-3/50014-2.
- [32] Y.Y. Villanueva, D.R. Liu, P.T. Cheng, Pulsed laser deposition of zinc oxide, *Thin Solid Films.* 501 (2006) 366–369. doi:10.1016/j.tsf.2005.07.152.
- [33] L. Znaidi, Sol-gel-deposited ZnO thin films: A review, *Mater. Sci. Eng. B Solid-State Mater. Adv. Technol.* 174 (2010) 18–30. doi:10.1016/j.mseb.2010.07.001.
- [34] Z.L. Wang, Zinc oxide nanostructures: Growth, properties and applications, *J. Phys. Condens. Matter.* 16 (2004) 829–858. doi:10.1088/0953-8984/16/25/R01.
- [35] W. Gao, Z. Li, Nanostructures of zinc oxide, *Int. J. Nanotechnol.* 6 (2009) 245–257. doi:10.1504/IJNT.2009.022917.
- [36] D. Kudryashov, A. Babichev, E. Nikitina, A. Gudovskikh, P. Kladko, Photoluminescence observation from zinc oxide formed by magnetron sputtering at room temperature, *J. Phys. Conf. Ser.* 643 (2015) 2–6. doi:10.1088/1742-6596/643/1/012013.
- [37] Ü. Özgür, D. Hofstetter, H. Morkoç, ZnO devices and applications: A review of current status and future prospects, *Proc. IEEE.* 98 (2010) 1255–1268. doi:10.1109/JPROC.2010.2044550.
- [38] Z.L. Wang, Novel Nanostructures and Nanodevices of ZnO, *Zinc Oxide Bulk, Thin Film. Nanostructures.* (2006) 339–370. doi:10.1016/B978-008044722-3/50010-5.
- [39] W. Gao, Z. Li, ZnO thin films produced by magnetron sputtering, *Ceram. Int.* 30 (2004)

- 1155–1159. doi:10.1016/j.ceramint.2003.12.197.
- [40] G.C. Yi, Semiconductor Nanostructures for Optoelectronic Devices, *Nanosci. Technol.* 58 (2012). doi:10.1007/978-3-642-22480-5.
- [41] D. Depla, S. Mahieu, J.E. Greene, *Sputter Deposition Processes*, Third Edit, Elsevier Ltd., 2010. doi:10.1016/B978-0-8155-2031-3.00005-3.
- [42] S. Thiagarajan, A. Sanmugam, D. Vikraman, *Facile Methodology of Sol-Gel Synthesis for Metal Oxide Nanostructures*, *Recent Appl. Sol Gel Synth.* (2017) 1–16. doi:10.5772/intechopen.68708.
- [43] S. Heinonen, J.-P. Nikkanen, H. Hakola, E. Huttunen-Saarivirta, M. Kannisto, L. Hyvärinen, M. Järveläinen, E. Levänen, Effect of temperature and concentration of precursors on morphology and photocatalytic activity of zinc oxide thin films prepared by hydrothermal route, *IOP Conf. Ser. Mater. Sci. Eng.* 123 (2016) 012030. doi:10.1088/1757-899X/123/1/012030.
- [44] R. Pietruszka, B.S. Witkowski, S. Gieraltowska, P. Caban, L. Wachnicki, E. Zielony, K. Gwozdz, P. Bieganski, E. Placzek-Popko, M. Godlewski, New efficient solar cell structures based on zinc oxide nanorods, *Sol. Energy Mater. Sol. Cells.* 143 (2015) 99–104. doi:10.1016/j.solmat.2015.06.042.
- [45] S. Heinonen, M. Kannisto, J.-P. Nikkanen, E. Huttunen-Saarivirta, M. Karp, E. Levänen, Photocatalytic and antibacterial properties of ZnO films with different surface topographies on stainless steel substrate, *Thin Solid Films.* 616 (2016) 842–849. doi:10.1016/j.tsf.2016.10.002.
- [46] K.S. Egorova, V.P. Ananikov, Toxicity of Metal Compounds : Knowledge and Myths, *Organometallics.* 36 (2017) 4071–4090. doi:10.1021/acs.organomet.7b00605.
- [47] M.-Z. Chen, W.-S. Chen, S.-C. Jeng, S.-H. Yang, Y.-F. Chung, Liquid crystal alignment on zinc oxide nanowire arrays for LCDs applications, *Opt. Express.* 21 (2013) 29277. doi:10.1364/OE.21.029277.
- [48] S.Y. Li, C.Y. Lee, T.Y. Tseng, Copper-catalyzed ZnO nanowires on silicon (1 0 0) grown by vapor-liquid-solid process, *J. Cryst. Growth.* 247 (2003) 357–362. doi:10.1016/S0022-0248(02)01918-8.
- [49] H. He, J.H. Hsu, C.W. Wang, H.N. Lih, L.J. Chen, Z.L. Wang, Pattern and feature designed growth of ZnO nanowire arrays for vertical devices, *J. Phys. Chem. B.* 110 (2006) 50–53. doi:10.1021/jp055180j.
- [50] Y. Zhang, K. Yu, D. Jiang, Z. Zhu, H. Geng, L. Luo, Zinc oxide nanorod and nanowire for humidity sensor, *Appl. Surf. Sci.* 242 (2005) 212–217. doi:10.1016/j.apsusc.2004.08.013.
- [51] M. Marie, S. Mandal, O. Manasreh, An Electrochemical Glucose Sensor Based on Zinc Oxide Nanorods, *Sensors.* 15 (2015) 18714–18723. doi:10.3390/s150818714.
- [52] S. Chaudhary, A. Umar, K.K. Bhasin, S. Baskoutas, Chemical sensing applications of ZnO nanomaterials, *Materials (Basel).* 11 (2018) 1–38. doi:10.3390/ma11020287.
- [53] Y. Yang, W. Guo, K.C. Pradel, G. Zhu, Y. Zhou, Y. Zhang, Y. Hu, L. Lin, Z.L. Wang, Pyroelectric nanogenerators for harvesting thermoelectric energy, *Nano Lett.* 12 (2012) 2833–2838. doi:10.1021/nl3003039.
- [54] Z.L. Wang, Energy harvesting for self-powered nanosystems, *Nano Res.* 1 (2008) 1–8. doi:10.1007/s12274-008-8003-x.
- [55] A. Khan, M. Ali Abbasi, M. Hussain, Z. Hussain Ibupoto, J. Wissting, O. Nur, M. Willander, Piezoelectric nanogenerator based on zinc oxide nanorods grown on textile cotton fabric, *Appl. Phys. Lett.* 101 (2012) 193506 1–4. doi:10.1063/1.4766921.
- [56] P. Hiralal, H.E. Unalan, G.A.J. Amaratunga, Nanowires for energy generation, *Nanotechnology.* 23 (2012). doi:10.1088/0957-4484/23/19/194002.
- [57] M.S. Al-Ruqeishi, T. Mohiuddin, B. Al-Habsi, F. Al-Ruqeishi, A. Al-Fahdi, A. Al-

- Khusaibi, Piezoelectric nanogenerator based on ZnO nanorods, *Arab. J. Chem.* 12 (2019) 5173–5179. doi:10.1016/j.arabjc.2016.12.010.
- [58] Q. Zhang, C.S. Dandeneau, X. Zhou, G. Cao, ZnO Nanostructures for Dye-Sensitized Solar Cells, *Adv. Mater.* 21 (2009) 4087–4108. doi:10.1002/adma.200803827.
- [59] N. Singh, R.M. Mehra, A. Kapoor, T. Soga, ZnO based quantum dot sensitized solar cell using CdS quantum dots, *J. Renew. Sustain. Energy.* 4 (2012). doi:10.1063/1.3683531.
- [60] M.R. Hoffmann, S.T. Martin, W. Choi, D.W. Bahnemann, D.W. Bahnemann, Environmental Applications of Semiconductor Photocatalysis *Environmental Applications of Semiconductor Photocatalysis*, *Chem. Rev.* 95 (1995) 69–96. doi:10.1021/cr00033a004.
- [61] A.G. Cuevas, K. Balangcod, T. Balangcod, A. Jasmin, Surface morphology, optical properties and antibacterial activity of zinc oxide films synthesized via spray pyrolysis, *Procedia Eng.* 68 (2013) 537–543. doi:10.1016/j.proeng.2013.12.218.
- [62] C. Hariharan, Photocatalytic degradation of organic contaminants in water by ZnO nanoparticles: Revisited, *Appl. Catal. A Gen.* 304 (2006) 55–61. doi:10.1016/j.apcata.2006.02.020.
- [63] B. Dindar, S. Içli, Unusual photoreactivity of zinc oxide irradiated by concentrated sunlight, *J. Photochem. Photobiol. B* 140 (2001) 263–268. doi:10.1016/S1010-6030(01)00414-2.
- [64] C.A.K. Gouvea, F. Wypych, S.G. Moraes, N. Dur, N. Nagata, P. Peralta-zamora, Semiconductor-assisted photocatalytic degradation of reactive dyes in aqueous solution, *J. Photochem. Photobiol. B* 40 (2000) 433–440. doi:10.1016/s0045-6535(99)00313-6.
- [65] S. Söyrinki, Structured ZnO and Al<sub>2</sub>O<sub>3</sub> / Ag Surfaces Saara Söyrinki Structured ZnO and Al<sub>2</sub>O<sub>3</sub> / Ag Surfaces Antibacteriality , Photocatalytic Activity and Durability *Julkaisu 1599 • Publication 1599 Tampere 2018*, Tampere University of Technology, Tampere, Finland, 2018.
- [66] K.A. Chandler, J.C. Hudson, Iron and Steel, in: *Corros. Third Ed.*, 2013: pp. 3:3-3:22. doi:10.1016/B978-0-08-052351-4.50033-9.
- [67] T. Ohtsuka, M. Matsuda, In situ Raman spectroscopy for corrosion products of zinc in humidified atmosphere in the presence of sodium chloride precipitate, *Corrosion*. 59 (2003) 407–413. doi:10.5006/1.3277572.
- [68] P. Delahay, M. Pourbaix, P. Van Rysselberghe, Potential-pH Diagram of Zinc and its Applications to the Study of Zinc Corrosion, *J. Electrochem. Soc.* 98 (1951) 101. doi:10.1149/1.2778110.
- [69] P.T. Gilbert, The Nature of Zinc Corrosion Products, *J. Electrochem. Soc.* 99 (1952) 16. doi:10.1149/1.2779652.
- [70] Y. Meng, L. Liu, D. Zhang, C. Dong, Y. Yan, A.A. Volinsky, L.N. Wang, Initial formation of corrosion products on pure zinc in saline solution, *Bioact. Mater.* 4 (2019) 87–96. doi:10.1016/j.bioactmat.2018.08.003.
- [71] E. Diler, B. Lescop, S. Rioual, G. Nguyen Vien, D. Thierry, B. Rouvellou, Initial formation of corrosion products on pure zinc and MgZn<sub>2</sub> examined by XPS, *Corros. Sci.* 79 (2014) 83–88. doi:10.1016/j.corsci.2013.10.029.
- [72] M. Esmaily, N. Mortazavi, J.E. Svensson, L.G. Johansson, Evidence for an Unusual Temperature Dependence of the Atmospheric Corrosion of Zinc, *J. Electrochem. Soc.* 163 (2016) C864–C872. doi:10.1149/2.0751614jes.
- [73] R.A. Reichle, K.G. McCurdy, L.G. Hepler, Zinc Hydroxide: Solubility Product and Hydroxy-complex Stability Constants from 12.5–75 °C, *Can. J. Chem.* 53 (1975) 3841–3845. doi:10.1139/v75-556.
- [74] A. Krężel, W. Maret, The biological inorganic chemistry of zinc ions, *Arch. Biochem. Biophys.* 611 (2016) 3–19. doi:10.1016/j.abb.2016.04.010.
- [75] D.O. Miles, P.J. Cameron, D. Mattia, Hierarchical 3D ZnO nanowire structures via fast

- anodization of zinc, *J. Mater. Chem. A.* 3 (2015) 17569–17577. doi:10.1039/C5TA03578C.
- [76] Y.S. Choi, S. Nešić, Determining the corrosive potential of CO<sub>2</sub> transport pipeline in high pCO<sub>2</sub>-water environments, *Int. J. Greenh. Gas Control.* 5 (2011) 788–797. doi:10.1016/j.ijggc.2010.11.008.
- [77] C. a. Laska, M. Auinger, P.U. Biedermann, D. Iqbal, N. Laska, J. De Strycker, K.J.J. Mayrhofer, Effect of hydrogen carbonate and chloride on zinc corrosion investigated by a scanning flow cell system, *Electrochim. Acta.* 159 (2015) 198–209. doi:10.1016/j.electacta.2015.01.217.
- [78] M. Sahli, *Über die Basischen zinkcarbonate*, Bern University, 1956.
- [79] J.L. Jambor, Studies of basic copper and zinc Carbonates: I-synthetic zinc carbonates and their relationship to hydrozincite, *Can. Mineralogist.* 8 (1964) 92–108.
- [80] I. Odnevall, Atmospheric corrosion of field exposed zinc, Royal Institute of Technology, 1994.
- [81] F. Zhu, D. Persson, D. Thierry, Formation of corrosion products an open and confined metal surfaces exposed to periodic wet/dry conditions - A comparison between zinc and electrogalvanized steel, *Corrosion.* 57 (2001) 582–590. doi:10.5006/1.3280514.
- [82] E. Dlugokencky, P. Tans, NOAA ESRL Global Monitoring Laboratory, Boulder, Colorado, USA, 2020.
- [83] R.M. Cuéllar-Franca, A. Azapagic, Carbon capture, storage and utilisation technologies: A critical analysis and comparison of their life cycle environmental impacts, *J. CO2 Util.* 9 (2015) 82–102. doi:10.1016/j.jcou.2014.12.001.
- [84] F.D. Meylan, V. Moreau, S. Erkmann, CO<sub>2</sub> utilization in the perspective of industrial ecology, an overview, *J. CO2 Util.* 12 (2015) 101–108. doi:10.1016/j.jcou.2015.05.003.
- [85] Eric W. Lemmon, M.O. McLinden, D.G. Friend, Thermophysical Properties of Fluid Systems, NIST Chem. Webb. (2016). doi:https://doi.org/10.18434/T4D303.
- [86] M. Raventós, S. Duarte, R. Alarcón, Application and Possibilities of Supercritical CO<sub>2</sub> Extraction in Food Processing Industry: An Overview, *Food Sci. Technol. Int.* 8 (2002) 269–284. doi:10.1106/108201302029451.
- [87] N. Spycher, K. Pruess, J. Ennis-King, CO<sub>2</sub>-H<sub>2</sub>O mixtures in the geological sequestration of CO<sub>2</sub>. I. Assessment and calculation of mutual solubilities from 12 to 100°C and up to 600 bar, *Geochim. Cosmochim. Acta.* 67 (2003) 3015–3031. doi:10.1016/S0016-7037(03)00273-4.
- [88] M. Aegerter, N. Leventis, M. Koebel, *Aerogels handbook (Advances in Sol-Gel Derived Materials and Technologies)*, Springer, 2011. doi:10.1007/978-1-4614-1957-0.
- [89] B.R. Linter, G.T. Burstein, Reactions of pipeline steels in carbon dioxide solutions, *Corros. Sci.* 41 (1999) 117–139. doi:10.1016/S0010-938X(98)00104-8.
- [90] W. Renpu, Oil and Gas Well Corrosion and Corrosion Prevention, *Adv. Well Complet. Eng.* (2011) 617–700. doi:10.1016/b978-0-12-385868-9.00018-x.
- [91] T. Falk, J.-E. Svensson, L.-G. Johansson, The Role of Carbon Dioxide in the Atmospheric Corrosion of Zinc, *J. Electrochem. Soc.* 145 (1998) 39–44. doi:10.1149/1.1838207.
- [92] M. Nordsveen, S. Nešić, R. Nyborg, A. Stangeland, A mechanistic model for carbon dioxide corrosion of mild steel in the presence of protective iron carbonate films - Part 1: Theory and verification, *Corrosion.* 59 (2003) 443–456. doi:10.5006/1.3277576.
- [93] E. Chaix, C. Guillaume, V. Guillard, Oxygen and Carbon Dioxide Solubility and Diffusivity in Solid Food Matrices: A Review of Past and Current Knowledge, *Compr. Rev. Food Sci. Food Saf.* 13 (2014) 261–286. doi:10.1111/1541-4337.12058.
- [94] R. Barker, Y. Hua, A. Neville, Internal corrosion of carbon steel pipelines for dense-phase CO<sub>2</sub> transport in carbon capture and storage (CCS) – a review, *Int. Mater. Rev.* 62

- (2017) 1–31. doi:10.1080/09506608.2016.1176306.
- [95] Y. Hua, S. Mohammed, R. Barker, A. Neville, Comparisons of corrosion behaviour for X65 and low Cr steels in high pressure CO<sub>2</sub>-saturated brine, *J. Mater. Sci. Technol.* 41 (2020) 21–32. doi:10.1016/j.jmst.2019.08.050.
- [96] Y. Hua, R. Barker, T. Charpentier, M. Ward, A. Neville, Relating iron carbonate morphology to corrosion characteristics for water-saturated supercritical CO<sub>2</sub> systems, *J. Supercrit. Fluids.* 98 (2015) 183–193. doi:10.1016/j.supflu.2014.12.009.
- [97] W. Lu, H. Guo, I.M. Chou, R.C. Burruss, L. Li, Determination of diffusion coefficients of carbon dioxide in water between 268 and 473K in a high-pressure capillary optical cell with in situ Raman spectroscopic measurements, *Geochim. Cosmochim. Acta.* 115 (2013) 183–204. doi:10.1016/j.gca.2013.04.010.
- [98] F.M. Song, D.W. Kirk, J.W. Graydon, D.E. Cormack, Predicting carbon dioxide corrosion of bare steel under an aqueous boundary layer, *Corrosion.* 60 (2004) 736–748. doi:10.5006/1.3287853.
- [99] R. Barker, D. Burkle, T. Charpentier, H. Thompson, A. Neville, A review of iron carbonate (FeCO<sub>3</sub>) formation in the oil and gas industry, *Corros. Sci.* 142 (2018) 312–341. doi:10.1016/j.corsci.2018.07.021.
- [100] S. Sarrade, D. Féron, F. Rouillard, S. Perrin, R. Robin, J.C. Ruiz, H.A. Turc, Overview on corrosion in supercritical fluids, *J. Supercrit. Fluids.* 120 (2017) 335–344. doi:10.1016/j.supflu.2016.07.022.
- [101] J.S. Loring, C.J. Thompson, C. Zhang, Z. Wang, H.T. Schaeff, K.M. Rosso, In situ infrared spectroscopic study of brucite carbonation in dry to water-saturated supercritical carbon dioxide, *J. Phys. Chem. A.* 116 (2012) 4768–4777. doi:10.1021/jp210020t.
- [102] J.S. Loring, C.J. Thompson, Z. Wang, A.G. Joly, D.S. Sklarew, H.T. Schaeff, E.S. Ilton, K.M. Rosso, A.R. Felmy, In situ infrared spectroscopic study of forsterite carbonation in wet supercritical CO<sub>2</sub>, *Environ. Sci. Technol.* 45 (2011) 6204–6210. doi:10.1021/es201284e.
- [103] J.S. Loring, J. Chen, P. Bénézeth, O. Qafoku, E.S. Ilton, N.M. Washton, C.J. Thompson, P.F. Martin, B.P. McGrail, K.M. Rosso, A.R. Felmy, H.T. Schaeff, Evidence for Carbonate Surface Complexation during Forsterite Carbonation in Wet Supercritical Carbon Dioxide, *Langmuir.* 31 (2015) 7533–7543. doi:10.1021/acs.langmuir.5b01052.
- [104] A. Dugstad, M. Halseid, B. Morland, A.O. Sivertsen, Corrosion in dense phase CO<sub>2</sub> - The impact of depressurisation and accumulation of impurities, *Energy Procedia.* 37 (2013) 3057–3067. doi:10.1016/j.egypro.2013.06.192.
- [105] J. Tauc, R. Grigorovici, A. Vancu, Optical Properties and Electronic Structure of Amorphous Germanium, *Phys. Status Solidi.* 15 (1966) 627–637. doi:10.1002/pssb.19660150224.
- [106] G. Cui, Z. Yang, J. Liu, Z. Li, A comprehensive review of metal corrosion in a supercritical CO<sub>2</sub> environment, *Int. J. Greenh. Gas Control.* 90 (2019) 102814. doi:10.1016/j.ijggc.2019.102814.
- [107] J.S. Lim, Y.Y. Lee, H.S. Chun, Phase equilibria for carbon dioxide-ethanol-water system at elevated pressures, *J. Supercrit. Fluids.* 7 (1994) 219–230. doi:10.1016/0896-8446(94)90009-4.
- [108] J.D. Yoo, K. Ogle, P. Volovitch, The effect of synthetic zinc corrosion products on corrosion of electrogalvanized steel: I. Cathodic reactivity under zinc corrosion products, *Corros. Sci.* 81 (2014) 11–20. doi:10.1016/j.corsci.2013.11.045.
- [109] T.H. Muster, A. Bradbury, A. Trinchi, I.S. Cole, T. Markley, D. Lau, S. Dligatch, A. Bendavid, P. Martin, The atmospheric corrosion of zinc: The effects of salt concentration, droplet size and droplet shape, *Electrochim. Acta.* 56 (2011) 1866–1873. doi:10.1016/j.electacta.2010.09.099.

- [110] R.J. Jiang, Y.F. Cheng, Mechanism of electrochemical corrosion of steel under water drop, *Electrochem. Commun.* 35 (2013) 8–11. doi:10.1016/j.elecom.2013.07.019.
- [111] Z. Hu, Q. Chen, Z. Li, Y. Yu, L.M. Peng, Large-scale and rapid synthesis of ultralong ZnO nanowire films via anodization, *J. Phys. Chem. C.* 114 (2010) 881–889. doi:10.1021/jp9094744.
- [112] Y. Sawada, M. Murakami, T. Nishide, Thermal analysis of basic zinc carbonate. Part 1. Carbonation process of zinc oxide powders at 8 and 13°C, *Thermochim. Acta.* 273 (1996) 95–102. doi:10.1016/0040-6031(95)02631-2.
- [113] C. Sun, Y. Wang, J. Sun, X. Lin, X. Li, H. Liu, X. Cheng, Effect of impurity on the corrosion behavior of X65 steel in water-saturated supercritical CO<sub>2</sub> system, *J. Supercrit. Fluids.* 116 (2016) 70–82. doi:10.1016/j.supflu.2016.05.006.
- [114] W. Preis, H. Gamsjäger, (Solid + solute) phase equilibria in aqueous solution. XIII. Thermodynamic properties of hydrozincite and predominance diagrams for (Zn<sup>2+</sup>+ H<sub>2</sub>O+CO<sub>2</sub>), *J. Chem. Thermodyn.* 33 (2001) 803–819. doi:10.1006/jcht.2000.0794.
- [115] M.C. Hales, R.L. Frost, Synthesis and vibrational spectroscopic characterisation of synthetic hydrozincite and smithsonite, *Polyhedron.* 26 (2007) 4955–4962. doi:10.1016/j.poly.2007.07.002.
- [116] D. Lindström, I. Odnevall Wallinder, Long-term use of galvanized steel in external applications. Aspects of patina formation, zinc runoff, barrier properties of surface treatments, and coatings and environmental fate, *Environ. Monit. Assess.* 173 (2011) 139–153. doi:10.1007/s10661-010-1377-8.
- [117] F.Z. Mahjoubi, A. Khalidi, M. Abdennouri, N. Barka, Zn–Al layered double hydroxides intercalated with carbonate, nitrate, chloride and sulphate ions: Synthesis, characterisation and dye removal properties, *J. Taibah Univ. Sci.* 11 (2017) 90–100. doi:10.1016/j.jtusci.2015.10.007.
- [118] N. Ohkuma, Y. Funayama, H. Ito, N. Mizutani, M. Kato, Adsorption and reaction of CO<sub>2</sub> gas on the surface of ZnO fine particles in the atmosphere., *Hyomen Kagaku.* 9 (1988) 452–458. doi:10.1380/jsssj.9.452.
- [119] D. Packham, Surface energy, surface topography and adhesion, *Int. J. Adhes. Adhes.* 23 (2003) 437–448. doi:10.1016/S0143-7496(03)00068-X.
- [120] R. Wahab, S.G. Ansari, Y.S. Kim, M.A. Dar, H.S. Shin, Synthesis and characterization of hydrozincite and its conversion into zinc oxide nanoparticles, *J. Alloys Compd.* 461 (2008) 66–71. doi:10.1016/j.jallcom.2007.07.029.
- [121] Z.C. Orel, Preparation and characterization of zinc hydroxide carbonate and porous zinc oxide particles, *28 (2008) 2915–2921.* doi:10.1016/j.jeurceramsoc.2008.05.003.
- [122] E. Turianicová, M. Kaňuchová, A. Zorkovská, M. Holub, Z. Bujňáková, E. Dutková, M. Baláž, L. Findoráková, M. Balintová, A. Obut, CO<sub>2</sub> utilization for fast preparation of nanocrystalline hydrozincite, *J. CO<sub>2</sub> Util.* 16 (2016) 328–335. doi:10.1016/j.jcou.2016.08.007.
- [123] L. Zhu, W. Zeng, Room-temperature gas sensing of ZnO-based gas sensor: A review, *Sensors Actuators, A Phys.* 267 (2017) 242–261. doi:10.1016/j.sna.2017.10.021.
- [124] J.-P. Nikkanen, S. Heinonen, P. Väisänen, V. Saarimaa, A. Markkula, T. Paunikallio, A. Kaleva, E. Levänen, Convenient extraction method for quantification of thin zinc patina layers, *Surf. Interface Anal.* 50 (2018) 564–570. doi:10.1002/sia.6429.
- [125] B. Wei, K. Zheng, Y. Ji, Y. Zhang, Z. Zhang, X. Han, Size-dependent bandgap modulation of zno nanowires by tensile strain, *Nano Lett.* 12 (2012) 4595–4599. doi:10.1021/nl301897q.
- [126] M. Nolan, S. O’Callaghan, G. Fagas, J.C. Greer, T. Frauenheim, Silicon nanowire band gap modification, *Nano Lett.* 7 (2007) 34–38. doi:10.1021/nl061888d.
- [127] B. Wang, J. Zhao, J. Jia, D. Shi, J. Wan, G. Wang, Structural, mechanical, and electronic

- properties of ultrathin ZnO nanowires, *Appl. Phys. Lett.* 93 (2008) 2006–2009. doi:10.1063/1.2951617.
- [128] J. Kumar, A. Kumar Srivastava, Band gap narrowing in zinc oxide-based semiconductor thin films, *J. Appl. Phys.* 115 (2014). doi:10.1063/1.4870709.
- [129] V. Srikant, D.R. Clarke, On the optical band gap of zinc oxide, *J. Appl. Phys.* 83 (1998) 5447–5451. doi:10.1063/1.367375.
- [130] J.P. Wang, Z.Y. Wang, B.B. Huang, Y.D. Ma, Y.Y. Liu, X.Y. Qin, X.Y. Zhang, Y. Dai, Oxygen Vacancy Induced Band-Gap Narrowing and Enhanced Visible Light Photocatalytic Activity of ZnO, *ACS Appl. Mater. Interfaces.* 4 (2012) 4024–4030. doi:10.1021/am300835p.
- [131] N. Palmu, Sinkkioksidin-nanorakenteiden valmistaminen ylikriittisen hiilidioksidin avulla, Master's Thesis, Tampere University, Finland, 2020.





# PUBLICATIONS



# PUBLICATION

I

## **Dissolution-Induced Nanowire Synthesis on Hot-Dip Galvanized Surface in Supercritical Carbon Dioxide**

A. Kaleva, V. Saarimaa, S. Heinonen, J.-P. Nikkanen, A. Markkula, P. Väisänen, E. Levänen

Nanomaterials, Vol 7(7), 181  
<https://doi.org/10.3390/nano7070181>

**Publication reprinted with the permission of the copyright holders.**





Communication

# Dissolution-Induced Nanowire Synthesis on Hot-Dip Galvanized Surface in Supercritical Carbon Dioxide

Aaretti Kaleva <sup>1,\*</sup> , Ville Saarimaa <sup>2</sup>, Saara Heinonen <sup>1</sup>, Juha-Pekka Nikkanen <sup>1</sup>, Antti Markkula <sup>3</sup>, Pasi Väisänen <sup>3</sup> and Erkki Levänen <sup>1</sup>

<sup>1</sup> Laboratory of Materials Science, Tampere University of Technology, P.O. Box 589, FI-33101 Tampere, Finland; saara.heinonen@tut.fi (S.H.); juha-pekka.nikkanen@tut.fi (J.-P.N.); erkki.levanen@tut.fi (E.L.)

<sup>2</sup> Top Analytica Oy, Ruukinkatu 4, FI-20540 Turku, Finland; ville.saarimaa@topanalytica.com

<sup>3</sup> SSAB Europe Oy, Harvialantie 420, FI-13300 Hämeenlinna, Finland; antti.markkula@ssab.com (A.M.); pasi.vaisanen@ssab.com (P.V.)

\* Correspondence: aaretti.kaleva@tut.fi; Tel.: +358-50-447-8715

Received: 7 June 2017; Accepted: 7 July 2017; Published: 11 July 2017

**Abstract:** In this study, we demonstrate a rapid treatment method for producing a needle-like nanowire structure on a hot-dip galvanized sheet at a temperature of 50 °C. The processing method involved only supercritical carbon dioxide and water to induce a reaction on the zinc surface, which resulted in growth of zinc hydroxycarbonate nanowires into flower-like shapes. This artificial patina nanostructure predicts high surface area and offers interesting opportunities for its use in industrial high-end applications. The nanowires can significantly improve paint adhesion and promote electrochemical stability for organic coatings, or be converted to ZnO nanostructures by calcining to be used in various semiconductor applications.

**Keywords:** zinc hydroxycarbonate; nanowire; supercritical carbon dioxide

## 1. Introduction

Hot-dip galvanized (HDG) coatings are widely used in automotive and construction industries. These zinc coatings are most often the outermost material surfaces, which is why they require sufficient corrosion protection and good aesthetics [1]. Painting is the most common method for improving the aforementioned properties. However, the galvanized surface usually needs additional surface modification before painting, e.g., chemical pretreatment, to provide satisfactory adhesion to the substrate [2]. Weathering of a HDG surface means deliberately corroding the surface to produce a patina layer that contains dissolution products of zinc. This patina layer hinders the corrosion rate of the material and enhances paint adhesion [3–5]. In atmospheric corrosion, formation of the patina layer on HDG coating starts by zinc reacting with oxygen from air producing zinc oxide (ZnO). Another initial corrosion product is zinc hydroxide (Zn(OH)<sub>2</sub>), which forms when moisture is present. Subsequently, ZnO and Zn(OH)<sub>2</sub> then react over time with carbon dioxide (CO<sub>2</sub>) forming zinc hydroxycarbonates. After several years of exposure to the atmosphere when no other contaminants are present, the patina layer consists mostly of a type of zinc hydroxycarbonate called hydrozincite (Zn<sub>5</sub>(CO<sub>3</sub>)<sub>2</sub>(OH)<sub>6</sub>) [1,6,7]. The formed patina enhances paint adhesion by promoting chemical bonding and increasing the roughness of the HDG surface, thus creating anchorage points [5,8]. Waiting for the natural patina to form on HDG is used as a pretreatment before coating the surface to provide better adhesion properties [4]. A disadvantage of the traditional weathering process is that the formation of a fully developed patina layer can take from eight months to two years' time for it to be ready for painting [4]. Consequently, there may be a great interest in industry for the possibility to produce an artificial patina of zinc using a fast and versatile method described in our study.

According to the literature, zinc hydroxycarbonates with similar composition to those corrosion products found in naturally forming patinas are possible to be transformed into ZnO nanostructures simply by calcination [9,10]. This opens other interesting applications for our method to alter zinc surfaces using supercritical carbon dioxide (scCO<sub>2</sub>), i.e., the possibility to produce photocatalytic nanostructured ZnO. The scCO<sub>2</sub> treatment is fast and uses no harmful chemicals compared to conventional hydrothermal synthesis techniques commonly used for ZnO nanowire synthesis [11]. These nanostructures of zinc oxide have been used in high-end technological applications such as dye-sensitized solar cells [12–14], piezoelectrics [15] and different types of sensors [16,17]. Furthermore, similar nanowire structures might be used in flexible energy storage systems, supercapacitors, solar and hybrid devices [18–23].

Processing with scCO<sub>2</sub> has been of great interest in materials research because of its green processing properties and wide range of applicability to various processes. It is used to produce many nanostructures, including nanowires, using different kinds of approaches for the nanostructure synthesis [24–27]. The corrosive behaviour of scCO<sub>2</sub> on metals has been studied previously. When scCO<sub>2</sub> and water (H<sub>2</sub>O) are in contact with steel, they react together by forming a compact and protective iron carbonate layer on the steel surface [28,29].

This study presents a rapid and an environmentally friendly method utilizing scCO<sub>2</sub> for producing an artificial patina layer on a HDG surface. This scCO<sub>2</sub> treatment utilizes only two simple reactants: CO<sub>2</sub> and H<sub>2</sub>O.

## 2. Results and Discussion

### 2.1. SEM Imaging and EDS Analysis

We can see a significant change in the surface structure between an untreated HDG surface (Figure 1a) and the scCO<sub>2</sub>-treated sample (Figure 1b). The scCO<sub>2</sub> treatment produced thin and long nanowires. The nanowires grow mostly straight from the surface but a few seem to have curved towards the tip of the nanowire. Minor branching of the nanowires can be seen as well. The nanowires seem to grow in many angles from single nucleation points. These nucleation points may be caused by pitting type corrosion. In these conditions, the local zinc corrosion around the pits create favourable conditions for nanowire growth as previously suggested in a study by Miles and Mattia [9]. The growth angle from the nucleation points vary from more perpendicular to almost parallel to the surface. Consequently, the overall nanowire growth results in formation of flower-like shapes. Structures with similar morphology and composition have been formed on zinc in previous studies where zinc surface was anodized in the presence of carbonate-containing electrolytes [9,10]. The underlying substrate surface can be seen through the nanowires, which indicates that the surface is not completely covered by the structure.

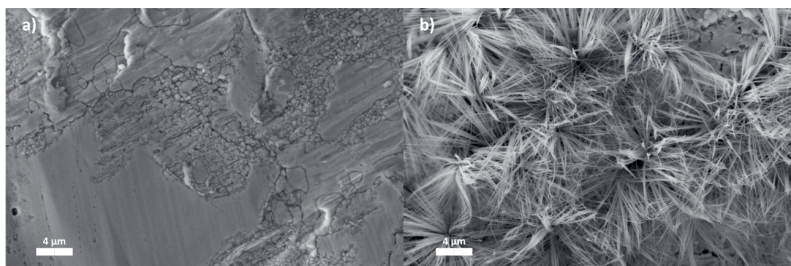


**Figure 1.** SEM images of rolled hot-dip galvanized (HDG) surface (a) and scCO<sub>2</sub>-treated surface (b).

The energy dispersive spectrometer (EDS) results show that on the reference surface (without the scCO<sub>2</sub> treatment), the elemental composition was: 8.0 at % oxygen, 2.2 at % aluminum and 89.8 at %

zinc. The nanowire structure contained 15.9 at % carbon, 62.9 at % oxygen, 0.1 at % aluminum and 21.1 at % zinc. The amounts of carbon and oxygen present in the nanowire structure could indicate the presence of zinc hydroxycarbonate. The EDS analysis also shows that both the reference zinc surface and the  $\text{scCO}_2$ -treated surface contain trace amounts of aluminum. The aluminum from the galvanizing bath reacts with oxygen in air to form aluminum oxide ( $\text{Al}_2\text{O}_3$ ) on the surface of the HDG sheet [30]. Residual aluminum can also be detected after alkaline cleaning treatment [31]. The presence of aluminum in the  $\text{scCO}_2$  treated sample confirms the uneven surface coverage by the nanowire structure.

## 2.2. FTIR Measurements

The Fourier transform infrared spectroscopy (FTIR) spectrum of the zinc surface is presented in Figure 2. A broad absorption peak can be seen at  $3260\text{ cm}^{-1}$  which refers to OH stretching vibration, indicating the presence of hydroxyl groups in the structure [32,33]. The presence of hydroxyl groups is supported by a small band at  $1614\text{ cm}^{-1}$  which is attributed to interlayer  $\text{H}_2\text{O}$  bending [34]. Intense double peak at  $1516\text{ cm}^{-1}$  and  $1380\text{ cm}^{-1}$  is an indication of antisymmetric  $\nu_3$  stretching modes of carbonates [6,33]. This double peak is typical for zinc hydroxycarbonates containing both carbonate and hydroxyl groups, e.g., hydrozincite [35]. Peak at  $1076\text{ cm}^{-1}$  is attributed to  $\nu_1$  stretching of carbonates and is usually inactive in IR-measurements [33,35,36]. However, due to distortion-caused reduction in symmetry of the carbonate this band can become IR-active [33]. Further indication of carbonate presence is due to peaks  $865\text{ cm}^{-1}$ ,  $835\text{ cm}^{-1}$  and  $740\text{ cm}^{-1}$ , which are attributed to carbonate bending modes of  $\nu_2$ , out-of-plane  $\nu_2$  and  $\nu_4$ , respectively [32,33,36]. Hales et al. stated that the presence of multiple  $\nu_2$  modes is also an indication of symmetry reduction of the carbonate anion, which coheres well with presence of the  $1076\text{ cm}^{-1}$  peak. Finally, a small absorption peak at  $465\text{ cm}^{-1}$  can be seen as well, which is an indication of some presence of zinc oxide [37,38]. Moreover, in a study where hydrozincite was synthesized from ZnO, water and  $\text{CO}_2$ , a similar peak can be found which was attributed to zinc oxide [39]. Since the nanowire structure does not cover the whole surface according to Figure 1b, it is likely that the presence of ZnO is measured from the sample surface rather than the nanowire structure.

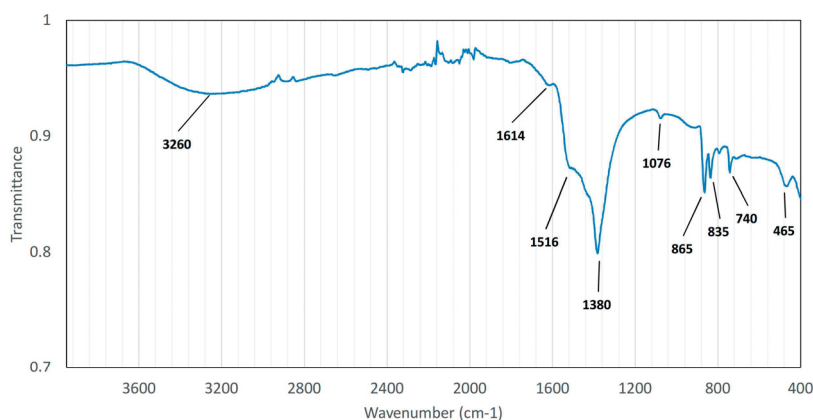


**Figure 2.** FTIR spectrum measured directly from the sample surface containing the nanowire structure.

## 2.3. XPS Measurements

The XPS survey spectrum of the nanowire-containing surface can be seen from Figure 3. Zinc presence can be seen from Zn  $2p_{1/2}$ , Zn  $2p_{3/2}$ , Zn 3s and Zn LMM peaks. Clear indication of oxygen presence can be concluded from peaks O 1s, O KLL and carbon presence from peak C 1s. In addition,

the surface contains also aluminum due to peaks Al 2s and Al 2p. These results are in good agreement with the EDS results.

The oxygen content was calculated from the X-ray photoelectron spectroscopy (XPS) data from three different points and it was on average 55.3 at %. A minor ZnO presence can be concluded from the FTIR results as well as Al<sub>2</sub>O<sub>3</sub> presence from the XPS results. However, it can be said that these alone cannot explain the high amount of oxygen on the surface. Therefore, it is expected that the origin of the measured oxygen is derived from the nanowire structure in a form of a zinc hydroxycarbonate.

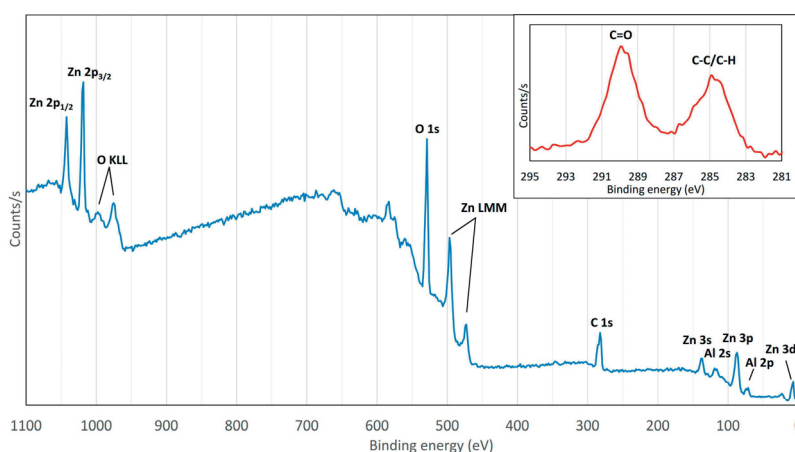


**Figure 3.** XPS survey spectrum of the scCO<sub>2</sub>-treated sample surface. The spectrum of the C 1s peak is presented in the insert after the sample had gone through mild sputtering.

The insert in Figure 3 shows the C 1s peak. The surface had gone through mild sputtering prior to the analysis in order to confirm that the detected carbon was not present solely as an impurity. We can see two separate peaks at 289.9 eV and 285.0 eV. The latter peak is assigned to C–H and C–C bonding originating from adventitious carbon and, therefore, it is not part of the nanowire structure [31,40,41]. However, the peak at 289.9 eV indicates the presence of carbonate groups in the structure. [31,41]. The peak position is typical for zinc hydroxycarbonates, which is in accordance with the FTIR results [9].

The FTIR and XPS results are in agreement that the nanowire structure contains both hydroxyl and carbonate groups, which agrees with zinc hydroxycarbonate substance. This is supported also by the EDS results. The FTIR spectrum fits well with hydrozincite, a type of zinc hydroxycarbonate, according to earlier studies [33,39]. However, Jambor et al. has stated that the FTIR spectrum is near identical for different zinc hydroxycarbonates exhibiting slightly different stoichiometric compositions [35]. Therefore, a more detailed analysis of the exact composition will be carried out in forthcoming studies.

All in all, the reaction in the scCO<sub>2</sub> treatment involves HDG surface, H<sub>2</sub>O and scCO<sub>2</sub>. Zinc surface forms ZnO already in atmosphere by reacting with oxygen [42]. It is commonly known that ZnO acts as an intermediate reaction product for the formation of zinc hydroxycarbonates in atmospheric corrosion [1,33]. Moreover, ZnO has also been used as a starting material in hydrozincite powder synthesis together with H<sub>2</sub>O and pressurized CO<sub>2</sub> [39]. H<sub>2</sub>O can react directly with zinc [1] or with ZnO [42] to produce Zn(OH)<sub>2</sub>. Zn(OH)<sub>2</sub> is easily dissolved into H<sub>2</sub>O and so it can further react with CO<sub>2</sub> to produce zinc hydroxycarbonates [42]. However, it has also been proposed that Zn(OH)<sub>2</sub> can dehydrate back into ZnO and then react with H<sub>2</sub>O and CO<sub>2</sub> to produce zinc hydroxycarbonates [1]. When CO<sub>2</sub> dissolves into H<sub>2</sub>O it produces carbonic acid (H<sub>2</sub>CO<sub>3</sub>) that dissociates into HCO<sub>3</sub><sup>−</sup> and CO<sub>3</sub><sup>2−</sup> ions. The concentration of HCO<sub>3</sub><sup>−</sup> is far greater than CO<sub>3</sub><sup>2−</sup> in the treatment conditions used, which is why HCO<sub>3</sub><sup>−</sup> is more likely to be involved in the formation of the zinc hydroxycarbonate [28].



This is because  $\text{HCO}_3^-$  is unlikely to dissociate in acidic conditions due to its high  $\text{pK}_a$  of over 10 [43]. Moreover, in earlier studies it has been concluded that the  $\text{HCO}_3^-$  ions are responsible for the zinc hydroxycarbonate formation [9,44]. To the best of our knowledge, formation of similar nanowire structures in atmospheric corrosion of zinc has not been reported in literature. Factors influencing the formation of the seemingly crystalline structure can be affected by much higher treatment pressure and  $\text{CO}_2$  concentration compared to atmospheric conditions. This is supported by earlier studies where partial pressure has been noticed to affect the formation of zinc corrosion products [33,45].

### 3. Materials and Methods

#### 3.1. Materials

A rolled HDG steel sheet with a coating mass of  $275 \text{ g Zn/m}^2$  provided by SSAB Europe Oy was used as a substrate material. The zinc layer was  $>99\%$  pure with small amounts of alloying elements, e.g., aluminum. The sample dimensions were 25 mm width, 50 mm height and 0.5 mm thickness. The sample was cleaned using an alkaline treatment (Gardoclean 338, Chemetall, Frankfurt, Germany) to remove aluminum oxide layer from the outer surface. Only deionized water, with a conductivity of 2–10  $\mu\text{S}$ , and carbon dioxide ( $\geq 97\%$ , AGA, Espoo, Finland) were used for the  $\text{scCO}_2$  treatment.

#### 3.2. $\text{scCO}_2$ Apparatus and Sample Preparation

The  $\text{scCO}_2$  treatments were performed using a Thar Technologies Inc. (Pittsburgh, PA, USA) RESS 250 system. The schematic of the system is presented in Figure 4. The  $\text{CO}_2$  flows initially from a siphon-tubed bottle. The  $\text{CO}_2$  is then cooled by a circulating cooling system to keep it in a liquid state so that it can be pumped into the reaction chamber by a PC-controlled high-pressure piston pump. Before the  $\text{CO}_2$  enters the reaction chamber, it is preheated to gaseous or supercritical state. The reaction chamber is made of 316SS steel and it has an internal heating system built into the walls. The co-solvent pump is used to pump co-solvents during experiments in high-pressures. The PC-controlled automatic back-pressure regulator (ABPR) controls the depressurization rate of the  $\text{CO}_2$  before it flows out from the top of the reaction chamber. Needle valves (V1 and V2) are used to control the pressure inside the system.

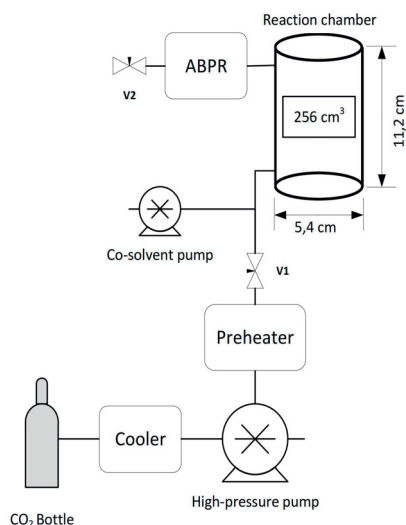


Figure 4. Schematic presentation of the  $\text{scCO}_2$  apparatus.

The sample was prepared in the following manner. The HDG sheet was placed into the reaction chamber on a sample holder and the valve V2 was closed to ensure that no pressure drop occurred during the treatment. Then the chamber was closed and filled with CO<sub>2</sub> after which it was heated to 50 °C and pressurized to 300 bar pressure. Valve V1 was then closed and 5 mL of deionized water was introduced to the chamber using the co-solvent pump. The duration of the treatment was 60 min. When the treatment had finished, the valve V2 was opened and the reaction chamber was carefully depressurized of CO<sub>2</sub> during 10 min using the ABPR.

### 3.3. Characterization Techniques

The sample surface was characterized with a field emission scanning electron microscope (FE-SEM, ZEISS ultra plus, Jena, Germany) with energy dispersive spectrometer (EDS, Oxford Instruments INCA Energy 350, Abingdon, UK) using a 15.0 kV acceleration voltage. The EDS results were taken as average values from three separate points on the sample surfaces. FTIR (Bruker Tensor 27, Billerica, MA, USA) with attenuated total reflection (ATR) diamond sample holder and DLATGS detector was used to analyse the composition of the nanowires in the spectral range of 3950–400 cm<sup>-1</sup>. The FTIR measurements were done directly from the sample surface. X-ray photoelectron spectroscopy (XPS) (PHI Quantum 2000, Chanhassen, MN, USA) was used for the surface elemental analysis. A monochromated Al K $\alpha$  beam (50 W, 15 kV) with a 200  $\mu$ m spot size was used to obtain the C 1s spectrum. Mild sputtering of the sample surface was performed with Ar<sup>+</sup> ions. The C 1s peak at 285.0 eV was used for the charge-shift correction.

## 4. Conclusions

A rapid formation of a nanowire structure was obtained on a HDG sheet using only supercritical carbon dioxide and water. The SEM imaging showed that the nanowires had a needle-like shape and they grew from distinct nucleation points on the surface into flower-like structures. The formation of the nanowires was due to a reaction between the zinc surface, water and carbon dioxide. According to the FTIR and XPS analysis, the nanowire structure consisted of hydroxyl and carbonate groups, which is also supported by the EDS results. Therefore, the nanowires are most likely a type of zinc hydroxycarbonate with a proposed stoichiometric formula of Zn<sub>x</sub>(CO<sub>3</sub>)<sub>y</sub>(OH)<sub>z</sub>. Determination of the exact composition as well as the reaction path remains a task for subsequent studies. The method presented in this study shows a great potential for its use as a pretreatment before coating to enhance the paint adhesion and electrochemical properties of the zinc/coating interface. Additionally, the nanowire structure may be used as starting material to produce a ZnO structure that could be used in high-end technological applications, e.g., sensors and dye-sensitized solar cells.

**Acknowledgments:** Digital, Internet, Materials & Engineering Co-Creation (DIMECC) (formally FIMECC) and its HYBRIDS materials program is acknowledged for financial support. This work was also supported by an Academy of Finland project: Green processing of functional surface by supercritical carbon dioxide (decision number 304782).

**Author Contributions:** A.K. conceived and designed the experiments, carried out FTIR characterizations, and analyzed the data; V.S., A.M., P.V. contributed materials. V.S. performed XPS measurements; S.H. carried out SEM imaging; A.K., J.N. and E.L. designed the study; A.K. wrote the manuscript with critical output from all co-authors.

**Conflicts of Interest:** The authors declare no conflict of interest.

## References

1. Zhang, X.G. *Corrosion and Electrochemistry of Zinc*; Springer: Boston, MA, USA, 1996; ISBN 978-1-4757-9879-1.
2. Puomi, P.; Fagerholm, H.M.; Rosenholm, J.B.; Jyrkäs, K. Comparison of different commercial pretreatment methods for hot-dip galvanized and Galfan coated steel. *Surf. Coat. Technol.* **1999**, *115*, 70–78. [CrossRef]
3. Cabanelas, I.; Collazo, A.; Izquierdo, M.; Nóvoa, X.R.; Pérez, C. Influence of galvanised surface state on the duplex systems behaviour. *Corros. Sci.* **2007**, *49*, 1816–1832. [CrossRef]

4. Malone, J.F. Painting hot-dip galvanized sheet. *Mater. Perform.* **1992**, *31*, 39–42.
5. Collazo, A.; Pérez, C.; Izquierdo, M.; Merino, P. Evaluation of environmentally friendly paints over weathering galvanised steel. *Prog. Org. Coat.* **2003**, *46*, 197–210. [CrossRef]
6. Lindström, D.; Odnevall Wallinder, I. Long-term use of galvanized steel in external applications. Aspects of patina formation, zinc runoff, barrier properties of surface treatments, and coatings and environmental fate. *Environ. Monit. Assess.* **2011**, *173*, 139–153. [CrossRef]
7. Odnevall, I. A comparison between analytical methods for zinc specimens exposed in a rural atmosphere. *J. Electrochem. Soc.* **1991**, *138*, 1923–1928. [CrossRef]
8. Packham, D. Surface energy, surface topography and adhesion. *Int. J. Adhes. Adhes.* **2003**, *23*, 437–448. [CrossRef]
9. Miles, D.O.; Mattia, D. Hierarchical 3D ZnO nanowire structures via fast anodization of zinc. *J. Mater. Chem. A* **2015**, *3*, 17569–17577. [CrossRef]
10. Hu, Z.; Chen, Q.; Li, Z.; Yu, Y.; Peng, L.M. Large-scale and rapid synthesis of ultralong ZnO nanowire films via anodization. *J. Phys. Chem. C* **2010**, *114*, 881–889. [CrossRef]
11. Kołodziejczak-Radzimska, A.; Jesionowski, T. Zinc oxide—From synthesis to application: A review. *Materials (Basel)* **2014**, *7*, 2833–2881. [CrossRef]
12. Han, J.; Fan, F.; Xu, C.; Lin, S.; Wei, M.; Duan, X.; Wang, Z.L. ZnO nanotube-based dye-sensitized solar cell and its application in self-powered devices. *Nanotechnology* **2010**, *21*, 405203. [CrossRef] [PubMed]
13. Afifi, A.; Tabatabaei, M. Efficiency investigation of dye-sensitized solar cells based on the zinc oxide nanowires. *Orient. J. Chem.* **2014**, *30*, 155–160. [CrossRef]
14. Lin, C.-Y.; Lai, Y.-H.; Chen, H.-W.; Chen, J.-G.; Kung, C.-W.; Vittal, R.; Ho, K.-C. Highly efficient dye-sensitized solar cell with a ZnO nanosheet-based photoanode. *Energy Environ. Sci.* **2011**, *4*, 3448–3455. [CrossRef]
15. Khan, A.; Ali Abbasi, M.; Hussain, M.; Hussain Ibupoto, Z.; Wissting, J.; Nur, O.; Willander, M. Piezoelectric nanogenerator based on zinc oxide nanorods grown on textile cotton fabric. *Appl. Phys. Lett.* **2012**, *101*, 193506. [CrossRef]
16. Marie, M.; Mandal, S.; Manasreh, O. An electrochemical glucose sensor based on zinc oxide nanorods. *Sensors* **2015**, *15*, 18714–18723. [CrossRef] [PubMed]
17. Zhang, Y.; Yu, K.; Jiang, D.; Zhu, Z.; Geng, H.; Luo, L. Zinc oxide nanorod and nanowire for humidity sensor. *Appl. Surf. Sci.* **2005**, *242*, 212–217. [CrossRef]
18. Gao, Z.; Song, N.; Li, X. Microstructure design of hybrid CoO @ NiO and graphene nano-architectures for flexible high performance supercapacitors. *J. Mater. Chem. A Mater. Energy Sustain.* **2015**, *3*, 14833–14844. [CrossRef]
19. Bao, L.; Zang, J.; Li, X. Flexible Zn<sub>2</sub>SnO<sub>4</sub>/MnO<sub>2</sub> Core/Shell nanocable? Carbon microfiber hybrid composites for high-performance supercapacitor electrodes. *Nano Lett.* **2011**, *11*, 1215–1220. [CrossRef] [PubMed]
20. Gao, Z.; Yang, W.; Wang, J.; Song, N.; Li, X. Flexible all-solid-state hierarchical NiCo<sub>2</sub>O<sub>4</sub>/porous graphene paper asymmetric supercapacitors with an exceptional combination of electrochemical properties. *Nano Energy* **2015**, *13*, 306–317. [CrossRef]
21. Gao, Z.; Bumgardner, C.; Song, N.; Zhang, Y.; Li, J.; Li, X. Cotton-textile-enabled flexible self-sustaining power packs via roll-to-roll fabrication. *Nat. Commun.* **2016**, *7*, 1–12. [CrossRef] [PubMed]
22. Gao, Z.; Song, N.; Zhang, Y.; Li, X. Cotton textile enabled, all-solid-state flexible supercapacitors. *RSC Adv.* **2015**, *5*, 15438–15447. [CrossRef]
23. Zhang, Y.; Gao, Z.; Song, N.; Li, X. High-performance supercapacitors and batteries derived from activated banana-peel with porous structures. *Electrochim. Acta* **2016**, *222*, 1257–1266. [CrossRef]
24. Cansell, F.; Aymonier, C. Design of functional nanostructured materials using supercritical fluids. *J. Supercrit. Fluids* **2009**, *47*, 508–516. [CrossRef]
25. Wang, K.; Wei, M.; Morris, M.A.; Zhou, H.; Holmes, J.D. Mesoporous titania nanotubes: Their preparation and application as electrode materials for rechargeable lithium batteries. *Adv. Mater.* **2007**, *19*, 3016–3020. [CrossRef]
26. Zhang, X.; Heinonen, S.; Levänen, E. Applications of supercritical carbon dioxide in materials processing and synthesis. *RSC Adv.* **2014**, *4*, 61137–61152. [CrossRef]
27. Sanli, D.; Bozbag, S.E.; Erkey, C. Synthesis of nanostructured materials using supercritical CO<sub>2</sub>: Part I. Physical transformations. *J. Mater. Sci.* **2012**, *47*, 2995–3025. [CrossRef]

28. Choi, Y.S.; Nešić, S. Determining the corrosive potential of CO<sub>2</sub> transport pipeline in high pCO<sub>2</sub>-water environments. *Int. J. Greenh. Gas Control* **2011**, *5*, 788–797. [CrossRef]
29. Cole, I.S.; Paterson, D.A.; Corrigan, P.; Sim, S.; Birbilis, N. State of the aqueous phase in liquid and supercritical CO<sub>2</sub> as relevant to CCS pipelines. *Int. J. Greenh. Gas Control* **2012**, *7*, 82–88. [CrossRef]
30. Biber, H.E. Scanning auger microprobe study of hot-dipped regular-spangle galvanized steel: Part I. Surface composition of As-produced sheet. *Metall. Trans. A* **1988**, *19*, 1603–1608. [CrossRef]
31. Berger, R.; Bexell, U.; Stavlid, N.; Grehk, T.M. The influence of alkali-degreasing on the chemical composition of hot-dip galvanized steel surfaces. *Surf. Interface Anal.* **2006**, *38*, 1130–1138. [CrossRef]
32. Su, B.; Li, M.; Shi, Z.; Lu, Q. From superhydrophilic to superhydrophobic: Controlling wettability of hydroxide zinc carbonate film on zinc plates. *Langmuir* **2009**, *25*, 3640–3645. [CrossRef] [PubMed]
33. Hales, M.C.; Frost, R.L. Synthesis and vibrational spectroscopic characterisation of synthetic hydrozincite and smithsonite. *Polyhedron* **2007**, *26*, 4955–4962. [CrossRef]
34. Zahra, F.; Khalidi, A.; Abdennouri, M. Zn–Al layered double hydroxides intercalated with carbonate, nitrate, chloride and sulphate ions: Synthesis, characterisation and dye removal properties. *Integr. Med. Res.* **2016**, *11*, 90–100. [CrossRef]
35. Jambor, J.L. Studies of basic copper and zinc Carbonates: I-synthetic zinc carbonates and their relationship to hydrozincite. *Can. Mineral.* **1964**, *8*, 92–108.
36. Cheng, J.; Poduska, K. A strategy for hydroxide exclusion in nanocrystalline solid-state metathesis products. *Nanomaterials* **2013**, *3*, 317–324. [CrossRef] [PubMed]
37. Hong, R.Y.; Li, J.H.; Chen, L.L.; Liu, D.Q.; Li, H.Z.; Zheng, Y.; Ding, J. Synthesis, surface modification and photocatalytic property of ZnO nanoparticles. *Powder Technol.* **2009**, *189*, 426–432. [CrossRef]
38. Zhang, X.; Liu, X.; Odnevall Wallinder, I.; Leygraf, C. The protective role of hydrozincite during initial corrosion of a Cu40Zn alloy in chloride-containing laboratory atmosphere. *Corros. Sci.* **2015**, *103*, 20–29. [CrossRef]
39. Turianicová, E.; Káňuchová, M.; Zorkovská, A.; Holub, M.; Bujnáková, Z.; Dutková, E.; Baláz, M.; Findoráková, L.; Balintová, M.; Obut, A. CO<sub>2</sub> utilization for fast preparation of nanocrystalline hydrozincite. *J. CO<sub>2</sub> Util.* **2016**, *16*, 328–335. [CrossRef]
40. Diler, E.; Lescop, B.; Rioual, S.; Nguyen Vien, G.; Thierry, D.; Rouvellou, B. Initial formation of corrosion products on pure zinc and MgZn<sub>2</sub> examined by XPS. *Corros. Sci.* **2014**, *79*, 83–88. [CrossRef]
41. Ballerini, G.; Ogle, K.; Barthés-Labrousse, M.G. The acid-base properties of the surface of native zinc oxide layers: An XPS study of adsorption of 1,2-diaminoethane. *Appl. Surf. Sci.* **2007**, *253*, 6860–6867. [CrossRef]
42. Graedel, T.E. Corrosion mechanisms for zinc exposed to the atmosphere. *J. Electrochem. Soc.* **1989**, *136*, 193C–203C. [CrossRef]
43. Hastings, B.; Sendroy, J. The effect of variation in ionic strength on the apparent first and second dissociation constants of carbonic acid. *J. Biol. Chem.* **1925**, *65*, 445–455.
44. O'Connor, M.F. A study of the kinetics of the basic zinc carbonate formation reaction. *Z. Naturforsch B* **1975**, *30*, 665–668. [CrossRef]
45. Falk, T.; Svensson, J.-E.; Johansson, L.-G. The role of carbon dioxide in the atmospheric corrosion of zinc. *J. Electrochem. Soc.* **1998**, *145*, 39–44. [CrossRef]



# PUBLICATION II

## **Synthesis of ZnO nanowires with supercritical carbon dioxide and post heat treatment**

A. Kaleva, J.-P. Nikkanen, S. Heinonen, V. Saarimaa, T. Vuorinen, M. Honkanen, L. Hyvärinen, E. Levänen

Nanotechnology, Vol 29, 445601  
<https://doi.org/10.1088/1361-6528/aada69>

**Publication reprinted with the permission of the copyright holders.**

**This is the Accepted Manuscript version of an article accepted for publication in Nanotechnology. IOP Publishing Ltd is not responsible for any errors or omissions in this version of the manuscript or any version derived from it. The Version of Record is available online at <https://doi.org/10.1088/1361-6528/aada69>**



# Synthesis of ZnO nanowires with supercritical carbon dioxide and post heat treatment

Aaretti Kaleva<sup>1</sup>, Juha-Pekka Nikkanen<sup>1</sup>, Saara Heinonen<sup>1</sup>, Ville Saarimaa<sup>2</sup>, Tommi Vuorinen<sup>3</sup>, Mari Honkanen<sup>1</sup>, Leo Hyvärinen<sup>1</sup> and Erkki Levänen<sup>1</sup>

<sup>1</sup>Laboratory of Materials Science, Tampere University of Technology P.O. Box 589, FI-33101 Tampere, Finland

<sup>2</sup>Top Analytica Oy, Ruukinkatu 4, FI-20540 Turku, Finland

<sup>3</sup>VTT Technical Research Centre of Finland Ltd, P.O. Box 1300, FI-33101 Tampere

E-mail: aaretti.kaleva@tut.fi

Received xxxxxx

Accepted for publication xxxxxx

Published xxxxxx

## Abstract

ZnO nanowires are used in applications such as gas sensors and solar cells. This work presents a novel synthesis route for ZnO nanowires using supercritical carbon dioxide and post heat treatment. The method used supercritical carbon dioxide and a precursor solution as reactants to form nanowires on a galvanized surface. After the supercritical carbon dioxide treatment, the substrate was heat treated. The surfaces were characterized with SEM, TEM, EDS, FTIR, XRD and optical spectroscopy. The FTIR results showed that the surface structure had changed from zinc hydroxycarbonate to ZnO during the heat treatment. The nanowires were slightly bent due to the heat treatment according to the SEM images. The presence of ZnO was further confirmed with XRD. The bandgap of the structure was determined by reflectance measurements and showed a value of 3.23 eV. The synthesis method presented in this study offers a unique approach into the formation of ZnO nanowires in a facile, rapid and environmentally friendly process.

Keywords: scCO<sub>2</sub>, zinc oxide, zinc hydroxy carbonate, flower-like, nanoflower, hot-dip galvanized, corrosion

## 1. Introduction

Zinc oxide (ZnO) is a n-type semiconductor material which has various properties including intrinsic antibacteriality, photocatalytic activity as well as piezo- and pyroelectricity [1,2]. ZnO has also a relatively wide bandgap (3.37 eV) and a large exciton binding energy (60 mV) which makes it an attractive material in electronic and optoelectronic applications [1,3]. Furthermore, ZnO nanowires are used in gas sensors, dye-sensitized solar cells and mechanical energy harvesting applications [1].

The use of nanomaterials has been shown to contribute to the emergence of unique electrical, mechanical, chemical and

optical material properties [3]. Therefore, synthesis of nanostructured materials has been a widely discussed topic among researchers [2,4–7]. Synthesis of nanostructured ZnO in particular has shown a great interest because they can be prepared with multiple methods and in varying morphologies [8]. Nanostructures of ZnO e.g., nanowires, nanoparticles and nanoflowers, have been synthesized with spray pyrolysis [9], thermal evaporation [10], chemical vapour deposition [11] or hydrothermal synthesis [12]. However, most of these methods require a variety of chemicals, multiple processing steps and long synthesis times [1].

Synthesis of ZnO nanostructures often starts with forming zinc hydroxycarbonate nanostructures as an intermediate step,

after which they are converted into ZnO by post heat treatment [13–16]. Zinc hydroxycarbonates substances are also formed in nature due to atmospheric corrosion process of zinc. In this corrosion process, the zinc surface reacts gradually with carbon dioxide (CO<sub>2</sub>) and water (H<sub>2</sub>O) that originate from air and humidity [17]. Our previous work showed that arranged nanowires of zinc hydroxycarbonate can be synthesized through the same corrosion process in high CO<sub>2</sub> pressure and slightly elevated temperature. This method used supercritical carbon dioxide (scCO<sub>2</sub>) and water as the only reactants [18]. Moreover, we presented that the process could be enhanced by the addition of a catalyst to increase the surface coverage of the nanowires on zinc. We also proposed that this method could be used as a pretreatment for galvanized surfaces to promote adhesion before coating [19,20].

Generally, scCO<sub>2</sub> has many attractive properties that make it a good solvent or reaction medium for variety of processes e.g., powder synthesis, coating and drug encapsulation [21,22]. These processes often utilize scCO<sub>2</sub> as a solvent because of its high density that leads to good dissolving capabilities. Moreover, the density of scCO<sub>2</sub> can be altered by changing the pressure that modifies the dissolving properties as well. Processing with scCO<sub>2</sub> is considered a green technique because it is non-flammable, non-toxic, inexpensive and has a great availability as a by-product of the industry [22]. ScCO<sub>2</sub> is rarely used as a reactant itself but some corrosion and carbon sequestration studies have also investigated the effect of scCO<sub>2</sub> on different mineral and metal surfaces. These studies show the formation of carbonates on the surfaces of different minerals and metals in the presence of water and scCO<sub>2</sub> [23–25].

In this research, we demonstrate a unique method for synthesizing ZnO nanowires. The method utilizes a two-step process where scCO<sub>2</sub> treatment is combined with subsequent heat treatment. This method is rapid, environmentally friendly and requires only simple processing routes compared to commonly used ZnO synthesis techniques. Moreover, the utilization of CO<sub>2</sub> in the manufacture of the material can offer additional benefits such as cleaner environment and sustainability.

## 2. Materials and methods

A rolled hot-dip galvanized steel was used as a substrate material. SSAB Europe Oy provided the galvanized substrate which had a zinc coating weight of 275 g/m<sup>2</sup>. The purity of the zinc coating was > 99% with aluminium as an alloying element. The residual aluminium oxide on the surface was removed with an alkaline treatment (Gardoclean 338, Chemetall) before the scCO<sub>2</sub>-treatment. The precursor solution was composed of 0.5 mass-% copper (II) hexafluoroacetylacetonate hydrate (Cu(hfac)<sub>2</sub>·xH<sub>2</sub>O, Sigma-Aldrich) catalyst dissolved in 5 ml deionized water/ethanol (40/60 vol-%) solution.

The scCO<sub>2</sub>-treatment was performed in a cylindrical reaction chamber. The substrate was first placed inside the chamber which was then heated and pressurized with CO<sub>2</sub> (≥ 97%, AGA) to 50 °C and 300 bar, respectively. Consequently, the precursor solution was then introduced to the system after which the synthesis was carried out for 60 minutes. Finally, the CO<sub>2</sub> was vented out of the system and the substrate was cleaned with ethanol and pressurized air. A more detailed depiction of the treatment procedure and the scCO<sub>2</sub> apparatus is described in our previous study with the exception of the catalyst [18]. The post heat treatment was performed at 400 °C for one hour in a furnace in ambient atmosphere.

The sample surfaces were examined with field emission scanning electron microscope (FE-SEM, ZEISS ultra plus) and energy dispersive spectrometer (EDS, Oxford Instruments INCA Energy 350). Sample prepared from the heat-treated structure was imaged also with transmission electron microscope (TEM, JEOL JEM 2010) with EDS (Thermo Scientific Noran Vantage). The sample for TEM studies was prepared by scraping the surface of the heat-treated sample with a surgical blade and applied into a nickel TEM grid with a holey carbon film. The chemical structure of the samples was characterized with FTIR (Bruker Tensor 27) before and after heat treatment. The crystal structure of the heat-treated surface was examined with XRD (Panalytical Empyrean, monochromatized CuK<sub>α</sub> radiation over a range of 20° < 2θ < 60°) using grazing incidence x-ray diffraction measurement (GIXRD) that is specifically intended for thin film characterization.

To determine the optical bandgap for the prepared samples, the absorption spectra were recorded in reflectance mode with a spectrophotometer (Shimadzu UV 3600) equipped with an integrating sphere coated with barium sulphate. Barium sulphate was also used as a reference for reflectance. The spectra were recorded from 800 nm to 220 nm with a 2 nm interval.

## 3. Results and discussion

### 3.1. Microscopy characterizations

SEM pictures (Fig. 1) show the nanowire structure from the exact same area on the zinc surface before and after heat treatment. The scCO<sub>2</sub>-treated surface was composed of nanowires that had grown from individual initiation points into flower-like shapes during the synthesis. This suggests that the nanowire growth was initiated from local zinc dissolution



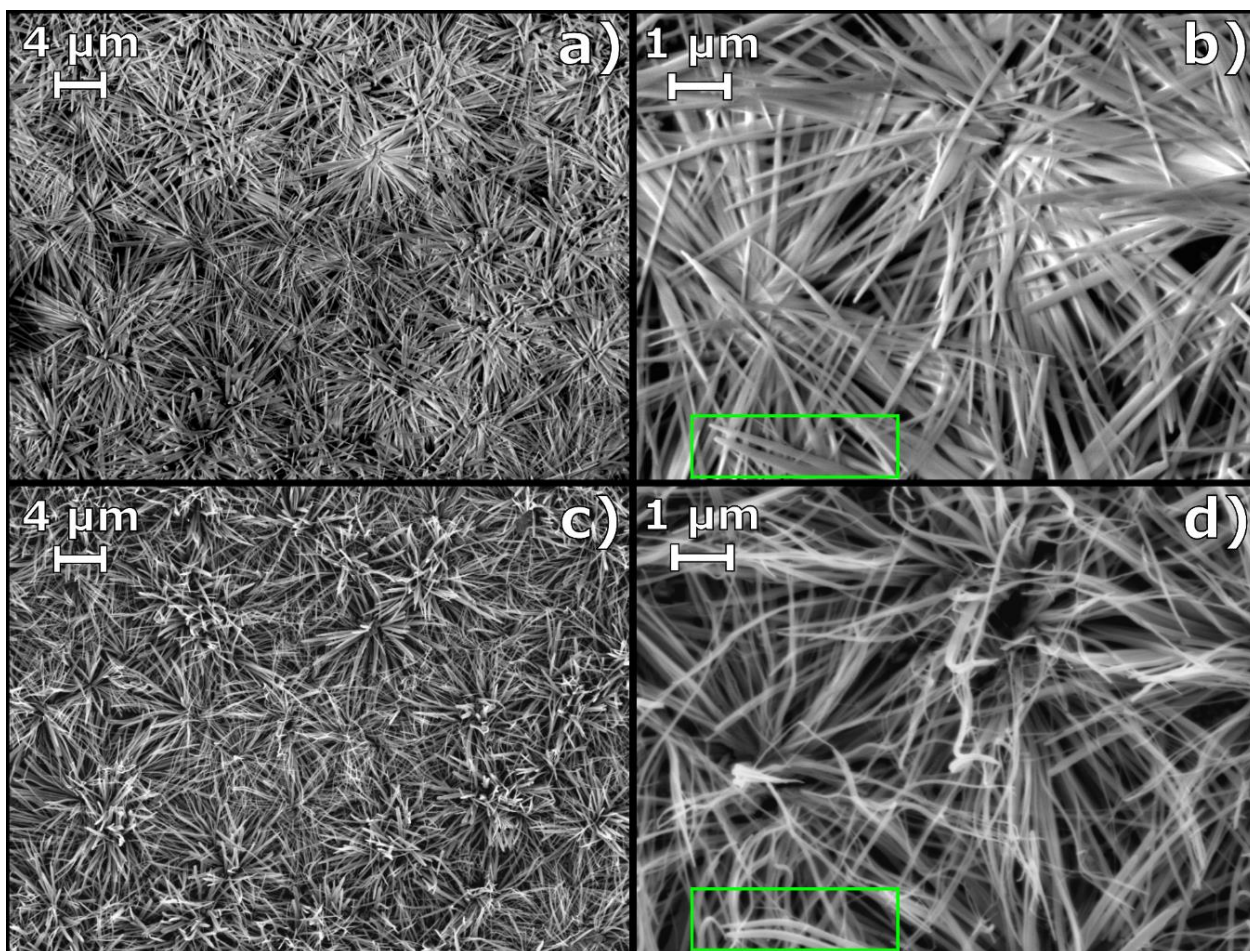


**Figure 1.** SEM pictures of the zinc surface after scCO<sub>2</sub> treatment (a and b) and after post heat treatment (c and d). The highlighted green areas represent the same area on the surface before and after heat treatment.

as a result of pitting corrosion. These pits would serve as initiation points for the structures that eventually grow into full-sized nanoflowers. This is supported by previous studies where a similar dissolution process was used for zinc hydroxycarbonate nanowire synthesis by anodization of pure zinc in carbonate-containing solution [13,26]. In the study by Mah et al., it is shown step-by-step how zinc is first dissolved from distinct areas forming pits on the surface which is then followed by subsequent nanoflower growth [26]. Over time, the amount of pits increase and the nanowires grow in length. These processes eventually lead to excellent surface coverage by the nanowires as can be seen from the SEM pictures.

Figure 1 (c–d) shows the same sample surface before and after the heat treatment. The SEM pictures were taken from the exact same area on the surface to accurately determine the morphology change induced by the heat treatment. Overall, the as-grown nanowires are mostly straight with some of the nanowires exhibiting only slight curving. After the heat treatment, it is evident that the nanowires were bent towards the tips. The green highlighted areas in Figures 1 (b) and 1 (c) were added to further illustrate the differences in two distinct

nanowires that clearly show the bending behavior due to the heat treatment. However, the lower magnification pictures (Fig. 1 (a) and (c)) show that the flower-like pattern of the nanowires has been well preserved. Changes in ZnO nanowire morphology due to heat treatment has also been shown in other studies, although similar bending was not observed [13,26]. The bending can be attributed to the change in the chemical structure of the nanowires from zinc hydroxycarbonate to ZnO.

The reactants that form the nanowires on to the substrate are CO<sub>2</sub>, water and Zn<sup>2+</sup> ions derived from the zinc surface. First, the CO<sub>2</sub> is dissolved in water forming carbonic acid and thus bicarbonate ions (HCO<sub>3</sub><sup>-</sup>) which creates a corrosive atmosphere for the zinc [27]. Simultaneously, water is dissolved into the CO<sub>2</sub> atmosphere due to elevated solvation power of scCO<sub>2</sub> which allows the water to come in contact with the zinc surface [28]. Consequently, the CO<sub>2</sub> saturated water then reacts with the zinc surface gradually forming zinc hydroxide (Zn(OH)<sub>2</sub>) and eventually zinc hydroxycarbonate due to the reaction with hydroxyl and bicarbonate ions. This process is similar to the atmospheric corrosion of zinc that

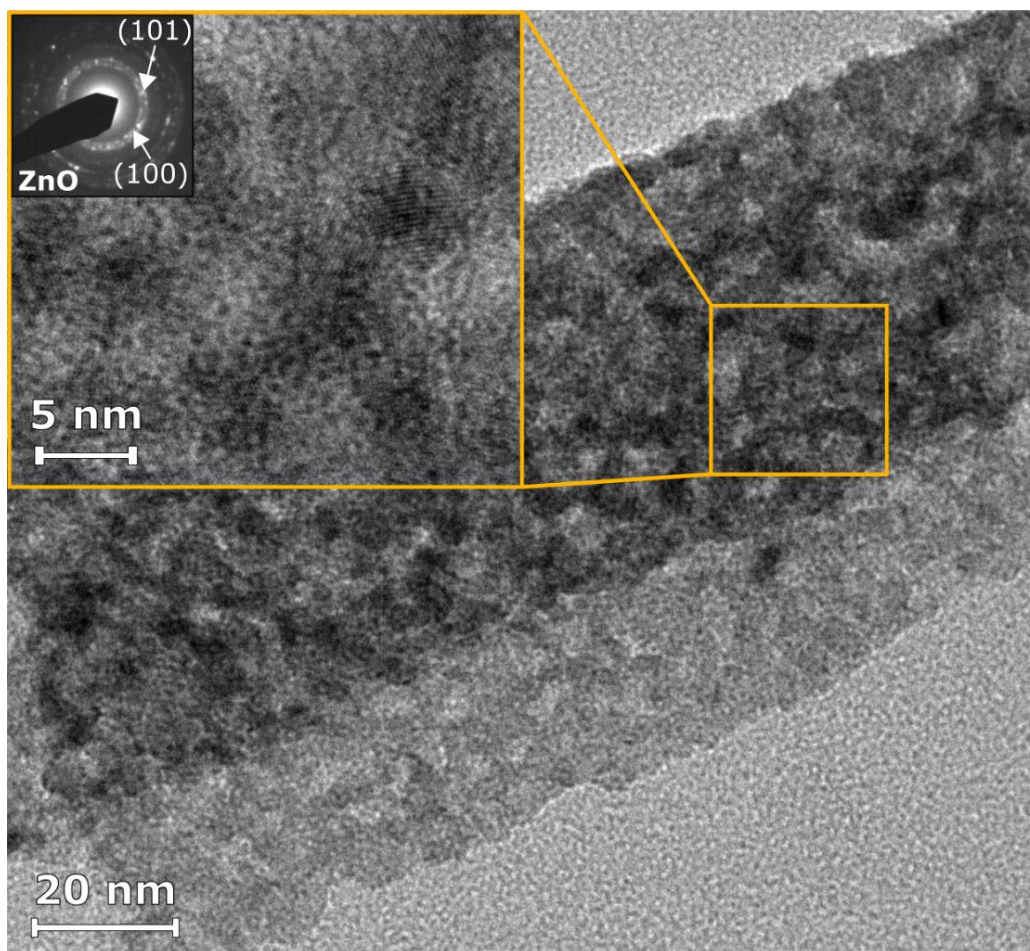


**Figure 2.** TEM image of an individual nanowire from heat-treated surface. Higher magnification picture and the SAED pattern can be seen from the inset.

occurs in nature [27]. This is supported by previous studies which describe a similar reaction sequence in the formation of zinc hydroxycarbonate structures [13,26]. Furthermore, an analogous carbonation reaction in water saturated  $\text{scCO}_2$  has been shown by Loring *et al.* in a study where carbonates were formed on mineral surfaces [25].

The FESEM-EDS measurements (not shown) showed that copper was present on the surface before and after heat treatment. The amount of copper on both surfaces was 1–2 at-%. Copper originated from the catalyst  $\text{Cu}(\text{hfac})_2$  which was chosen due to its high solubility to  $\text{scCO}_2$  as well as the presence of copper ions [29]. It is assumed that during the synthesis, copper ions from the solution are reduced on the surface of zinc as metallic copper due to oxidation of the less-noble zinc. Consequently, more zinc ions dissolve and are readily available for the formation of zinc hydroxycarbonate nanowires. Thus, it is likely that most of the copper is located on the zinc surface below the nanowire structure. This anodic dissolution process increases the surface coverage of the nanowires due to higher amount of free zinc ions compared to reaction without a copper catalyst.

TEM picture (Fig. 2) was taken from the nanowire structure that had been scraped off the heat-treated sample surface. The picture shows an individual needle with a higher magnification of the structure presented in the inset together with a selected area electron diffraction (SAED) pattern taken from the same area. The SAED pattern shows that the needles are ZnO, which agrees well with XRD and FTIR results shown later. Moreover, the SAED pattern and the presence of lattice fringes in the TEM image indicate that the needles are nanocrystalline. In many ZnO nanowire synthesis methods, *i.e.* hydrothermal synthesis, the nanowires are typically single crystalline, smooth walled and hexagonal shaped rods [16]. In this study, the nanowires were polycrystalline with more needle-like morphology and the surface was rougher as can be seen from the TEM picture. Polycrystalline ZnO nanowires have been obtained by other methods as well without any noticeable difference in material properties compared to single-crystalline nanowires [13–15]. The TEM-EDS of individual nanowires showed no presence of copper. This further confirms the notion that the copper ions merely act as a catalyst in the  $\text{scCO}_2$  process and that they are not involved in the growth of the actual nanowire structure.

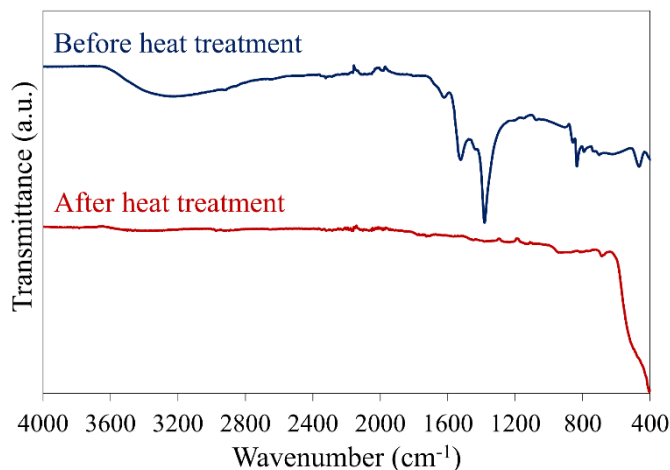


**Figure 3.** FTIR spectra of the surface before and after heat treatment.

### 3.2. Chemical structure determination

The FTIR measurements were taken from the sample surfaces before and after the heat treatment (Fig. 3). In the sample before heat treatment, the presence of hydroxyl-groups are shown by a broad absorption peak between 3200–3300  $\text{cm}^{-1}$  and small peak at 1614  $\text{cm}^{-1}$  [30–32]. Double peak at 1516  $\text{cm}^{-1}$  and 1380  $\text{cm}^{-1}$  is an indication of antisymmetric  $\nu_3$  stretching modes of carbonates which is typical for zinc hydroxycarbonates i.e., hydrozincite [31,33,34]. Peaks at 865  $\text{cm}^{-1}$ , 835  $\text{cm}^{-1}$  and 740  $\text{cm}^{-1}$  are assigned to carbonate bending [30,31,35]. Moreover, a peak at 1076  $\text{cm}^{-1}$  is present and it could be representative of carbonate  $\nu_1$  stretching which usually is IR inactive [31,34,35]. However, Hales et al. stated that distortion can induce reduction of symmetry that makes the IR peak visible [31]. This observation would be consistent with the fact that the zinc hydroxycarbonate structure synthesized here is not identical, although similar, to hydrozincite found in literature [31,34,35]. Zinc hydroxycarbonates can occur with different ratios of zinc, carbonate and hydroxyl groups which causes distortion in the lattice structure when compared with hydrozincite [17,34,36]. Consequently, it is likely that the nanowires formed in the  $\text{scCO}_2$  treatment are composed of a zinc hydroxycarbonate that is not specifically hydrozincite.

The spectrum after the heat treatment shows mostly a straight line with one peak below 400  $\text{cm}^{-1}$  that goes out of the measuring range. This can be attributed to ZnO [37,38]. This dramatic change in the surface chemical structure during the heat treatment is due to the release of  $\text{CO}_2$  and  $\text{H}_2\text{O}$  from the zinc hydroxycarbonate structure. The nanowires are gradually converted into ZnO due to the elevated temperature [13]. The decomposition process of zinc hydroxycarbonates follows the decomposition of hydrozincite which is presented in equation (1) [39].

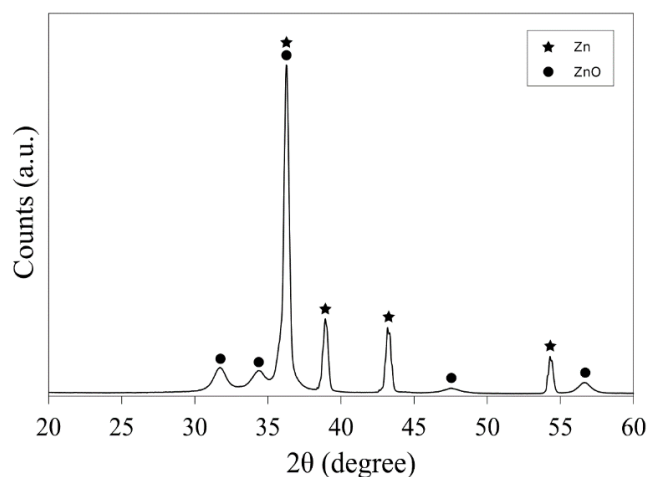
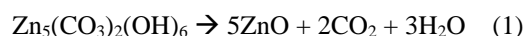


**Figure 4.** GIXRD spectrum of the heat treated surface.



The presence of ZnO on the heat-treated surface was confirmed by GIXRD measurement. The spectrum of the heat-treated nanowire surface is presented in Fig. 4. Most of the peaks correspond well with JCPDS (Joint Committee on Powder Diffraction Standard) card number 36-1451 for wurtzite ZnO. The remaining three peaks at 39, 43 and 54 are due to metallic zinc (JCPDS 01-078-9363) originating from the substrate below the nanowires. This is because the x-rays can still penetrate through the topmost layer in GIXRD measurements as has been shown by other studies as well [40,41].

### 3.3. Bandgap measurements

The measurements for bandgap determination of the surfaces are presented in Fig. 5. The absorption spectra show rather high background absorption with a value of approximately 0.8. This arises from the relative difference of reflectance of the sample and the barium sulphate reference. The heat-treated film has steep cut-off at approximately 380 nm, while, the film before heat treatment does not show any cut-off in absorption.

The optical bandgap was determined by using the Tauc plot [42]. In ZnO the transition from valence band to the conduction band is direct and allowed. Thus, in the Tauc plot  $(\alpha h\nu)^2$  was drawn as a function of energy. In the calculation,  $\alpha$  is absorbance,  $h$  is the Planck constant, and  $\nu$  is frequency. Linear fit was applied to the part, which corresponds the rise in the absorption spectrum at the optical cut-off. Due to high background absorption, the bandgap was determined from the crossing point of the linear fit at the optical cut-off and the linearly fitted baseline, as shown in the inset of Fig. 5. This

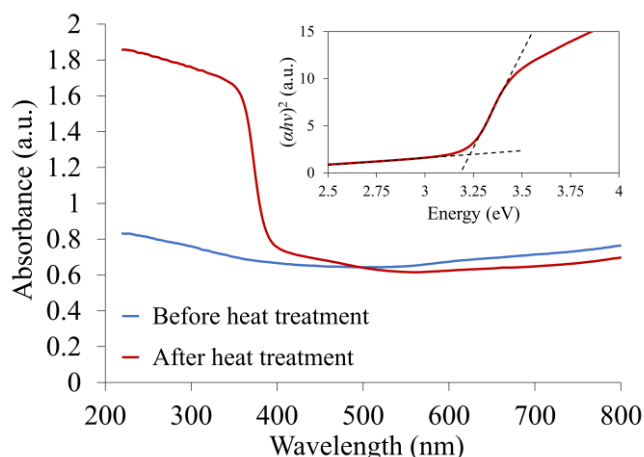


**Figure 5.** The absorption spectra for the samples measured in reflectance mode. The Tauc plot for the heat-treated film is shown in the inset.

will give the value of 3.23 eV for the optical bandgap which was lower than normally reported for ZnO [43]. No bandgap was observed for the sample before heat-treatment within the measuring range.

Compared to other ZnO structures the bandgap had been slightly lowered from 3.37 eV to 3.23 eV [1,3]. The TEM investigations showed no presence of copper within the nanowires which indicates that the narrowed bandgap is not a consequence of doping atoms from the precursor. It is more likely that the narrowing is due to structural changes and specifically size-dependance of nanowires in relation to bandgap. Several studies indicate that the bandgap in nanowire structures can change as the diameter of the nanowire changes [44–46]. Narrowing of the ZnO bandgap is beneficial especially in photocatalytic applications or tuning the emitting properties of light emitting diodes [47–49].

#### 4. Conclusions

ZnO nanowires were synthesized on a zinc surface with the use of supercritical carbon dioxide and a precursor solution consisting of water and a  $\text{Cu}^{2+}$  based catalyst. The synthesis method was rapid, environmentally friendly and facile compared to common ZnO synthesis techniques. A dissolution-induced reaction between the reactants resulted in the growth of zinc hydroxycarbonate nanowires that could be then heat-treated into nanocrystalline ZnO nanowires. The nanowires were arranged into nanoflowers and had excellent coverage of the galvanized surface. Copper was found on the sample surfaces but not from individual nanowires which suggests that the sole purpose of the copper ions is to catalyze the reaction. The heat treatment resulted in slight bending towards the tips of the nanowires due to material loss from the nanowires. The bandgap of the ZnO surface was slightly narrowed (3.23 eV) compared to bulk ZnO (3.37 eV). This research showed initial results for producing functional ZnO

nanowires with  $\text{scCO}_2$  treatment and post heat treatment. However, further research is required regarding the influence of processing parameters on the morphology and functional properties of the ZnO nanowires.

#### Acknowledgements

This work was supported by Academy of Finland project: Green processing of functional surface by supercritical carbon dioxide (decision no. 304782). SSAB Oy Europe is also acknowledged for their support.

#### References

- [1] Kolodziejczak-Radzimska A and Jesionowski T 2014 Zinc oxide—from synthesis to application: A review *Materials (Basel)*. **7** 2833–81
- [2] Heinonen S, Kannisto M, Nikkanen J-P, Huttunen-Saarivirta E, Karp M and Levänen E 2016 Photocatalytic and antibacterial properties of ZnO films with different surface topographies on stainless steel substrate *Thin Solid Films* **616** 842–9
- [3] Wang Z L 2004 Zinc oxide nanostructures: Growth, properties and applications *J. Phys. Condens. Matter* **16** 829–58
- [4] Nikkanen J-P, Heinonen S, Huttunen-Saarivirta E, Honkanen M and Levänen E 2013 Photocatalytically active titanium dioxide nanopowders: Synthesis, photoactivity and magnetic separation *IOP Conf. Ser. Mater. Sci. Eng.* **47** 012066
- [5] Nikkanen J-P, Huttunen-Saarivirta E, Salminen T, Hyvärinen L, Honkanen M, Isotahdon E, Heinonen S and Levänen E 2015 Enhanced photoactive and photoelectrochemical properties of  $\text{TiO}_2$  sol-gel coated steel by the application of  $\text{SiO}_2$  intermediate layer *Appl. Catal. B Environ.* **174–175** 533–43
- [6] Nikkanen J-P, Kanerva T, Pore V, Kivelä T, Levänen E and Mäntylä T 2011 Photoactive  $\text{TiO}_2$ , nanopowder synthesized at low temperature without a catalyst *J. Ceram. Sci. Technol.* **102** 97–102
- [7] Heinonen S, Nikkanen J-P, Kaleva A, Hyvärinen L and Levänen E 2017 Structured ZnO films: Effect of copper nitrate addition to precursor solution on topography, band gap energy and photocatalytic activity *IOP Conf. Ser. Mater. Sci. Eng.* **175** 012042
- [8] Djurišić A B, Chen X, Leung Y H and Man Ching Ng A 2012 ZnO nanostructures: growth, properties and applications *J. Mater. Chem.* **22** 6526
- [9] Cuevas A G, Balangcod K, Balangcod T and Jasmin A 2013 Surface morphology, optical properties and antibacterial activity of zinc oxide films synthesized via spray pyrolysis *Procedia Eng.* **68** 537–43
- [10] Khan A and Kordesch M E 2005 Effect of substrate temperature on the growth and luminescence properties of ZnO nanostructures *Phys. E Low-Dimensional Syst. Nanostructures* **30** 51–54
- [11] Ito Y, Sakai O and Tachibana K 2010 Study of plasma enhanced chemical vapor deposition of ZnO films by non-thermal plasma jet at atmospheric pressure *Thin Solid Films* **518** 3513–6
- [12] Saarenpää H, Sariola-Leikas E, Pyymäki Perros A, Kontio J M, Efimov A, Hayashi H, Lipsanen H, Imahori H, Lemmetyinen H and Tkachenko N V. 2012 Self-assembled

- porphyrins on modified zinc oxide nanorods: Development of model systems for inorganic-organic semiconductor interface studies *J. Phys. Chem. C* **116** 2336–43
- [13] Miles, David O. Mattia D 2015 Hierarchical 3D ZnO nanowire structures via fast anodization of zinc *J. Mater. Chem. A* **3** 17569–77
- [14] Hu Z, Chen Q, Li Z, Yu Y and Peng L-M 2010 Large-scale and rapid synthesis of ultralong ZnO nanowire films via anodization *J. Phys. Chem. C* **114** 881–9
- [15] Zaraska L, Mika K, Hnida K E, Gajewska M, Lojewski T, Jaskuła M and Sulka G D 2017 High aspect-ratio semiconducting ZnO nanowires formed by anodic oxidation of Zn foil and thermal treatment *Mater. Sci. Eng. B* **226** 94–8
- [16] Heinonen S, Nikkanen J-P, Hakola H, Huttunen-Saarivirta E, Kannisto M, Hyvärinen L, Järveläinen M and Levänen E 2016 Effect of temperature and concentration of precursors on morphology and photocatalytic activity of zinc oxide thin films prepared by hydrothermal route *IOP Conf. Ser. Mater. Sci. Eng.* **123** 012030
- [17] Veleva L, Acosta M and Meraz E 2009 Atmospheric corrosion of zinc induced by runoff *Corros. Sci.* **51** 2055–62
- [18] Kaleva A, Saarimaa V, Heinonen S, Nikkanen J-P, Markkula A, Väisänen P and Levänen E 2017 Dissolution-Induced Nanowire Synthesis on Hot-Dip Galvanized Surface in Supercritical Carbon Dioxide *Nanomaterials* **7** 181
- [19] Saarimaa V, Kaleva A, Nikkanen J-P, Heinonen S, Levänen E, Väisänen P, Markkula A and Juhanoja J 2017 Supercritical carbon dioxide treatment of hot dip galvanized steel as a surface treatment before coating *Surf. Coatings Technol.* **331** 137–42
- [20] Saarimaa V, Kaleva A, Paunikallio T, Nikkanen J-P, Heinonen S, Levänen E, Väisänen P and Markkula A 2018 Convenient extraction method for quantification of thin zinc patina layers *Surf. Interface Anal.* **50** 564–70
- [21] Kaleva A, Heinonen S, Nikkanen J-P and Levänen E 2017 Synthesis and crystallization of titanium dioxide in supercritical carbon dioxide (scCO<sub>2</sub>) *IOP Conf. Ser. Mater. Sci. Eng.* **175** 012034
- [22] Zhang X, Heinonen S and Levänen E 2014 Applications of supercritical carbon dioxide in materials processing and synthesis *RSC Adv.* **4** 61137–52
- [23] Choi Y S and Nešić S 2011 Determining the corrosive potential of CO<sub>2</sub> transport pipeline in high pCO<sub>2</sub>-water environments *Int. J. Greenh. Gas Control* **5** 788–97
- [24] Cole I S, Paterson D A, Corrigan P, Sim S and Birbilis N 2012 State of the aqueous phase in liquid and supercritical CO<sub>2</sub> as relevant to CCS pipelines *Int. J. Greenh. Gas Control* **7** 82–8
- [25] Loring J S, Thompson C J, Wang Z, Joly A G, Sklarew D S, Schaefer H T, Ilton E S, Rosso K M and Felmy A R 2011 In situ infrared spectroscopic study of forsterite carbonation in wet supercritical CO<sub>2</sub> *Environ. Sci. Technol.* **45** 6204–10
- [26] Mah C F, Beh K P, Yam F K and Hassan Z 2016 Rapid Formation and Evolution of Anodized-Zn Nanostructures in NaHCO<sub>3</sub> Solution *ECS J. Solid State Sci. Technol.* **5** M105–12
- [27] Zhang X G 1996 *Corrosion and Electrochemistry of Zinc* (Boston, MA: Springer US)
- [28] Spycher N, Pruess K and Ennis-King J 2003 CO<sub>2</sub>-H<sub>2</sub>O mixtures in the geological sequestration of CO<sub>2</sub>. I. Assessment and calculation of mutual solubilities from 12 to 100°C and up to 600 bar *Geochim. Cosmochim. Acta* **67** 3015–31
- [29] Garriga R, Pessey V, Weill F, Chevalier B, Etourneau J and Cansell F 2001 Kinetic study of chemical transformation in supercritical media of bis(hexafluoroacetylacetonate)copper (II) hydrate *J. Supercrit. Fluids* **20** 55–63
- [30] Su B, Li M, Shi Z and Lu Q 2009 From superhydrophilic to superhydrophobic: Controlling wettability of hydroxide zinc carbonate film on zinc plates *Langmuir* **25** 3640–5
- [31] Hales M C and Frost R L 2007 Synthesis and vibrational spectroscopic characterisation of synthetic hydrozincite and smithsonite *Polyhedron* **26** 4955–62
- [32] Mahjoubi F Z, Khalidi A, Abdennouri M and Barka N 2017 Zn–Al layered double hydroxides intercalated with carbonate, nitrate, chloride and sulphate ions: Synthesis, characterisation and dye removal properties *J. Taibah Univ. Sci.* **11** 90–100
- [33] Lindström D and Odnevall Wallinder I 2011 Long-term use of galvanized steel in external applications. Aspects of patina formation, zinc runoff, barrier properties of surface treatments, and coatings and environmental fate *Environ. Monit. Assess.* **173** 139–53
- [34] Jambor J L 1964 Studies of basic copper and zinc Carbonates: I-synthetic zinc carbonates and their relationship to hydrozincite *Can. minearalogist* **8** 92–108
- [35] Cheng J and Poduska K 2013 A Strategy for hydroxide exclusion in nanocrystalline solid-state metathesis products *Nanomaterials* **3** 317–24
- [36] Sahli M 1956 *Über die Basischen zinkcarbonate*. (Bern University)
- [37] Ramimoghdam D, Hussein M Z Bin and Taufiq-Yap Y H 2013 Synthesis and characterization of ZnO nanostructures using palm olein as biotemplate *Chem Cent J* **7** 71–81
- [38] Becheri A, Dürr M, Lo Nostro P and Baglioni P 2008 Synthesis and characterization of zinc oxide nanoparticles: Application to textiles as UV-absorbers *J. Nanoparticle Res.* **10** 679–89
- [39] Liu Y, Zhao J, Zhang H, Zhu Y and Wang Z 2004 Thermal decomposition of basic zinc carbonate in nitrogen atmosphere *Thermochim. Acta* **414** 121–3
- [40] Sato M, Kimura M, Yamashita M, Konishi H, Fujimoto S, Tabira Y, Doi T, Kamimura T, Nagoshi M, Suzuki S, Nakayama T and Ohtsuka T 2006 Atomic-Structure Characterization of Passive Film of Fe by Grazing Incidence X-ray Scattering at SPring-8 *Passivation of Metals and Semiconductors, and Properties of Thin Oxide Layers* (Elsevier) pp 95–100
- [41] Parellada-Monreal L, Castro-Hurtado I, Martínez-Calderón M, Rodríguez A, Olaizola S M, Gamarra D, Lozano J and Mandayo G G 2018 Study of sputtered ZnO modified by Direct Laser Interference Patterning: Structural characterization and temperature simulation *Appl. Surf. Sci.* **441** 331–40
- [42] Tauc J, Grigorovici R and Vancu A 1966 Optical Properties and Electronic Structure of Amorphous Germanium *Phys. status solidi* **15** 627–37
- [43] Samarasekera P and Wijesinghe U 2017 Optical properties of spin coated Cu doped ZnO nanocomposite films *Georg. Electron. Sci. Journals Phys.* **2** 41–50

- [44] Wei B, Zheng K, Ji Y, Zhang Y, Zhang Z and Han X 2012 Size-dependent bandgap modulation of zno nanowires by tensile strain *Nano Lett.* **12** 4595–9
- [45] Nolan M, O'Callaghan S, Fagas G, Greer J C and Frauenheim T 2007 Silicon nanowire band gap modification *Nano Lett.* **7** 34–8
- [46] Wang B, Zhao J, Jia J, Shi D, Wan J and Wang G 2008 Structural, mechanical, and electronic properties of ultrathin ZnO nanowires *Appl. Phys. Lett.* **93** 2006–9
- [47] Kumar J and Kumar Srivastava A 2014 Band gap narrowing in zinc oxide-based semiconductor thin films *J. Appl. Phys.* **115**
- [48] Srikant V and Clarke D R 1998 On the optical band gap of zinc oxide *J. Appl. Phys.* **83** 5447–51
- [49] Wang J P, Wang Z Y, Huang B B, Ma Y D, Liu Y Y, Qin X Y, Zhang X Y and Dai Y 2012 Oxygen Vacancy Induced Band-Gap Narrowing and Enhanced Visible Light Photocatalytic Activity of ZnO *ACS Appl. Mater. Interfaces* **4** 4024–30

# PUBLICATION III

## **Supercritical carbon dioxide treatment of hot dip galvanized steel as a surface treatment before coating**

V. Saarimaa, A. Kaleva, J.-P. Nikkanen, S. Heinonen, E. Levänen, P. Väisänen, M.  
Markkula, J. Juhanoja

Surface & Coatings Technology, Vol. 331, pp. 137 – 142  
<https://doi.org/10.1016/j.surfcoat.2017.10.047>

**Publication reprinted with the permission of the copyright holders.**







## Supercritical carbon dioxide treatment of hot dip galvanized steel as a surface treatment before coating



Ville Saarimaa<sup>a,\*</sup>, Aaretti Kaleva<sup>b</sup>, Juha-Pekka Nikkanen<sup>b</sup>, Saara Heinonen<sup>b</sup>, Erkki Levänen<sup>b</sup>, Pasi Väisänen<sup>c</sup>, Antti Markkula<sup>c</sup>, Jyrki Juhanoja<sup>a</sup>

<sup>a</sup> Top Analytica Oy, Ruukinkatu 4, FI-20540 Turku, Finland

<sup>b</sup> Laboratory of Materials Science, Tampere University of Technology, FI-33101 Tampere, Finland

<sup>c</sup> SSAB Europe Oy, Harvialantie 420, FI-13300 Hämeenlinna, Finland

### ARTICLE INFO

#### Keywords:

Hot dip galvanized steel  
Zinc  
Patina  
Supercritical carbon dioxide  
Coatings  
Corrosion resistance  
Basic zinc carbonate

### ABSTRACT

Supercritical carbon dioxide (scCO<sub>2</sub>) treatment was employed for rapid formation of a zinc patina layer on hot dip galvanized (HDG) steel. In the presence of H<sub>2</sub>O and a Cu precursor, an artificial patina consisting of two distinctive phases was formed: a dense ~1 μm layer of anhydrous ZnCO<sub>3</sub> adjacent to native zinc coating, and a needle-like porous structure showing resemblance to hydrozincite (Zn<sub>5</sub>(CO<sub>3</sub>)<sub>2</sub>(OH)<sub>6</sub>). The artificial patina layer significantly decreased the surface free energy of HDG, which was evidenced also by good wettability by a polyester melamine coating. Furthermore, the needle-like patina surface structure stayed intact through the coating process, indicating improved coating adhesion. ScCO<sub>2</sub> treatment facilitates rapid and impurity-free surface treatment of hot dip galvanized steel, and could be used to tailor novel adhesion and corrosion promoting surface morphologies.

### 1. Introduction

Hot dip galvanized (HDG) steel is a widely used raw material in façades, roofings and other construction elements. Corrosion resistance and aesthetical properties of HDG steel elements are typically improved by organic coatings [1]. Coating can take place in a continuous color coating line, by post-painting the material in a machine workshop or at the end use site after installation. It is known that a certain degree of weathering is required for outdoor elements prior to coating in order to bring about good adhesion between the paint and the metal surface [1–3]. For example, coating of HDG roofings may take place a couple of years after the installation. Atmospheric corrosion is an aqueous process driven by electrochemical mechanisms [4]. A fresh hot dip galvanized zinc surface is very prone to react with the surrounding environment. Zinc oxide and hydroxide are the first corrosion products to appear on a galvanized surface [1,2,5]. In the presence of CO<sub>2</sub> and H<sub>2</sub>O, these initial corrosion products are slowly converted to stable basic zinc carbonates [1,5]. The formed patina layer electrochemically stabilizes the zinc surface, forming a compact passivation layer that inhibits Zn<sup>2+</sup> dissolution [6]. Hydrozincite, Zn<sub>5</sub>(CO<sub>3</sub>)<sub>2</sub>(OH)<sub>6</sub>, is the main corrosion product formed in long-term outdoor exposure when little contaminants are present [7–11]. Hydrozincite is generally considered to be responsible of the improved adhesion and corrosion protection

properties for coated galvanized material [1–3]. In outdoor exposure, however, the formed patina layer is often composed of a mixture of zinc corrosion products, depending on the ions (such as Cl<sup>−</sup> and SO<sub>4</sub><sup>2−</sup>) that are present [12–14]. Due to impurities, weathered galvanized surfaces also require cleaning prior to coating [15]. The cleaning process removes some of the zinc coating [16]. Furthermore, most of the corroded Zn is removed from the patina layer by runoff water, decreasing the functional life of the product [13]. In a recent study, average annual runoff rate for a hot dip galvanized zinc coating in rural atmosphere was about 0.29 μm, while the average corrosion rate was 0.46 μm [17]. The runoff rates vary a lot depending on the local conditions [18].

Treatments of Zn in supercritical CO<sub>2</sub> (scCO<sub>2</sub>) in the presence of H<sub>2</sub>O have recently been reported, mainly since the formation of ZnO nanoparticles is of great interest because of the photoelectric properties of nanodimensional ZnO material [19,20]. In such conditions, formation of basic zinc carbonates has been reported [19]. The partial pressure of CO<sub>2</sub> readily affects the formation of zinc corrosion products [21–23], and the presence of H<sub>2</sub>O enhances the mobility of ions and has a corrosion promoting effect [14,24]. Partial dissolution of CO<sub>2</sub> in H<sub>2</sub>O also decreases the pH [20]. Also, atmospheric corrosion is enhanced by the presence of CO<sub>2</sub> due to acidification of the surface electrolyte [21,22].

Synthesis of a patina layer, composed of reaction products of

\* Corresponding author.

E-mail address: [ville.saarimaa@topanalytica.com](mailto:ville.saarimaa@topanalytica.com) (V. Saarimaa).

zinc in the presence of  $H_2O$  and  $scCO_2$  on HDG steel, was recently reported by Kaleva et al. [25]. In that study, the patina was characterized as zinc hydroxy carbonate nanowires. In this study, a more uniform patina growth was aspired by using a  $Cu(hfac)_2$  (copper (II) hexafluoroacetylacetonate hydrate) precursor solution in  $H_2O/EtOH$  (40/60 vol%). The precursor was used to enhance the reaction by increasing the amount of zinc ions to be available for the formation of patina structures through anodic dissolution.  $Cu(hfac)_2$  was used for its good solubility to  $scCO_2$ , and  $EtOH$  was used to dissolve the precursor and further increase solubility of water to  $scCO_2$  [26,27]. The main goal of this study was to investigate  $scCO_2$  treatment of HDG sheets as a surface treatment before coating. The layer of Zn corrosion products formed by  $scCO_2$  treatment was named artificial patina in order to distinguish it from weathered HDG samples (naturally forming patina). The artificial patina was characterized by SEM imaging, and FTIR and XPS measurements. The surface properties ( $H_2O$  contact angle and surface free energy (Sfe) measurements) were evaluated and some samples were coated in order to study the paintability.

## 2. Materials and methods

Hot dip galvanized material (~0.2% Al in the zinc bath) with a total coating mass of  $275 \text{ g Zn/m}^2$  from SSAB Europe Oy was used. A mild alkaline cleaning of the HDG samples was performed according to the guidelines of the cleaning chemical provider (Gardoclean 338, Chemetall) before the  $scCO_2$  treatment. The outdoor exposed HDG sheets had the same Zn coating weight and composition as the fresh HDG material. The outdoor exposure was carried out in Southern Finland in unsheltered inland conditions for 6 years. The polyester melamine primer (Becker Industrial Coatings Ltd.) and top coat (The Valspar Finland Corporation Oy) were applied in the laboratory by bar coating. The applied coatings were cured in a laboratory oven (model H12-850AA, Aalborg Company). The PMT (peak metal temperature) values were  $228 \text{ }^\circ\text{C}$  for the primer and  $230 \text{ }^\circ\text{C}$  for the top coat, and the dry film thicknesses were  $6 \mu\text{m}$  for the primer and  $20 \mu\text{m}$  for the top coat.

The  $scCO_2$  treatment was performed in a cylindrical vessel (height 11 cm, diameter 5.4 cm, volume  $256 \text{ cm}^3$ ). A HDG sample ( $5 \times 10 \text{ cm}$ ) was placed in the vessel, and the vessel was pressurized to 300 bar with  $CO_2$  ( $\geq 97\%$ , AGA). A co-solvent pump was utilized to introduce a precursor solution consisting of 0.5 mass%  $Cu(hfac)_2$  (copper (II) hexafluoroacetylacetonate hydrate, Sigma-Aldrich) in 5 ml of deionized  $H_2O/EtOH$  (40/60 vol%) to enhance the dissolution of zinc from the surface of HDG sample. The reaction was carried out for 60 min at  $50 \text{ }^\circ\text{C}$ .

Contact angle (CA) measurements were performed using a CAM 200 Optical Contact Angle Meter (KSV Instruments Ltd). Three liquids (water, ethylene glycol and diiodomethane) were used and the Sfe (surface free energy) was calculated according to the Wu method. Scanning electron microscopy (SEM) characterization was performed using a JEOL JSM-6335F instrument. Preparation of cross sections was carried out at with an Ilion + Advantage Precision Cross-Section System (Model 693, Gatan Inc., USA). Element analysis was performed using X-ray photoelectron spectroscopy (XPS) (PHI Quantum 2000). The spectra were obtained using monochromated Al  $K\alpha$  beam (50 W, 15 kV) with a  $200 \mu\text{m}$  spot size. The survey spectra were measured at 117.4 eV pass energy and 1.0 eV step size, while the C1s spectra were measured at 46.95 eV pass energy and 0.2 eV step size. Sputtering was performed with  $Ar^+$ -ions, and the sputtering depth was calculated using a  $SiO_2$  reference sample. The C1s peak at 285.0 eV was used for charge-shift correction. Several spectra on different spots on the sample were recorded to confirm the findings. The FTIR measurements were performed with Bruker Vertex 70 instrument at the Materials Chemistry Group at the University of Turku. The sample holder was Harrick Diamond ATR, and the spectra were recorded with a RT-LaTGS detector yielding a  $4 \text{ cm}^{-1}$  resolution. The number of scans for each spectrum

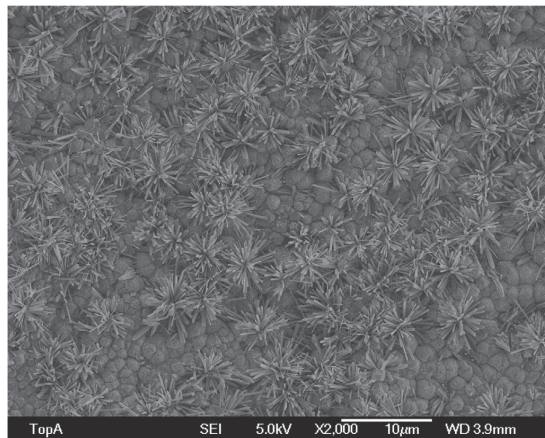


Fig. 1. Top view of the artificial patina on a HDG sample.

was 64, and the wavelength area was  $4500\text{--}450 \text{ cm}^{-1}$ . The samples for FTIR measurements were collected by gently scraping off material from the patina surface with a stainless steel surgical blade (Paragon).

## 3. Results

### 3.1. SEM imaging of artificial patina

Two distinctive structures could be observed on the HDG surface after  $scCO_2$  treatment (Fig. 1). Firstly, flowers composed of needle-like structures were seen. Secondly, a granular surface structure was present. Cross section imaging confirmed the presence of the two structures (Fig. 2). The dense patina layer seemed to cover the whole surface and occupied a thickness of about  $1 \mu\text{m}$ , while the needle-formed structures (or flowers) stretched out from the surface forming a several  $\mu\text{m}$  thick porous surface on top of the dense patina layer. In the cross section image, a somewhat nodular structure was observed (Fig. 2). Growth of the patina initiates from distinct points on the surface, and through further growth it spreads across the surface sealing the metal surface. The structures continue growing in multiple directions while spreading, which leads to thickening of the structure at the initiation points. As a consequence, the layer thickness may not be homogeneous.

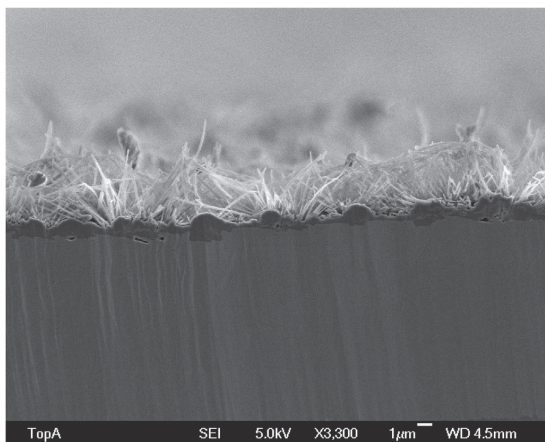


Fig. 2. Cross section of a HDG sample after  $scCO_2$  treatment.

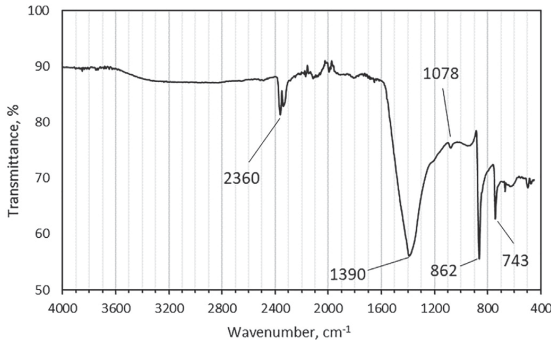


Fig. 3. FTIR spectrum of the dense patina layer.

Also in atmospheric conditions, zinc patina has been reported to have a compact inner layer and a porous outer layer [28]. However, similar extensively protruding outer layer structures that were obtained in the scCO<sub>2</sub> treatment have not been reported for outdoor exposure samples. Thin needle-shaped mineral crystals occur rarely in natural zinc deposits [8]. Needle-like structures (or nanotubes) have been obtained by supercritical CO<sub>2</sub> fluid treatment of zinc sputtered on glass substrate [29]. In the presence of H<sub>2</sub>O, nanotubes with a diameter of 30–50 nm were grown from the surface at 60 °C. Similarly, Miles et al. [30] obtained nanoflowers as a result of anodization of zinc in the presence of KHCO<sub>3</sub>.

### 3.2. FTIR and XPS measurements

FTIR measurements showed that the visually different forms of artificial patina were also chemically different (Figs. 3 and 4). The both patina forms had a double peak at ~2360 cm<sup>-1</sup>, which is attributed to adsorbed CO<sub>2</sub>. The dense patina layer showed stretching bands representative of carbonate vibrations: 1390 cm<sup>-1</sup> ( $\nu_3$  CO<sub>3</sub><sup>2-</sup> antisymmetric stretching vibration), and sharp bands at ~862 cm<sup>-1</sup> ( $\nu_2$  mode of CO<sub>3</sub><sup>2-</sup>) and ~743 cm<sup>-1</sup> ( $\nu_4$  in phase bending mode) (Fig. 3) [13,31]. The dense patina layer was composed of an anhydrous zinc carbonate because of the single strong absorption band at about 1400 cm<sup>-1</sup> and absence of OH bands [9]. The result is interesting, since anhydrous ZnCO<sub>3</sub> is difficult to prepare and it is not present in naturally forming patina of outdoor exposure samples [10,11].

For the needle-like structure, the band at ~3230 cm<sup>-1</sup> is typical for hydrozincite (Fig. 4). Basic zinc carbonates always contain some adsorbed water, and the stretching band at 3230 cm<sup>-1</sup> is related to OH stretching of molecular water [8,14,17]. The band at 1618 cm<sup>-1</sup> is representative of the OH bending [32]. The weak band at 1078 cm<sup>-1</sup> is

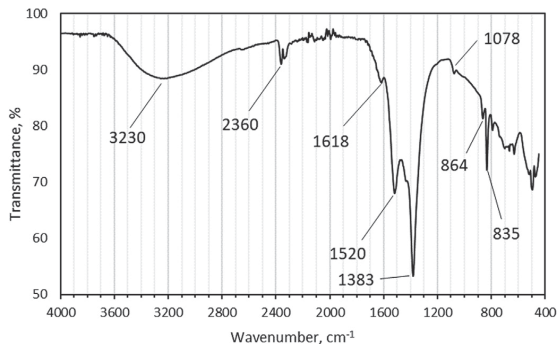


Fig. 4. FTIR spectrum of the needle-like patina layer.

attributed to the (CO<sub>3</sub>)<sup>2-</sup>  $\nu_1$  band, which should not be infrared active but has proposed to become activated because of distortion caused reduction in the symmetry of the carbonate [23]. The band at 1078 cm<sup>-1</sup> was present in both patina structures. In hydrozincite, a weak peak at ~953 cm<sup>-1</sup> is typically present, indicating the metal-hydroxide deformation [11,33]. In the needle-formed patina spectrum, however, this deformation was missing. Two bands at 1520 and 1383 cm<sup>-1</sup> ( $\nu_3$  modes of carbonate) were observed for the needle-like structure. For basic zinc carbonates, twin maxima appear near 1400 cm<sup>-1</sup> that are attributed to CO<sub>3</sub><sup>2-</sup> groups [9,33,34]. In some studies, the splitting of the  $\nu_3$  into two bands has been shown to depend on the synthesis of Zn<sub>5</sub>(OH)<sub>6</sub>(CO<sub>3</sub>)<sub>2</sub> [35]. The presence of a bending mode at 835 cm<sup>-1</sup> ( $\nu_2$  mode of CO<sub>3</sub><sup>2-</sup>) showed resemblance to basic zinc hydrocarbonate structures [35]. Two typical internal vibration assignments for carbonate at 707 and 743 cm<sup>-1</sup> ( $\nu_4$  antisymmetric OCO bending mode) were present to a very low extent [13,35,36]. The spectrum of needle-like patina showed more resemblance to synthetic hydrozincites than hydrozincites formed in outdoor exposure [17,37]. Many forms of synthetic zinc hydrocarbonates have been reported, the reaction routes are complex and the proportions of adsorbed and structurally bound water or hydroxyl are difficult to determine [8–10,23,30,38]. Zincite (ZnO) is typically present in exposed HDG sheets [7,13]. ZnO (~450 cm<sup>-1</sup>) was not detected in the FTIR spectra of the dense patina or needle-like patina (Figs. 3 and 4).

Zinc, oxygen and carbon were identified on the patina surface by XPS (Fig. 5). Aluminum oxide is typically found in trace amounts on the surface of hot dip galvanized coatings [39]. Contrary to our previous study, aluminum was not observed here, which is an indication that a better surface coverage was obtained with the use of a precursor [25]. Furthermore, the patina surface was free of impurities (other than carbon contamination), and elements present in the precursor solution (Cu and F) were not found. The carbon signal in the C1s spectra was divided into two peaks (Fig. 6). The peak at lower binding energy (285.0 eV) disappeared after mild sputtering, which is typical for carbon contamination. The peak at higher binding energy, 290.0 eV, remained after sputtering. The binding energy shift of this magnitude between the CC/CH and COO<sup>-</sup> has been observed, when the carboxyl component is involved in hydrogen bonding [40]. The result confirms the formation of carbonates during the scCO<sub>2</sub> treatment [30,41–43].

### 3.3. Reaction routes to artificial patina formation

For formation of basic zinc carbonates on a galvanized surface, presence of zinc ions is required. Zinc ions could be released by (i) electrochemical anodization of zinc, (ii) introducing metal ions that are more noble than zinc, e.g. copper used in this study (reduction-oxidation reaction), (iii) chemically dissolving zinc or (iv) by adding a zinc precursor such as zinc acetate [20,30].

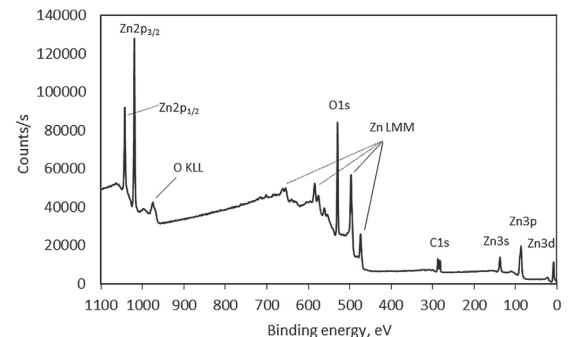


Fig. 5. XPS survey spectrum of the scCO<sub>2</sub> treated HDG surface.

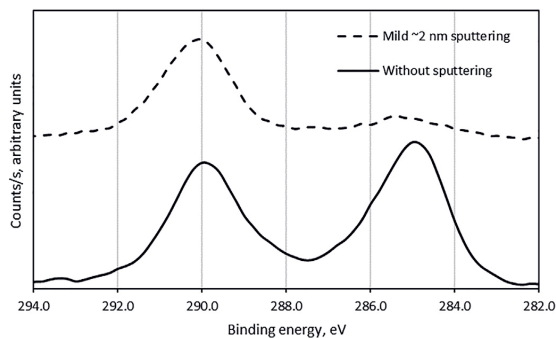


Fig. 6. XPS spectra recorded on a  $\text{scCO}_2$  treated HDG surface.

In the  $\text{scCO}_2$  treatment, no reaction products were obtained in the absence of  $\text{H}_2\text{O}$ . The presence of water in a supercritical  $\text{CO}_2$  system facilitated the extraction of zinc metal ions. This is probably due to dissociation of carbonic acid ( $\text{HCO}_3^-$ ) and acidification of water [44]. The formed zinc ions reacted with carbonate (and hydroxide) ions. Zinc carbonates could also be formed after release of zinc ions by introducing a carbonate source (such as  $\text{KHCO}_3$ ) [30]. In the absence of  $\text{CO}_2$  (the closed vessel was heated up in the presence of  $\text{H}_2\text{O}$  in  $\text{O}_2$  atmosphere, resulting in increased pressure because of vaporization of  $\text{H}_2\text{O}$ ), the only corrosion product was  $\text{ZnO}$ , which is in accordance with earlier findings [5]. Treatment of  $\text{ZnO}$  crystals in the presence of  $\text{H}_2\text{O}$  and  $\text{CO}_2$  atmosphere has been reported to result in formation of hydrozincite ( $\text{Zn}_5(\text{CO}_3)_2(\text{OH})_6$ ) or smithsonite ( $\text{ZnCO}_3$ ) [5,11]. It is noteworthy that no traces of  $\text{ZnO}$  were observed in the FTIR spectra, which could indicate that the patina formation reaction did not proceed via  $\text{ZnO}$  formation. Formation of the artificial patina in the pressurized vessel required thus the presence of both  $\text{CO}_2$  and  $\text{H}_2\text{O}$  [45,46].

In the presence of  $\text{CO}_2$  and  $\text{H}_2\text{O}$ , temperature and pressure have been reported to have an important role on the corrosion rate [47]. Moreover, it is obvious that the presence of copper enhances the corrosion rate of zinc due to its noble character. However, the optimization of the treatment time, pressure or concentration of  $\text{Cu}$  was not yet carried out here but will be made in our future studies.

### 3.4. $\text{H}_2\text{O}$ contact angle and Sfe measurements

The changes in the surface chemistry of a  $\text{scCO}_2$  treated sample and an unprotected outdoor exposure sample were evaluated by  $\text{H}_2\text{O}$  contact angle and surface energy measurements (Figs. 7 and 8). The water contact angle on a fresh zinc surface was about  $60^\circ$ , which implies moderate wetting. The both patina surfaces had  $\text{H}_2\text{O}$  contact angles way above  $100^\circ$ . Hydrozincite has been shown to increase hydrophobicity [43]. Although the zinc (hydroxy)carbonates clearly increased the hydrophobicity of a zinc coating, their protective role depends on many parameters [43]. The artificial patina sample had even

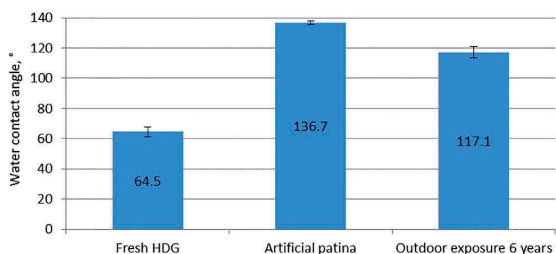


Fig. 7. Water contact angles on fresh HDG and patina surfaces.

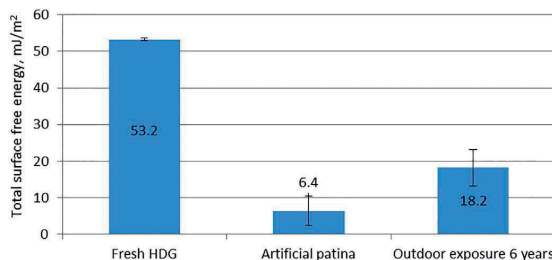


Fig. 8. Total free surface energy (according to Wu) of different surfaces.

higher water contact angle than the outdoor exposed sample, which could be due to a more homogeneous and even patina barrier. In outdoor exposure, the zinc surface of hot dip galvanized steel samples is known to undergo various corrosion processes depending on the atmosphere. The patina on outdoor exposed samples varies a lot in terms of thickness, composition and presence of impurities [12,14,33]. The surface free energy was much lower on both patina samples than on the fresh HDG. The results indicate good paintability of the artificial patina surface, since outdoor exposed samples typically provide better wettability and paint adhesion than fresh HDG samples [1–3]. Based on the results of our study, formation of a paintability promoting zinc patina layer, i.e. the process that during weathering takes up to several years, can be accomplished within 1 h.

### 3.5. SEM imaging of coated samples

HDG samples were coated with polyester melamine primer and topcoat after the  $\text{scCO}_2$  treatment. No further surface conditioning was performed prior to coating. Excellent wettability was observed. SEM cross section images showed clearly that the needle-like patina stayed intact through the bar coating and oven curing of the sample at a peak metal temperature of  $230^\circ\text{C}$  (Fig. 9). This is of great importance, since the forces applied during the coating might have destroyed the delicate patina structure. Carbonates also undergo thermal decomposition, in the end producing  $\text{ZnO}$ ,  $\text{CO}_2$  and  $\text{H}_2\text{O}$  [48]. For instance, a basic zinc carbonate  $\text{Zn}_3(\text{CO}_3)_2(\text{OH})_4 \cdot 2\text{H}_2\text{O}$  has been shown to start to decompose at  $220\text{--}250^\circ\text{C}$ , producing an endothermic weight loss, with the termination at  $340^\circ\text{C}$  [11,49,50]. However, the coating surface after double oven curing at  $230^\circ\text{C}$  showed no degradation, and the different coating layers in the cross section images were intact (Fig. 9).

## 4. Conclusions

Formation and properties of a  $\text{scCO}_2$ -induced artificial patina layer on hot dip galvanized steel were investigated with an emphasis on the utilization of the layer as a surface treatment before coating. The formed patina was composed of two distinctive layers; a uniformly covering dense, anhydrous  $\text{ZnCO}_3$  layer adjacent to the metallic Zn coating, and a needle-like structure on the outermost surface. The composition of the needle-like structure resembled that of basic zinc carbonates, which are typical corrosion products in outdoor exposed HDG. Artificial patina formation increased the hydrophobicity of the HDG surface remarkably, thus stabilizing the zinc surface. Good wettability of the patina surface by an organic melamine polyester coating was obtained. The needle-like patina structure remained intact within the cured coating, indicating improved adhesion properties.

In outdoor exposure, the formation of an adhesion-promoting hydrozincite ( $\text{Zn}_5(\text{CO}_3)_2(\text{OH})_6$ ) patina layer on a zinc surface is a long process characterized by strong dependency on the prevailing conditions (humidity and ions), presence of impurities (pollutants) and zinc runoff. By  $\text{scCO}_2$  treatment, a dense patina barrier with adhesion promoting needle-like roughness on the outer surface was produced with

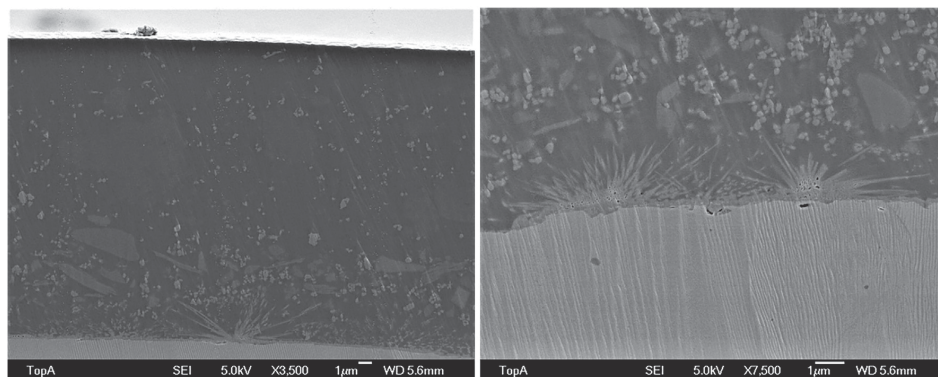


Fig. 9. SEM cross section images of a coated HDG sample, showing intact needle-like patina structure under the coating.

several advantages. The process of patina formation by the  $\text{scCO}_2$  treatment is well controlled, rapid, free of impurities, and no Zn runoff takes place. The work will be continued by careful determination of the artificial patina composition, optimization of the application parameters and testing of coated artificial patina samples in terms of adhesion and corrosion resistance.

#### Acknowledgments

Milla Suominen is acknowledged for the assistance with the FTIR measurements at the University of Turku. Digital, Internet, Materials & Engineering Co-Creation (DIMECC) (formally FIMECC) and its HYBRIDS materials program is acknowledged for financial support.

#### References

- [1] J.F. Malone, Painting hot dip galvanized steel, *Mater. Perform.* 31 (1992) 39–42.
- [2] K.J. Dunham, Preparing hot-dip galvanized steel surfaces for painting or powder coating: a primer, *Met. Finish.* 100 (2002) 20–25.
- [3] I. Cabanelas, A. Collazo, M. Izquierdo, X.R. Nóvoa, C. Pérez, Influence of galvanized surface state on the duplex systems behavior, *Corros. Sci.* 49 (2007) 1816–1832.
- [4] L. Veleva, R.D. Kane, B.S. Covino Jr., S.D. Cramer (Ed.), *Atmospheric Corrosion in ASM Handbook Vol 13A, Corrosion: Fundamentals, Testing and Protection*, ASM International Materials Park, Ohio, 2003, pp. 196–209.
- [5] E.A. Anderson, M.L. Fuller, Corrosion of zinc, *Met. Alloy.* 10 (1939) 282–287.
- [6] E.D. Mor, A.M. Beccaria, Effect of temperature on the corrosion of copper and zinc in synthetic sea water, *Corrosion* 31 (1975) 275–279.
- [7] F.R. Morral, X-ray analysis of corrosion products from galvanized sheet, Proceedings of the 77th General Meeting, Wernersville, USA, 1940, pp. 279–288.
- [8] S. Ghose, The crystal structure of hydrozincite,  $\text{Zn}_5(\text{OH})_6(\text{CO}_3)_2$ , *Acta Cryst* 17 (1964) 1051–1057.
- [9] J.L. Jambor, Studies of basic copper and zinc carbonates: I - synthetic zinc carbonates and their relationship to hydrozincite, *Can. Mineral.* 8 (1964) 92–108.
- [10] A.K. Alwan, P.A. Williams, Mineral formation from aqueous solution. Part I. The deposition of hydrozincite,  $\text{Zn}_5(\text{OH})_6(\text{CO}_3)_2$ , from natural waters, *Transit. Met. Chem.* 4 (1979) 128–132.
- [11] I. Odnevall, C. Leygraf, Comparison between analytical methods for zinc specimens exposed in a rural atmosphere, *J. Electrochem. Soc.* 138 (1991) 1923–1928.
- [12] E. Almeida, M. Morcillo, R. Rosales, Atmospheric corrosion of zinc part 2: marine atmospheres, *Br. Corros. J.* 35 (2000) 289–296.
- [13] A.K. Neufeld, I.S. Cole, Using Fourier transform infrared analysis to detect corrosion products on the surface of metals exposed to atmospheric conditions, *Corrosion* 53 (1997) 788–799.
- [14] Q. Qu, C. Yan, Y. Wan, C. Cao, Effects of NaCl and  $\text{SO}_2$  on the initial atmospheric corrosion of zinc, *Corros. Sci.* 44 (2002) 2789–2803.
- [15] C. Barnes, Painting of galvanized steel, *T. I. Met. Finish.* 65 (1987) 127–131.
- [16] D. Bueche, Preparing galvanized surfaces before topcoating, *J. Prot. Coat. Linings* 13 (1996) 9–13.
- [17] D. Lindström, I. Odnevall, Long-term use of galvanized steel in external applications. Aspects of patina formation, zinc runoff, barrier properties of surface treatments, and coatings and environmental fate, *Environ. Monit. Assess.* 173 (2011) 139–153.
- [18] E.M. Morcillo, R. Rosales, Atmospheric corrosion of zinc part 1: rural and urban atmospheres, *Br. Corros. J.* 35 (2000) 284–288.
- [19] A.A. Vostrikov, O.N. Fedyayeva, A.V. Shishkin, M.Ya. Sokol, ZnO nanoparticles formation by reactions of bulk Zn with  $\text{H}_2\text{O}$  and  $\text{CO}_2$  at sub-and supercritical conditions: II. Morphology and properties of nanoparticles, *J. Supercrit. Fluids* 48 (2009) 161–166.
- [20] W.-H. Lin, T.-F. Mark Chang, Y.-H. Lu, T. Sato, M. Sone, K.-H. Wei, Y.-J. Hsu, Supercritical  $\text{CO}_2$ -assisted electrochemical deposition of mesocrystals for practical photoelectrochemical applications, *J. Phys. Chem. C* 117 (2013) 25596–25603.
- [21] T. Falk, J.-E. Svensson, L.-G. Johansson, The role of  $\text{CO}_2$  and NaCl on the atmospheric corrosion of zinc. A laboratory study, *J. Electrochem. Soc.* 145 (1998) 2993–2999.
- [22] T. Falk, J.-E. Svensson, L.-G. Johansson, The role of carbon dioxide in the atmospheric corrosion of zinc. A laboratory study, *J. Electrochem. Soc.* 145 (1998) 39–44.
- [23] M.C. Hales, R.L. Frost, Synthesis and vibrational spectroscopic characterization of synthetic hydrozincite and smithsonite, *Polyhedron* 26 (2007) 4955–4962.
- [24] M.F. O'Connor, A study of the kinetics of the basic zinc carbonate formation reaction, *Z. Naturforsch.* 30b (1975) 665–668.
- [25] A. Kaleva, V. Saarimaa, S. Heinonen, J.-P. Nikkanen, A. Markkula, P. Väisänen, E. Levänen, Dissolution induced nanowire synthesis on hot-dip galvanized surface in supercritical carbon dioxide ( $\text{scCO}_2$ ), *Nanomater.-Basel* 181 (2017) 1–8.
- [26] A.F. Lagalante, B.N. Hansen, T.J. Bruno, R.E. Sievers, Solubilities of copper(II) and chromium(III)  $\beta$ -diketonates in supercritical carbon dioxide, *Inorg. Chem.* 34 (1995) 5781–5785.
- [27] N.E. Durling, O.J. Catchpole, S.J. Tallon, J.B. Grey, Measurement and modelling of the ternary phase equilibria for high pressure carbon dioxide-ethanol-water mixtures, *Fluid Phase Equilib.* 252 (2007) 103–113.
- [28] S. Thomas, N. Birbilis, M.S. Venkatraman, I.S. Cole, Self-repairing oxides to protect zinc: review, discussion and prospects, *Corros. Sci.* 69 (2013) 11–22.
- [29] K.-C. Chang, T.-M. Tsai, T.-C. Chang, Y.-E. Syu, H.-C. Huang, Y.-C. Hung, T.-F. Young, D.-S. Gan, N.-J. Ho, Low-temperature synthesis of ZnO nanotubes by supercritical  $\text{CO}_2$  fluid treatment, *Electrochem. Solid-State Lett.* 14 (2011) K47–K50.
- [30] D.O. Miles, P.J. Cameron, D. Mattia, Hierarchical 3D ZnO nanowire structures via fast anodization of zinc, *J. Mater. Chem. A* 3 (2015) 17569–17577.
- [31] R.L. Frost, W.N. Martens, D.L. Wain, M.C. Hales, Infrared and infrared emission spectroscopy of the zinc carbonate mineral smithsonite, *Spectrochim. Acta A* 70 (2008) 1120–1126.
- [32] F.Z. Mahjoubi, A. Khalidi, M. Abdennouri, N. Barka, Zn-Al layered double hydroxides intercalated with carbonate, nitrate and sulphate ions: synthesis, characterization and dye removal properties, *J. Taibah Univ. Sci.* 11 (2017) 90–100.
- [33] A.K. Neufeld, I.S. Cole, A.M. Bond, S.A. Furman, The initiation mechanism of corrosion of zinc by sodium chloride particle deposition, *Corros. Sci.* (2002) 555–572.
- [34] D. Stoilova, V. Koleva, V. Vassileva, Infrared study of some synthetic phases of malachite ( $\text{Cu}_2(\text{OH})_2\text{CO}_3$ )-hydrozincite ( $\text{Zn}_5(\text{OH})_6(\text{CO}_3)_2$ ) series, *Spectrochim. Acta A* 58 (2002) 2051–2059.
- [35] R. Sanna, G. De Giudici, A.M. Scoriapino, C. Floris, M. Casu, Investigation of the hydrozincite structure by infrared and solid-state NMR spectroscopy, *Am. Mineral.* 98 (2013) 1219–1226.
- [36] C.K. Huang, P.F. Kerr, Infrared study of the carbonate minerals, *Am. Mineral.* 45 (1960) 311–325.
- [37] N. Koga, H. Tanaka, Thermal decomposition of copper (II) and zinc carbonate hydroxides by means of TG-MS, *J. Therm. Anal. Calorim.* 82 (2005) 725–729.
- [38] W. Zabinski, The problem of stacking order in natural hydrozincite, *Can. Mineral.* 8 (1966) 649–652.
- [39] H.E. Biber, Scanning auger microprobe study of hot-dipped regular-spangle galvanized steel: part I. Surface composition of as-produced sheet, *Metall. Trans. A* 19A (1988) 1603–1608.
- [40] G. Ballerini, K. Ogle, M.-G. Barthès-Labrousse, The acid-base properties of the surface of native zinc oxide layers: an XPS study of adsorption of 1,1-diaminoethane, *Appl. Surf. Sci.* 253 (2007) 6860–6867.
- [41] J.F. Moulder, W.F. Stickle, P.E. Sobol, K.D. Bomben, R.C. King Jr., J. Chastain (Ed.), *Handbook of X-ray Photoelectron Spectroscopy*, Physical Electronics, Inc., Minnesota, 1995, pp. 40–41.

- [42] J. Duchoslav, M. Arndt, T. Keppert, G. Luckeneder, D. Stifter, XPS investigation on the surface chemistry of corrosion products on ZnMgAl-coated steel, *Anal. Bioanal. Chem.* 405 (2013) 7133–7144.
- [43] X. Zhang, Z. Liu, I. Odnevall Wallinder, C. Leygraf, The protective role of hydrozincite during initial corrosion of a Cu<sub>40</sub>Zn alloy in chloride-containing laboratory atmosphere, *Corros. Sci.* 103 (2016) 20–29.
- [44] K.L. Toews, R.M. Shroll, C.M. Wai, pH defining equilibrium between water and supercritical CO<sub>2</sub>. Influence on SFE of organics and metal chelates, *Anal. Chem.* 67 (1995) 4040–4043.
- [45] N. Ohkuma, Y. Funayama, H. Ito, N. Mizutani, M. Kato, Adsorption and reaction of CO<sub>2</sub> gas on the surface of ZnO fine particles in the atmosphere, *J. Surf. Sci. Soc. Jpn.* 9 (1988) 452–458.
- [46] A. Dugstad, B. Morland, S. Clausen, Corrosion of transport pipelines for CO<sub>2</sub> – effect of water ingress, *Energy Procedia* 4 (2011) 3063–3070.
- [47] A. Dugstad, M. Halseid, B. Morland, Testing of CO<sub>2</sub> specifications with respect to corrosion and bulk phase reactions, *Energy Procedia* 63 (2014) 2547–2556.
- [48] G. Rayner-Canham, *Descriptive Organic Chemistry*, W.H. Freeman and Company, New York, 2000, p. 509.
- [49] Y. Sawada, M. Murakami, T. Nishide, Thermal analysis of basic zinc carbonate. Part 1. Carbonation process of zinc oxide powders at 8 and 13 °C, *Thermochim. Acta* 273 (1996) 95–102.
- [50] N. Kanari, D. Mishra, Thermal decomposition of zinc carbonate hydroxide, *Thermochim. Acta* 410 (2004) 93–100.

# PUBLICATION IV

## **Tailoring of Versatile Surface Morphologies on Hot Dip Galvanized Steel in Wet CO<sub>2</sub>: Aspects on Formation, Barrier Properties, and Utilization as a Substrate for Coatings**

V. Saarimaa, A. Kaleva, J.-P. Nikkanen, J. Manni, C. Lange, T. Paunikallio, T. Laihinen, S. Heinonen, E. Levänen, P. Väisänen, A. Markkula

ACS Applied Materials & Interfaces, Vol. 10, pp. 21730–21739  
<https://doi.org/10.1021/acsami.8b05034>

**Publication reprinted with the permission of the copyright holders.**





# Tailoring of Versatile Surface Morphologies on Hot Dip Galvanized Steel in Wet CO<sub>2</sub>: Aspects on Formation, Barrier Properties, and Utilization as a Substrate for Coatings

Ville Saarimaa,<sup>\*,†</sup> Aaretti Kaleva,<sup>‡</sup> Juha-Pekka Nikkanen,<sup>‡</sup> Jere Manni,<sup>†</sup> Carl Lange,<sup>†</sup> Teemu Paunikallio,<sup>†</sup> Tero Laihinne,<sup>†</sup> Saara Heinonen,<sup>‡</sup> Erkki Levänen,<sup>‡</sup> Pasi Väisänen,<sup>§</sup> and Antti Markkula<sup>§</sup>

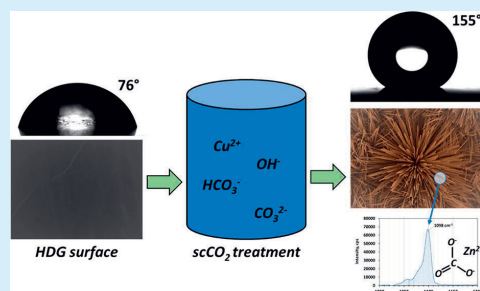
<sup>†</sup>Top Analytica Oy, Ruukinkatu 4, FI-20540 Turku, Finland

<sup>‡</sup>Laboratory of Materials Science, Tampere University of Technology, FI-33101 Tampere, Finland

<sup>§</sup>SSAB Europe Oy, Harvialantie 420, FI-13300 Hämeenlinna, Finland

**ABSTRACT:** Zinc carbonate and a mixed-phase zinc carbonate were precipitated selectively on hot dip galvanized steel in the presence of CO<sub>2</sub> and water. The zinc carbonate was precipitated as a uniform layer with cubic superficial appearance, while the mixed-phase zinc carbonate was precipitated as nanowires. The distinct structures could be formed separately or as a dual structure with nanowires on the outermost surface. The barrier properties were improved by the both patina forms; a significant increase in surface hydrophobicity was obtained. The dual patina structure was successfully coated with an organic coating, and the intact wet CO<sub>2</sub>-induced patina with both structures was confirmed within the coating. The formed carbonates can be further converted to zinc oxide by calcination, preserving the delicate structures, which opens a wide range of potential applications for the nanostructured ZnO in a variety of future electronic and optoelectronic devices.

**KEYWORDS:** galvanized steel, zinc carbonate, nanowires, supercritical carbon dioxide, Raman, XPS, dynamic contact angle



## 1. INTRODUCTION

Hierarchical metal oxide nanostructures have in the recent years gained interest as attractive building blocks for new electronic and optoelectronic devices and gas sensors and can have improved performance in catalysis, fuel cells, and tissue engineering.<sup>1–3</sup> Such semiconducting materials are typically formed via carbonation and oxidation reactions. For instance, formation of ZnO nanowires can be accomplished by thermal treatment after anodic oxidation, metallorganic chemical vapor deposition, or electrochemical deposition.<sup>2,4–6</sup> However, the established reaction routes often require high temperature, expensive and complex experimental setup, multiple reaction steps, and long reaction time. Wet supercritical carbon dioxide (scCO<sub>2</sub>) treatment has been proposed as a medium for zinc carbonate (or oxide) nanowire synthesis.<sup>7,8</sup> CO<sub>2</sub> is abundantly available and cost efficient, and the synthesis can be carried out in a single process step.<sup>7</sup> Furthermore, the zinc carbonation products can be converted to zinc oxide by thermal treatment, which opens a wide range of future applications for materials produced via scCO<sub>2</sub> synthesis.<sup>9,10</sup>

The reactions of different metals and minerals in wet scCO<sub>2</sub> are not yet thoroughly understood, but tentative reaction sequences can be constructed with the available studies. First, although CO<sub>2</sub> is a corrosive gas, synthesis of Zn nanostructures

is very limited in dry scCO<sub>2</sub>.<sup>11,12</sup> In a supercritical carbon dioxide environment, in the presence of water, formation of carbonic acid (CO<sub>2</sub> + H<sub>2</sub>O ⇌ H<sub>2</sub>CO<sub>3</sub>) takes place.<sup>13,14</sup> Carbonic acid is dissociated into HCO<sub>3</sub><sup>2-</sup> at a pH range of 3.7–10.3 (at 25 °C).<sup>15</sup> The zinc dissolution is initiated by acidification of the metal surface by the carbonate ions, which increase the surface conductivity and enhance dissolution of outermost surface layers.<sup>11,14–18</sup> The initial zinc dissolution can be further accelerated by addition of ions of metals more noble than Zn, thus introducing reduction–oxidation reactions on the surface. In aqueous solutions, Zn<sup>2+</sup> exists as stable hydrated ions, which can form complexes in the presence of different ions (OH<sup>-</sup>, HCO<sub>3</sub><sup>2-</sup>).<sup>5,19</sup> The very first corrosion products of zinc appear in the form of hydrated Zn<sup>2+</sup> compounds as a very thin film on the metal surface.<sup>14,19–22</sup> The liquid water functions as an effective solvent, but also as a reservoir for the anionic and cationic species (Zn<sup>2+</sup>, OH<sup>-</sup>, HCO<sub>3</sub><sup>-</sup>, CO<sub>3</sub><sup>2-</sup>).<sup>8,18,23,24</sup> This thin reactive interface separates the solid material from the wet CO<sub>2</sub> interface.<sup>12</sup> The formed complexes can in acidic conditions further undergo con-

Received: March 28, 2018

Accepted: June 5, 2018

Published: June 5, 2018

densation via the olation mechanism, resulting in various zinc carbonates.<sup>3,5,21,25</sup> For instance, the growth of microscopic Zn-containing nanowires is initiated from so-called nanoplatforms and proceeds to larger nanoflowers or bundles of nanowires that are increased in length by whisker growth mechanism.<sup>5,7,8</sup> The predominant phases are strongly influenced by temperature, pressure, and reaction time.<sup>11</sup> The question whether the corrosion process proceeds via a CO<sub>2</sub>-saturated water film on a Zn surface or through direct diffusion from the water-saturated CO<sub>2</sub> gas or both is still under debate.<sup>11</sup>

Raman spectroscopy has recently gained interest in characterization of coatings, their degradation, and corrosion products.<sup>12,26–30</sup> The lateral resolution of Raman is much higher than that of FTIR and the molecular water that is present in most zinc corrosion products does not disturb the measurements, since the water sensitivity is very low. Raman spectroscopy is a scattering technique, where molecular vibrations result in a shift in the wavelength of the incident light beam, while in FTIR the molecular vibrations induced by the incident beam shift the molecule to a higher vibrational energy state and thus absorb energy. The molecular information obtained by these two methods is complementary, and as a thumb rule the functional groups that cause strong Raman scattering result in weak IR absorption and vice versa.<sup>31</sup> For instance, Raman scattering is typically strong for symmetric, nonpolar molecules, while IR absorption is strong for asymmetric and polar molecules. In this work, Raman and FTIR spectroscopy, in addition to X-ray photoelectron spectroscopy (XPS), were applied for identification of the compounds precipitated on hot dip galvanized steel in a wet CO<sub>2</sub> medium.

Corrosion protection and self-healing properties of zinc corrosion products have been intensively investigated during the past years.<sup>22,32</sup> These properties have been attributed to formation of a passive layer that inhibits further oxidation of zinc.<sup>33</sup> The inhibitive layer can be a result of interactions between a fresh metal surface and the prevailing environment, or it can be intentionally formed as a synthesis or post-treatment product. The protective properties are derived from hindering of transport of electroactive species to the metal surface.<sup>27</sup> Most of the research has focused on naturally forming zinc patina, and the barrier protection properties of synthesized zinc patina have been scarcely investigated. Hydrophobicity of the formed patina layers was investigated in this study.

In our previous studies, a wet scCO<sub>2</sub>-induced dual patina structure was formed at a pressure of 300 bar.<sup>7,34</sup> However, selective precipitation of different patina compounds was not achieved. In this study, the patina structures were precipitated at lower pressures (65 and 80 bar), allowing selective growth of different patina morphologies on separate samples. This study comprises characterization of the different carbonate structures formed in a wet CO<sub>2</sub> medium at well-defined and repeatable experimental setups. Furthermore, the barrier properties were evaluated by static and dynamic contact angle measurements, and the properties as a substrate for coating are discussed.

## 2. MATERIALS AND METHODS

**2.1. Materials and Samples.** Unpassivated hot dip galvanized steel (~0.2% Al in the zinc bath) with a total zinc coating mass of 275 g/m<sup>2</sup> from SSAB Europe Oy was used. Alkaline cleaning of the samples was performed with Gardoclean 338 (Chemetall) before the scCO<sub>2</sub> treatment according to the supplier's instructions for the

chemical. The wet CO<sub>2</sub> treatments were performed as described by Kaleva et al.<sup>7</sup> An HDG sample (5 × 10 cm) was placed in the vessel, and the vessel was pressurized with CO<sub>2</sub> (≥97%, AGA). A precursor solution consisting of 0.5 m-% Cu(hfac)<sub>2</sub> (copper(II) hexafluoroacetylacetonate hydrate, Sigma-Aldrich) in 5 mL of deionized H<sub>2</sub>O/EtOH (40/60 vol %) was introduced in selected samples using a cosolvent pump. The reactions were carried out for 60 min. Sample 3 was prepared in subsupercritical conditions, adding liquid CO<sub>2</sub> and H<sub>2</sub>O in the reaction vessel without the precursor.

Samples prepared in the following conditions were examined in this study: (1) 80 bar (scCO<sub>2</sub>), 40 °C, 5 mL of Cu(hfac)<sub>2</sub> solution "dense patina with dense and nanowire layers"; (2) 80 bar (scCO<sub>2</sub>), 60 °C, 5 mL of Cu(hfac)<sub>2</sub> solution "dense patina layer"; and (3) 65 bar (<scCO<sub>2</sub>), 25 °C, 0.5 mL of H<sub>2</sub>O "nanowire patina layer".

Samples for electron probe microanalysis and cross-sectional RAMAN measurement were coated with a polyester melamine coating (Beckers Industrial Coatings Ltd.) and cured to a peak temperature of 228 °C. The degree of curing was evaluated by solvent resistance rub test (ASTM D4752) using methyl ethyl ketone as the solvent.

**2.2. Surface Characterization.** Scanning electron microscopy (SEM) characterization was performed using JEOL JSM-6335F and JEOL JSM-IT100 instruments. Cross sections for SEM characterization were prepared using an Ilion+ Advantage Precision Cross-section System (Model 693, Gatan Inc., USA). Element mapping was carried out using an electron probe microanalyzer (EPMA) with wavelength-dispersive X-ray spectrometers (JEOL JXA-8600). The signals were collected at 15 kV and 50 nA.

Element analysis was performed with X-ray photoelectron spectroscopy (XPS, PHI Quantum 2000) using monochromated Al K $\alpha$  beam (50W, 15 kV) with a 100  $\mu$ m spot size. The carbon peak (C 1s) at 284.9 eV was used for charge-shift correction. Samples for copper oxidation stage measurements were prepared by immersing the substrates in a precursor solution for 25 s, followed by air drying.

Vibrational spectroscopy was performed by FTIR and Raman. The FTIR measurements were performed with a Bruker Vertex 70 instrument on a Harrick Diamond ATR sample holder with a RT-LaTGS detector, yielding a 4 cm<sup>-1</sup> resolution. Raman measurements were performed with a Renishaw inVia Qontor confocal Raman microscope. The spectra were recorded at 532 nm excitation using a grating of 1800 l/mm. The resolution was 4 cm<sup>-1</sup>. The data were collected using a 100 $\times$  objective, and the signal-to-noise ratio was improved by spectral accumulation.

Water contact angle measurements were performed with an OCA 50 instrument (DataPhysics Instruments GmbH). Deionized water was used, and the droplet volume was 10  $\mu$ L. The untreated HDG sample was wiped with H<sub>2</sub>O and isopropanol prior to measurement. Static contact angles were reported after 15 s of surface contact. The dynamic contact angles were obtained with a tilting base unit that was operated at 0.50 deg/s. The step size was 0.10°, and 2 frames per second were collected. The tilting angle for the advancing ( $\theta_A$ ) and receding ( $\theta_R$ ) contact angles was determined using the drop base diameter (BD).

## 3. RESULTS AND DISCUSSION

### 3.1. Use of Cu Precursor to Catalyze Carbonate Precipitation.

**3.1.1. Oxidative Effect of the Cu Precursor.** In our previous studies, addition of an inorganic precursor to the scCO<sub>2</sub> treatment enhanced precipitation of carbonates on a HDG surface.<sup>7,34</sup> To investigate the effect of the copper(II) hexafluoroacetylacetonate hydrate precursor, droplets of that reagent were applied separately on a glass slide and on a hot dip galvanized steel sample. The droplets were air-dried and the oxidation state of copper was analyzed by XPS (Figures 1 and 2). Shake-up lines occur when outgoing photoelectrons interact with valence electrons and excite them to a higher energy level.<sup>35,36</sup> Shake-up satellites are present in Cu(II) containing samples but absent in Cu(O) and Cu(I) containing

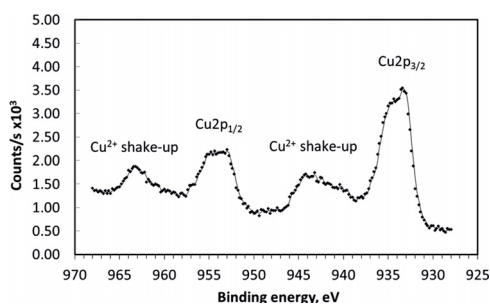


**Figure 1.** XPS spectrum of Cu  $2p_{1/2}$  and Cu  $2p_{3/2}$  peaks, measured from dried precursor solution on a glass slide.

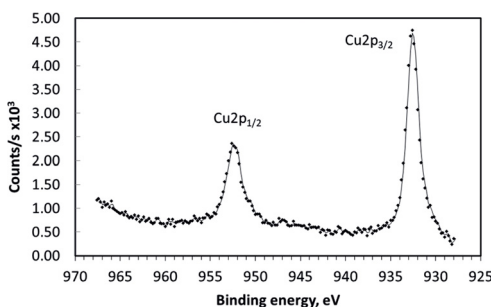


**Figure 2.** XPS spectrum of Cu  $2p_{1/2}$  and Cu  $2p_{3/2}$  peaks, measured from dried precursor solution on a HDG sample.

samples and can thus be used for identification of chemical states.<sup>35,36</sup> Cu (0) and Cu (I) species have statistically rather similar binding energy values.<sup>36</sup> According to the literature, the Cu  $2p_{3/2}$  photoelectron line is centered at 932.7 eV for Cu(0) and at 933.6 eV for Cu(II), which is in accordance with our measurements (Figures 1 and 2).<sup>35</sup> It was observed that the shakeup peaks were absent in a precursor solution droplet dried on an HDG sample, while they were present in the similarly prepared sample on a glass slide (Figures 1 and 2). This experiment confirms the oxidative effect of the precursor solution on the HDG surface, and thus supports the augmented patina formation in the presence of the precursor.

**3.1.2. Mapping of Cu within the  $scCO_2$ -Induced Patina Layer.** A cross section of a coated sample was prepared for electron probe microanalysis. A dense patina sample (sample 2) with a polyester melamine coating was studied to avoid excessive emission of electrons from the edge of the specimen (so-called edge effect). The patina layer was easily distinguished from the metallic Zn, since the Zn intensity within the patina layer was lower than on the metallic zinc (Figure 3). The amount of Cu within the analyzed area was small, which can be concluded from the heavy background signal even in the metallic zinc area. The detected trace amounts of Cu were located within the patina layer. The Cu residues were located at a sharp line, which resembles the initial native metallic zinc coating layer. Because of the high interaction volume of electrons within the sample, a more specific location is difficult to obtain.<sup>37</sup> Dissolution of metallic zinc during the  $scCO_2$  treatment most probably caused the patina layer to grow deeper into the metallic zinc coating,

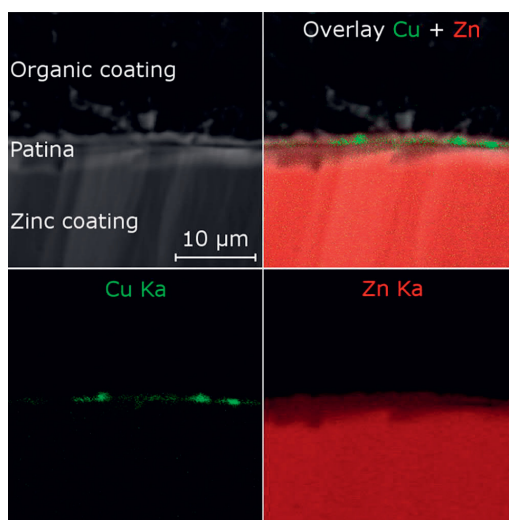


**Figure 3.** EPMA element maps of Zn and Cu measured from a cross section of a coated patina sample (sample 2).

encapsulating the initially reduced Cu within the forming patina layer. It is noteworthy that no Cu was observed at the final patina/Zn(0) interface, which indicates that the precursor was mostly active in the early stages of the patina formation. A slightly nodular occurrence of Cu supports the previously proposed patina growth mechanism, where the zinc corrosion is initiated at distinct spots on the surface, and gradually spreads in multiple directions.<sup>34</sup>

### 3.2. Characterization of the Patina Surfaces.

**3.2.1. SEM Imaging.** SEM cross section images of samples 1–3 are shown in Figures 4–6. Sample 1 shows a dual structure with a dense patina layer adjacent to metallic zinc and a rod-like structure on top of the dense patina layer, similar to what was reported earlier.<sup>34</sup> However, in this study the synthesis was carried out at a significantly lower pressure. The rods were grouped into larger nanoflowers that were seemingly grown from a common initiation point (Figure 4). Similar nanowire structures have been observed as a result of anodization and  $scCO_2$  fluid treatments.<sup>6,8,38</sup> The rod-like nanowires in this study had a nonuniform size distribution and nontapered ends (Figure 4). When the synthesis was performed at the same pressure (80 bar), with elevated temperature (40 → 60 °C), the rod-like structure did not appear on the surface (Figure 5). The top view of the sample 2 showed a nodular surface structure, which, however, in the cross-cut image fully covered the metallic zinc substrate (Figure 5). At a higher magnification, a cubical surface of the nodules was revealed with flat facets that had a size of a few hundred nanometers. Although various  $CO_2$ -assisted hierarchical structures have been reported for metal oxides and carbonates, the cubic surface morphology that was observed in the absence of rod-like morphology has not been reported earlier.

Temperature and pressure have been reported to strongly affect formation of different carbonate structures.<sup>11</sup> For example, pure hydrozincite has previously been synthesized from ZnO by a mechanochemical process at ambient

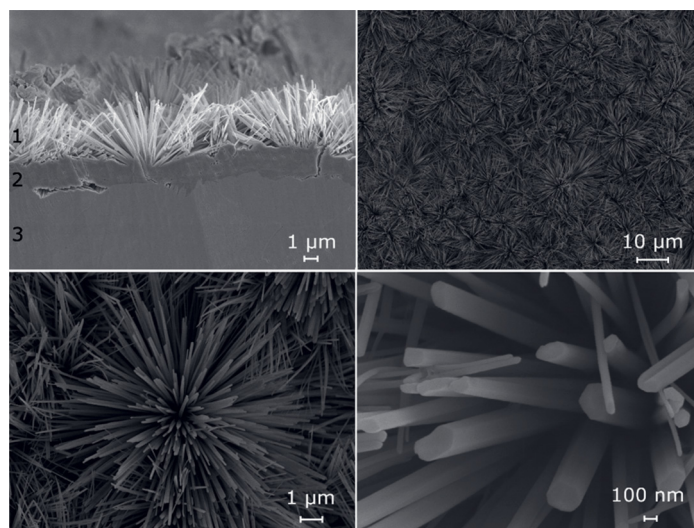


**Figure 4.** SEM images of sample 1 prepared at 80 bar (scCO<sub>2</sub>), 40 °C, and with the addition of 5 mL of Cu(hfac)<sub>2</sub> solution: 1 = nanowire patina layer, 2 = dense patina layer, 3 = zinc substrate.

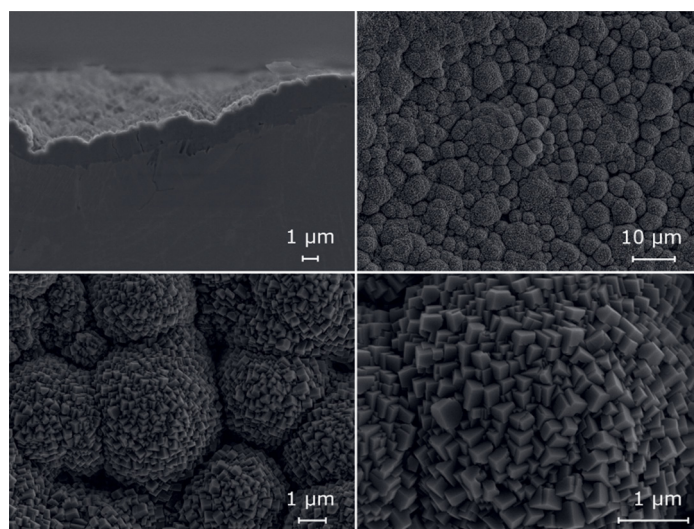


**Figure 5.** SEM images of sample 2 prepared at 80 bar (scCO<sub>2</sub>), 60 °C, and with the addition of 5 mL of Cu(hfac)<sub>2</sub> solution.

temperature and pressure in the presence of gaseous CO<sub>2</sub> and liquid H<sub>2</sub>O, while zinc carbonate was not formed.<sup>39</sup> In our study, decreasing the reaction pressure to 65 bar and the temperature to 25 °C (ambient temperature), caused the patina layer to be composed solely of the rod-like morphology (Figure 6). The rod-like morphology was similar to that synthesized at a higher pressure, but the flowers were less pronounced. In the cross-cut image, the rod-like elements did not have singular growth points, and the growth of the rods was more evenly distributed across the zinc substrate than in sample 1.

Crystal growth and morphology are influenced by available constituents and applied atmosphere and are derived from the need of the constituents to precipitate as energetically lowest stable crystals.<sup>40,41</sup> Regular crystalline structures are typically an indication of pure constituents. Given the different morphologies of the two obtained patina forms, and the fact that the nanowires prevail on the surface, it is logical that the growth of the two different structures is promoted by different atmospheres in the vessel, which affect the supply of carbonate and hydroxide ions via changes in the CO<sub>2</sub> solubility.<sup>42</sup> The needle-like patina has a similar form with previously reported rod-like precipitated carbonate whiskers.<sup>43,44</sup> The nontapered

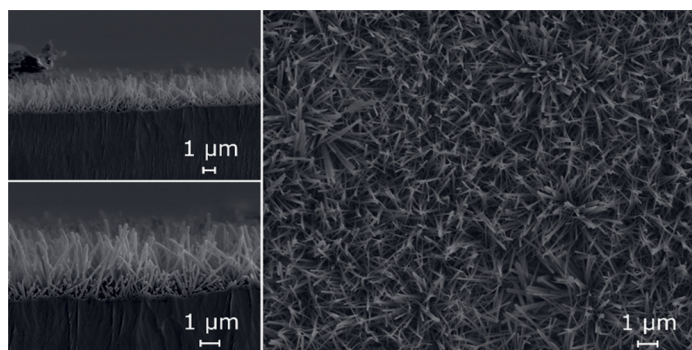


Figure 6. SEM images sample 3 prepared at 65 bar ( $\text{scCO}_2$ ), 25 °C, and with the addition of 0.5 mL of  $\text{H}_2\text{O}$ .

edges of the rods indicate a dynamic whisker growth mechanism with stepwise deposition as the principal synthesis mechanism.<sup>40,41</sup> It has been observed that the whisker growth is favored when the acidity of the medium increases, since it increases the zinc ion concentration.<sup>43</sup>

### 3.2.2. Chemical Characterization of Patina Structures.

**3.2.2.1. XPS Measurements.** The main components on the surfaces of the different patina structures were zinc, oxygen and carbon (Figure 7). Minor amounts of fluorine were also

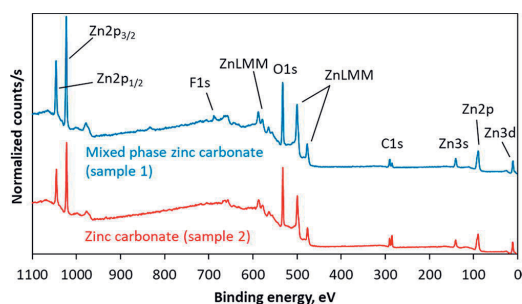


Figure 7. XPS spectra recorded from the top of both patina structures. The spectra were offset for clarity.

detected, which were considered as residues from the precursor solution. Copper was not detected on the surface. Atomic-% concentrations of C, O, and Zn are presented in Table 1. Adventitious carbon was separated from the C 1s pertaining to carbonate groups. The presence of carbonates was evident for both morphologies. No sputtering was performed, since the intensities of the different peaks were strong even without sputtering (very low amount of carbon as impurity). Furthermore, extended X-ray exposure can affect the oxidation stages of elements and cause uncontrolled variations in the atomic ratios of different elements.<sup>45</sup> The standard deviations of the element concentrations were very small, which indicates homogeneous structures. The dense patina structure has previously been assigned to  $\text{ZnCO}_3$  by FTIR.<sup>34</sup> The atomic ratios for  $\text{ZnCO}_3$  are 1:1:3 (Zn:C:O). In this study, the XPS data shows somewhat higher contribution of oxygen, which could be due to adsorption of humidity on the sample surface from the air (Table 1).<sup>46</sup> In the nanowire patina, the ratios of carbon and oxygen differ from the dense

Table 1. Atomic-percent of Zn, O, and C on the Patina Surfaces (Three Parallel Spots Were Measured)

binding energy (eV)	dense patina		nanowire patina	
	average	Stdev	average	Stdev
C 1s hydrozincite	290.2	14.0	0.2	7.9
C 1s adventitious	284.9	23.4	1.2	15.3
O 1s	532.2	48.5	0.8	55.1
Zn 2p3	1022.4	14.1	0.3	21.6

	atomic ratios			
	dense patina		nanowire patina	
	average	Stdev	average	Stdev
Zn	1.0	0.0	1.0	0.0
C	1.0	0.0	0.4	0.0
O	3.5	0.0	2.5	0.0

patina. Similar results were obtained for the both nanowire samples (samples 1 and 3), and they are not shown separately in the results. For each Zn atom, there was less C and O than in the dense patina. The atomic ratios of different elements in hydrozincite,  $\text{Zn}_5(\text{CO}_3)_2(\text{OH})_6$ , are 1.0:0.4:2.4 (Zn:C:O), which is very close to the obtained 1.0:0.4:2.5 ratio (Table 1). However, XPS measurements alone are insufficient to identify Zn corrosion products.<sup>47</sup>

**3.2.2.2. Raman and IR Measurements.** Raman and IR techniques can be utilized to distinguish polymorphs with the same chemical composition and to identify elements incorporated into mineral lattices.<sup>48</sup> The infrared and Raman spectra provide complementary information regarding the chemical structure.<sup>49</sup> Bands due to the stretching vibrations of symmetrical molecules (i.e., infrared inactive bands) can be observed by Raman. Polar groups yield strong infrared bands, but are very weak in Raman.<sup>49,50</sup> The free  $\text{CO}_3^{2-}$  ion has four normal vibrational modes: symmetric stretching vibration ( $\nu_1$ ), symmetric bending mode ( $\nu_2$ ), asymmetric stretching vibration ( $\nu_3$ ), and asymmetric bending mode ( $\nu_4$ ). These modes occur around 1100 ( $\nu_1$ ), 800 ( $\nu_2$ ), 1400 ( $\nu_3$ ), and 700  $\text{cm}^{-1}$  ( $\nu_4$ ).<sup>51–53</sup> The exact band positions are characteristic for different carbonate species, since the degeneracies and IR and Raman activities are affected by distortion of the symmetry of the carbonate anion.<sup>11,12,48</sup>

**Dense Patina.** The Raman spectrum of the dense patina was clear in terms of peak separation from the background and

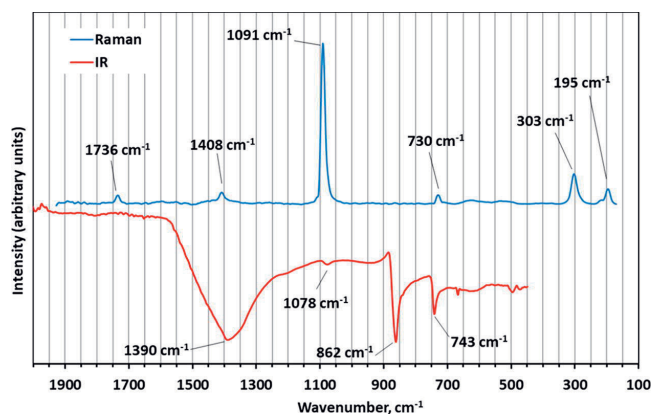


Figure 8. Raman and FTIR spectra of the patina sample 2 (dense patina).

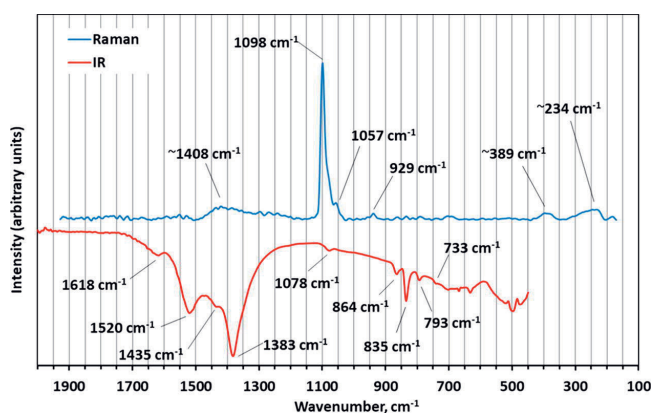


Figure 9. Raman and FTIR spectra of the carbonate nanowires (sample 1). Identical spectrum was obtained for sample 3.

peak sharpness, which implies a well-ordered crystalline structure (Figure 8). Four main carbonate vibrations were observed. The most intense band in Raman spectra at  $1091\text{ cm}^{-1}$  is due to  $\nu_1$  symmetric stretching mode.<sup>54</sup> In the IR spectrum, the  $\nu_1$  mode (at  $1078\text{ cm}^{-1}$ ) should be inactive but becomes active because of symmetry reduction of the carbonation anion through distortion.<sup>54–56</sup> The  $\nu_3$  antisymmetric stretching mode was observed at  $1408$  (Raman) and  $1390\text{ cm}^{-1}$  (IR). A band related to  $\nu_2$  symmetric bending mode was observed only in the IR spectrum (at  $862\text{ cm}^{-1}$ ), which is in accordance with the literature.<sup>54</sup> The  $\nu_4$  antisymmetric bending mode was observed with both methods, at  $730\text{ cm}^{-1}$  in the Raman spectrum and at  $743\text{ cm}^{-1}$  in the IR spectrum.<sup>54</sup> In the Raman spectrum, two prominent peaks were observed at  $303$  and  $195\text{ cm}^{-1}$ . These bands are assigned to lattice modes.<sup>48</sup> Zincite (ZnO) is a typical corrosion product of zinc in atmospheric conditions.<sup>17,57</sup> However, ZnO is unstable in the conditions applied in this study, and was not detected.<sup>52,58,59</sup> On the basis of the vibrational spectroscopic measurement the composition of the dense patina corresponds to that of  $\text{ZnCO}_3$ .<sup>51</sup>

**Nanowire Patina.** The Raman spectrum of the nanowire patina showed a sharp band at  $1098\text{ cm}^{-1}$  and several broad

low intensity bands, which suggests a more amorphous nature than for the dense patina (Figure 9). The both nanowire patina samples (samples 1 and 3) yielded similar spectra, and thus only the spectrum for sample 1 is shown. The sharp band at  $1098\text{ cm}^{-1}$  is assigned to the  $\nu_1$  symmetric stretching mode.<sup>54</sup> This band had a shoulder at lower wavenumbers, which has been attributed to overlapping  $\nu_1$  symmetric C–O stretching bands.<sup>11</sup> The  $\nu_1$  mode was observed also in the IR spectrum at  $1078\text{ cm}^{-1}$ . An OH bending was observed in the IR spectrum at  $1618\text{ cm}^{-1}$ , which arises from structural water.<sup>11</sup> In our previous study we also observed a broad IR absorption peak at  $\sim 3230\text{ cm}^{-1}$ , which arises from  $\text{OH}^-$  stretching modes from OH groups that are hydrogen bonded to the oxygen atom within the carbonate group that is not coordinatively bonded to metal ions.<sup>34,60,61</sup> The IR spectrum also contains  $\nu_3$  symmetric stretching modes at  $1520$  and  $1383\text{ cm}^{-1}$ . Splitting of the  $\nu_3$  stretching mode means lower symmetry of the carbonate and is typical for hydrozincite.<sup>48,54</sup> However, an additional unidentified band was observed at  $1435\text{ cm}^{-1}$ . The difference between the patina forms in the number of bands in this region is ascribed to the symmetry reduction of the OH-group-containing form of patina.<sup>54</sup>

Two sharp medium-intensity  $\nu_3$  bands should be present in the Raman spectrum of hydrozincite at 1545 and 1380  $\text{cm}^{-1}$ , but they were not present in the nanowire patina, which confirms that the structure of the nanowire patina deviates from that of hydrozincite.<sup>54</sup> A very low intensity  $\nu_2$  symmetric bending mode band was present in the IR spectrum at 864  $\text{cm}^{-1}$ . A very weak  $\nu_4$  antisymmetric bending mode was observed in the IR spectrum at 733  $\text{cm}^{-1}$ . The numerous IR bands in the low wavelength region may be attributed to structural distortion. Broad Raman bands were observed at around 390 and 230  $\text{cm}^{-1}$ . Similar bands have been observed for hydrozincite, but they have not been defined yet.<sup>24,54,62</sup>

The symmetric stretching mode ( $\nu_1$ ) was composed of several individual bands (Figure 10). The results suggest that

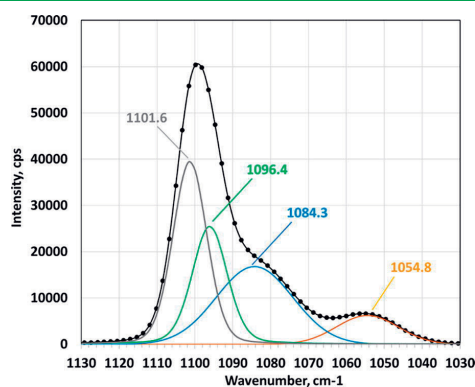


Figure 10. Curve fitting of the  $\nu_1$  symmetric bending mode for the nanowire patina.

the nanowire patina was a mixed phase of different zinc carbonates, and only the  $\text{ZnCO}_3$  (dense patina) was synthesized as a single phase.<sup>6</sup> Smithsonite ( $\text{ZnCO}_3$ ) and hydrozincite are the known natural secondary minerals of zinc.<sup>52</sup> In nature, basic zinc carbonates are often associated with smithsonite and other minerals.<sup>54</sup> The  $\nu_1$  band position for pure hydrozincite is at about 1060–1070  $\text{cm}^{-1}$ , which is somewhat higher than the lowest band for the nanowire patina (1054.8  $\text{cm}^{-1}$ ) (Figure 10).<sup>12,24,54,56,62</sup> Also, none of the bands show an exact match to  $\text{ZnCO}_3$ . Differences in coordination between carbonate ions and zinc ions (change in lattice structure) strongly affect the vibration frequencies and their intensities.<sup>55,62</sup>

Some minerals have been observed to occur in different morphologies despite the same chemical composition.<sup>11</sup> However, the measurements of this study do not support that conclusion. The closest analogy to the formation of the detected patina morphologies in the literature at the moment can be found in the work by Loring et al.<sup>11</sup> They observed that in wet  $\text{scCO}_2$ ,  $\text{Mg}(\text{HCO}_3)(\text{OH})\cdot 2\text{H}_2\text{O}$  was the main carbonation product at 35 °C, while  $\text{MgCO}_3$  dominated at 75 °C. The behavior was proposed to be caused by the reluctance of hydrated, metastable magnesium to exchange its OH-groups for carbonate. At higher temperature the energy barrier for ligand exchange is exceeded and the dehydration is completed.

Exposure to high-power laser beam may alter sample composition and cause dehydration by photoabsorption or

photo-oxidation.<sup>58</sup> However, in our measurements the multimodal  $\nu_1$  band occurred in same band ratios in several measurements from different nanowire samples and sample locations. Bands for  $\text{ZnO}$  were not observed for the samples even at long accumulation times, which shows that degradation did not take place during the Raman measurements.<sup>12,26,58</sup> The spectrum of nanowire patina does not either match those of hydroxy carbonates containing  $\text{Cu}^{2+}$ , which fortifies the conclusion that the nanowire patina is a mixed phase composed of carbonates with multimodal coordination to  $\text{Zn}^{2+}$  and  $\text{OH}^-$  groups.<sup>6,8,61,63</sup> It is clear from the cross-cut images that the nanowires were formed on top of the dense patina structure. The nanowire formation may follow a model where zinc surface is covered with a porous film with a reactive inner phase.<sup>19</sup> As the surface is not yet sealed by the  $\text{ZnCO}_3$  nodules at the early stages of  $\text{scCO}_2$  synthesis, the inner layer beneath the nodules is still reactive and functions as a source for  $\text{Zn}^{2+}$ . The intermediates ( $\text{Zn}(\text{OH})^+$ ) formed at that layer escape from the pores by diffusion, and precipitate with  $\text{HCO}_3^-$  ions at the tips of the whiskers. The synthesis of the nanowires thus proceeds via whisker growth mechanism with formation of polynuclear coordination complexes by means of hydroxyl groups as bridges.

**3.3. Barrier Effect of Patina.** The water contact angle for untreated HDG is typically  $<90^\circ$  (Figure 11).<sup>34</sup> Static contact

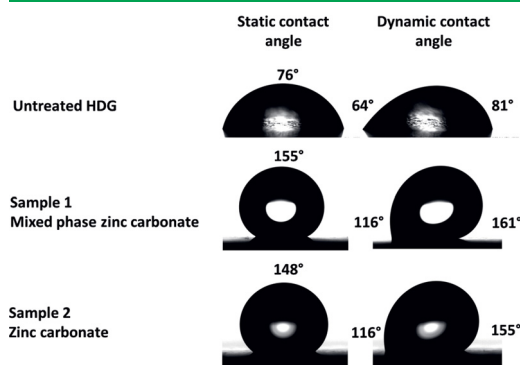
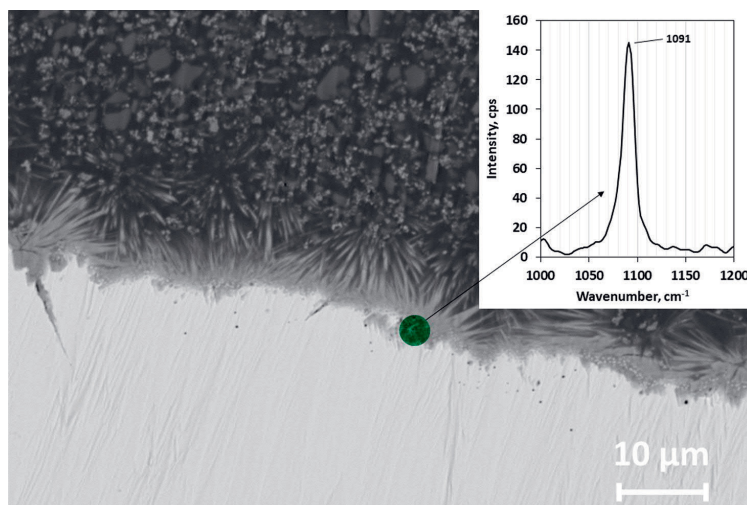


Figure 11. Static and dynamic water contact angles on an untreated HDG sample and patina samples.

angle measurements showed a significant increase in hydrophobicity for the  $\text{scCO}_2$ -induced patina samples compared to untreated HDG (Figure 11). Furthermore, the contact angle hysteresis ( $\theta_A - \theta_R$ ) was much higher for the patina surface than for the untreated HDG, which is an indication of higher roughness. Hierarchically structured films can show surface energy properties that significantly deviate from those of the bulk material. Significantly improved corrosion resistance of various metals has been reported after application of superhydrophobic surface films by direct synthesis or post-treatment.<sup>64</sup> Such surfaces range from thin films to hierarchically arranged nanostructures, and the application methods include wet chemical reaction, etching, hydrothermal treatment, anodization, electrodeposition, and sol-gel method.<sup>64</sup> All superhydrophobic surfaces are in principle to some extent able to withstand chemical attacks in aqueous solutions, but the corrosion protection effect of hierarchically delicate structures may be strongly affected by mechanical damage,



**Figure 12.** SEM image of a low-angle cross cut of a polyester-coated patina sample. A Raman measurement from surface of metallic zinc is shown in the upper right corner.

UV irradiation, and extended exposure to a specific environment.<sup>64</sup> The investigations on the robustness and stability of the  $\text{scCO}_2$ -induced patina coatings are thus necessary to clarify the suitability of such coatings for different applications and will be carried out in our next evaluations.

**3.4. Patina as a Substrate for Organic Coatings.** Good spreading of a polyester melamine coating was achieved on the patina surface, as reported earlier.<sup>34</sup> The solvent resistance rub test confirmed full curing of the coating. In cross section imaging, no air pockets were detected within the porous nanowire structure, indicating that the wetting of the nanowire patina surface follows the Wenzel model (Figure 12).<sup>64</sup> The thermal stability of some synthetic carbonates is limited to temperatures  $<200$  °C.<sup>65</sup> A sharp  $\nu_1$  symmetric bending mode at  $1091\text{ cm}^{-1}$  was observed at the metallic zinc/coating interface by Raman (insert in Figure 12). That mode pertains to  $\text{ZnCO}_3$ . The organic coating did not contain any carbonates. A good spectrum for this mode was obtained only in the proximity of the metallic zinc, which is because the metal enhances the scattering of the compounds adjacent to it. Measurements further away from the metal caused poor peak to background ratio, and degradation of the coating occurred when the laser power was increased substantially. The measurement parameters are still under optimization, but at this point it can be concluded that no heat-induced decomposition was observed at least for the  $\text{ZnCO}_3$  patina.<sup>65</sup> Outdoor exposure of the coated samples is ongoing, but these preliminary findings indicate that the patina layer improves barrier properties of zinc, and the nanowires show good compatibility with organic coatings. Enhanced paint adhesion may also be achieved, since whiskers have been reported to have high strength, and that their strength approaches that of theoretical value for perfect crystals.<sup>41,66</sup>

## 4. CONCLUSIONS

Accelerated precipitation of zinc oxidation and carbonation products on zinc substrate was studied in the presence of wet

$\text{CO}_2$ . Two distinct morphologies were obtained on hot dip galvanized steel: nodular zinc carbonate with cubic fine structure on the surface, and nanowires composed of a mixed phase basic zinc carbonate. The pure zinc carbonate layer was grown at 80 bar and 60 °C from numerous individual initiation points until the surface was sealed with nodules that had a diameter of  $<10\text{ }\mu\text{m}$ . The cross sectional thickness of the nodular, dense patina layer was about  $1\text{--}2\text{ }\mu\text{m}$ . At decreased temperature ( $60 \rightarrow 40$  °C), in addition to the nodular  $\text{ZnCO}_3$  layer, a nanowire morphology appeared on the outermost surface. The nodular layer had similar thickness, while the nanowires were grouped into flowers that stretched some  $3\text{--}5\text{ }\mu\text{m}$  from the surface. The nontapered ends of the wires and their visual appearance indicated that the growth of the nanowires proceeded by whisker growth mechanism. Additionally, since the nanowires appeared on top of the nodular structure, their growth was presumably facilitated by diffusion of hydrated zinc ions during the synthesis from the reactive inner phase beneath the nodules that had not yet sealed the surface. At lower pressure and temperature (65 bar, 25 °C), the nodular patina layer was not formed, but the surface was composed of pure nanowires with more evenly distributed growth initiation points and less pronounced grouping to flower structures. The Cu precursor that was used to enhance the growth initiation did not participate in the patina growth, as it was not detected as a structural element in any of the precipitated structures but remained reduced at the initial metallic zinc surface beneath the patina. The wet  $\text{CO}_2$  reaction route opens new opportunities to manufacture tailored nanostructure films for various applications. As such, the patina precipitated in wet  $\text{scCO}_2$  environment significantly increases the hydrophobicity of the HDG coating. Long-term corrosion protection can be achieved by applying organic coatings on the  $\text{scCO}_2$ -treated HDG. The patina showed full compatibility with a polyester melamine coating, and the delicate patina morphology was preserved within the coating. The morphologies synthesized in wet  $\text{CO}_2$  can thus find end applications as such, or as seed materials for more developed



applications. The obtained morphologies can be easily converted to ZnO by thermal treatment without losing the fine structure. These materials have potential for utilization in electronic and optoelectronic devices, and sensors.

## AUTHOR INFORMATION

### Corresponding Author

\*Tel.: +358 44 099 6335. E-mail: ville.saarimaa@topanalytica.com.

### ORCID<sup>®</sup>

Ville Saarimaa: 0000-0001-6394-0161

### Notes

The authors declare no competing financial interest.

## ACKNOWLEDGMENTS

Digital, Internet, Materials & Engineering Co-Creation (DIMECC) and its HYBRIDS materials program is acknowledged for financial support.

## REFERENCES

- (1) Anžlovar, A.; Marinšek, M.; Orel, Z. C.; Žigon, M. Basic Zinc Carbonate as a Precursor in the Solvothermal Synthesis of Nano-Zinc Oxide. *Mater. Des.* **2015**, *86*, 347–353.
- (2) Zehani, E.; Hassani, S.; Lussion, A.; Vigneron, J.; Etcheberry, A.; Galtier, P.; Sallet, V. Reconstruction of Perfect ZnO Nanowires Facets with High Optical Quality. *Appl. Surf. Sci.* **2017**, *411*, 374–378.
- (3) Zakharova, G. S.; Täschner, C.; Kolb, T.; Jähne, C.; Leonhardt, A.; Büchner, B.; Klingeler, R. Morphology Controlled NH<sub>4</sub>V<sub>3</sub>O<sub>8</sub>-Microcrystals by Hydrothermal Synthesis. *Dalt. Trans.* **2013**, *42* (14), 4897–4902.
- (4) Lin, W.; Chang, T.; Lu, Y.; Sato, M.; Wei, K.; Hsu, Y.; et al. Supercritical CO<sub>2</sub>-Assisted Electrochemical Deposition on ZnO Mesocrystals for Practical Photoelectrochemical Applications. *J. Phys. Chem. C* **2013**, *117* (48), 25596–25603.
- (5) Zaraska, L.; Mika, K.; Syrek, K.; Sulka, G. D. Formation of ZnO Nanowires during Anodic Oxidation of Zinc in Bicarbonate Electrolytes. *J. Electroanal. Chem.* **2017**, *801* (8), 511–520.
- (6) Miles, D.; Cameron, P.; Mattia, D. Hierarchical 3D ZnO Nanowire Structures via Fast Anodization of Zinc. *J. Mater. Chem. A* **2015**, *3* (34), 17569–17577.
- (7) Kaleva, A.; Saarimaa, V.; Heinonen, S.; Nikkanen, J.-P.; Markkula, A.; Väisänen, P.; Levänen, E. Dissolution-Induced Nanowire Synthesis on Hot-Dip Galvanized Surface in Supercritical Carbon Dioxide. *Nanomaterials* **2017**, *7* (7), 181–190.
- (8) Mah, C. F.; Beh, K. P.; Yam, F. K.; Hassan, Z. Rapid Formation and Evolution of Anodized-Zn Nanostructures in NaHCO<sub>3</sub> Solution. *ECS J. Solid State Sci. Technol.* **2016**, *5* (10), M105–M112.
- (9) Kanari, N.; Mishra, D.; Gaballah, I.; Dupré, B. Thermal Decomposition of Zinc Carbonate Hydroxide. *Thermochim. Acta* **2004**, *410* (1–2), 93–100.
- (10) Saarimaa, V.; Kaleva, A.; Paunikallio, T.; Nikkanen, J.-P.; Heinonen, S.; Väisänen, E.; Väisänen, P.; Markkula, A. Convenient Extraction Method for Quantification of Thin Zinc Patina Layers. *Surf. Interface Anal.* **2018**, *50* (5), 564–570.
- (11) Loring, J.; Thompson, C.; Zhang, C.; Wang, Z.; Schaeff, H.; Rosso, K. Situ Infrared Spectroscopic Study of Brucite Carbonation in Dry to Water-Saturated Supercritical Carbon Dioxide. *J. Phys. Chem. A* **2012**, *116*, 4768–4777.
- (12) Hölzl, G.; Luckeneder, G.; Duchaczek, H.; Kleber, C.; Hassel, A. W. Evolution and Interaction of Corrosive Species during the Initial NaCl Particle Induced Corrosion on Zinc Coated Skin-Passed Steel. *Corros. Sci.* **2017**, *127*, 222–229.
- (13) Davis, A.; Oliver, B. A Vibrational-Spectroscopic Study of the Species Present in the CO<sub>2</sub>-H<sub>2</sub>O System. *J. Solution Chem.* **1972**, *1* (4), 329–339.
- (14) O'Connor, M. A Study of the Kinetics of the Basic Zinc Carbonate Formation Reaction. *Z. Naturforsch., B: J. Chem. Sci.* **1975**, *30b*, 665–668.
- (15) Toews, K.; Wai, C.; Shroll, R.; et al. PH-Defining Equilibrium between Water and Supercritical CO<sub>2</sub>. Influence on SFE of Organics and Metal Mhelates. *Anal. Chem.* **1995**, *67* (22), 4040–4043.
- (16) Timma, C.; Lostak, T.; Janssen, S.; Flock, J.; Mayer, C. Surface Investigation and Tribological Mechanism of a Sulfate-Based Lubricant Deposited on Zinc-Coated Steel Sheets. *Appl. Surf. Sci.* **2016**, *390*, 784–794.
- (17) Falk, T.; Svensson, J.; Johansson, L. The Role of Carbon Dioxide in the Atmospheric Corrosion of Zinc. *J. Electrochem. Soc.* **1998**, *145* (1), 39–44.
- (18) Loring, J.; Thompson, C.; Wang, Z.; Joly, A.; Sklarew, D.; Schaeff, H.; Ilton, E.; Rosso, K.; Felmy, A. In Situ Infrared Spectroscopic Study of Forsterite Carbonation in Wet Supercritical CO<sub>2</sub>. *Environ. Sci. Technol.* **2011**, *45* (14), 6204–6210.
- (19) Bockelmann, M.; Reining, L.; Kunz, U.; Turek, T. Electrochemical Characterization and Mathematical Modeling of Zinc Passivation in Alkaline Solutions: A Review. *Electrochim. Acta* **2017**, *237*, 276–298.
- (20) Mokaddem, M.; Volovitch, P.; Ogle, K. The Anodic Dissolution of Zinc and Zinc Alloys in Alkaline Solution. I. Oxide Formation on Electroplated Steel. *Electrochim. Acta* **2010**, *55* (27), 7867–7875.
- (21) Diler, E.; Lescop, B.; Rioual, S.; Nguyen Vien, G.; Thierry, D.; Rouvellou, B. Initial Formation of Corrosion Products on Pure Zinc and MgZn<sub>2</sub> Examined by XPS. *Corros. Sci.* **2014**, *79*, 83–88.
- (22) Prestat, M.; Holzer, L.; Lescop, B.; Rioual, S.; Zaubitzer, C.; Diler, E.; Thierry, D. Microstructure and Spatial Distribution of Corrosion Products Anodically Grown on Zinc in Chloride Solutions. *Electrochem. Commun.* **2017**, *81* (May), 56–60.
- (23) Gaur, A.; Park, J. W.; Jang, J. H. Metal-Carbonate Formation from Ammonia Solution by Addition of Metal Salts - An Effective Method for CO<sub>2</sub> capture from Landfill Gas (LFG). *Fuel Process. Technol.* **2010**, *91* (11), 1500–1504.
- (24) Falgayrac, G.; Sobanska, S.; Bremard, C. Raman Diagnostic of the Reactivity between ZnSO<sub>4</sub> and CaCO<sub>3</sub> Particles in Humid Air Relevant to Heterogeneous Zinc Chemistry in Atmosphere. *Atmos. Environ.* **2014**, *85*, 83–91.
- (25) Patrinoiu, G.; Calderón-Moreno, J. M.; Culita, D. C.; Birjega, R.; Ene, R.; Carp, O. Eco-Friendly Synthetic Route for Layered Zinc Compound and Its Conversion to ZnO with Photocatalytic Properties. *Solid State Sci.* **2013**, *23*, 58–64.
- (26) Hugot-Le Goff, A.; Joiret, S.; Saidani, B.; Wiart, R. In-Situ Raman Spectroscopy Applied to the Study of the Deposition and Passivation of Zinc in Alkaline Electrolytes. *J. Electroanal. Chem. Interfacial Electrochem.* **1989**, *263* (1), 127–135.
- (27) Carbuicchio, M.; Ciprian, R.; Ospitali, F.; Palombarini, G. Morphology and Phase Composition of Corrosion Products Formed at the Zinc-Iron Interface of a Galvanized Steel. *Corros. Sci.* **2008**, *50* (9), 2605–2613.
- (28) Zhang, W.; Smith, R.; Lowe, C. Confocal Raman Microscopy Study of the Melamine Distribution in Polyester-Melamine Coil Coating. *J. Coatings Technol. Res.* **2009**, *6* (3), 315–328.
- (29) Hambrock, C.; Vincze-Minya, K.; Hild, S.; Hassel, A. W. Raman Imaging for Surface Characterisation of Annealed Electrical Steel Surfaces. *Phys. Status Solidi A* **2014**, *211* (6), 1429–1438.
- (30) Song, Y.; Tang, J.; Hu, J.; Yang, H.; Gu, W.; Fu, Y.; Ji, X. Interfacial Assistant Role of Amine Additives on Zinc Electrodeposition from Deep Eutectic Solvents: An In Situ X-Ray Imaging Investigation. *Electrochim. Acta* **2017**, *240*, 90–97.
- (31) Perez-Guaíta, D.; Kochan, K.; Rütther, A.; Heraud, P.; Quintas, Q.; Wood, B. Multimodal Imaging of Cells and Tissues: All Photons Are Welcome. *Spectroscopy Eur.* **2017**, *29* (5), 6–9.
- (32) Thomas, S.; Birbilis, N.; Venkatraman, M. S.; Cole, I. S. Self-Repairing Oxides to Protect Zinc: Review, Discussion and Prospects. *Corros. Sci.* **2013**, *69*, 11–22.

- (33) Falk, T.; Svensson, J.; Johansson, L. The Influence of CO<sub>2</sub> and NaCl on the Atmospheric Corrosion of Zinc, a Laboratory Study. *J. Electrochem. Soc.* **1998**, *145* (9), 2993–2999.
- (34) Saariama, V.; Kaleva, A.; Nikkanen, J. P.; Heinonen, S.; Levänen, E.; Väisänen, P.; Markkula, A.; Juhanoja, J. Supercritical Carbon Dioxide Treatment of Hot Dip Galvanized Steel as a Surface Treatment before Coating. *Surf. Coat. Technol.* **2017**, *331*, 137–142.
- (35) Moulder, J.; Stickle, W.; Sobol, P.; Bomben, K. *Handbook of X-Ray Photoelectron Spectroscopy*; Chastain, J., King, R., Jr., Eds.; Physical Electronics, Inc.: USA, 1995.
- (36) Biesinger, M. C.; Lau, L. W. M.; Gerson, A. R.; Smart, R. S. C. Resolving Surface Chemical States in XPS Analysis of First Row Transition Metals, Oxides and Hydroxides: Sc, Ti, V, Cu and Zn. *Appl. Surf. Sci.* **2010**, *257* (3), 887–898.
- (37) Goldstein, J.; Newbury, D.; Joy, D.; Lyman, C.; Echlin, P.; Lifshin, E.; Sawyer, L.; Michael, J. *Scanning Electron Microscopy and X-Ray Microanalysis*, 3rd ed.; Springer: US, 2013.
- (38) Chang, K.; Tsai, T.; Chang, T.; Syu, Y.; Huang, H.; Hung, Y.; Young, T.; Gan, D.; Ho, N. Low-Temperature Synthesis of ZnO Nanotubes by Supercritical CO<sub>2</sub> Fluid Treatment. *Electrochem. Solid-State Lett.* **2011**, *14* (9), K47–K50.
- (39) Turianicová, E.; Kaňuchová, M.; Zorkovská, A.; Holub, M.; Bujňáková, Z.; Dutková, E.; Baláž, M.; Findoráková, L.; Balintová, M.; Obut, A. CO<sub>2</sub> utilization for Fast Preparation of Nanocrystalline Hydrozincite. *J. CO<sub>2</sub> Util.* **2016**, *16*, 328–335.
- (40) Wang, N.; Chen, M.; Ni, H. Preparation of Magnesium Carbonate Whisker from Magnesite Tailings. *IOP Conf. Ser.: Mater. Sci. Eng.* **2011**, *18*, 222013.
- (41) Helveg, S.; Sehested, J.; Rostrup-Nielsen, J. R. Whisker Carbon in Perspective. *Catal. Today* **2011**, *178* (1), 42–46.
- (42) Wiebe, R.; Gaddy, V. The Solubility of Carbon Dioxide in Water at Various Temperatures from 12 to 40° and at Pressures to 500 atm. *J. Am. Chem. Soc.* **1940**, *62* (4), 815–817.
- (43) Mohanan Pillai, K.; Ittyachen, M. A. Growth and Kinetic Studies of Lead Carbonate Whiskers in Silica Gel. *Pramana* **1978**, *10* (6), 613–619.
- (44) Wang, N.; Chen, M.; Ni, H. W. Preparation of Magnesium Carbonate Whisker from Magnesite Tailings. *IOP Conf. Ser.: Mater. Sci. Eng.* **2011**, *18*, 222013.
- (45) Biesinger, M. C.; Hart, B. R.; Polack, R.; Kobe, B. A.; Smart, R. S. C. Analysis of Mineral Surface Chemistry in Flotation Separation Using Imaging XPS. *Miner. Eng.* **2007**, *20* (2), 152–162.
- (46) Saw, K. G.; Ibrahim, K.; Lim, Y. T.; Chai, M. K. Self-Compensation in ZnO Thin Films: An Insight from X-Ray Photoelectron Spectroscopy, Raman Spectroscopy and Time-of-Flight Secondary Ion Mass Spectroscopy Analyses. *Thin Solid Films* **2007**, *515* (5), 2879–2884.
- (47) Duchoslav, J.; Arndt, M.; Keppert, T.; Luckeneder, G.; Stifter, D. XPS Investigation on the Surface Chemistry of Corrosion Products on ZnMgAl-Coated Steel. *Anal. Bioanal. Chem.* **2013**, *405* (22), 7133–7144.
- (48) Hope, G.; Woods, R.; Munce, C. Raman Microprobe Mineral Identification. *Miner. Eng.* **2001**, *14* (12), 1565–1577.
- (49) Socrates, G. *Infrared and Raman Characteristic Group Frequencies. Tables and Charts*, 3rd ed.; John Wiley & Sons, Ltd.: England, 2001.
- (50) Guerra-López, J. R.; Echeverría, G. A.; Güida, J. A.; Viña, R.; Punte, G. Synthetic Hydroxyapatites Doped with Zn(II) Studied by X-Ray Diffraction, Infrared, Raman and Thermal Analysis. *J. Phys. Chem. Solids* **2015**, *81*, 57–65.
- (51) Frost, R.; Hales, M.; Wain, D. Raman Spectroscopy of Smithsonite. *J. Raman Spectrosc.* **2008**, *39* (1), 108–114.
- (52) Frost, R. L.; Martens, W. N.; Wain, D. L.; Hales, M. C. Infrared and Infrared Emission Spectroscopy of the Zinc Carbonate Mineral Smithsonite. *Spectrochim. Acta, Part A* **2008**, *70* (5), 1120–1126.
- (53) Nyquist, R.; Kagel, R. *Handbook of Infrared and Raman Spectra of Inorganic Compounds and Organic Salts, Vol. 4 Infrared Spectra of Inorganic Compound (3800–45 cm<sup>-1</sup>)*; Academic Press, Inc.: San Diego, CA, 1997.
- (54) Hales, M. C.; Frost, R. L. Synthesis and Vibrational Spectroscopic Characterisation of Synthetic Hydrozincite and Smithsonite. *Polyhedron* **2007**, *26* (17), 4955–4962.
- (55) Adler, H.; Kerr, P. Infrared Absorption Frequency Trends for Anhydrous Normal Carbonates. *Am. Mineral.* **1963**, *48*, 124–137.
- (56) Cheng, J.; Poduska, K. A Strategy for Hydroxide Exclusion in Nanocrystalline Solid-State Metathesis Products. *Nanomaterials* **2013**, *3* (3), 317–324.
- (57) Zhang, X.; Liu, X.; Odneval Wallinder, I.; Leygraf, C. The Protective Role of Hydrozincite during Initial Corrosion of a Cu<sub>40</sub>Zn Alloy in Chloride-Containing Laboratory Atmosphere. *Corros. Sci.* **2016**, *103*, 20–29.
- (58) Ohtsuka, T.; Matsuda, M. In Situ Raman Spectroscopy for Corrosion Products of Zinc in Humidified Atmosphere in the Presence of Sodium Chloride Precipitate. *Corrosion* **2003**, *59* (5), 407–413.
- (59) Beck, L.; Gutiérrez, P. C.; Miro, S.; Miserque, F. Ion Beam Modification of Zinc White Pigment Characterized by Ex Situ and In Situ M-Raman and XPS. *Nucl. Instrum. Methods Phys. Res., Sect. B* **2017**, *409*, 96–101.
- (60) Ghose, S. The Crystal Structure of Hydrozincite. *Acta Crystallogr.* **1964**, *17* (8), 1051–1057.
- (61) Stoilova, D.; Koleva, V.; Vassileva, V. Infrared Study of Some Synthetic Phases of Malachite (Cu<sub>2</sub>(OH)<sub>2</sub>CO<sub>3</sub>)-Hydrozincite (Zn<sub>5</sub>(OH)<sub>6</sub>(CO<sub>3</sub>)<sub>2</sub>) Series. *Spectrochim. Acta, Part A* **2002**, *58* (9), 2051–2059.
- (62) Bouchard, M.; Smith, D. C. Evaluating Raman Microscopy for the Non-Destructive Archaeometry of Corroded Coins: A Powerful Technique for Conservation Studies. *Asian Chem. Lett.* **2001**, *5* (3), 157–170.
- (63) Burgio, L.; Clark, R. J. H. *Spectrochim. Acta, Part A* **2001**, *57*, 1491.
- (64) Zhang, D.; Wang, L.; Qian, H.; Li, X. Superhydrophobic Surfaces for Corrosion Protection: A Review of Recent Progresses and Future Directions. *J. Coatings Technol. Res.* **2016**, *13* (1), 11–29.
- (65) Yang, J.; Cheng, H.; Frost, R. L. Synthesis and Characterisation of Cobalt Hydroxy Carbonate Co<sub>2</sub>CO<sub>3</sub>(OH)<sub>2</sub>nanomaterials. *Spectrochim. Acta, Part A* **2011**, *78* (1), 420–428.
- (66) Herring, C.; Galt, J. Elastic and Plastic Properties of Very Small Metal Specimens. *Phys. Rev.* **1952**, *85*, 1060–1061.

PUBLICATION  
V

**Formation of corrosion products on zinc in wet supercritical and subcritical  
CO<sub>2</sub>: In-situ spectroscopic study**

A. Kaleva, T. Tassaing, V. Saarimaa, G. Le Bourdon, P. Väisänen, A.  
Markkula, E. Levänen

Corrosion Science, Vol. 174, 108850  
<https://doi.org/10.1016/j.corsci.2020.108850>

**Publication reprinted with the permission of the copyright holders.**





## Formation of corrosion products on zinc in wet supercritical and subcritical CO<sub>2</sub>: In-situ spectroscopic study



A. Kaleva<sup>a,\*</sup>, T. Tassaing<sup>b</sup>, V. Saarimaa<sup>c</sup>, G. Le Bourdon<sup>b</sup>, P. Väisänen<sup>d</sup>, A. Markkula<sup>d</sup>, E. Levänen<sup>a</sup>

<sup>a</sup> Unit of Materials Science and Environmental Engineering, Tampere University, P.O. Box 589, FI-33101 Tampere, Finland

<sup>b</sup> Institut des Sciences Moléculaires, UMR 5255 CNRS-Université de Bordeaux, 351 Cours de la Libération, 33405 Talence Cedex, France

<sup>c</sup> Top Analytica, Ruukinkatu 4, FI-20540 Turku, Finland

<sup>d</sup> SSAB Europe, Harvialantie 420, FI-13300 Hämeenlinna, Finland

### ARTICLE INFO

#### Keywords:

Zinc  
Raman spectroscopy  
IR spectroscopy  
SEM  
Oxidation  
Acid corrosion

### ABSTRACT

Formation of corrosion products on zinc was investigated with in-situ Raman and FTIR when exposed to wet supercritical carbon dioxide (scCO<sub>2</sub>) and subsequent depressurization. Zinc oxide (ZnO) and smithsonite (ZnCO<sub>3</sub>) formed on zinc in scCO<sub>2</sub>. The dissolved water precipitated as liquid water in the reaction cell during depressurization. Formation of ZnO, ZnCO<sub>3</sub> and a needle-like zinc hydroxy carbonate species on zinc was observed inside a sessile water droplet during conditions simulating the depressurization phase. Addition of oxygen accelerated the formation of the carbonate species due to higher cathodic activity that increased zinc dissolution.

### 1. Introduction

Zinc is widely used for corrosion protection in galvanized steels by providing sacrificial protection. The surface of galvanized steel typically has poor adhesion to organic coatings and requires an adhesion layer that is currently obtained by chemical surface treatments of zinc within the industry [1,2]. However, the chemicals used in the treatments are harmful for the environment, which has led to the search of alternative methods [3,4]. Carbonates formed on zinc surfaces due to atmospheric corrosion have shown exceptional improvement in corrosion resistance of zinc, as well as better adhesion for organic coatings that are later applied [5–9]. Therefore, artificially grown carbonate layer produced with a scCO<sub>2</sub>-treatment method would provide advantageous surface properties as shown in our previous studies [10,11]. The present study aims to investigate in detail the interactions of zinc, CO<sub>2</sub> and water that occur in the wet supercritical and subcritical CO<sub>2</sub> conditions during the treatment.

Zinc carbonates are insoluble corrosion products that form when metallic zinc is exposed to atmospheric CO<sub>2</sub> and humidity. Examples of these carbonates are, e.g. hydrozincite (Zn<sub>5</sub>(CO<sub>3</sub>)<sub>2</sub>(OH)<sub>6</sub>), other zinc hydroxy carbonates and smithsonite (ZnCO<sub>3</sub>) [12,13]. The formation of the naturally grown carbonates starts by reactions between zinc, oxygen and water that form initial corrosion products such as zinc oxide (ZnO) and zinc hydroxide (Zn(OH)<sub>2</sub>) [14]. As atmospheric CO<sub>2</sub> dissolves into rainwater and air humidity, it reacts with water to form

carbonic acid (H<sub>2</sub>CO<sub>3</sub>). Carbonic acid further dissociates into bicarbonate (HCO<sub>3</sub><sup>−</sup>) and carbonate (CO<sub>3</sub><sup>2−</sup>) ions that react with the initial corrosion products to form zinc carbonates when the water is in contact with the zinc surface [7,14]. The water layer will then dry in air and subsequently wet again in a repeating cyclical process and results in better coverage of the carbonate layer on zinc [7,15]. However, this process could take up to two years for a fully-developed carbonate layer to form before the application of organic coatings is viable [5]. Consequently, an accelerated carbonate formation process would be effective.

The concentration of CO<sub>2</sub> is one of the limiting factors in zinc carbonate formation [16]. When CO<sub>2</sub> is heated and pressurized, it becomes supercritical with a vastly higher concentration of CO<sub>2</sub> compared to the atmosphere [17]. Supercritical CO<sub>2</sub> (scCO<sub>2</sub>) is also capable of dissolving water which allows water to react with substances in the entire volume of the reaction cell. Furthermore, carbonates are shown to form on mineral surfaces, i.e. magnesium silicates, as well as steel surfaces when exposed to scCO<sub>2</sub> saturated with water [18–20].

We previously observed the formation of carbonate structures on galvanized steel in a wet scCO<sub>2</sub> treatment and showed its viability as a pretreatment method before organic coating application [10,11]. While the applicability of this treatment has already been demonstrated, more information on the formation process needs to be obtained for a fundamental understanding of the treatment process. This study investigated the interactions between zinc, water and pressurized CO<sub>2</sub> in

\* Corresponding author.

E-mail address: [aaretti.kaleva@tuni.fi](mailto:aaretti.kaleva@tuni.fi) (A. Kaleva).

<https://doi.org/10.1016/j.corsci.2020.108850>

Received 14 April 2020; Received in revised form 9 June 2020; Accepted 30 June 2020

Available online 04 July 2020

0010-938X/ © 2020 The Authors. Published by Elsevier Ltd. This is an open access article under the CC BY license (<http://creativecommons.org/licenses/by/4.0/>).

the wet  $\text{scCO}_2$  phase as well as in the presence of a liquid water layer under subcritical  $\text{CO}_2$  conditions. The formation of zinc carbonates on the zinc surface was measured during the wet  $\text{scCO}_2$  treatment by in-situ Raman and FTIR methods. The interactions of a liquid water layer on zinc was studied with sessile droplet tests with in-situ Raman. Furthermore, the effect of oxygen on corrosion product formation was investigated.

## 2. Materials and methods

The substrate material used was zinc sheet (99,9 m-%, Alfa Aesar) that was cut into circular specimens ( $d = 12$  mm). Two holes ( $d = 1$  mm) were drilled into the specimens to allow  $\text{CO}_2$  to enter between the sample and window in the cell setup. The specimen surfaces were ground and polished with silicon carbide paper to a mirror finish and ultrasonically cleaned in ethanol to prevent oxidation.  $\text{CO}_2$  (99,95 %) and  $\text{O}_2$  (99,99 %) were obtained from Air Liquide. All experiments were conducted in a stainless-steel cell with a volume of 5.4 mL [21].

### 2.1. Wet $\text{scCO}_2$ tests (in-situ Raman and FTIR)

Raman and FTIR are distinguished methods for in-situ investigation of carbonate formation [22,23]. The schematic of the sample setup of the  $\text{scCO}_2$  experiments can be seen from Fig. 1. The samples were fixed into the cell parallel to the measurement window. In-situ Raman and FTIR measurements were done for the  $\text{scCO}_2$  experiments. Signals were recorded through the window, as presented in Fig. 1. Water and a magnetic stirrer were placed in a container at the bottom of the cell. The amount of water (0.2 mL) used in the experiments was in excess of what  $\text{scCO}_2$  can dissolve at the chosen treatment conditions [24]. The water in the  $\text{scCO}_2$  tests was placed in a distant container inside the cell to ensure no liquid water emulsion droplets could contact the sample surface. The setup of the cell was the same for measurements in both Raman and FTIR except for different window material. Sapphire was used for the Raman experiments and Calcium fluoride ( $\text{CaF}_2$ ) for the FTIR measurements because of sapphire's high absorption of infrared radiation in the measurement range.

The treatments were conducted under a  $\text{CO}_2$  pressure of 100 bar with two different sample temperatures of 40 °C and 60 °C. Specimens were kept in static conditions for 120 min after which the reaction cell was slowly depressurized for 15 min. Separate samples were exposed for in-situ Raman and in-situ FTIR measurements. The total amount of samples was four, as seen in Table 1.

The in-situ spectra for the FTIR measurements in Fig. 8 were processed due to multiple overlapping peaks between reaction species. Consequently, the influence of  $\text{CO}_2$  and dissolved water was mitigated

**Table 1**

Sample conditions for the  $\text{scCO}_2$  tests.

100 bar $\text{CO}_2$		
40 °C	Raman	FTIR
60 °C	Raman	FTIR

by subtracting the 10-minute spectrum from the subsequent measurement spectra. The subtraction helps to detect the time-dependent structural changes on the zinc surface without the influence of the surrounding  $\text{scCO}_2$  phase.

### 2.2. Sessile droplet tests (in-situ Raman)

The sample schematic for the sessile droplet experiments can be seen in Fig. 2. In-situ Raman measurements and optical imaging were conducted for the droplet experiments. The sample was fixed to the cell similarly to  $\text{scCO}_2$  experiments except for a longer distance between the sample and window to eliminate contact between droplet and window. The experiments were conducted by placing the droplet on the sample surface before transferring it to the cell setup. The sample with the droplet was quickly moved to the experimental setup to start the experiment to prevent oxidation before introducing the gases. The surface of the zinc under the droplet was measured with Raman prior to the experiment to ensure no oxidation had occurred. The droplet size used in all experiments was 3  $\mu\text{L}$  ( $D = 2.19 \pm 0.06$  mm). The optical images were taken from the middle of the droplet for each test. Sapphire window was used for the experiments.

The experiment conditions of the droplet tests was temperature of 22 °C (room temperature) in 5 bar  $\text{CO}_2$  pressure. The tests were performed without extra oxygen (Sample A) and with additional 2 bar of  $\text{O}_2$  (Sample B) as shown in Table 2.

### 2.3. Characterization

Scanning electron microscopy (SEM) characterization was performed with JEOL JSM-IT500 together with integrated EDS detector (JEOL, silicon drift detector). The samples were also characterized with XRD (Panalytical Empyrean, monochromatized  $\text{CuK}\alpha$  radiation,  $5 < 2\theta < 80$ ) by using grazing incidence measurement (GIXRD) to focus the analysis on the topmost layer of the samples.

The Raman experiments were done using Jobin-Yvon Horiba XploRA confocal Raman microscope equipped with a 50X objective and a laser diode with a maximum power of 45 mW [21]. The spectral range of 200 – 1900  $\text{cm}^{-1}$  was recorded with a grating of 1800 l/mm and resolution of 4  $\text{cm}^{-1}$ . The measurements used  $\lambda = 532$  nm wavelength

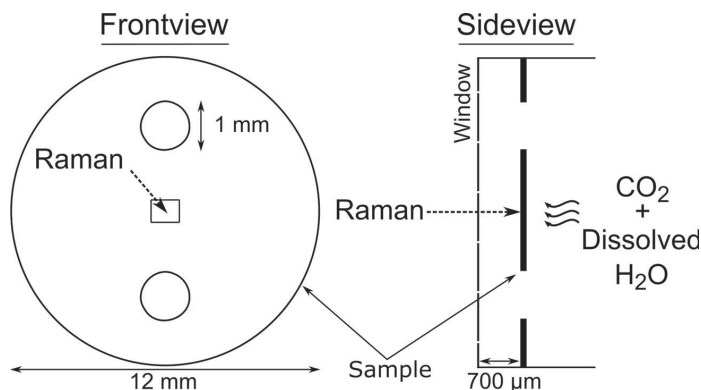


**Fig. 1.** Schematic of the sample setup in the wet  $\text{scCO}_2$  tests.

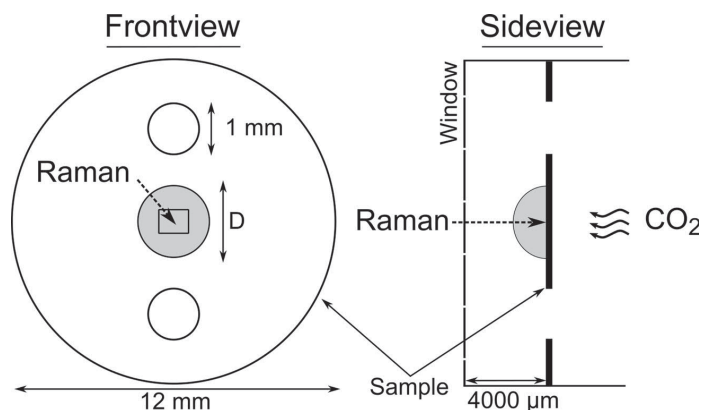


Fig. 2. Schematic of the sample setup in the droplet tests.

Table 2

Sample conditions for the sessile droplet tests.

	5 bar CO <sub>2</sub>	5 bar CO <sub>2</sub> 2 bar O <sub>2</sub>
22 °C	Sample A	Sample B

and 100 % laser power. Two 60 s spectra acquisitions were taken for each measurement to improve the signal-to-noise ratio.

The infrared experiments were performed using an FTIR microscope working in transfection mode coupled with a high-pressure cell [25]. The FTIR microscope consists in a ThermoOptek interferometer (type 6700) with a globar source and KBr/Ge beamsplitters coupled to an infrared microscope (NicPlan, Nicolet) equipped with a 15X cassegrain objective and an MCT (Mercury Cadmium Telluride) detector to investigate the spectral range from 400 to 7500 cm<sup>-1</sup>. Single beam spectra recorded with a 2 cm<sup>-1</sup> resolution were obtained after the Fourier transformation of 32 accumulated interferograms.

### 3. Results and discussion

#### 3.1. In-situ wet scCO<sub>2</sub> tests (Raman and FTIR)

The optical images that were taken during the in-situ Raman tests in wet scCO<sub>2</sub> (Fig. 3) show the appearance of dark spatters on the Zn-surface due to the wet scCO<sub>2</sub> treatment at both treatments performed in 40 °C and 60 °C. The zinc surface is rapidly covered with the spatters at 40 °C in the first 30 min, and continue to significantly increase in

quantity by the end of the treatment. The 60 °C sample showed a similar behaviour as the 40 °C sample but with considerably less change on the surface. The dark spatters indicate the early stages of corrosion on the zinc surface, which is initiated by the dissolved water in the scCO<sub>2</sub> phase as no free water is present.

The Raman spectra taken from designated spots shown in the optical images (white circles) can be seen in Fig. 4. The weak peaks observed between 400 – 500 cm<sup>-1</sup> and at 730 cm<sup>-1</sup> that are present in all in-situ spectra (5–120 minutes) are due to the sapphire window used in the experiments. There is no noticeable Raman signal during the first 90 min in either sample even though there was an apparent visual change on the surfaces as seen from Fig. 3. At 120 min, the Raman spectrum of the 40 °C sample indicates the presence of ZnCO<sub>3</sub> due to  $\nu_1$  symmetric stretching mode at 1093 cm<sup>-1</sup> and lattice mode at 300 cm<sup>-1</sup> [26]. In the 60 °C sample, no carbonate peaks could be detected in the in-situ spectra, but a broad and small intensity peak at 570 cm<sup>-1</sup> appears at 120 min. Earlier studies suggest that this peak corresponds to nanosized zinc oxide (ZnO) [14,27,28]. ZnO is generally considered to be an intermediate reaction step before the formation of carbonate species or other zinc corrosion products [7,17]. The ZnO formation in these experiments could be due to the reaction between zinc and dissolved oxygen that forms ZnCO<sub>3</sub> in subsequent reactions with CO<sub>3</sub><sup>2-</sup> and HCO<sub>3</sub><sup>-</sup> ions. The oxygen could derive from the remaining dissolved oxygen in the water or the air confined inside the cell.

The ex-situ spectra were taken after the experiments from the sample surfaces without the measurement window. Both samples show peaks at 1093 cm<sup>-1</sup>, 300 cm<sup>-1</sup> and a new peak at 730 cm<sup>-1</sup> which is the  $\nu_4$  antisymmetric bending mode of ZnCO<sub>3</sub> [26]. The samples also show a broad peak at around 570 cm<sup>-1</sup> with an intensity that varied

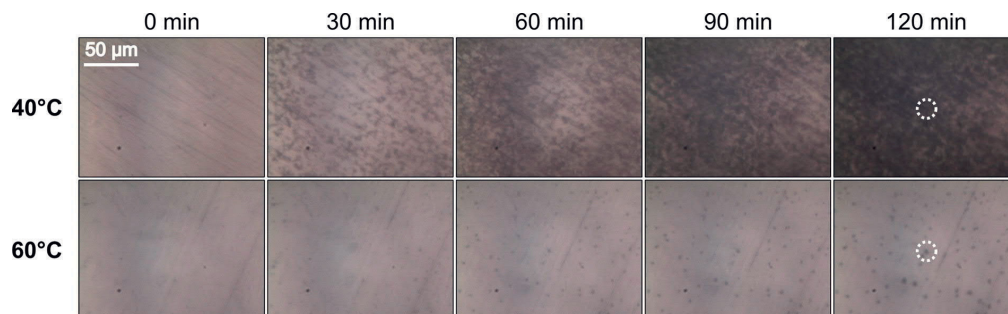


Fig. 3. In-situ optical images of Zn samples in wet scCO<sub>2</sub> at 100 bar pressure and treatment temperatures of 40 °C and 60 °C. The circles indicate the area where the Raman signal was measured (2 μm Raman spot size).

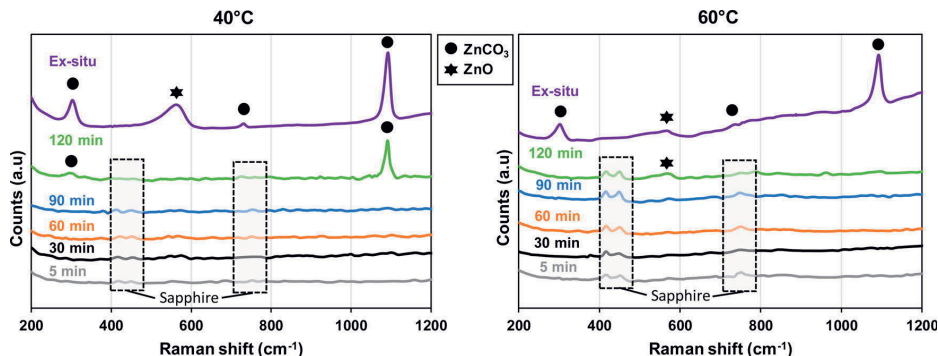


Fig. 4. In-situ and ex-situ Raman spectra of Zn samples in wet scCO<sub>2</sub> at 100 bar pressure and treatment temperatures of 40 °C and 60 °C.

independently compared to other peaks when measured from multiple places. The presence of the peak is likely due to residues of the initial corrosion product, ZnO, that did not react further to form carbonates.

The dark spatters that initially grew on the surface (Fig. 3) could be corrosion pits where initial zinc corrosion products formed. It is unambiguous from the 40 °C sample that ZnCO<sub>3</sub> does eventually form in the dark spatters either directly or through intermediate species, e.g. ZnO, as a result of corrosion in wet scCO<sub>2</sub>. The growth of the carbonate is also supported by the carbonate seen in the 60 °C sample even though no signal was detected during the in-situ experiment. The amount of the reaction products could likely be negligible for Raman to detect the carbonate species until a sufficient amount formed.

The SEM images in Fig. 5 show the morphology of the carbonate structures after the treatments in 40 °C (a) and 60 °C (b). Irregularly shaped carbonate structures formed on the 40 °C sample similar to the spherical structures with fine cubic features that we reported in our earlier studies [11]. The 60 °C sample shows dark spatters on the surface, which could indicate the initial stages of corrosion product formation. Both the structures seen in 40 °C and darker areas in 60 °C were identified with ex-situ Raman measurements as ZnCO<sub>3</sub> with traces of ZnO (Fig. 4). The EDS measurements showed the presence of only zinc, carbon and oxygen in the structures in both samples (not shown).

Based on the SEM and optical images as well as the in-situ Raman data, it is evident that the amount of reaction products is higher in the 40 °C sample compared to the 60 °C sample, which could be due to the differences in the amount of dissolved water at different temperatures. The absolute amounts of dissolved water in scCO<sub>2</sub> (Fig. 6) in our treatment conditions were calculated by implementing EOS-equations derived by Spycher et al. [24].

The increased amount of dissolved water in the scCO<sub>2</sub> phase will

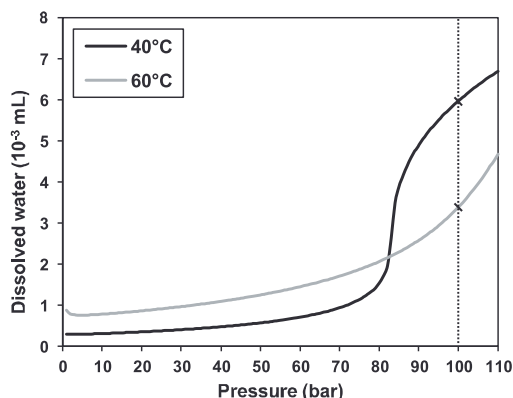


Fig. 6. The absolute amount of dissolved water in the scCO<sub>2</sub> according to the EOS-calculations using equations derived by Spycher et al. [24].

likely enhance the formation of reaction products on zinc, which is shown to be the case for steel in wet scCO<sub>2</sub> atmosphere [29,30]. The reaction dynamics of the carbonate formation could be affected by thermodynamic considerations as well due to the temperature difference. However, corrosion studies of zinc at atmospheric conditions show more corrosion in higher rather than lower temperatures, oppositely as observed in the scCO<sub>2</sub> tests [7,31]. Therefore, the effect of dissolved water amount is likely a more significant factor for the carbonate formation, although temperature itself might still have an

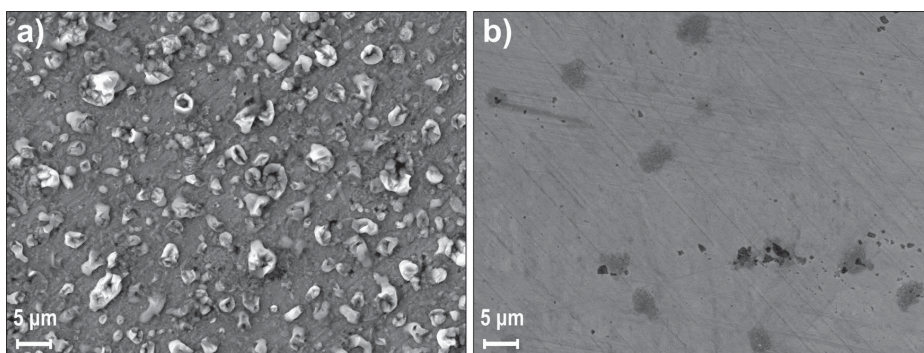


Fig. 5. SEM images of the Raman samples a) 40 °C and b) 60 °C.



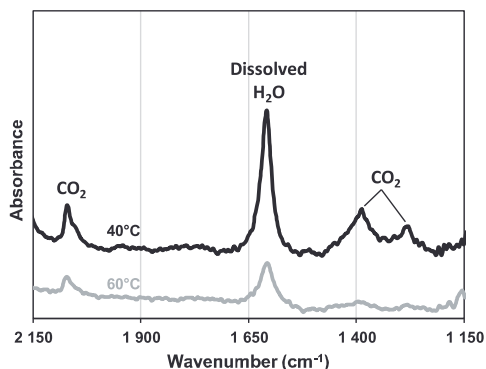


Fig. 7. In-situ FTIR spectra at 10-minute holding time of Zn samples in wet scCO<sub>2</sub> at 100 bar pressure and treatment temperatures of 40 °C and 60 °C.

impact on the reactions.

The in-situ FTIR experiments were performed with the same treatment parameters and in the same pressure cell as the in-situ Raman experiments. The goal of the FTIR measurements was to measure a larger representative area (100 μm × 100 μm) of the sample surfaces in contrast to the single point measurements (2 μm × 2 μm) done in the Raman studies. Furthermore, the presence of dissolved water and liquid water could be determined much more accurately. The FTIR spectra were recorded in the range of 1150 – 2150 cm<sup>-1</sup> for the treatments in both temperatures. The measurement spectra after 10 min can be seen from Fig. 7. The peaks of CO<sub>2</sub> shown in the spectra at 2000 – 2150 cm<sup>-1</sup> are assigned to a combination mode of the OCO bend ( $\nu_2$ ), and the symmetric stretch ( $\nu_1$ ) and the Fermi resonance peaks at 1387 cm<sup>-1</sup> and mode 1281 cm<sup>-1</sup> are respectively assigned to the symmetric stretching mode ( $\nu_1$ ) and the overtone of the OCO bending mode ( $2\nu_2$ ). The peak at 1607 cm<sup>-1</sup> is from HOH bending mode of dissolved water in the scCO<sub>2</sub> phase [32]. At 10 min treatment time, only CO<sub>2</sub> and dissolved water were detected in the FTIR spectra.

The intensity of the dissolved water peak correlates directly with the amount of dissolved water in CO<sub>2</sub> [32]. It can be seen that the amount of water is more significant at 40 °C compared to 60 °C, as discussed earlier in the Raman results. By the same token, the intensity of the CO<sub>2</sub> peaks put in evidence the lower density of CO<sub>2</sub> at 60 °C ( $\rho(\text{CO}_2, 60^\circ\text{C}) = 290 \text{ kg/m}^3$ ) compared to 40 °C ( $\rho(\text{CO}_2, 40^\circ\text{C}) = 630 \text{ kg/m}^3$ ) at the same pressure. The 10-minute measurements were chosen as references

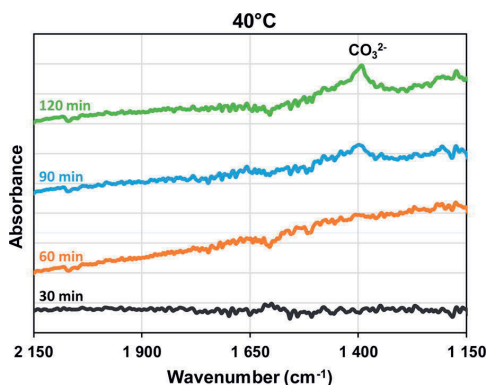


Fig. 8. In-situ FTIR spectra at 30, 60, 90 and 120 min holding times of Zn samples in wet scCO<sub>2</sub> at 100 bar pressure and treatment temperature of 40 °C. The spectra have been processed by subtracting the 10-minute spectrum.

for the rest of the in-situ spectra since no other species were detected at this point in the treatment. It was also a sufficient time to ensure homogeneous mixing of the water into the scCO<sub>2</sub>. The final processed spectra for the in-situ measurements at 40 °C and treatment times of 30, 60, 90 and 120 min are shown in Fig. 8.

The 40 °C sample shows the emergence of a peak at 1390 cm<sup>-1</sup> that is typical for  $\nu_3$  antisymmetric stretching of CO<sub>3</sub><sup>2-</sup> for ZnCO<sub>3</sub> [26]. The measurements show that the carbonate formation started between 60- and 90-minutes holding times. Although FTIR or Raman signal of the corrosion products was not detected in the early stages of the treatment, the formation likely started earlier as visually observed from the in-situ images (Fig. 3). Liquid water was not detected on the surface during the treatment period. However, it is likely that a small water layer is present on the zinc surface to enable carbonate growth. Due to prior observation about the insensitivity of Raman and FTIR to small amounts of carbonates, the signal from a minute liquid water film on the zinc surface could also be challenging to detect. The 60 °C sample did not show any significant formation of carbonates in the FTIR spectra similarly as in Raman tests (Fig. S1, supporting information). The FTIR results are in good agreement with the earlier Raman measurements and confirm that the carbonate forms similarly even on a larger scale on the zinc surface.

In-situ FTIR spectra were also recorded during the depressurization after the 120-minute treatment (Fig. 9). The influence of CO<sub>2</sub> or dissolved water was not eliminated in these spectra so that the total behaviour of depressurization could be observed. Along with the wavenumber range 1150 – 2150 cm<sup>-1</sup> also the OH-region between 3000 – 3500 cm<sup>-1</sup> is presented.

The 40 °C spectrum shows a decrease in CO<sub>2</sub> pressure as the peaks 2070 cm<sup>-1</sup> and 1300 cm<sup>-1</sup> reduce in intensity. The overlapping peak of CO<sub>2</sub> and ZnCO<sub>3</sub> at 1390 cm<sup>-1</sup> decreases in intensity when CO<sub>2</sub> pressure decreases. However, the peak remains after CO<sub>2</sub> removal showing ZnCO<sub>3</sub> presence. The intensity of the dissolved water peak at 1607 cm<sup>-1</sup> is decreasing accordingly, and a slight peak at 1650 cm<sup>-1</sup> can be seen during 5–15 min of depressurization. This peak corresponds to the presence of liquid water which is further confirmed by the emergence of a broad peak at 3200 cm<sup>-1</sup> which is the vibration of OH-groups in water [23]. Liquid water appears when the dissolved water in the scCO<sub>2</sub> phase starts to precipitate as water [33]. The precipitation of water is a result of the decreasing solubility of water in scCO<sub>2</sub> as the pressure and temperature drop, especially below the supercritical point (74 bar, 31 °C). As the saturation level of the dissolved water drops, it starts to precipitate inside the pressure cell. Towards the end of depressurization, the liquid water peak and OH-vibration have

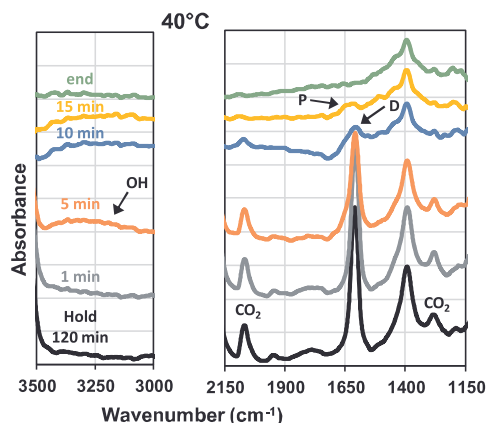


Fig. 9. In-situ spectra of FTIR 40 °C sample during depressurization. Letter “D” denotes dissolved water, and “P” precipitated water.

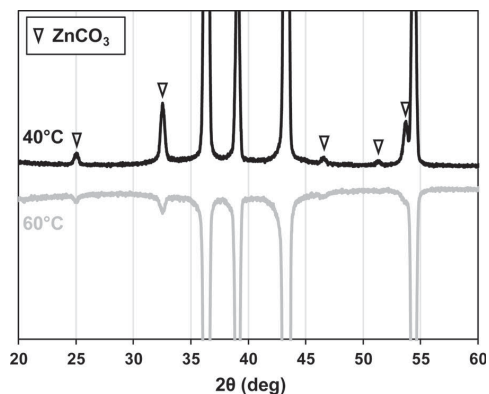


Fig. 10. XRD spectra of in-situ Raman samples. The unmarked peaks are characteristic of metallic zinc.

disappeared. Water could not be detected after all  $\text{CO}_2$  had been removed, and therefore no significant amount of the precipitated water came in contact with the zinc surface. Consequently, the majority of the precipitated water likely stayed in between the window and the sample and had a negligible effect on the zinc surface. However, a thicker water layer that forms with higher amounts of precipitation might affect the zinc surface more significantly, which is studied in the following chapter.

The XRD results of the Raman samples are shown in Fig. 10. The XRD peaks indicate the presence of  $\text{ZnCO}_3$  and metallic zinc from the substrate in all samples, which confirms the earlier Raman and FTIR results. XRD measurements of the FTIR samples showed identical results. Since no other carbonate species was observed, the formation of anhydrous  $\text{ZnCO}_3$  on zinc is the prevalent reaction in wet  $\text{scCO}_2$  phase.

### 3.2. In-situ sessile droplet tests (Raman)

We previously observed a needle-like zinc hydroxy carbonate species in similar treatment conditions which did not form in the  $\text{scCO}_2$  tests performed here [10,11,34–36]. Higher amounts of water precipitation compared to this study have shown to impact the corrosion of the sample surface in other studies during depressurization of  $\text{scCO}_2$  [29,37,38]. Therefore, the effect of a water layer on zinc in pressurized  $\text{CO}_2$  was investigated further with sessile droplet tests. As dissolved oxygen in water has been shown to affect the corrosion of zinc considerably due to its significant role in cathodic action [7,39], the effect of  $\text{O}_2$  gas addition was investigated as well.

The SEM images of the in-situ tests performed at 5 bar of  $\text{CO}_2$  and  $22^\circ\text{C}$  (room temperature) are shown in Fig. 11. Sample A is without extra oxygen and sample B with the addition of 2 bar of  $\text{O}_2$ . Additionally, the same tests were performed at  $40^\circ\text{C}$  temperature. The reaction conditions simulated the end of the depressurization phase of the  $\text{scCO}_2$  treatments. A needle-like structure arranged in flower shapes is observed in both samples. The needle-structure covers the entire droplet area in sample B with oxygen, whereas some areas of the surface of sample A remain exposed. The partial pressure of oxygen in the reaction for sample B is ten times higher than for sample A that is only exposed to one atmospheric pressure of air that remained in the cell after  $\text{CO}_2$  addition. Consequently, the availability of the dissolving oxygen in sample A diminishes, resulting in decreased reactivity due to insufficient cathodic action. Sample A also shows the presence of spherical structures on the zinc surface which might be hidden under the needle structure in sample B. The needle structure was much more prevalent compared to the spherical structure. The main difference in the  $40^\circ\text{C}$  samples (Fig. S3, supporting information) compared to the

$22^\circ\text{C}$  samples was more presence of the spherical structure instead of the needle structure. The morphology of the structures observed here in this study is identical to species shown in our previous studies, where the structures formed under  $\text{scCO}_2$  conditions [10,11,34–36]. Corrosion products are not observed outside the droplet area without the presence of water in the  $\text{CO}_2$  phase. As discussed earlier, the water dissolved in  $\text{scCO}_2$  induced growth of  $\text{ZnCO}_3$  in the immediate proximity of the zinc surface. Conversely,  $\text{CO}_2$  dissolved in a thick water layer resulted in the growth of the needle-like structure. The needle-like structure protrudes significantly from the surface [11] but not outside the droplet. Therefore, a thick water film is required for the needle-like structure to grow, which further explains its absence in the  $\text{scCO}_2$  phase.

Fig. 12 shows the in-situ optical images for samples A and B taken from the middle of the droplet. Dark deposits appear rapidly on sample B during the first 10 min. In contrast, only small changes occurred in sample A at the same time. Raman spectrum taken at 5 min from the middle of the image of sample B corresponds to  $\text{ZnO}$  (Fig. 13). Consequently, the oxygen addition accelerated the corrosion process considerably in the early stages of the test. However, both samples showed considerable reactivity at 60 min based on visual appearance.

The in-situ spectra of sample B are presented in Fig. 13.  $\text{ZnO}$  has not formed without the presence of  $\text{CO}_2$  or  $\text{O}_2$  as seen from the first spectrum (No  $\text{CO}_2$ ) which is taken just before the introduction of the gases. However,  $\text{ZnO}$  forms rapidly within the first 5 min of the experiment. The presence of  $\text{ZnO}$  continues until 45 min into the treatment without the presence of other species. Subsequently, a peak at  $1099\text{ cm}^{-1}$  emerges that was identified as the needle structure. The in-situ tests confirmed that the formation of  $\text{ZnCO}_3$  also occurred in the later stages of the experiment (Fig. S4, supporting information). The delayed formation of the carbonates is consistent in all samples, which is likely due to insufficient  $\text{CO}_2$  concentration early in the experiment. The diffusion of  $\text{CO}_2$  is relatively slow in water [40] and limits the reaction for the carbonate formation. The  $\text{ZnO}$  peak diminishes as the reaction progresses and disappears when the needle structure starts to grow. The conversion of  $\text{ZnO}$  to carbonate indicates that  $\text{ZnO}$  acts as an intermediate corrosion product, as was discussed earlier in the  $\text{scCO}_2$  section.

The ex-situ Raman spectra of the structures in sample A are presented in Fig. 14. The results show the presence of peaks  $300\text{ cm}^{-1}$ ,  $730\text{ cm}^{-1}$  and  $1093\text{ cm}^{-1}$  which correspond to  $\text{ZnCO}_3$  and a peak at  $570\text{ cm}^{-1}$  previously identified as nanosized  $\text{ZnO}$ . The needle structure had a different spectrum as the spherical structure with only a single distinct peak at  $1099\text{ cm}^{-1}$  that had a shoulder peak at  $1049\text{ cm}^{-1}$  as well as lower intensity peaks at  $235\text{ cm}^{-1}$  and  $390\text{ cm}^{-1}$ . The spectra of both structures were well in accordance with our earlier study on the same structures [11].

The XRD of the needle structure and hydrozincite reference are shown in Fig. 15. The spectrum does not match to any common zinc hydroxy carbonates, i.e. hydrozincite. However, the spectrum closely resembles structures zinc hydroxy carbonates synthesized by various techniques in other studies [41–44]. These studies, as well as our earlier characterizations, expect the chemical structure of the needles to be hydrated zinc hydroxy carbonate of form  $\text{Zn}_n(\text{CO}_3)_b(\text{OH})_c\cdot d\text{H}_2\text{O}$ . However, the exact stoichiometric composition remains unknown.

Illustration of the reactions occurring inside the droplet is presented in Fig. 16. Three main reactions take place in the formation of the reaction products.

- 1  $\text{Zn}^{2+}$  dissolution (Anodic reaction)
- 2  $\text{O}_2$  dissolution (Cathodic reaction)
- 3  $\text{CO}_2$  dissolution resulting in the formation of carbonic acid

Zinc dissolution is required for any zinc corrosion product formation. This anodic activity must be balanced by a cathodic reaction that could be either hydrogen gas evolution or dissolution of oxygen from the surroundings. The common cathodic reaction for corrosion of zinc is

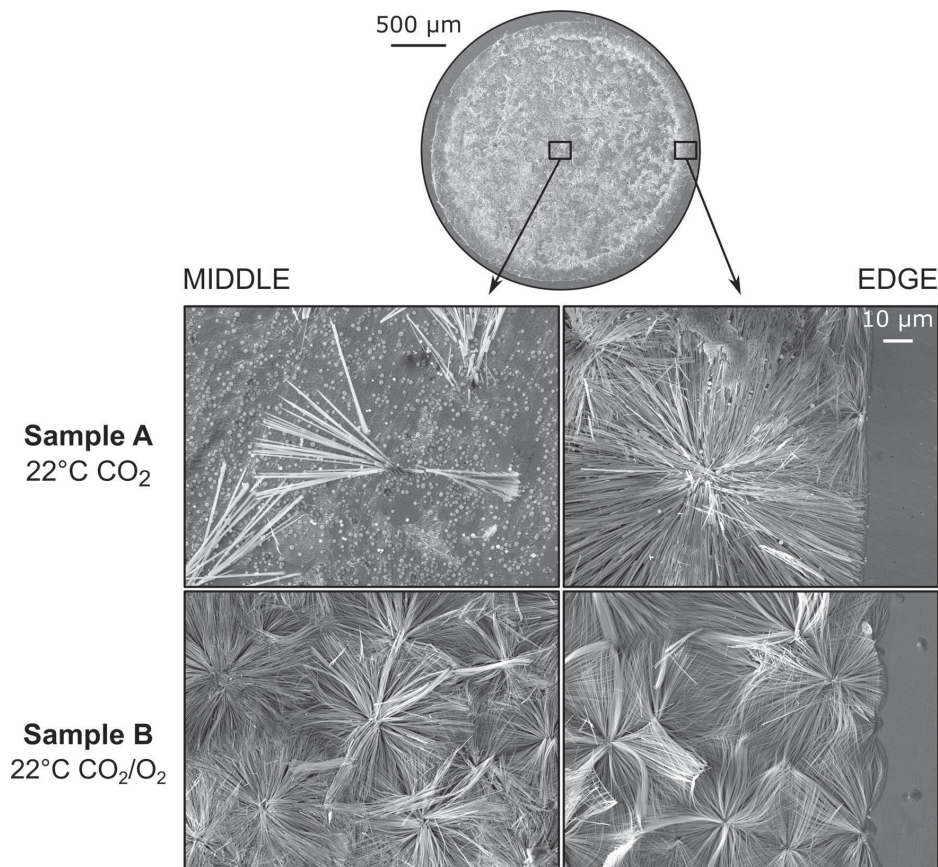


Fig. 11. SEM images of the droplet experiment of sample A and sample B. The upper droplet image (Sample A) shows where the middle and edge droplet images were taken. The left and right images show the higher magnification images of the middle and edge of the droplet, respectively.

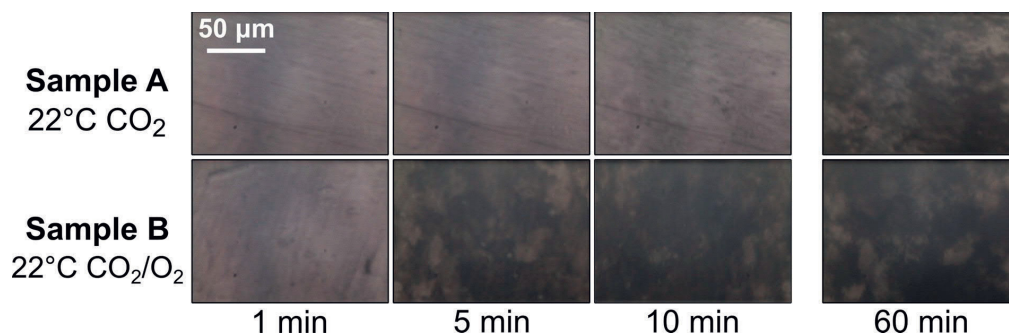


Fig. 12. In-situ optical images of sample A and sample B from the middle of the water droplet.

typically oxygen dissolution according to earlier studies [7,8,45,46]. As the oxygen dissolves, it reacts with water and produces hydroxyl-ions ( $\text{OH}^-$ ). The drastic effect of oxygen seen in sample B supports the accelerative effect on the reactions as a result of increased cathodic action that leads to  $\text{Zn}^{2+}$  ion dissolution. Some hydrogen evolution could also be possible due to acidic conditions and much lower availability of oxygen in sample A. The oxygen dissolution in the droplets occurs at the outer edge which usually results in higher cathodic activity and

alkalinity at the edge of the droplet. Conversely, oxygen depletion and its insufficient diffusion rate to replace the oxygen causes higher anodic activity in the middle region of the droplet [45–47]. As was seen from the SEM images (Fig. 11), more needle structure concentrated at the edge areas rather than the middle of the droplet. As the oxygen content in sample A is limited, the reaction is likely to occur at the edges where is better availability of all reaction constituents,  $\text{CO}_2$  and  $\text{O}_2$ .

As the  $\text{Zn}^{2+}$  ion concentration increases inside the droplet, they

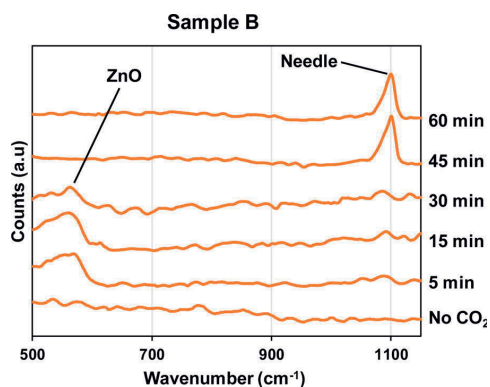


Fig. 13. In-situ Raman measurements of sample B from the middle of the water droplet (centre of Fig. 12).

start to react together to form ZnO. It is commonly known that also zinc hydroxide (Zn(OH)<sub>2</sub>) is one of the main corrosion products of zinc that could form either before, after or simultaneously with ZnO [7,48,49]. In a study by Ohtsuka et al., they detected the formation of both ZnO and Zn(OH)<sub>2</sub> by in-situ Raman investigations in atmospheric conditions [14]. However, the measurements in our study did not detect Zn(OH)<sub>2</sub>. Since high CO<sub>2</sub> concentration leads to acidic conditions with approximate water pH of 3–4 [50], the absence of Zn(OH)<sub>2</sub> precipitates could be due to high CO<sub>2</sub> concentration as it is more stable at alkaline conditions [51,52]. After the formation of ZnO, it likely reacts with the dissociated carbonic acid to form ZnCO<sub>3</sub> and Zn<sub>a</sub>(CO<sub>3</sub>)<sub>b</sub>(OH)<sub>c</sub>·dH<sub>2</sub>O. The conversion of ZnO to carbonates is further supported by a study where ZnO powder was converted into zinc hydroxy carbonate under humid CO<sub>2</sub> atmosphere [53]. The reaction could proceed by either redissolution and precipitation, or directly with the HCO<sub>3</sub><sup>-</sup> and CO<sub>3</sub><sup>2-</sup> ions [54].

The needle structure was the prevalent reaction product compared to ZnCO<sub>3</sub> in room temperature. Similar zinc hydroxy carbonate structures have been shown to be more stable compounds in lower temperatures [42]. Furthermore, Hu et al. showed the formation of similar needle structures in lower temperatures but resulted in spherical structures, similar to ZnCO<sub>3</sub>, in higher temperatures when anodizing

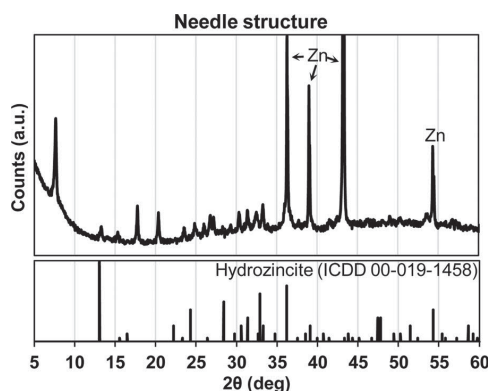


Fig. 15. XRD spectrum of the needle structure (with residual metallic zinc) separated from the surface. The spectrum of hydrozincite is presented as a reference.

zinc foils [55].

Diffusion of the gaseous species, CO<sub>2</sub> and O<sub>2</sub>, crucially affects the supply of the ionic species required for the formation of the corrosion products in the droplet experiments. The initial reactivity of the surface was significantly accelerated when O<sub>2</sub> was added due to increased cathodic activity that facilitated Zn<sup>2+</sup> dissolution. Nevertheless, mainly ZnO was present in the early stages of the experiments with only little carbonates formed. The diffusion of CO<sub>2</sub> limits the carbonate formation and only in the latter part of the experiment, the carbonates started to fully develop. Although diffusion is an essential factor in the droplet experiments, it has less effect in the depressurization phase of the scCO<sub>2</sub> treatments where the precipitation of water could result in carbonate formation as well. During depressurization, the droplets forming from the precipitated water are immediately saturated by the surrounding gases because of their small size [56]. Consequently, more rapid formation of the carbonates as seen in our previous studies is possible during the depressurization phase of the scCO<sub>2</sub> treatment compared to the droplet experiments shown in this study [11,34–36].

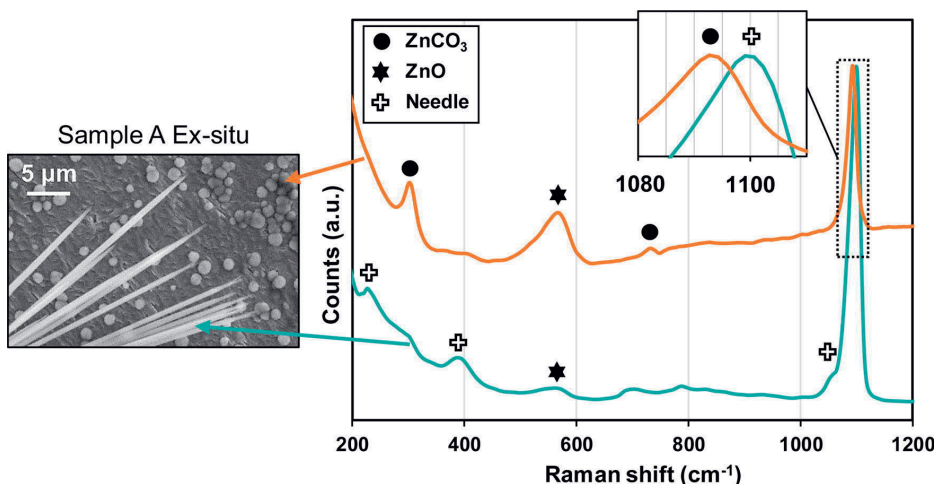


Fig. 14. Ex-situ Raman spectra of sample A (22 °C with CO<sub>2</sub>).

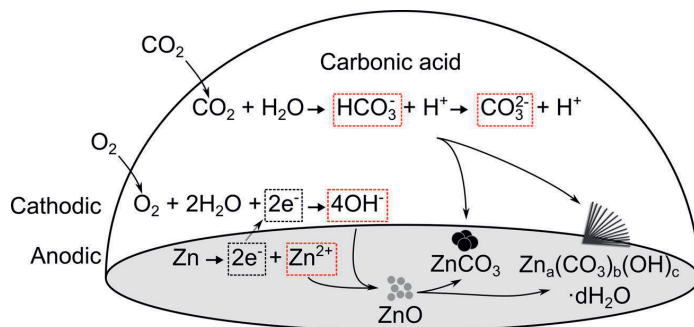


Fig. 16. Reactions involved in the droplet for carbonate formation.

#### 4. Conclusions

The effect of wet  $\text{scCO}_2$  treatments on zinc surfaces was investigated with in-situ optical imaging, Raman and FTIR. The study aimed to obtain an overview of the reactions involved in the formation of corrosion products in  $\text{scCO}_2$  phase and the following depressurization in the pretreatment. It was also shown that Raman and FTIR suited well for the in-situ characterization of the corrosion products and reaction kinetics.

The tests in wet  $\text{scCO}_2$  showed the growth of  $\text{ZnCO}_3$  and a presence of ZnO on the zinc surface during the treatments. According to the optical images, distinct dark spatters appeared on the zinc surface as initiation points for the corrosion products and gradually increased in quantity as the treatment progressed.  $\text{ZnCO}_3$  eventually formed on these areas. This behaviour was homogeneous throughout the surface, which was confirmed by the FTIR results and SEM observations. The  $\text{ZnCO}_3$  formation was more prevalent in  $40^\circ\text{C}$  compared to  $60^\circ\text{C}$  due to the higher amount of dissolved water in the  $\text{scCO}_2$ .

The dissolved water in the  $\text{scCO}_2$  phase precipitated as a liquid water layer during the depressurization of the cell. Thus, in order to simulate the depressurization phase in the  $\text{scCO}_2$  treatment, the effect of liquid water on the zinc surface was investigated further by sessile droplet tests at lower temperatures and pressures. ZnO formed in the initial stages of the experiments. As the experiment progressed, the droplet tests showed the growth of  $\text{ZnCO}_3$  and a needle-like structure that was not observed in  $\text{scCO}_2$ . Initial ZnO formation followed by carbonate formation could indicate the conversion of the ZnO to the carbonate structures. The role of oxygen was important for the reaction as it significantly increased the rate of zinc ion dissolution by enhancing cathodic action. The carbonate species formed only in the later stages of the experiments, which was likely due to a limited rate of  $\text{CO}_2$  diffusion. However, the diffusion rate is not expected to be a limiting factor in the depressurization phase of  $\text{scCO}_2$  treatment due to much shorter diffusion lengths and continuously increasing droplet size.

The presence of a water layer is paramount for the formation of both carbonate structures. Although the role of  $\text{scCO}_2$  phase is less pronounced for the actual carbonate formation, it enables the growth of the carbonates as well as the contact of the precipitated water to reach all surfaces throughout the cell volume during the depressurization.

#### Data availability

The raw/processed data required to reproduce these findings cannot be shared at this time due to technical or time limitations.

#### CRedit authorship contribution statement

A. Kaleva: Conceptualization, Methodology, Investigation, Writing - original draft. T. Tassaing: Resources, Validation. V. Saarimaa:

Resources, Writing - review & editing. G. Le Bourdon: Resources, Data curation. P. Väisänen: Funding acquisition, Writing - review & editing. A. Markkula: Funding acquisition, Writing - review & editing. E. Levänen: Supervision.

#### Declaration of Competing Interest

The authors declare that they have no known competing financial interests or personal relationships that could have appeared to influence the work reported in this paper.

#### Acknowledgements

This work was carried out through the doctoral school of industrial innovations (DSII) program as part of the research activities of Tampere University with financial support from SSAB Europe which is gratefully acknowledged.

#### Appendix A. Supplementary data

Supplementary material related to this article can be found, in the online version, at doi:<https://doi.org/10.1016/j.corsci.2020.108850>.

#### References

- [1] X. Zhang, Cr(VI) And Cr(III)-Based Conversion Coatings on Zinc, Hunan University, 2005.
- [2] P. Tuomi, H.M. Fagerholm, J.B. Rosenholm, K. Jyrkäs, Comparison of different commercial pretreatment methods for hot-dip galvanized and Galfan coated steel, Surf. Coatings Technol. 115 (1999) 70–78, [https://doi.org/10.1016/S0257-8972\(99\)00170-X](https://doi.org/10.1016/S0257-8972(99)00170-X).
- [3] O. Gharbi, S. Thomas, C. Smith, N. Birbilis, Chromate replacement: what does the future hold? Npj Mater. Degrad. 2 (2018) 12, <https://doi.org/10.1038/s41529-018-0034-5>.
- [4] T.S.N.S. Narayanan, Surface pretreatment by phosphate conversion coatings - a review, Rev. Adv. Mater. Sci. 9 (2005) 130–177.
- [5] J.F. Malone, Painting hot-dip galvanized sheet, Mater. Perform. 31 (1992) 39–42.
- [6] I. Cabanelas, A. Collazo, M. Izquierdo, X.R. Nóvoa, C. Pérez, Influence of galvanised surface state on the duplex systems behaviour, Corros. Sci. 49 (2007) 1816–1832, <https://doi.org/10.1016/j.corsci.2006.10.018>.
- [7] X.G. Zhang, Corrosion and Electrochemistry of Zinc, Springer US, Boston, MA, 1996, <https://doi.org/10.1007/978-1-4757-9877-7>.
- [8] J.D. Yoo, K. Ogle, P. Volovitch, The effect of synthetic zinc corrosion products on corrosion of electrogalvanized steel: I. Cathodic reactivity under zinc corrosion products, Corros. Sci. 81 (2014) 11–20, <https://doi.org/10.1016/j.corsci.2013.11.045>.
- [9] W. He, I. Odneval Wallinder, C. Leygraf, A laboratory study of copper and zinc runoff during first flush and steady-state conditions, Corros. Sci. 43 (2001) 127–146, [https://doi.org/10.1016/S0010-938X\(00\)00066-4](https://doi.org/10.1016/S0010-938X(00)00066-4).
- [10] V. Saarimaa, A. Kaleva, J.-P. Nikkanen, S. Heinonen, E. Levänen, P. Väisänen, A. Markkula, J. Juhanaja, Supercritical carbon dioxide treatment of hot dip galvanized steel as a surface treatment before coating, Surf. Coatings Technol. 331 (2017) 137–142, <https://doi.org/10.1016/j.surfcoat.2017.10.047>.
- [11] V. Saarimaa, A. Kaleva, J.P. Nikkanen, J. Manni, C. Lange, T. Paunikallio, T. Laihinne, S. Heinonen, E. Levänen, P. Väisänen, A. Markkula, Tailoring of versatile surface morphologies on hot dip galvanized steel in wet  $\text{CO}_2$ : aspects on

- formation, barrier properties, and utilization as a substrate for coatings, *ACS Appl. Mater. Interfaces* 10 (2018) 21730–21739, <https://doi.org/10.1021/acsami.8b05034>.
- [12] D. Lindström, I. Odnevall Wallinder, Long-term use of galvanized steel in external applications. Aspects of patina formation, zinc runoff, barrier properties of surface treatments, and coatings and environmental fate, *Environ. Monit. Assess.* 173 (2011) 139–153, <https://doi.org/10.1007/s10661-010-1377-8>.
- [13] A.M. Beccaria, Zinc layer characterization on galvanized steel by chemical methods, *Corrosion* 46 (1990) 906–912, <https://doi.org/10.5006/1.3580857>.
- [14] T. Ohtsuka, M. Matsuda, In situ Raman spectroscopy for corrosion products of zinc in humidified atmosphere in the presence of sodium chloride precipitate, *Corrosion* 59 (2003) 407–413, <https://doi.org/10.5006/1.3277572>.
- [15] F. Zhu, D. Persson, D. Thierry, Formation of corrosion products on an open and confined metal surfaces exposed to periodic wet/dry conditions - a comparison between zinc and electrogalvanized steel, *Corrosion* 57 (2001) 582–590, <https://doi.org/10.5006/1.3280514>.
- [16] T. Falk, J.-E. Svensson, L.-G. Johansson, The role of carbon dioxide in the atmospheric corrosion of zinc, *J. Electrochem. Soc.* 145 (1998) 39–44, <https://doi.org/10.1149/1.1838207>.
- [17] R. Lindström, J.-E. Svensson, L.-G. Johansson, The atmospheric corrosion of zinc in the presence of NaCl - the influence of carbon dioxide and temperature, *J. Electrochem. Soc.* 147 (2000) 1751–1757, <https://doi.org/10.1149/1.1393429>.
- [18] R.M. Cuéllar-Franca, A. Azapagic, Carbon capture, storage and utilisation technologies: a critical analysis and comparison of their life cycle environmental impacts, *J. CO<sub>2</sub> Util.* 9 (2015) 82–102, <https://doi.org/10.1016/j.jcou.2014.12.001>.
- [19] T. Bruhn, H. Naims, B. Olfe-Kräutlein, Separating the debate on CO<sub>2</sub> utilisation from carbon capture and storage, *Environ. Sci. Policy* 60 (2016) 38–43, <https://doi.org/10.1016/j.envsci.2016.03.001>.
- [20] Y.S. Choi, S. Nešić, Determining the corrosive potential of CO<sub>2</sub> transport pipeline in high pCO<sub>2</sub>-water environments, *Int. J. Greenh. Gas Control.* 5 (2011) 788–797, <https://doi.org/10.1016/j.ijggc.2010.11.008>.
- [21] C. Quilfen, T. Tassaing, D. Uzio, C. Aymonier, In situ Raman investigation of the preparation of HDS catalyst precursors using sCCO<sub>2</sub>, *J. Supercrit. Fluids* 141 (2018) 104–112, <https://doi.org/10.1016/j.supflu.2017.12.018>.
- [22] V. Prigiobbe, M. Hánchez, M. Werner, R. Baciocchi, M. Mazzotti, Mineral carbonation process for CO<sub>2</sub> sequestration, *Energy Procedia* 1 (2009) 4885–4890, <https://doi.org/10.1016/j.egypro.2009.02.318>.
- [23] J.S. Loring, C.J. Thompson, Z. Wang, A.G. Joly, D.S. Sklarew, H.T. Schaeff, E.S. Ilton, K.M. Rosso, A.R. Felmy, In situ infrared spectroscopic study of forsterite carbonation in wet supercritical CO<sub>2</sub>, *Environ. Sci. Technol.* 45 (2011) 6204–6210, <https://doi.org/10.1021/es201284e>.
- [24] N. Spycher, K. Pruess, J. Ennis-King, CO<sub>2</sub>-H<sub>2</sub>O mixtures in the geological sequestration of CO<sub>2</sub>. I. Assessment and calculation of mutual solubilities from 12 to 100 °C and up to 600 bar, *Geochim. Cosmochim. Acta* 67 (2003) 3015–3031, [https://doi.org/10.1016/S0016-7037\(03\)00273-4](https://doi.org/10.1016/S0016-7037(03)00273-4).
- [25] M. Champeau, J.-M. Thomassin, C. Jérôme, T. Tassaing, In situ FTIR micro-spectroscopy to investigate polymeric fibers under supercritical carbon dioxide: CO<sub>2</sub> sorption and swelling measurements, *J. Supercrit. Fluids* 90 (2014) 44–52, <https://doi.org/10.1016/j.supflu.2014.03.006>.
- [26] M.C. Hales, R.L. Frost, Synthesis and vibrational spectroscopic characterisation of synthetic hydrozincite and smithsonite, *Polyhedron* 26 (2007) 4955–4962, <https://doi.org/10.1016/j.poly.2007.07.002>.
- [27] W. Bin Cai, D.A. Scherson, In situ Raman spectroscopy of zinc electrodes in alkaline solutions, *J. Electrochem. Soc.* 150 (2003) 217–223, <https://doi.org/10.1149/1.1563651>.
- [28] A. Rumyantseva, S. Kostcheev, P.-M. Adam, S.V. Gaponenko, S.V. Vaschenko, O.S. Kulakovich, A.A. Ramanenka, D.V. Guzatov, D. Korbutyak, V. Dzhagan, A. Stroyuk, V. Shvalgin, Nonresonant surface-enhanced Raman scattering of ZnO quantum dots with Au and Ag nanoparticles, *ACS Nano* 7 (2013) 3420–3426, <https://doi.org/10.1021/nl400307a>.
- [29] M. Xu, W. Li, Y. Zhou, X.X. Yang, Z. Wang, Z. Li, Effect of pressure on corrosion behavior of X60, X65, X70, and X80 carbon steels in water-unsaturated supercritical CO<sub>2</sub> environments, *Int. J. Greenh. Gas Control* 51 (2016) 357–368, <https://doi.org/10.1016/j.ijggc.2016.06.002>.
- [30] A.Q. Liu, C. Bian, Z.M. Wang, X. Han, J. Zhang, Flow dependence of steel corrosion in supercritical CO<sub>2</sub> environments with different water concentrations, *Corros. Sci.* 134 (2018) 149–161, <https://doi.org/10.1016/j.corsci.2018.02.027>.
- [31] G.L. Cox, Effect of temperature on the corrosion of zinc, *Ind. Eng. Chem.* 23 (1931) 902–904, <https://doi.org/10.1021/ie50260a011>.
- [32] J.S. Loring, C.J. Thompson, Z. Wang, A.G. Joly, D.S. Sklarew, H.T. Schaeff, E.S. Ilton, K.M. Rosso, A.R. Felmy, In situ infrared spectroscopic study of forsterite carbonation in wet supercritical CO<sub>2</sub>, *Environ. Sci. Technol.* 45 (2011) 6204–6210, <https://doi.org/10.1021/es201284e>.
- [33] Y. Hua, R. Barker, T. Charpentier, M. Ward, A. Neville, Relating iron carbonate morphology to corrosion characteristics for water-saturated supercritical CO<sub>2</sub> systems, *J. Supercrit. Fluids* 98 (2015) 183–193, <https://doi.org/10.1016/j.supflu.2014.12.009>.
- [34] A. Kaleva, V. Saarimaa, S. Heinonen, J.-P. Nikkanen, A. Markkula, P. Väisänen, E. Levänen, Dissolution-induced nanowire synthesis on hot-dip galvanized surface in supercritical carbon dioxide, *Nanomaterials*. 7 (2017) 181, <https://doi.org/10.3390/nano7070181>.
- [35] A. Kaleva, J.-P. Nikkanen, S. Heinonen, V. Saarimaa, T. Vuorinen, M. Honkanen, L. Hyvärinen, E. Levänen, Synthesis of ZnO nanowires with supercritical carbon dioxide and post heat treatment, *Nanotechnology* 29 (2018), <https://doi.org/10.1088/1361-6528/aa69445601>.
- [36] J.-P. Nikkanen, S. Heinonen, P. Väisänen, V. Saarimaa, A. Markkula, T. Paunikallio, A. Kaleva, E. Levänen, Convenient extraction method for quantification of thin zinc patina layers, *Surf. Interface Anal.* 50 (2018) 564–570, <https://doi.org/10.1002/sia.6429>.
- [37] Y. Hua, S. Mohammed, R. Barker, A. Neville, Comparisons of corrosion behaviour for X65 and low Cr steels in high pressure CO<sub>2</sub>-saturated brine, *J. Mater. Sci. Technol.* 41 (2020) 21–32, <https://doi.org/10.1016/j.jmst.2019.08.050>.
- [38] A. Dugstad, M. Halseid, B. Morland, A.O. Sivertsen, Corrosion in dense phase CO<sub>2</sub> - the impact of depressurisation and accumulation of impurities, *Energy Procedia* 37 (2013) 3057–3067, <https://doi.org/10.1016/j.egypro.2013.06.192>.
- [39] S. Garrade, D. Féron, F. Rouillard, S. Perrin, R. Robin, J.C. Ruiz, H.A. Turc, Overview on corrosion in supercritical fluids, *J. Supercrit. Fluids* 120 (2017) 335–344, <https://doi.org/10.1016/j.supflu.2016.07.022>.
- [40] C. Belgodere, J. Dubessy, D. Vautrin, M.C. Caumon, J. Sterpenich, J. Pironon, P. Robert, A. Randi, J.P. Birat, Experimental determination of CO<sub>2</sub> diffusion coefficient in aqueous solutions under pressure at room temperature via Raman spectroscopy: impact of salinity (NaCl), *J. Raman Spectrosc.* 46 (2015) 1025–1032, <https://doi.org/10.1002/jrs.4742>.
- [41] D.O. Miles, P.J. Cameron, D. Mattia, Hierarchical 3D ZnO nanowire structures via fast anodization of zinc, *J. Mater. Chem. A* 3 (2015) 17569–17577, <https://doi.org/10.1039/C5TA03578C>.
- [42] Y. Sawada, M. Murakami, T. Nishide, Thermal analysis of basic zinc carbonate. Part 1. Carbonation process of zinc oxide powders at 8 and 13 °C, *Thermochim. Acta* 273 (1995) 95–102, [https://doi.org/10.1016/0040-6031\(95\)02631-2](https://doi.org/10.1016/0040-6031(95)02631-2).
- [43] S. Zhang, H. Fortier, J.R. Dahn, Characterization of zinc carbonate hydroxides synthesized by precipitation from zinc acetate and potassium carbonate solutions, *Mater. Res. Bull.* 39 (2004) 1939–1948, <https://doi.org/10.1016/j.matresbull.2004.05.023>.
- [44] N. Ohkuma, Y. Funayama, H. Ito, N. Mizutani, M. Kato, Reaction of carbon dioxide containing water vapor with ZnO fine particles, *Nippon. Kagaku Kaishi* 53 (1987) 802–806, <https://doi.org/10.1246/nikkashi.1987.802>.
- [45] R.J. Jiang, Y.F. Cheng, Mechanism of electrochemical corrosion of steel under water drop, *Electrochem. Commun.* 35 (2013) 8–11, <https://doi.org/10.1016/j.elecom.2013.07.019>.
- [46] T.H. Muster, A. Bradbury, A. Trinchi, I.S. Cole, T. Markley, D. Lau, S. Dligatch, A. Bendavid, P. Martin, The atmospheric corrosion of zinc: the effects of salt concentration, droplet size and droplet shape, *Electrochim. Acta* 56 (2011) 1866–1873, <https://doi.org/10.1016/j.electacta.2010.09.099>.
- [47] N.S. Azmat, K.D. Ralston, B.C. Muddle, I.S. Cole, Corrosion of Zn under acidified marine droplets, *Corros. Sci.* 53 (2011) 1604–1615, <https://doi.org/10.1016/j.corsci.2011.01.044>.
- [48] E. Diler, B. Lescop, S. Rioual, G. Nguyen Vien, D. Thierry, B. Rouvellou, Initial formation of corrosion products on pure zinc and MgZn<sub>2</sub> examined by XPS, *Corros. Sci.* 79 (2014) 83–88, <https://doi.org/10.1016/j.corsci.2013.10.029>.
- [49] I. Odnevall Wallinder, C. Leygraf, A critical review on corrosion and runoff from zinc and zinc-based alloys in atmospheric environments, *Corrosion* 73 (2017) 1016–1077, <https://doi.org/10.5006/2458>.
- [50] B. Meysami, M.O. Balaban, A.A. Teixeira, Prediction of pH in model systems pressurized with carbon dioxide, *Biotechnol. Prog.* 8 (1992) 149–154, <https://doi.org/10.1021/bp00014a009>.
- [51] R.A. Reichle, K.G. McCurdy, L.G. Hepler, Zinc Hydroxide, Solubility product and hydroxy-complex stability constants from 12.5–75 °C, *Can. J. Chem.* 53 (1975) 3841–3845, <https://doi.org/10.1139/v75-556>.
- [52] A. Krężel, W. Maret, The biological inorganic chemistry of zinc ions, *Arch. Biochem. Biophys.* 611 (2016) 3–19, <https://doi.org/10.1016/j.abb.2016.04.010>.
- [53] E. Turianicová, M. Káňuchová, A. Zorkovská, M. Holub, Z. Bujnáková, E. Dutková, M. Baláz, L. Findoráková, M. Balintová, A. Obut, CO<sub>2</sub> utilization for fast preparation of nanocrystalline hydrozincite, *J. CO<sub>2</sub> Util.* 16 (2016) 328–335, <https://doi.org/10.1016/j.jcou.2016.08.007>.
- [54] I. Odnevall, Atmospheric Corrosion of Field Exposed Zinc, Royal Institute of Technology, 1994.
- [55] Z. Hu, Q. Chen, Z. Li, Y. Yu, L.M. Peng, Large-scale and rapid synthesis of ultralong ZnO nanowire films via anodization, *J. Phys. Chem. C* 114 (2010) 881–889, <https://doi.org/10.1021/jp9094744>.
- [56] N.S. Azmat, K.D. Ralston, B.C. Muddle, I.S. Cole, Corrosion of Zn under fine size aerosols and droplets using inkjet printer deposition and optical profilometry quantification, *Corros. Sci.* 53 (2011) 3534–3541, <https://doi.org/10.1016/j.corsci.2011.06.028>.

# PUBLICATION VI

## **Time-of-flight secondary ion mass spectrometry study of zinc carbonation in the presence of stable oxygen-18 and deuterium isotopes**

V. Saarimaa, A. Kaleva, J.-P. Nikkanen, E. Levänen, P. Väisänen, A. Markkula

Materials Chemistry and Physics, Vol. 256, 123673  
<https://doi.org/10.1016/j.matchemphys.2020.123673>

**Publication reprinted with the permission of the copyright holders.**







Materials science communication



## Time-of-flight secondary ion mass spectrometry study of zinc carbonation in the presence of stable oxygen-18 and deuterium isotopes

Ville Saarimaa<sup>a,\*</sup>, Aaretti Kaleva<sup>b</sup>, Juha-Pekka Nikkanen<sup>b</sup>, Erkki Levänen<sup>b</sup>, Pasi Väisänen<sup>c</sup>, Antti Markkula<sup>c</sup>

<sup>a</sup> Top Analytica, Ruukinkatu 4, FI-20540, Turku, Finland

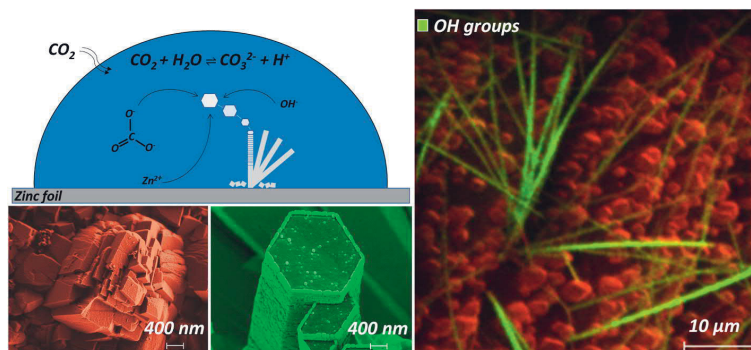
<sup>b</sup> Materials Science and Environmental Engineering, Tampere University, FI-33101, Tampere, Finland

<sup>c</sup> SSAB Europe, Harvialantie 420, FI-13300, Hämeenlinna, Finland

### HIGHLIGHTS

- <sup>18</sup>O and deuterium isotopes were used to study reaction routes in humid supercritical carbon dioxide carbonation.
- Isotopes in the formed reaction products were mapped by ToF-SIMS.
- The presence of hydroxyl groups was unambiguously observed in Zn carbonate nanowires.
- Zn carbonate was discerned from zinc hydroxy carbonate by ToF-SIMS mapping of deuterium.
- ToF-SIMS is an efficient tool to investigate reaction routes in synthesis of novel nanomaterials.

### GRAPHICAL ABSTRACT



### ARTICLE INFO

#### Keywords:

Supercritical carbon dioxide  
Zinc foil  
<sup>18</sup>O-water  
Deuterium  
ToF-SIMS

### ABSTRACT

Zinc foil was carbonated in supercritical  $\text{CO}_2$  in the presence of water containing stable <sup>18</sup>O or deuterium isotopes. The carbonation resulted in precipitation of zinc carbonate crystals with hexagonal and cubic morphologies until the source of hydroxyl groups was depleted. Time-of-flight secondary ion mass spectrometry was utilized to map the isotopes in the precipitates. The isotopes were detected in the precipitated structures, which confirms the formation of carbonic acid as the initial corrosion procedure step, followed by zinc dissolution. This finally leads to the arrangement of zinc ions with carbonate ions, and storage of OH-groups between  $\text{ZnCO}_3$  layers as  $\text{Zn}(\text{OH})_2$  or molecular water. The results completed chemical composition data obtained with molecular spectroscopy. Mapping of the distribution of hydrogen and oxygen isotopes by ToF-SIMS provided essential information on the reaction routes of carbonation in a humid  $\text{scCO}_2$  environment.

\* Corresponding author.

E-mail address: [ville.saarimaa@topanalytica.com](mailto:ville.saarimaa@topanalytica.com) (V. Saarimaa).

<https://doi.org/10.1016/j.matchemphys.2020.123673>

Received 2 July 2020; Received in revised form 7 August 2020; Accepted 10 August 2020

Available online 14 August 2020

0254-0584/© 2020 Elsevier B.V. All rights reserved.

## 1. Introduction

Metallic zinc is easily oxidized in a humid atmosphere, which results in rapid formation of various simple zinc oxides and hydroxides [1]. These initial zinc corrosion products are in the presence of CO<sub>2</sub> slowly converted into more complex compounds, with basic zinc carbonates (Zn<sub>x</sub>(CO<sub>3</sub>)<sub>y</sub>(OH)<sub>z</sub>) accounting for most of the species in atmospheres free of contaminants [2]. Compared to salt-induced corrosion processes, carbonation is a slow process [3]. In outdoor exposure, an unprotected zinc substrate receives a carbonated outer layer within some months or years, depending on the local atmosphere, while in laboratory experiments with abundant CO<sub>2</sub> supply the same end products can be formed even in some days or weeks [4,5]. The time required for the formation of stable zinc compounds is further decreased to minutes or hours when a zinc substrate is exposed to humid supercritical carbon dioxide (scCO<sub>2</sub>) [6]. Contrary to outdoor exposure, scCO<sub>2</sub>-assisted precipitation of zinc compounds in laboratory produces zinc compounds with a well-defined morphology. The formed precipitates are free of impurities, and such layers are thus suitable for many advanced application areas either as such or as a seed layer for synthetization of functional materials [7–11].

Most of the research related to reactions of metals in humid carbon dioxide-rich environments has been conducted in the area of CO<sub>2</sub> capture plants [12–18], but some similarities can be found in carbonation of minerals [19–23]. It is well known that carbonic acid is formed when water is present in a scCO<sub>2</sub> medium (CO<sub>2</sub> + H<sub>2</sub>O ⇌ H<sub>2</sub>CO<sub>3</sub>) [24,25]. Release of ions from a zinc substrate is locally induced by the carbonic acid, and the presence of carbonate ions promotes precipitation of zinc (hydroxy) carbonates that proceeds until the supply of zinc ions and carbonate ions is depleted [6,26–29]. Zinc carbonate and zinc hydroxy carbonate are some of the main reaction products in humid CO<sub>2</sub>-assisted zinc carbonation [30]. The reaction steps were recently investigated by ex-situ and in-situ FTIR and Raman measurements [31,32]. In humid scCO<sub>2</sub> systems, a thin layer of liquid water is proposed to be present on the corroding surface, allowing interaction of the different ions (Zn<sup>2+</sup>, OH<sup>-</sup>, HCO<sub>3</sub><sup>-</sup>, CO<sub>3</sub><sup>2-</sup>) [21,33]. The early corrosion products, that is nanoscale ZnO platforms, serve as initiation points for the carbonate growth [34]. The growth of individual structures is governed by the reaction temperature and pressure. Hydrated metal species are more prone to exchange their OH-groups for carbonate at higher temperature, which favors formation of zinc carbonate (cubic structures) [20,32]. On the contrary, lower temperatures increase retention of OH-groups, which favors formation of zinc hydroxy carbonate (nanowires). Water is required for formation of both structures. The cubic structures (anhydrous carbonates) are primarily formed at elevated pressure at supercritical state (high amount of dissolved water), while the growth of nanowires (OH-group containing carbonates) is fastest at lower pressure

where the capacity of CO<sub>2</sub> to dissolve water is decreased and water is precipitated on the metal surface [34].

However, the presence of hydroxyl groups in the formed precipitates cannot always be completely resolved by molecular spectroscopy [21, 35]. Furthermore, the exact reaction routes in various carbonation processes are not yet fully understood. The purpose of this study was to clarify the role of hydroxyl groups in humid scCO<sub>2</sub>-assisted carbonation of zinc.

Time-of-flight secondary ion spectroscopy is an important surface sensitive analytical technique capable of distinguishing different ions based on their mass [36–38]. ToF-SIMS has proven efficient in analyzing the chemical composition of corroded surfaces [39–41], and <sup>18</sup>O-water and D<sub>2</sub>O tracers have been utilized to corrode specimens for specific investigations [42,43]. Although the quantitative accuracy of ToF-SIMS is delimited, the lateral resolution is optimal for mapping of ion fragments in corrosion products [37,43,44]. In addition to corrosion product characterization, ToF-SIMS has been proven efficient in determination of structure and morphology of other nanomaterials [45], and recently in analysis of spatial distribution of components in photoelectrodes [46] and battery materials [47].

In this study, deuterium (<sup>2</sup>H) and oxygen-18 (<sup>18</sup>O)-marked waters were used in scCO<sub>2</sub>-assisted synthesis of zinc carbonate species on zinc foil, and the presence of these isotopes was mapped in the formed nanostructures.

## 2. Materials and methods

### 2.1. Substrate

Zinc foil (0.62 mm thick, 99.9% zinc, Alfa Aesar) was used in all the experiments. The zinc foils were polished in ethanol using SiC paper with grit sizes of 800, 1200, 2000 and 4000. Finally, the samples were cleaned with ethanol and dried.

### 2.2. H<sub>2</sub>O-assisted carbonation

The following isotopes were used: deuterium oxide (D<sub>2</sub>O, 99.9 atom-% D, Sigma Aldrich, Canada) and <sup>18</sup>O water (≥99 atom-% <sup>18</sup>O, Taiyo Nippon Sanso Corporation, Japan). The exposures were carried out by first applying a droplet of water (approx. Volume 5 μL) on zinc foil, followed by scCO<sub>2</sub> treatment in a batch reactor at 300 bar and 50 °C. Then a new droplet of the same water was applied on the same area of zinc, followed by submersion in liquid CO<sub>2</sub>, and carbonation at 65 bar and 22 °C. In both cases, the treatment was carried out until the water droplets were depleted. The dual exposure was performed to produce two different nanostructures on the same zinc foils [32].

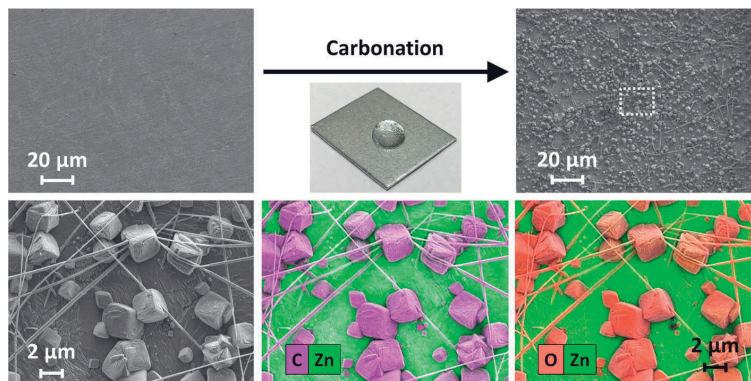


Fig. 1. SEM images and EDS element maps of humid carbonation products on a zinc surface.

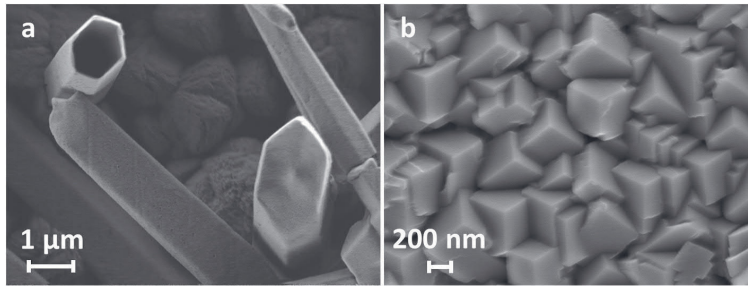


Fig. 2. Close-up SEM images of nanowires (a) and cubic structures (b).

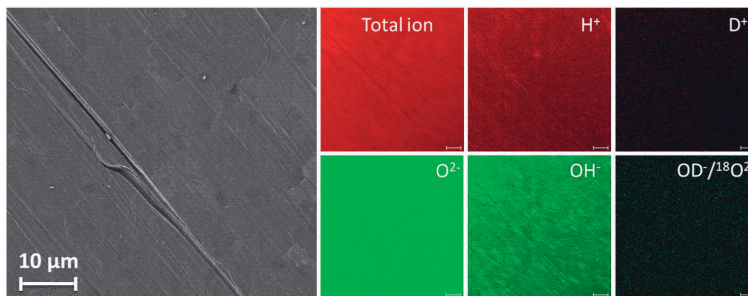


Fig. 3. Ion distributions of a zinc foil exposed to  $\text{scCO}_2$  in the absence of water.

### 2.3. Surface characterizations

A Zeiss Gemini instrument was employed for SEM imaging of the precipitates. A Bruker QUANTAX FlatQUAD energy dispersive spectrometry (EDS) system was used for element mapping. The signals were collected using a 3 kV accelerating voltage, a 1.2 nA current and a 0.5  $\mu\text{m}$  Mylar window. Time-of-flight secondary ion mass spectrometry (ToF-SIMS, Phi Trift II) was employed for mapping of ions. The measurements were carried out at 25 kV and 50  $\mu\text{m}$  raster size for a total mapping time of about 1 h. Mild sputtering (30 nC) with  $\text{Ga}^+$  ions preceded the measurements. Fourier transform infrared spectroscopy was performed with a Bruker Alpha instrument at 2  $\text{cm}^{-1}$  resolution. The measurements were performed in the region 375–4000  $\text{cm}^{-1}$  with a single reflection diamond ATR.

## 3. Results and discussion

### 3.1. SEM imaging of a carbonated zinc foil

After humid carbonation, two different morphologies were observed on the surface: long nanowires and cubic structures (Fig. 1). The original smooth zinc foil was also visible in the background. The presence of carbon and oxygen was confirmed in both structures by EDS mapping, indicating the presence of carbonate compounds. The close-up images confirm that the zinc carbonate crystals can grow in size in cubic or hexagonal forms that in the literature have been proposed to initiate from small nano-polycrystalline regions on the surface (Fig. 2) [14,17, 33,48]. Furthermore, also hollow nanowires were observed, which have not been reported earlier (Fig. 2a).

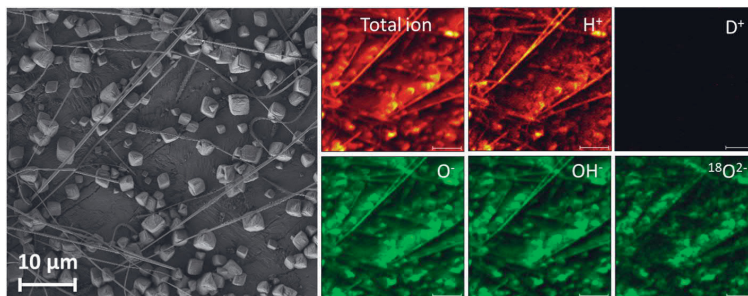


Fig. 4. Ion distributions on  $\text{scCO}_2$  treated zinc foil after carbonation in the presence of  $^{18}\text{O}$ -water.

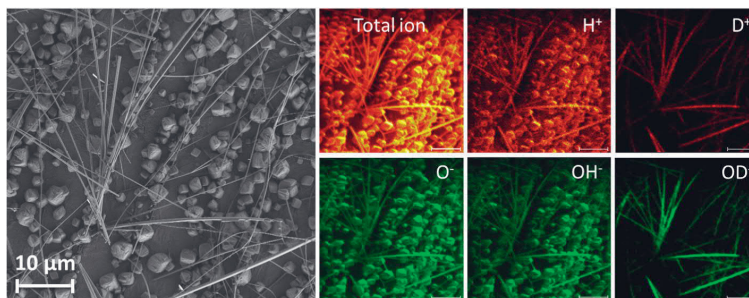


Fig. 5. Ion distributions on ScCO<sub>2</sub> treated zinc foil after carbonation in the presence of D<sub>2</sub>O.

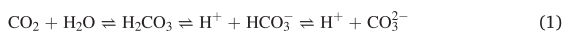
### 3.2. ToF-SIMS mapping of carbonated zinc foils

#### 3.2.1. Dry carbonation

SEM image of a zinc foil exposed to dry carbonation, and the ToF-SIMS ion maps from the same area, are shown in Fig. 3. The sample featured a flat, polished surface without visible corrosion products, but with contributions from oxygen and hydroxyl groups evenly scattered across the surface. Adsorption of adventitious atmospheric hydrocarbons and humidity-induced hydroxyl groups onto sample surfaces can result in an increase of apparent surface contamination layer of up to few tens of atom-% [49,50]. No deuterium or <sup>18</sup>O-ions were detected. OD<sup>-</sup> and <sup>18</sup>O<sup>2-</sup> ions have overlapping masses, but neither fragment was detected, which means that their natural occurrence is very small and that they do not interfere with the experiments with isotope marked waters.

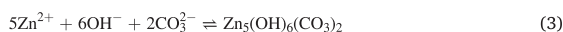
#### 3.2.2. Carbonation in the presence of <sup>18</sup>O-water

The presence of <sup>18</sup>O-water triggered precipitation of various compounds on the surface (Fig. 4). Zinc carbonate formation has previously been verified in a humid scCO<sub>2</sub> atmosphere [6]. In the ToF-SIMS element maps, H<sup>+</sup>, O<sup>2-</sup> and OH<sup>-</sup> ions were observed in both morphologies. Within the structures, some local intensity variations were observed that originate in the orientation of the structures related to the incoming ion beam and the detector (shadowing effect). Adsorption of adventitious surface contamination can be assumed to occur for this sample similarly as for the reference sample (Fig. 3) and the distribution of O<sup>2-</sup> or OH<sup>-</sup> ions can be smeared by the potential adsorbed contaminations and were not further examined. No deuterium was detected. <sup>18</sup>O<sup>2-</sup> was observed in the precipitates. Formation of carbonic acid is the initial step in zinc carbonation [13,14,51]:



The presence of carbonic acid triggers zinc dissolution that finally

leads to the formation of various zinc carbonate species in conjunction with dissolved zinc and carbonate and hydroxyl groups [14,52–54]:



The occurrence of <sup>18</sup>O in the formed precipitates confirms carry-over of <sup>18</sup>O species from the water droplet to carbonic acid and ultimately to zinc carbonate precipitates (Fig. 4).

#### 3.2.3. Carbonation in the presence of D<sub>2</sub>O

Utilization of deuterium-labeled water in the zinc carbonation enabled detection of hydroxyl groups within the formed corrosion products. In parallel to previous exposures, adventitious O<sup>-</sup> and OH<sup>-</sup> ions were widely observed, rendering their use in reaction route determination useless (Fig. 5). Importantly, D<sup>+</sup> and OD<sup>-</sup> ions showed selective occurrence in the nanowires and were not at all present in the background or the cubic structures. Firstly, this confirms that adsorption of water did not take place during the experiment (adsorbed deuterium-labeled water would be found all over the sample surface). The reactions were continued until the water droplet was depleted, and the introduced water was structurally bonded to the structure. Secondly, the result confirms that the cubic structures did not contain any structural water, but, on the contrary, the nanowires were rich in hydroxyl groups, implying zinc hydroxy carbonate-type precipitates. The obtained lateral resolution (0.6 μm, calculated using the width from 16% to 84% in the line scan [55]) is in line with what has previously been obtained for mineral samples with organic phases [43] (Fig. 6).

### 3.3. Molecular spectroscopy of the precipitates

Composition of zinc carbonate precipitates similar to the ones presented in this study has been previously characterized in the literature.

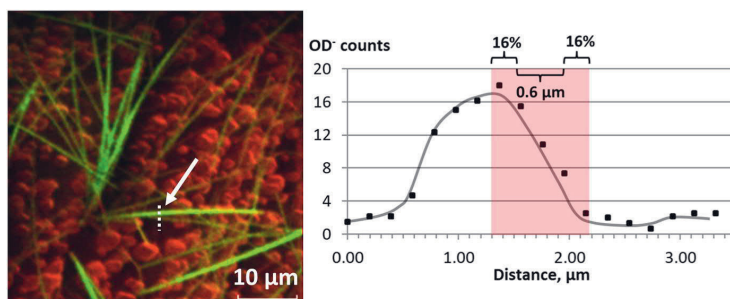


Fig. 6. Determination of instrument resolution from an individual nanowire (marked with an arrow). The ToF-SIMS element maps is an overlay map of OD<sup>-</sup> and total ion signals.

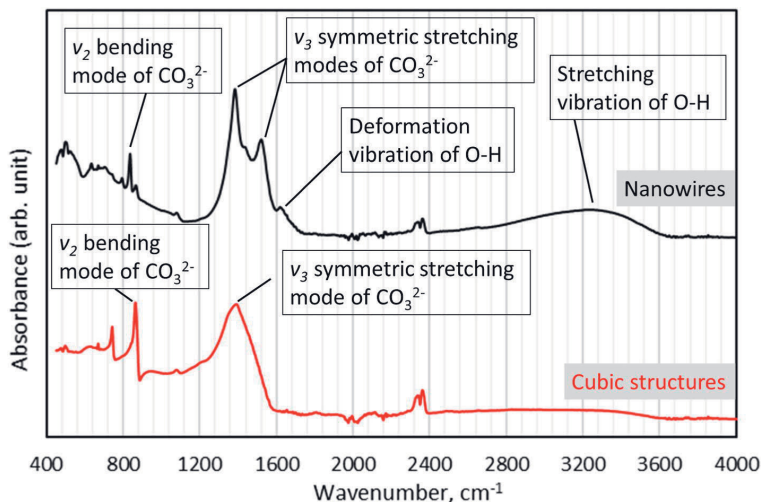


Fig. 7. FTIR spectra of the precipitates formed in humid carbonation of zinc.

Due to the complexity and the similarity of the precipitates, the compositional data in most reports is tentative [28,48,56,57]. FTIR spectra of the nanowires and the cubic structures are shown in Fig. 7. According to the literature [20,58], the bands at 1380 and 1520  $\text{cm}^{-1}$  (nanowires) and the band at 1390  $\text{cm}^{-1}$  (cubic structures) arise from the  $\nu_3$  symmetric stretching mode of  $\text{CO}_3^{2-}$ . The  $\nu_2$  bending modes of  $\text{CO}_3^{2-}$  are present at 835 and 860  $\text{cm}^{-1}$  (nanowires and cubic structures, respectively) [4,59]. In the nanowire structure, a broad band arising from the stretching vibration of O-H was seen at 2800–3600  $\text{cm}^{-1}$ . Hydrogen bonded OH groups that are not coordinately bonded to metal ions cause these stretching modes [50,57]. Furthermore, the absorbance of 1620  $\text{cm}^{-1}$  is assigned to the deformation vibration of O-H [20,60]. Associative hydroxyl groups (exhibiting hydrogen bonding) have decreased vibrational energy in comparison with free hydroxyl groups, and the wavenumber shifts to lower frequency [60]. The presence of OH groups in the nanowire structure, in addition to splitting of the  $\nu_3$  stretching mode, indicates a hydrozincite-type compound with alternating  $\text{Zn}(\text{OH})_2$  and  $\text{ZnCO}_3$  layers, which supports the findings of earlier studies [28,56,61]. A general structure for zinc hydroxy carbonate has been presented as two layers of  $\text{ZnCO}_3$  fitting between three layers of  $\text{Zn}(\text{OH})_2$  [62]. The structure is linking through two hydroxyl bridges between zinc bound by bidentate of carbonate [60]. Therefore, the coordination number of zinc is four [50]. Water can also be stored between the layers, linked to the complex by hydrogen bonding, the water molecules being located parallel to the carbonate groups that hold the complex zinc-containing sheets together [50,60,62,63]. The OH:CO<sub>3</sub> ratio may be variable, resulting in CO<sub>3</sub>-deficient, stacking-disordered phases [50]. The results in our earlier studies, obtained with X-ray diffraction (XRD), Raman spectroscopy and X-ray photoelectron spectroscopy (XPS) [32,34], support these findings.

#### 4. Conclusions

Zinc carbonate nanostructures were precipitated on zinc foils by humid carbonation using stable isotope-marked waters ( $\text{D}_2\text{O}$  and  $\text{H}_2^{18}\text{O}$ ) as tracers. The nanostructures grew in hexagonal or cubic forms from singular initiation points until the source of water was depleted. The distribution of the isotopes was successfully mapped by ToF-SIMS, which enabled assessment of reaction routes in the nanostructure synthesis. Growth of nanostructures was not observed in the absence of water. Presence of  $^{18}\text{O}^{2-}$  ions in the zinc precipitates confirmed the

proposed reaction route:  $^{18}\text{O}^{2-}$  ions were carried over from the  $^{18}\text{O}$ -water droplet to carbonic acid ( $\text{CO}_2 + \text{H}_2\text{O} \rightleftharpoons \text{H}_2\text{CO}_3$ ) and finally to zinc carbonate precipitate ( $\text{Zn}^{2+} + \text{CO}_3^{2-} \rightleftharpoons \text{ZnCO}_3$ ). Further, the use of  $\text{D}_2\text{O}$  revealed that the cubic structures were anhydrous, while the nanowires contained hydroxyl groups. Molecular spectroscopy confirmed the presence of structural hydroxyl groups. Use of isotope-marked water in exposures, combined with ToF-SIMS mapping, is a powerful tool to establish reaction routes and clarify compositions in carbonation of metals and minerals.

#### CRedit authorship contribution statement

**Ville Saarimaa:** Conceptualization, Investigation, Visualization, Data curation, Writing - original draft. **Aaretti Kaleva:** Conceptualization, Methodology, Writing - original draft. **Juha-Pekka Nikkanen:** Conceptualization. **Erkki Levänen:** Supervision, Writing - original draft. **Pasi Väisänen:** Supervision. **Antti Markkula:** Supervision.

#### Declaration of competing interest

The authors declare that they have no known competing financial interests or personal relationships that could have appeared to influence the work reported in this paper.

#### Appendix A. Supplementary data

Supplementary data to this article can be found online at <https://doi.org/10.1016/j.matchemphys.2020.123673>.

#### References

- [1] X.G. Zhang, *Corrosion and Electrochemistry of Zinc*, first ed., Springer Science+Business Media, LLC, New York, 1996.
- [2] I. Odneval, C. Leygraf, Comparison between analytical methods for zinc specimens exposed in a rural atmosphere, *J. Electrochem. Soc.* 138 (1991) 1923–1928.
- [3] V. Talakokula, S. Bhalla, R.J. Ball, C.R. Bowen, G.L. Pesce, R. Kurchania, B. Bhattacharjee, A. Gupta, K. Paine, Diagnosis of carbonation induced corrosion initiation and progression in reinforced concrete structures using piezo-impedance transducers, *Sensors Actuators, A Phys.* 242 (2016) 79–91, <https://doi.org/10.1016/j.sna.2016.02.033>.
- [4] T. Falk, J. Svensson, L. Johansson, The role of carbon dioxide in the atmospheric corrosion of zinc, *J. Electrochem. Soc.* 145 (1998) 39–44.

- [5] G. Roventi, T. Bellezze, E. Barbaresi, R. Fratesi, Effect of carbonation process on the passivating products of zinc in  $\text{Ca}(\text{OH})_2$  saturated solution, *Mater. Corros.* 64 (2013) 1007–1014, <https://doi.org/10.1002/maco.201206868>.
- [6] A. Kaleva, V. Saarimaa, S. Heinonen, J.-P. Nikkanen, A. Markkula, V. Väisänen, E. Levänen, Dissolution-induced nanowire synthesis on hot-dip galvanized surface in supercritical carbon dioxide, *Nanomaterials* 7 (2017) 181–190, <https://doi.org/10.3390/nano7070181>.
- [7] A. Anžlovar, M. Marinšek, Z.C. Orel, M. Žigon, Basic zinc carbonate as a precursor in the solvothermal synthesis of nano-zinc oxide, *Mater. Des.* 86 (2015) 347–353, <https://doi.org/10.1016/j.matdes.2015.07.087>.
- [8] E. Zehani, S. Hassani, A. Lussou, J. Vigneron, A. Etcheberry, P. Galtier, V. Sallet, Reconstruction of perfect ZnO nanowires facets with high optical quality, *Appl. Surf. Sci.* 411 (2017) 374–378, <https://doi.org/10.1016/j.apsusc.2017.03.201>.
- [9] G.S. Zakharova, C. Täschner, T. Kolb, C. Jähne, A. Leonhardt, B. Büchner, R. Klingeler, Morphology controlled  $\text{NH}_4\text{V}_3\text{O}_8$  microcrystals by hydrothermal synthesis, *Dalt., OR Trans.* 42 (2013) 4897–4902, <https://doi.org/10.1039/c3dr32550d>.
- [10] N. Kanari, D. Mishra, I. Gaballah, B. Dupré, Thermal decomposition of zinc carbonate hydroxide, *Thermochim. Acta* 410 (2004) 93–100, [https://doi.org/10.1016/S0040-6031\(03\)00396-4](https://doi.org/10.1016/S0040-6031(03)00396-4).
- [11] S. Heinonen, M. Kannisto, J.P. Nikkanen, E. Huttunen-Saarivirta, M. Karp, E. Levänen, Photocatalytic and antibacterial properties of ZnO films with different surface topographies on stainless steel substrate, *Thin Solid Films* 616 (2016) 842–849, <https://doi.org/10.1016/j.tsf.2016.10.002>.
- [12] A. Dugstad, M. Halseid, B. Morland, Testing of CO<sub>2</sub> specifications with respect to corrosion and bulk phase reactions, *Energy Procedia* 63 (2014) 2547–2556, <https://doi.org/10.1016/j.egypro.2014.11.277>.
- [13] M. Halseid, A. Dugstad, B. Morland, Corrosion and bulk phase reactions in CO<sub>2</sub> transport pipelines with impurities: review of recent published studies, *Energy Procedia* 63 (2014) 2557–2569, <https://doi.org/10.1016/j.egypro.2014.11.278>.
- [14] Y. Hua, R. Barker, T. Charpentier, M. Ward, A. Neville, Relating iron carbonate morphology to corrosion characteristics for water-saturated supercritical CO<sub>2</sub> systems, *J. Supercrit. Fluids* 98 (2015) 183–193, <https://doi.org/10.1016/j.supflu.2014.12.009>.
- [15] Y.S. Choi, S. Nestic, D. Young, Effect of impurities on the corrosion behavior of CO<sub>2</sub> transmission pipeline steel in supercritical CO<sub>2</sub>-water environments, *Environ. Sci. Technol.* 44 (2010) 9233–9238, <https://doi.org/10.1021/es102578c>.
- [16] T. Nesterova, K. Dam-Johansen, L.T. Pedersen, S. Kiil, Microcapsule-based self-healing anticorrosive coatings: capsule size, coating formulation, and exposure testing, *Prog. Org. Coating* 75 (2012) 309–318, <https://doi.org/10.1016/j.porgcoat.2012.08.002>.
- [17] Y.-S. Choi, S. Hassani, T.N. Vu, S. Nestic, A.Z.B. Abas, Effect of H<sub>2</sub>S on the corrosion behavior of pipeline steels in supercritical and liquid CO<sub>2</sub> environments, *Corrosion* 72 (2015) 999–1009.
- [18] B.H. Morland, M. Tjelta, T. Norby, G. Svenningsen, Acid reactions in hub systems consisting of separate non-reactive CO<sub>2</sub> transport lines, *Int. J. Greenh. Gas Control* 87 (2019) 246–255, <https://doi.org/10.1016/j.ijggc.2019.05.017>.
- [19] J.S. Loring, J. Chen, P. Bénézeth, O. Qafoku, E.S. Ilton, N.M. Washton, C. J. Thompson, P.F. Martin, B.P. McGrail, K.M. Rosso, A.R. Felmy, H.T. Schaeff, Evidence for carbonate surface complexation during forsterite carbonation in wet supercritical carbon dioxide, *Langmuir* 31 (2015) 7533–7543, <https://doi.org/10.1021/acs.langmuir.5b01052>.
- [20] J. Loring, C. Thompson, C. Zhang, Z. Wang, H. Schaeff, K. Rosso, In situ infrared spectroscopic study of brucite carbonation in dry to water-saturated supercritical carbon dioxide, *J. Phys. Chem.* 116 (2012) 4768–4777.
- [21] J. Loring, C. Thompson, Z. Wang, A. Joly, D. Sklarow, H. Schaeff, E. Ilton, K. Rosso, A. Felmy, In situ infrared spectroscopic study of forsterite carbonation in wet supercritical CO<sub>2</sub>, *Environ. Sci. Technol.* 45 (2011) 6204–6210.
- [22] J.H. Kwak, J.Z. Hu, R.V.F. Turcu, K.M. Rosso, E.S. Ilton, C. Wang, J.A. Sears, M. H. Engelhard, A.R. Felmy, D.W. Hoyt, The role of H<sub>2</sub>O in the carbonation of forsterite in supercritical CO<sub>2</sub>, *Int. J. Greenh. Gas Control* 5 (2011) 1081–1092, <https://doi.org/10.1016/j.ijggc.2011.05.013>.
- [23] A.R. Felmy, O. Qafoku, B.W. Arey, J.Z. Hu, M. Hu, H. Todd Schaeff, E.S. Ilton, N. J. Hess, C.I. Pearce, J. Feng, K.M. Rosso, Reaction of water-saturated supercritical CO<sub>2</sub> with forsterite: evidence for magnesite formation at low temperatures, *Geochem. Cosmochim. Acta* 91 (2012) 271–282, <https://doi.org/10.1016/j.gca.2012.05.026>.
- [24] A. Davis, B. Oliver, A vibrational-spectroscopic study of the species present in the CO<sub>2</sub>-H<sub>2</sub>O system, *J. Solut. Chem.* 1 (1972) 329–339.
- [25] M. O'Connor, A study of the kinetics of the basic zinc carbonate formation reaction, *Z. Naturforsch.* 30b (1975) 665–668.
- [26] G. Patrinoiu, J.M. Calderón-Moreno, D.C. Culita, R. Birjega, R. Ene, O. Carp, Eco-friendly synthetic route for layered zinc compound and its conversion to ZnO with photocatalytic properties, *Solid State Sci.* 23 (2013) 58–64, <https://doi.org/10.1016/j.solidstatesciences.2013.06.011>.
- [27] E. Diler, B. Lescop, S. Rioual, G. Nguyen Vien, D. Thierry, B. Rouvellou, Initial formation of corrosion products on pure zinc and MgZn<sub>2</sub> examined by XPS, *Corrosion Sci.* 79 (2014) 83–88, <https://doi.org/10.1016/j.corsci.2013.10.029>.
- [28] M. Shamsipur, S.M. Pourmortazavi, S.S. Hajimirsadeghi, M.M. Zahedi, M. Rahimi-Nasrabadi, Facile synthesis of zinc carbonate and zinc oxide nanoparticles via direct carbonation and thermal decomposition, *Ceram. Int.* 39 (2013) 819–827, <https://doi.org/10.1016/j.ceramint.2012.07.003>.
- [29] Y. Sato, H. Niki, T. Takamura, Effects of carbonate on the anodic dissolution and the passivation of zinc electrode in concentrated solution of potassium hydroxide, *J. Electrochem. Soc.* 118 (1971) 1269, <https://doi.org/10.1149/1.2408303>.
- [30] V. Saarimaa, A. Kaleva, J.P. Nikkanen, S. Heinonen, E. Levänen, V. Väisänen, A. Markkula, J. Juhanaja, Supercritical carbon dioxide treatment of hot dip galvanized steel as a surface treatment before coating, *Surf. Coating Technol.* 331 (2017) 137–142, <https://doi.org/10.1016/j.surfcoat.2017.10.047>.
- [31] V. Saarimaa, N. Fuentes, D. Persson, T. Zavalis, A. Kaleva, J.-P. Nikkanen, E. Levänen, G. Heydari, Assessment of pitting corrosion in bare and passivated (wet sCO<sub>2</sub>-induced patination and chemical passivation) hot-dip galvanized steel samples with SVET, FTIR, and SEM, *Mater. Corros.* (2020), <https://doi.org/10.1002/maco.202011653>.
- [32] V. Saarimaa, A. Kaleva, J.-P. Nikkanen, J. Manni, C. Lange, T. Paunikallio, T. Laihininen, S. Heinonen, E. Levänen, P. Väisänen, A. Markkula, Tailoring of versatile surface morphologies on hot dip galvanized steel in wet CO<sub>2</sub>: aspects on formation, barrier properties, and utilization as a substrate for coatings, *ACS Appl. Mater. Interfaces* 10 (2018) 21730–21739, <https://doi.org/10.1021/acsami.8b05034>.
- [33] C.F. Mah, K.P. Beh, F.K. Yam, Z. Hassan, rapid formation and evolution of anodized-Zn nanostructures in NaHCO<sub>3</sub> solution, *ECS J. Solid State Sci. Technol.* 5 (2016) M105–M112, <https://doi.org/10.1149/2.0061610jss>.
- [34] A. Kaleva, T. Tassaing, V. Saarimaa, G. Le Bourdon, P. Väisänen, A. Markkula, E. Levänen, Formation of corrosion products on zinc in wet supercritical and subcritical CO<sub>2</sub>: in-situ spectroscopic study, *Corrosion Sci.* 174 (2020), <https://doi.org/10.1016/j.corsci.2020.108850>.
- [35] M.C. Hales, R.L. Frost, Synthesis and vibrational spectroscopic characterisation of synthetic hydrozincite and smithsonite, *Polyhedron* 26 (2007) 4955–4962, <https://doi.org/10.1016/j.poly.2007.07.002>.
- [36] C.M. Choi, S.J. Lee, J.Y. Baek, J.J. Kim, M.C. Choi, ToF-SIMS analysis of an organic layer using toluene and its cluster ion beam projectiles generated by multiphoton ionization, *Appl. Surf. Sci.* 458 (2018) 805–809, <https://doi.org/10.1016/j.apsusc.2018.07.157>.
- [37] M. Kubicek, G. Holzelechner, A.K. Opitz, S. Larisegger, H. Hutter, J. Fleig, A novel ToF-SIMS operation mode for sub 100 nm lateral resolution: application and performance, *Appl. Surf. Sci.* 289 (2014) 407–416, <https://doi.org/10.1016/j.apsusc.2013.10.177>.
- [38] N. Klingner, R. Heller, G. Hlawacek, S. Faesko, J. von Borany, Time-of-flight secondary ion mass spectrometry in the helium ion microscope, *Ultramicroscopy* 198 (2018) 10–17, <https://doi.org/10.1016/j.ultramic.2018.12.014>.
- [39] M. Esmaily, P. Malmberg, M. Shahabi-Navid, J.E. Svensson, L.G. Johansson, A ToF-SIMS investigation of the corrosion behavior of Mg alloy AM50 in atmospheric environments, *Appl. Surf. Sci.* 360 (2016) 98–106, <https://doi.org/10.1016/j.apsusc.2015.11.002>.
- [40] J. Lehmusto, M. Bergelin, J. Sui, J. Juhanaja, B.J. Skrifvars, P. Yrjas, Applicability of ToF-SIMS and stable oxygen isotopes in KCl-induced corrosion studies at high temperatures, *Corrosion Sci.* 125 (2017) 1–11, <https://doi.org/10.1016/j.corsci.2017.05.022>.
- [41] J. Lehmusto, M. Bergelin, D. Lindberg, J. Juhanaja, The effect of oxygen source on the reaction mechanism of potassium chloride-induced high-temperature corrosion, *Corrosion* 74 (2018) 1431–1445.
- [42] K.A. Unocic, H.H. Elsenriency, M.P. Brady, H.M. Meyer, G.L. Song, M. Fayek, R. A. Meisner, B. Davis, Transmission electron microscopy study of aqueous film formation and evolution on magnesium alloys, *J. Electrochem. Soc.* 161 (2014) C302–C311, <https://doi.org/10.1149/2.024406jes>.
- [43] M. Senoner, W.E.S. Unger, SIMS imaging of the nanoworld: applications in science and technology, *J. Anal. At. Spectrom.* 27 (2012) 1050–1068, <https://doi.org/10.1039/c2ja30015j>.
- [44] E. Deloule, F. Albarède, S.M.F. Sheppard, Hydrogen isotope heterogeneities in the mantle from ion probe analysis of amphiboles from ultramafic rocks, *Earth Planet Sci. Lett.* 105 (1991) 543–553, [https://doi.org/10.1016/0012-821X\(91\)90191-J](https://doi.org/10.1016/0012-821X(91)90191-J).
- [45] N. Perkas, G. Amirian, G. Applertor, E. Efendiev, Y. Kaganovskii, A.V. Ghule, B.-J. Chen, Y.-C. Ling, A. Gedanken, Depositing silver nanoparticles on/in a glass slide by the sonochemical method, *Nanotechnology* 19 (2008), <https://iopscience.iop.org/article/10.1088/0957-4484/19/43/435604/pdf>.
- [46] H. Wu, Z. Zheng, C.Y. Toe, X. Wen, J.N. Hart, R. Amal, Y.H. Ng, A pulse electrodeposited amorphous tunnel layer stabilises Cu<sub>2</sub>O for efficient photoelectrochemical water splitting under visible-light irradiation, *J. Mater. Chem. A.* 8 (2020) 5638–5646, <https://doi.org/10.1039/d0ta00629g>.
- [47] N. Gauthier, C. Courrèges, J. Demeaux, C. Tessier, H. Martinez, Probing the in-depth distribution of organic/inorganic molecular species within the SEI of LTO/NMC and LTO/LMO batteries: a complementary ToF-SIMS and XPS study, *Appl. Surf. Sci.* 501 (2020) 144266, <https://doi.org/10.1016/j.apsusc.2019.144266>.
- [48] L. Zarakas, K. Mika, K. Syrek, G.D. Sulka, Formation of ZnO nanowires during anodic oxidation of zinc in bicarbonate electrolytes, *J. Electroanal. Chem.* 801 (2017) 511–520, <https://doi.org/10.1016/j.jelechem.2017.08.035>.
- [49] G.C. Smith, Evaluation of a simple correction for the hydrocarbon contamination layer in quantitative surface analysis by XPS, *J. Electron. Spectrosc. Relat. Phenom.* 148 (2005) 21–28, <https://doi.org/10.1016/j.elspec.2005.02.004>.
- [50] S. Ghose, The crystal structure of hydrozincite, *Acta Crystallogr.* 17 (1964) 1051–1057.
- [51] K. Toews, C. Wai, R. Shroll, pH-defining equilibrium between water and supercritical CO<sub>2</sub>. Influence on SFE of organics and metal mhealates, *Anal. Chem.* 67 (1995) 4040–4043.
- [52] A.K. Alwan, P.A. Williams, Mineral formation from aqueous solution. Part I. The deposition of hydrozincite, Zn<sub>5</sub>(OH)<sub>6</sub>(CO<sub>3</sub>)<sub>2</sub>, from natural waters, *Transit. Met. Chem.* 4 (1979) 128–132, <https://doi.org/10.1007/BF00618840>.
- [53] E. Turianicová, M. Kaňuchová, A. Zorkovská, M. Holub, Z. Bujňáková, E. Dutková, M. Baláz, L. Fíndoráková, M. Balintová, A. Obut, CO<sub>2</sub>utilization for fast

- preparation of nanocrystalline hydrozincite, *J. CO2 Util.* 16 (2016) 328–335, <https://doi.org/10.1016/j.jcou.2016.08.007>.
- [54] R. Frost, M. Hales, D. Wain, Raman spectroscopy of smithsonite, *J. Raman Spectrosc.* 39 (2008) 108–114.
- [55] T. Sakurada, S. Hashimoto, Y. Tsuchiya, S. Tachibana, M. Suzuki, K. Shimizu, Lateral resolution of EDX analysis with ultra low acceleration voltage SEM, *J. Surf. Anal.* 12 (2005) 118–121.
- [56] D. Miles, P. Cameron, D. Mattia, Hierarchical 3D ZnO nanowire structures via fast anodization of zinc, *J. Mater. Chem. A*. 3 (2015) 17569–17577.
- [57] D. Stoilova, V. Koleva, V. Vassileva, Infrared study of some synthetic phases of malachite (Cu<sub>2</sub>(OH)<sub>2</sub>CO<sub>3</sub>)-hydrozincite (Zn<sub>5</sub>(OH)<sub>6</sub>(CO<sub>3</sub>)<sub>2</sub>) series, *Spectrochim. Acta Part A Mol. Biomol. Spectrosc.* 58 (2002) 2051–2059, [https://doi.org/10.1016/S1386-1425\(01\)00677-1](https://doi.org/10.1016/S1386-1425(01)00677-1).
- [58] M.C. Hales, R.L. Frost, Synthesis and vibrational spectroscopic characterisation of synthetic hydrozincite and smithsonite, *Polyhedron* 26 (2007) 4955–4962, <https://doi.org/10.1016/j.poly.2007.07.002>.
- [59] N. LeBozec, D. Thierry, D. Persson, C.K. Riener, G. Luckeneder, Influence of microstructure of zinc-aluminium-magnesium alloy coated steel on the corrosion behavior in outdoor marine atmosphere, *Surf. Coating. Technol.* 374 (2019) 897–909, <https://doi.org/10.1016/j.surfcoat.2019.06.052>.
- [60] R. Sako, J. Sakai, Effect of curing temperature on coating structure and corrosion resistance of ammonium zirconium carbonate on galvanized steel surface, *Surf. Coating. Technol.* 219 (2013) 42–49, <https://doi.org/10.1016/j.surfcoat.2012.12.050>.
- [61] A. Kaleva, J. Nikkanen, S. Heinonen, V. Saarimaa, T. Vuorinen, E. Levänen, Synthesis of ZnO nanowires with supercritical carbon dioxide and post heat treatment, *Nanotechnology* 29 (2018) 1–7.
- [62] J.L. Jambor, Studies of basic copper and zinc carbonates: 1-synthetic zinc carbonates and their relationship of hydrozincite, *Can. Mineral.* 8 (1964) 92–108.
- [63] J.D. Yoo, K. Ogle, P. Volovitch, The effect of synthetic zinc corrosion products on corrosion of electrogalvanized steel: I. Cathodic reactivity under zinc corrosion products, *Corrosion Sci.* 81 (2014) 11–20, <https://doi.org/10.1016/j.corsci.2013.11.045>.







